

PHOTORESPONSIVE SYSTEMS FOR BIOMOLECULAR APPLICATIONS

DISSERTATION

zur Erlangung des Doktorgrades
der Naturwissenschaften

Vorgelegt beim Fachbereich
Biochemie, Chemie und Pharmazie
der Johann Wolfgang Goethe-Universität
in Frankfurt am Main

von

Christoph Kaiser

aus Rotthalmünster

Frankfurt am Main 2021
(D30)

Vom Fachbereich Biochemie, Chemie und Pharmazie der
Johann Wolfgang Goethe-Universität als Dissertation angenommen.

Dekan: Prof. Dr. Clemens Glaubitz

1. Gutachter: Prof. Dr. Josef Wachtveitl

2. Gutachter: Prof. Dr. Alexander Heckel

Datum der Disputation: _____

„Phantasie ist wichtiger als Wissen.

Wissen ist begrenzt, Phantasie aber umfasst die Welt.“

- Albert Einstein

Publikationen

(* - die Beiträge dieser Autoren sind als gleich anzusehen)

- [I] **Thermal, Photochromic and Dynamic Properties of Water-Soluble Spiropyrans**
C. Kaiser*, T. Halbritter*, A. Heckel, J. Wachtveitl,
ChemistrySelect **2017**, *2*, 4111-4123, DOI: 10.1002/slct.201700868.
- [II] **Pyridine-Spiropyran Derivative as a Persistent, Reversible Photoacid in Water**
T. Halbritter*, C. Kaiser*, J. Wachtveitl, A. Heckel,
J. Org. Chem. **2017**, *82*, 8040-8047, DOI: 10.1021/acs.joc.7b01268.
- [III] **Proton-Transfer Dynamics of Photoacidic Merocyanines in Aqueous Solution**
C. Kaiser, T. Halbritter, A. Heckel, J. Wachtveitl,
Chem. Eur. J. **2021**, *27*, 9160-9173, DOI: 10.1002/chem.202100168.
- [IV] **What Defines a Synthetic Riboswitch? - Conformational Dynamics of Ciprofloxacin Aptamers with Similar Binding Affinities but Varying Regulatory Potentials**
C. Kaiser, J. Schneider, F. Groher, B. Suess, J. Wachtveitl,
Nucleic Acids Res. **2021**, *49*, 3661-3671, DOI: 10.1093/nar/gkab166.
- [V] **A Light-Responsive RNA Aptamer for an Azobenzene Derivative**
T. S. Lotz*, T. Halbritter*, C. Kaiser, M. M. Rudolph, L. Kraus, F. Groher, S. Steinwand, J. Wachtveitl, A. Heckel, B. Suess,
Nucleic Acids Res. **2019**, *47*, 2029-2040, DOI: 10.1093/nar/gky1225.

The Interplay of Nanoconfinement and pH from the Perspective of a Dye-Reporter Molecule

R. Brilmayer*, M. Bodrecht*, C. Kaiser, H. Breitzke, B. Kumari, J. Wachtveitl, G. Buntkowsky, A. Andrieu-Brunsen,
ChemNanoMat **2020**, *6*, 1843-1853, DOI: 10.1002/cnma.202000423.

Konferenzbeiträge

- **CLiC/CEF Conference - "Design and Light Control"**
Niedernberg, 28.08.-01.09-2017
Poster: *Pyridine-Spiropyran Derivative as a Persistent, Reversible Photoacid in Water*
- **Fusion Conferences - "Frontiers in Photochemistry"**
Cancún Mexiko, 18-21.02.2018
Presentation: *Pyridine-Spiropyran Derivative as a Persistent, Reversible Photoacid in Water*
- **SFB 902 Symposium - "Understanding RNA-based Regulation in Cells"**
Campus Riedberg, Frankfurt/Main, 29-30.8.2018
Presentation: *Binding Dynamics of Antibiotic-Sensing RNA Aptamers*
- **SFB 902 - "Spring School"**
Online Meeting, 27-28.4.2021
Presentation: *Folding Dynamics of the Tetracycline-Binding Aptamer*
(Best presentation award)

Zusammenfassung

Die vorliegende Arbeit befasst sich einerseits mit der Untersuchung von Photoschaltern als niedermolekulare lichtsensitive Komponenten für biochemische Anwendungen und andererseits mit künstlichen RNA Aptameren als makromolekulare Regulationseinheiten zur Konstruktion von funktionellen Riboschaltern. Durch Kombination beider Schaltsysteme, konnte ein spezifisches RNA Aptamer entwickelt werden, dessen Ligandbindung erfolgreich und reversibel durch Lichteinwirkung steuerbar ist.

Photoschalter, die sich durch Licht reversibel in unterschiedliche isomere Formen umwandeln lassen, weisen ein außerordentliches Potenzial auf, um zielgerichtet lichtabhängige biochemische Systeme zu entwickeln. Neben den prominentesten Vertretern, den Azobenzolen, wurden hier in erster Linie Spiropyrane als alternative Photoschalter charakterisiert. In wässriger Lösung zeigt diese Verbindungsklasse ein sehr komplexes und vielversprechendes Verhalten, da die lichtinduzierte Strukturisomerisierung von der geschlossenen Spiropyranform hin zum ringgeöffneten Merocyanin mit einer drastischen Veränderung der elektronischen Beschaffenheit sowie der Polarität einher geht. Durch spektroskopische Studien mittels statischer und zeitaufgelöster Methoden wurden verschiedene Verbindungen im Hinblick auf ihre praktischen Schalteigenschaften und ihre Photodynamik im angeregten Zustand untersucht.

Die Py-BIPS Verbindungen **1** und **2**, wie auch die Nitro-BIPS Verbindungen **3** und **4**, zeigen in wässriger Lösung sowohl photo- als auch thermochrome Charakteristika. Sie können im neutralen pH-Bereich alle photochemisch gesteuert werden, wobei sie sich stark in den thermischen Reaktionsraten und in der Stabilisierung der offenen Merocyaninform unterscheiden. Während MePy-BIPS **1** als nahezu reines Spiropyran in Lösung vorliegt, wird das Gleichgewicht durch die elektronenziehenden Nitrogruppen der Verbindungen **3** und **4** stark zum Merocyanin hin verschoben. Interessanterweise bildet sich für das unmethylierte Py-BIPS **2** innerhalb weniger Minuten eine thermische Gleichverteilung zwischen beiden Isomeren. Durch Belichtung mit sichtbarem Licht kann diese gänzlich zur geschlossenen Form hin verschoben werden, wobei sich in diesem Fall das ursprüngliche Gleichgewicht

wieder thermisch regeneriert. In diesem Schaltmodus kann so eine für Spiropyrane außergewöhnlich hohe Schaltamplitude von etwa 50% über mehrere Zyklen stabil beibehalten werden. Darüber hinaus kann auf die Verwendung von schädlichem UV-Licht zur Ringöffnung verzichtet werden, wodurch eine photolytische Zersetzung der Substanz und auch potenzieller biologischer Zielsysteme verhindert wird.

Nach Protonierung des Phenolatsauerstoffes können Merocyanine als Photosäuren verwendet werden, die bei lichtinduziertem Ringschluss ein Proton freisetzen. Obwohl mechanistisch nicht zur Gänze geklärt, war diese Reaktivität bereits Bestandteil zahlreicher Studien und Anwendungen. Die hier präsentierte Py-BIPS Verbindung **2**, weist zudem eine weitere weniger saure Protonierungsstelle am Pyridinstickstoff auf, weshalb je nach pH-Wert verschiedene protonierte Spezies beider Isomere vorliegen. Allerdings unterscheiden sich die pK_s -Werte dieser Position für beide Photoisomere um zwei Einheiten. Der pK_s -Wert des Merocyanins HMC liegt bei 6.8, wohingegen für das Spiropyran HSP ein Wert von 4.8 bestimmt wurde. Aufgrund dieser Differenz kann das betreffende Proton im pH Bereich von etwa 4,5 bis 7,5 reversibel freigesetzt werden, was sogar in Form eines signifikanten pH-Sprunges detektierbar ist. Je nach verwendeter Proben- und Pufferkonzentration kann so eine lichtinduzierte pH-Erniedrigung um bis zu 1,5 Einheiten erreicht werden, wobei der Ausgangswert thermisch in weniger als 5 Minuten regeneriert wird.

Mit einem pK_s -Wert von 3.2 ist das phenolische Proton des Merocyanins HMCH deutlich saurer, wobei der pK_s -Wert dieser Position stark vom Substitutionsmuster der Substanz abhängt. Durch zeitaufgelöste transiente Absorptionsstudien konnte gezeigt werden, dass sich die beiden protonierten Merocyanine HMC und HMCH der Py-BIPS Verbindung **2** fundamental in ihrer Photosäurereaktivität unterscheiden. Während das Pyridiniumproton von HMC erst nach Ringschluss im Grundzustand freigesetzt wird, wird das phenolische Proton von HMCH direkt nach Anregung im angeregten Zustand auf das Lösemittel übertragen. HMC fungiert demnach als so genannter „Photoacid Generator“ im Gegensatz zu HMCH, welches als Photosäure im klassischen Sinn angesehen werden muss. HMCH sowie auch die protonierten photosauren Merocyanine von Nitro-BIPS **3** und Dinitro-BIPS **4** setzen ihr phenolisches Proton innerhalb von 1-2 ps nach Anregung frei. Mit Hilfe des thermodynamischen Försterzyklusmodells, wurde für die untersuchten Substanzen eine pK_s -Erniedrigung um etwa 8 Einheiten abgeschätzt. Mit stark negativen pK_s -

Werten im angeregten Zustand von etwa -4.5, zählen diese protonierten Merocyanine zu den stärksten bisher bekannten Photosäuren. Dies erweitert das Anwendungspotenzial von Spiropyran-Merocyanin Photoschaltern erheblich, da sie als ultraschnelle Protonendonoren eingesetzt werden können, um verschiedenste protonabhängige Prozesse zu adressieren.

Mit RNA-Konstrukten als biochemisch nutzbare Wirkstoffe oder auch als Zielsysteme können völlig neuartige pharmakologische Wirkmechanismen entwickelt werden, da RNA in der Lage ist auf unterschiedlichen zellulären Regulationsebenen zu agieren. Besonders so genannte Riboschalter stellen vielseitige Regulationselemente dar, die durch eine spezifische Ligandbindung an ihre Aptamerdomäne die Expression des nachfolgenden Genabschnittes regulieren können. Derartige Aptamermotive können prinzipiell für nahezu jeden erdenklichen Liganden durch einen repetitiven *in vitro* Selektionsprozess namens „Systematic Evolution of Ligands by Exponential Enrichment“ (SELEX) erzeugt werden. Um so gewonnene künstliche Aptamere als funktionelle Ligandbindungsmodule für *in vivo* Riboschalter verwenden zu können, müssen sie allerdings nicht nur eine hohe Ligandaffinität aufweisen, sondern bestimmte konformationelle Kriterien erfüllen. Eine ligandinduzierte dynamische Strukturänderung der RNA gilt als Voraussetzung für eine Aktivität als Riboschalter, wobei auch das Ausmaß der Vorfaltung des Aptamers sowie die Abhängigkeit der Tertiärstruktur von Magnesium eine tragende Rolle spielen. Funktionelle Aptamere sind außerdem zumeist deutlich weniger angereichert als nicht-funktionelle, was die Frage aufwirft inwiefern der Selektionsprozess dahingehend optimiert werden kann.

Die Untersuchungen des Tetrazyklin (TC) -bindenden Aptamers zeigen, dass Magnesium nicht nur zur Bildung einer bindungskompetenten Aptamerkonformation benötigt wird, sondern auch in den Ligandbindungsprozess involviert sein kann. Nach der Assoziation von TC an die Bindetasche des Aptamers wird eine strukturelle Adaption der RNA ausgelöst, die sich durch Änderungen der Tertiärstruktur zu entfernten Regionen fortpflanzt. Die finale Konformation in der Region der Dreifachhelix wird erst nach Ligandbindung in Abhängigkeit von Magnesium etabliert. Da das TC Aptamer bereits erfolgreich für unterschiedliche Riboschalter verwendet wurde, scheint die beschriebene Strukturänderung ausreichend zu sein, um eine regulatorische Funktionalität zu ermöglichen.

Zur Aufklärung essenzieller Unterschiede zwischen aktiven und inaktiven Aptameren wurden weiterhin drei Ciprofloxacin (CFX) -bindende Aptamere verglichen, die zwar ähnliche Affinitäten, aber stark unterschiedliche Regulationspotenziale aufweisen. Interessanterweise zeigt das CFX-bindende Aptamer A eine ähnliche Magnesiumabhängigkeit wie das TC Aptamer, aber keine regulatorische Aktivität. Die beiden anderen CFX Aptamerkandidaten preRS und RS weisen hingegen ein hohes Regulationspotenzial auf. Sie entstammen derselben Selektion, falten sich aber nahezu magnesiumunabhängig. Der Einfluss von Magnesium kann hier also kein Ausschlusskriterium sein, obwohl eine niedrige Kationenkonzentration während des SELEX-Prozesses generell zu bevorzugen ist. Ein funktioneller *in vivo* Riboschalter muss unter physiologischen Magnesiumbedingungen (0,5-1,5 mM) bindungs- und regulationsfähig sein. Zudem scheint eine erhöhte Verfügbarkeit von Magnesium zu einer präferierten Anreicherung stark vorgefalteter Aptamere von niedriger struktureller Komplexität zu führen.

Zeitaufgelösten Studien zufolge wird die Kinetik der Ligandbindung für alle drei CFX Aptamere durch zwei Schritte beschrieben – einer initialen Assoziation von CFX an die Bindetasche, gefolgt von einer strukturellen Adaption der Aptamere an den Liganden. In Anbetracht der Daten wird eine klare Korrelation zwischen den Regulationspotenzialen der drei RNA Aptamere und ihrer Bindungskinetik deutlich. Je schneller und irreversibler sich die strukturelle Anpassung der Aptamerkandidaten vollzieht, desto höher ist das verzeichnete Regulationspotenzial als translationeller *in vivo* Riboschalter. Der zweite Bindungsschritt ist damit energetisch stark begünstigt und beschleunigt. Außerdem wird die Lebensdauer des gebundenen Zustandes erhöht, was je nach Regulationsmechanismus ein kritischer Parameter sein kann. Im Gegensatz zu den aktiven Aptamerkandidaten preRS und RS, ist beim inaktiven A die Assoziation des Liganden bevorzugt. Die Bindetasche ist daher als stärker vorgeformt anzunehmen und die Strukturänderung damit als weniger ausgeprägt. Die Ergebnisse erlauben darüber hinaus Vorschläge für optimierte SELEX-Protokolle, so dass funktionelle Aptamere gezielter generiert werden können. Neben physiologischen Bedingungen in der Selektion, sind auch die einzelnen Wasch- und Elutionsschritte maßgeblich für die Eigenschaften von angereicherten Strukturmotiven.

Die erfolgreiche Kombination eines lichtabhängigen molekularen Schalters und eines künstlichen spezifischen RNA Aptamers ist ein bedeutender Schritt zur

Erlangung einer reversiblen Kontrolle über funktionale biomolekulare Systeme. Durch Integration von Azobenzol in die Struktur des Antibiotikums Chloramphenicol (Cm) konnte der photoschaltbare Ligand azoCm entwickelt werden, der hervorragende Schalteigenschaften in physiologischer Umgebung annimmt. Nachfolgend wurden systematisch modifizierte Selektionen durchgeführt, um Aptamere zu generieren die spezifisch nur an das stabile Isomer *trans*-azoCm binden. Im kritischen Belichtungsschritt konnten Aptamere, die nach *trans/cis*-Isomerisierung dissoziierten, aufgefangen und vervielfältigt werden. So wurde zunehmend ein bestimmtes Strukturmotiv angereichert, das für die Selektivität der Aptamere verantwortlich ist. Bei Untersuchung einiger ausgewählter Aptamere stellte sich ein Kandidat als vielversprechend heraus. Gegenüber *trans*-azoCm weist dieser eine Dissoziationskonstante von 545 nM auf, während die Affinitätsmessung mit *cis*-azoCm keine Ligandbindung anzeigte. Zuletzt konnte durch Zirkulardichroismus-basierte Schaltexperimente nachgewiesen werden, dass das ausgewählte Aptamer bei wiederholter lichtinduzierter Isomerisierung des Liganden tatsächlich eine reproduzierbar reversible Bindung und Strukturänderung vollzieht. Damit konnte der Entwicklungsprozess eines lichtabhängigen Systems aus Photoschalterligand und spezifischem RNA Aptamer erfolgreich abgeschlossen und etabliert werden.

Table of Contents

1	Introduction	1
2	Theoretical Framework	5
2.1	UV/vis Spectroscopy	5
2.2	Photochemical Relaxation Processes	7
2.3	Time-Resolved Spectroscopic Techniques	9
2.3.1	Transient Absorption Spectroscopy	9
2.3.2	Time-Correlated Single Photon Counting	17
2.3.3	Stopped-Flow Spectroscopy	18
2.4	Photoresponsive Biomolecular Systems	20
2.4.1	Organic Photoswitches	21
2.4.2	Spiropyran-Merocyanine Switches	23
2.4.3	Photoswitches in Biomolecular Assemblies	25
2.5	RNA Aptamers	26
2.5.1	Natural Riboswitches	26
2.5.2	Artificial RNA Aptamers	28
2.5.3	Engineered Riboswitches	29
3	Aim of This Work	33
4	Experimental Results	37
4.1	Photoswitches in Aqueous Solution	37
4.1.1	Photochromism of Water-Soluble Spiroyrans	38
4.1.2	pH-Gated Photochromism of Py-BIPS	45
4.1.3	Proton-Transfer Dynamics of Merocyanine Photoacids	49
4.2	Antibiotic-Binding RNA Aptamers	58
4.2.1	Folding of the TC-Binding Aptamer	58
4.2.2	Regulatory Potentials of CFX-Binding Aptamers	74
4.3	A Light-Responsive azoCm-Binding Aptamer	82
5	Conclusion	89
6	Bibliography	93
7	Publications	103
7.1	Declaration of the Own Contribution for Each Publication	103
7.2	Kaiser et al., <i>ChemistrySelect</i> 2017, 2	106

7.3 Halbritter et al., <i>J. Org. Chem.</i> 2017, 82.....	120
7.4 Kaiser et al., <i>Chem. Eur. J.</i> 2021, 27.....	129
7.5 Kaiser et al., <i>Nucleic Acids Res.</i> 2021, 49.....	144
7.6 Lotz et al., <i>Nucleic Acids Res.</i> 2019, 47	156
7.7 Brilmayer et al., <i>ChemNanoMat.</i> 2020, 6	169
List of Figures.....	181
List of Tables	186
Abbreviations	187
Appendix.....	189

1 INTRODUCTION

During the past century, the technical use of visible light and of electromagnetic radiation in general has moved increasingly into the focus of many industries and research fields. Achievements like the discovery of the photoelectric effect by A. Einstein in 1905^[1] and the preparation of the first practical solar cell at Bell Laboratories in 1954,^[2] enabled and fueled an entire energy sector. In parallel, novel artificial light sources were invented, which gave access to countless applications and scientific methodologies. The development of LEDs (light emitting diode) and in particular that of the first functional ruby laser (light amplification by stimulated emission of radiation) in 1960^[3] brought about a breakthrough in the utilization of light as an extraordinarily precise tool. Meanwhile, lasers have made their way into surveying and security technology, data processing and transmission, and even into medicine and scientific research. The development of sophisticated methodologies like ultrafast time-resolved spectroscopy^[4] or sub-diffraction microscopy,^[5] that allow for unprecedented analytical possibilities, were even awarded the Nobel Prize in 1999 and 2014, respectively. In 2018, also the elaboration of the chirped pulse amplification^[6] (CPA) principle to enable the generation of high energy laser pulses was honored with the Nobel prize together with the biomedical application of lasers as optical nanoscale tweezers.^[7]

The technical advances have tremendously extended our knowledge about photoinduced processes and the efficient conversion of light into other applicable forms of energy. Nature itself provides several excellent examples for highly efficient light-sensitive molecular systems that translate the energy of an incident photon into a distinct biochemical response. The leaf pigment chlorophyll, embedded in the light-harvesting complexes of plants, enables photosynthesis via photolytic oxidation of water, which in turn initiates a series of protein-coupled redox reactions. Other fascinating representatives for photoresponsive proteins are flavoproteins or phytochromes, that carry light-sensitive flavin or bilin chromophores, respectively, and are responsible for phototropic growth and shade avoidance of plants. Of course, also rhodopsins must be listed here that allow us to see as result of a structural

isomerization of the retinal chromophore that converts light energy into a change within the protein tertiary structure. Each of those light-dependent systems is furthermore fully reversible and the initial state is recovered rapidly.

In analogy to such natural energy conversion systems, the targeted manipulation of biochemical systems by use of light has become a growing area of endeavor in pharmacological and medical research. Light represents an outstanding external stimulus to address biomolecules. It can be operated non-invasively with unrivalled spatial and temporal precision and if applied properly it is harmless to biologic organisms. To gain light-control over a desired biochemical effect, a synthetic photoresponsive component can be employed to modify the biologic function of a target system. Taking advantage of the vast number of light-sensitive molecular fragments accessible through synthetic chemistry, the combination of photochemistry and pharmacology results in the evolving field of photopharmacology.^[8-10]

The most promising approach to design light-controlled systems with reversible functionality is to engage so-called photoswitches that enable an interconversion between two or more structurally different states with characteristic properties by irradiation with light. The change of molecular properties can be coupled to an environmental response by smart implementation of the photoswitch unit into a macromolecular assembly. For instance, target biomolecules such as enzymes, receptors or ion channels can be covalently modified with a photoswitch to change their conformation and thus their biologic function in a reversible light-dependent manner. Furthermore, photoswitch moieties can be successfully integrated into the molecular structures of bioactive small molecular compounds like receptor-agonists^[11] or antibiotics^[12] for application as freely diffusing ligand. Assuming the different photoisomeric states of such modified compounds adopt different pharmacokinetic properties, their activity can be manipulated reversibly through irradiation.

Among the great variety of biomolecules as potential targets for drug design, RNA plays an outstanding role. The discoveries of catalytically active ribozymes challenged the central dogma of biology stated by F. Crick^[13] in 1958 to explain the flow of genetic information in living cells from DNA to RNA and finally to functional proteins. RNA is not only capable of storing and mediating genetic information just as DNA, but it is also responsible for diverse cellular regulation mechanisms, like proteins. RNA is therefore able to act on different levels of gene expression and cellular metabolism

pathways. The prevailing RNA world hypothesis even recognizes RNA as the starting point of the evolution of life.^[14] At the latest since the approval of the mRNA vaccine for protection against the Coronavirus disease in 2020,^[15] it is clear that RNA-based drug design is about to become a key technology to solve long-standing medical problems and to explore fundamentally new pharmacological mechanisms of action.

With the discovery of riboswitches in 2002,^[16,17] a new class of regulatory mRNA elements moved into the focus of biochemical research. Riboswitches translate the sensing of a small molecular ligand by their aptamer domain into a change in the processing of the genetic information contained in the downstream expression platform. The function of these *cis*-regulatory switches relies on the highly diverse structural complexity of single-stranded RNA. Remarkably, an *in vitro* process called systematic evolution of ligands by exponential enrichment^[18] (SELEX) has been developed even earlier that makes it possible to produce artificial high affinity aptamers for actually any effector compound of choice. Given this opportunity, strong efforts were made to engineer artificial RNA aptamers into functional *in vivo* riboswitches as potential new pharmacological tools successfully.

This thesis aims at connecting the use of photoswitches in a photopharmacological context and the engineering of artificial riboswitches. On the one hand, spiropyran and azobenzene photoswitches are investigated in view of their applicability in biochemical environments. On the other hand, artificial antibiotic-sensing RNA aptamers are studied regarding essential factors for their *in vivo* regulatory capacities. Ultimately, the design process of a light-responsive RNA aptamer is presented that selectively binds to only one photoisomer of its photoswitch ligand. To elaborate on the different aspects of the individual projects, suitable static and time-resolved spectroscopic experiments are executed.

2 THEORETICAL FRAMEWORK

2.1 UV/VIS SPECTROSCOPY

To fully describe the properties of light, it must be treated as a particle and as a wave at the same time. This quantum mechanical concept, known as wave-particle-dualism, explains the non-classical behaviour of quantum objects in the realm of molecules, atoms or subatomic particles. Photons represent the elementary quanta of light, with discrete energy but without mass. Following the wave formalism, photons are composed of an oscillating electromagnetic field with the wavelength λ as its main characteristic. The entire electromagnetic spectrum, depicted in Figure 2.1, is divided in several ranges depending on the wavelength scale.

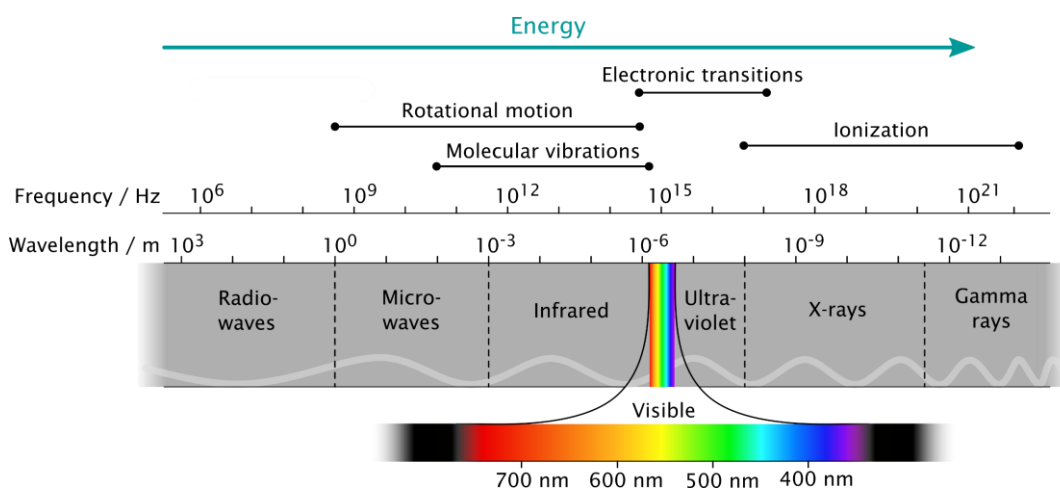


Figure 2.1. Illustration of the electromagnetic spectrum provided with scales of wavelength and frequency. The molecular transitions, corresponding to the different ranges of the spectrum are shown above.

The narrow visible part of the spectrum, that we are able to perceive, is centered in between the ultraviolet (UV) and the infrared (IR) region and extends from approximately 400 nm to 700 nm. The energy E of a photon is directly correlated with its wavelength λ or frequency ν , which is stated by the Planck-Einstein relation.

$$\Delta E = h \nu = \frac{h c}{\lambda} \quad (2.1)$$

Here, h represents Planck's constant and c represents the speed of light. In some contexts, the use of wavenumbers $\tilde{\nu}$ is also common, which represent the reciprocal wavelength. The diverse energetic scales of the different regions of the electromagnetic spectrum open up various possibilities for technical applications. Depending on the energy of the applied electromagnetic radiation, specific interactions with matter can be induced. If the energy of the incident photon is equal to the energy gap of an allowed transition between two energetic levels of the material, the essential resonance condition is fulfilled for absorption to take place and the respective transition is induced.

Molecular spectroscopy aims at investigating potential transitions, initiated upon absorption of photons and thus allows for an evaluation of specific molecular properties. By means of infrared (IR) spectroscopy or Raman spectroscopy, for example, molecular vibrations can be monitored. However, in optical or UV/vis spectroscopy, a wavelength range from roughly 200 nm to 800 nm is applied, which is suitable for investigating electronic transitions of molecules. The involved energetic levels are represented by the molecular orbitals, which dictate the distribution of electrons within the molecular scaffold. A typical transition would be an excitation of an electron from the highest occupied molecular orbital (HOMO) to the lowest unoccupied molecular orbital (LUMO). The HOMO refers to the electronic ground state of the molecule, while the LUMO serves as the first excited electronic state.

UV/vis spectroscopy of organic molecules is mostly conducted with sample solutions. The absorbance A is determined via Lambert-Beer's law^[19] (Equation 2.2) by measuring the ratio of the incident light intensity I_0 and the residual intensity I , transmitted through the sample.

$$A = -\lg \frac{I}{I_0} = \varepsilon c d \quad (2.2)$$

The absorbance furthermore depends on the concentration c of the sample solution, the substance specific molar extinction coefficient ε (which is a function of the wavelength) and the path length d , that the light passes through. Absorption spectra of organic molecules display the wavelength-dependent absorbance of the compound. The absorbance is typically measured as optical density (OD) of the sample solution and the linear behaviour of Lambert-Beer's law is restricted to very low concentrations. If a photon is absorbed and a discrete electronic transition occurs,

only a sharp absorption line is expected to appear in the spectrum. Though, the spectra of sample solutions at ambient temperature typically exhibit broadened absorption bands, which is due to several effects. First, there is a natural line width as consequence of Heisenberg's uncertainty principle. Second, the relatively high energy of UV/vis photons also induces lower energetic vibrational transitions that occur in parallel to electronic excitation. Apart from that, also effects like Doppler broadening^[20] or collisional broadening^[21] contribute to the observed width of absorption signals.

2.2 PHOTOCHEMICAL RELAXATION PROCESSES

The successful absorption of a photon with suitable energy promotes an organic molecule to an electronically excited state, with its own physicochemical properties. The absorbed energy can be consecutively released through different relaxation pathways, commonly illustrated by the Jablonski diagram (Figure 2.2).^[22] The electronic ground state, which is a singlet state with paired electrons, is denoted by S_0 and the first and second excited singlet states by S_1 and S_2 , respectively. In the triplet state T_1 , the electrons are unpaired and each of these electronic states can adopt a number of vibrationally hot states v_i . The possible relaxation pathways occur on different timescales and partially involve transitions between electronic as well as vibrational states.

Electronic excitation from the S_0 ground state to a higher singlet state takes place on a femtosecond ($\text{fs} = 10^{-15} \text{ s}$) time scale. This virtually instantaneous process is illustrated by vertical lines, as it takes place much faster than the displacement of the nuclei of the molecule, which is stated by the Born-Oppenheimer approximation^[23] and the Franck-Condon principle.^[24,25] The following excited state relaxation pathways can be subdivided in radiative and non-radiative pathways. If a vibrationally hot excited electronic state is populated, the respective vibrational ground state can be reached non-radiatively via vibrational cooling (VC). This proceeds rapidly within tens of fs to a few picoseconds ($\text{ps} = 10^{-12} \text{ s}$) and is mostly accompanied by solvent rearrangements around the excited molecule.

On a similar timescale, the excited electronic state can undergo internal conversion (IC) to the subjacent electronic state, if an energetically degenerate vibrational state

is available. As last non-radiative transition, a conversion of the S_1 state into the triplet state T_1 can occur via intersystem crossing (ISC). This process implies a change of the electron spin multiplicity and therefore occurs significantly slower. The time scale of ISC typically varies between milliseconds ($\text{ms} = 10^{-3} \text{ s}$) and nanoseconds ($\text{ns} = 10^{-8} \text{ s}$) depending on the molecule of interest.

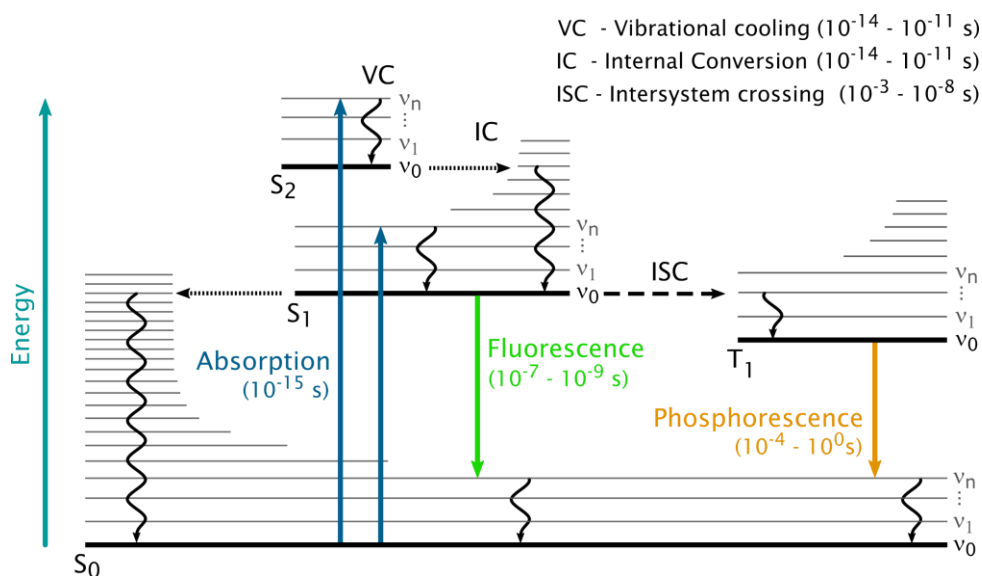


Figure 2.2. Jablonski diagram: photochemical relaxation pathways after absorption of a photon. Radiative transitions are indicated by solid coloured arrows and non-radiative transitions by black wavy or dashed arrows. S_i and T_i represent the involved electronic singlet and triplet states, respectively, and the states v_i indicate excited vibrational modes.

The radiative decay pathways are called fluorescence and phosphorescence. According to Kasha's rule,^[26] both spontaneous emission pathways occur from the vibrational ground state of the corresponding excited electronic state towards the electronic ground state. Fluorescence, as a singlet-singlet transition, takes place on the ns time scale and the fluorescence lifetime τ_f is an essential attribute of fluorophores. The emitted photons are of lower energy as the absorbed ones, due to the partial dissipation of energy by non-radiative pathways like VC or solvent redistribution. The spectral difference between the absorption and emission maxima is referred to as Stokes shift.^[22] Thus, fluorescence spectra typically appear as bathochromically shifted mirror images of the S_1 absorption bands. Phosphorescence on the other hand, occurs drastically slower and it can take up to seconds or even minutes, as it engages a spin inversion, just as ISC.

2.3 TIME-RESOLVED SPECTROSCOPIC TECHNIQUES

The photodynamics of excited molecules can proceed on substantially different time scales. Hence, the spectroscopic technique to monitor a specific pathway or timeframe of the photodynamics, must be chosen wisely. To access the time scales and the time-dependent pathways of interest, sophisticated time-resolved methodologies are required. Apparently, the achievable time-resolution should be significantly faster, than the investigated processes. The different experimental spectroscopic techniques, applied in this work, are explained in the following sections as well as their theoretical principles.

2.3.1 TRANSIENT ABSORPTION SPECTROSCOPY

An explicitly powerful tool to map ultrafast excited state dynamics in the UV/vis range within the femtosecond-nanosecond time scale is transient absorption (TA) spectroscopy.^[4] It is based on the pump/probe principle, which makes use of ultrashort laser pulses in order to achieve the required time-resolution. As shown in Figure 2.3, the output of a pulsed laser is split in two branches: (i) the pump pulse serves as excitation pulse to induce a desired electronic transition within the sample and (ii) the probe pulse senses the subsequent spectral response of the sample.

A temporal delay between both pulses is realized by introducing a variable delay stage in one of the branches. The difference of path lengths is then directly correlated with the relative time delay between the pulses at the sample position. In this way, a series of single spectra can be recorded in a time-resolved manner, by repetitive pumping and probing the sample while stepwise increasing the time delay. Taking the speed of light into account, micrometer step sizes of the delay stage result in femtosecond time delays between the two pulses. Typically, mechanical delay stages of approximately 30 cm length are used, which corresponds to a maximum time delay of few ns. This is also the technical upper limit of this approach, as the application of longer delay stages would entail increasing inaccuracies of the beam alignment. To overcome this limitation, the two pulses could also be provided by separate laser systems that are synchronized electronically. Yet, this solution lacks precision of the timing, especially at small delay times in the fs time scale.

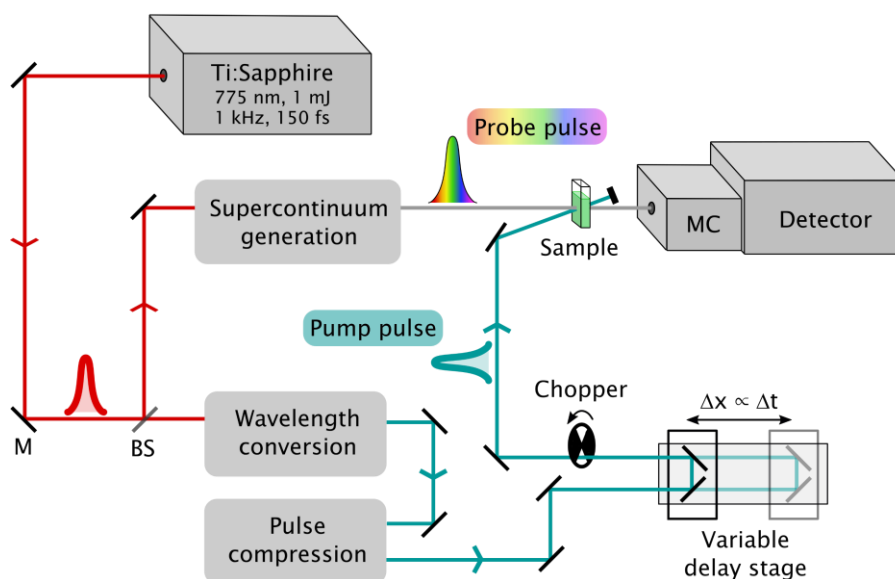


Figure 2.3. Schematic depiction of the applied UV/vis-pump/probe setup supplied by a pulsed Ti:Sapphire laser with a wavelength conversion and a pulse compression unit for the pump pulse and a variable delay stage as well as a chopping wheel. The probe pulse is converted into a supercontinuum, passes the sample, and is guided into the detection unit. MC - monochromator, M - mirror, BS - beam splitter.

To initiate a distinct electronic excitation, the pump pulse ought to be spectrally narrow and must be converted into the desired UV/vis wavelength. To this end, the fundamental output of the applied laser system can be subjected to different non-linear conversion processes, depending on the required wavelength. In contrast, the probe pulse should cover an extended spectral range to allow for broadband detection of the photodynamics. Via non-linear wavelength conversion, a supercontinuum (SC) probe pulse is generated, which then passes the sample and is guided through a monochromator into a spectrometer. The underlying principles and technical requirements for the execution of pump/probe experiments are explained in the following sections.

Generation of Ultrashort Pulses

To realize high intensity pulsed laser operation with fs pulse durations, the principle of modelocking is applied so that longitudinal modes within the laser resonator interfere constructively.^[27] In this work, the laser system *Clark MXR CPA 2001* was applied for the TA measurements. It consists of a continuous wave (cw) diode laser that pumps a passively modelocked erbium fiber oscillator to generate ultrashort pulses with a duration of roughly 100 fs and a central wavelength of 1550 nm. The

pulses are then frequency doubled in a non-linear crystal to obtain a central wavelength of 775 nm, but they are still of relatively low energy and must be further amplified. Therefore, the output of the fiber laser is coupled into a regenerative amplifier with a Ti³⁺-doped sapphire crystal (Ti:Sa, Ti³⁺:Al₂O₃) as laser medium. The population inversion in the Ti:Sa crystal is induced by another pump laser that comprises a Nd³⁺-doped yttrium-aluminium-garnet (Nd:YAG, Nd³⁺:Y₃Al₅O₁₂) crystal.

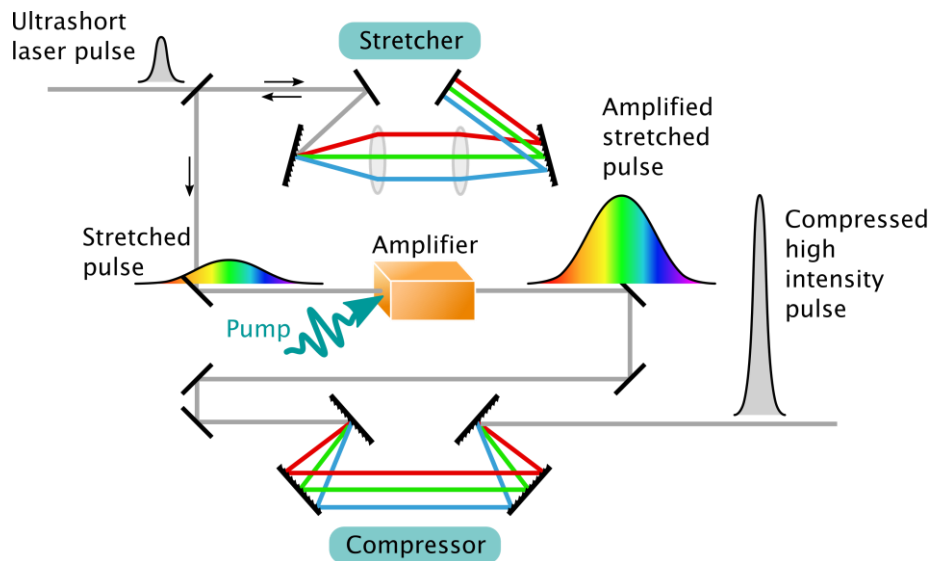


Figure 2.4. Principle of chirped pulse amplification (CPA). An ultrashort fs pulse of low intensity is stretched temporally, prior to amplification. The amplification medium is pumped simultaneously, which amplifies the stretched pulse. The pulse is then compressed again to a much higher intensity.

Via stimulated emission of the Ti:Sa crystal, the energy imparted is transferred to the 775 nm pulses, which can thus be amplified by several orders of magnitude. In order to prevent the optics from damage, the CPA principle^[6] is applied, which is illustrated in Figure 2.4. Prior to the amplification, the 775 nm pulses are stretched temporarily, whereby their intensity is lowered. After the stretched pulses are amplified, they are compressed again and finally decoupled from the resonator and guided towards the TA setup. This way, pulse durations of roughly 150 fs and energies of 800 μ J are obtained with a repetition rate of 1 kHz. The realization of the CPA principle is of exceptional importance since it enables the generation of drastically higher pulse energies than would be possible using a laser medium alone. The

invention of this principle in turn enabled numerous technical innovations based on pulsed lasers and especially high intensity pulses.

Non-linear Wavelength Conversion Processes

At elevated laser pulse intensities, non-linear optical (NLO) effects occur upon interaction with specific materials like non-linear crystals. In linear optics, the polarization of a material correlates linearly with the applied optical field. If the intensity of an incident laser pulse exceeds a certain threshold, the polarization yet responds in a non-linear way and becomes dependent on the electric field strength. The polarization $\vec{P}(t)$ is then defined by Equation 2.3 as a Taylor series of higher orders of the electric field $\vec{E}(t)$.

$$\vec{P}(t) = \varepsilon_0 \left(\sum_i \chi_i^{(1)} \vec{E}_i(t) + \sum_{i,j} \chi_{ij}^{(2)} \vec{E}_i(t) \vec{E}_j(t) + \sum_{i,j,k} \chi_{ijk}^{(3)} \vec{E}_i(t) \vec{E}_j(t) \vec{E}_k(t) + \dots \right) \quad (2.3)$$

The higher orders of non-linear susceptibilities of the material are represented by the tensors $\chi^{(2)}, \chi^{(3)} (\dots)$ and ε_0 is the dielectric constant. This phenomenon enables the interaction of multiple electromagnetic waves within a non-linear material. Mathematically, the propagation of a wave through a non-linear medium is described on basis of the Maxwell equations. The NLO processes are categorized by the order of the susceptibility χ , that determines the process. They furthermore depend on the applied material and on the crystal structure symmetry and the cut angle. Examples for non-linear crystals are β -barium borate (BBO, β -BaB₂O₄), potassium titanyl phosphate (KTP, KTiOPO₄) or lithium triborate (LBO, LiB₃O₅) but also more common materials like CaF₂ or glass exhibit non-linear properties under the influence of amplified laser pulses.

As mentioned earlier, broadband probe pulses are created by SC generation in a non-linear crystal. This process mainly originates from a superposition of third order NLO phenomena like self focusing and self phase modulation. Due to the Kerr effect, the refractive index of non-linear media varies with the laser pulse intensity, which

results in self focussing of the most intense contributions of a laser pulse. The spectral contributions of the incoming pulse experiences a shift in frequency because of self phase modulation, which broadens the pulse. The properties of the generated spectrum are dictated by the pulse properties as well as by the material. To create an SC in the vis range, the fundamental laser output is e.g. focused into a transparent sapphire or CaF_2 window.

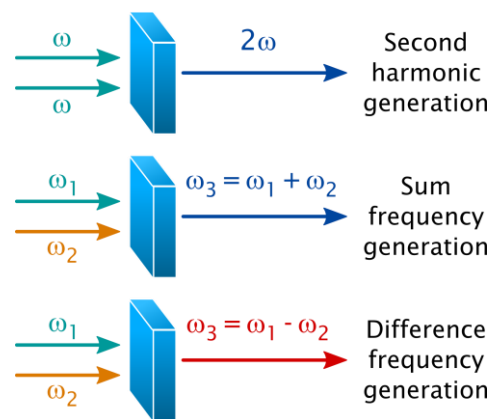


Figure 2.5. Second order non-linear frequency mixing processes of two incident pulses in a non-linear crystal.

Different to the probe pulse, the pump pulse should be spectrally narrow and depending on the sample, it has to be variable across the whole UV/vis range. Therefore, certain wavelength regions are accessible through particular NLO frequency mixing processes. If two different pulses are overlaid in a non-linear crystal and the phase matching condition is fulfilled, their angular frequencies ω can be combined in a second order process to a third output frequency (Figure 2.5).

When the obtained frequency equals the sum of the incident pulse frequencies, this is referred to as sum frequency generation (SFG). A special case thereof is second harmonic generation (SHG), where two pulses of similar frequencies are applied. Those possibilities can be used to create UV pulses, by combining two vis pulses in a BBO crystal. By applying SHG to the fundamental output (775 nm) of the herein used laser system, 388 nm pulses can be generated. Furthermore, also reduced frequencies in the IR range can be obtained by means of difference frequency generation (DFG) in a silver gallium sulfide (AGS, AgGaS_2) crystal for example.

A convenient method to create pulse wavelengths in the vis range, is non-collinear optical parametric amplification (NOPA) in a BBO crystal (Figure 2.6). Therefore, the fundamental is split and one part of it is frequency doubled by SHG to serve as pump pulse for the NOPA process. The other part of the fundamental is converted into a broadband SC by focusing into a sapphire window to be applied as NOPA seed. The

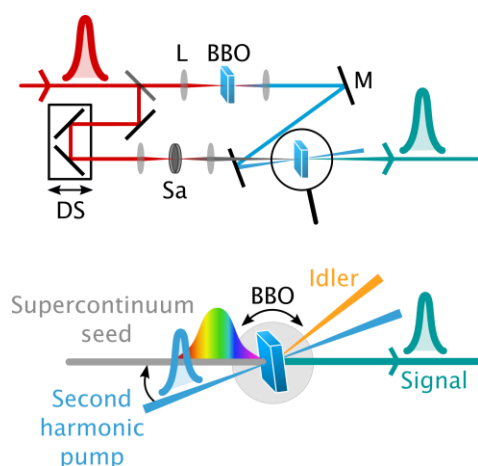


Figure 2.6. Schematic depiction of the setup assembly and the beam geometry for the NOPA process. L - Lens, M - mirror, DS - delay stage, Sa - sapphire window.

second harmonic pump and the SC seed are superimposed spatially within the BBO crystal, where the angle between the two pulses is critical for efficient amplification, as well as the inclination angle of the BBO. A variable delay stage is typically incorporated in the seed path, to adjust the temporal overlay of the pulses. The desired frequency can be amplified specifically to be finally used as pump pulse for sample excitation in a TA experiment. The wavelength range that is accessible via NOPA is restricted to the

seed spectrum which extends roughly from 470 nm to 800 nm, if a sapphire window is applied. To create variable wavelengths below 450 nm, the vis NOPA output can be subjected to an SFG process together with another fundamental pulse.

Execution of a Transient Absorption Experiment

The photoinduced spectral changes after optical excitation of a sample are extremely small, which is why the signals are measured in reference to the unexcited sample. Absorbance difference spectra are calculated by subtracting the ground state absorbance of the sample from the detected excited state signals. In the applied setup (Figure 2.3), this is realized by the implemented chopping scheme, where every second pump pulse is blocked by a chopper wheel. Thereby, every second probe pulse detects the sample absorbance without excitation (Figure 2.7). Moreover, different chopping schemes can be applied for other referencing protocols. To reduce the effect of scattered excitation light on the recorded data, it can be collected from the pump pulse in a third time frame without probe pulse. Furthermore, fluctuations of the probe light intensity could be compensated by parallel acquisition of a branch of the probe which does not pass the sample cuvette.

Because of the referencing to the unexcited sample absorbance, positive as well as negative signals are displayed in the resulting difference absorption spectra. They arise from different reasons, as illustrated in Figure 2.8. The pump pulse typically

excites roughly 5% of the molecules within the sample volume into a higher electronic state (S_1). The lack of molecules in the ground state after excitation, results in a higher detected probe intensity in the range of the S_0 - S_1 absorption band. Hence, a negative difference signal, denoted as ground state bleach (GSB), is recorded. Each photoreaction pathway that leads to a repopulation of the ground state entails a decrease of the negative GSB signal.

The population in the excited state can undergo excited state absorption (ESA) into higher states S_n , which is observed as positive difference signals. Similarly, every new state that is populated throughout the photoreaction, such as a photoproduct or an intermediate species, is indicated by positive signals. Last, the probe pulse can induce stimulated emission (SE) from the excited into the ground state. The emission results in a negative signal and usually resembles the steady-state fluorescence of the sample. What complicates the signal assignment, is the fact that all signals are detected simultaneously. Thus, a superposition spectrum is recorded with multiple contributions of overlaid signals, as shown in Figure 2.8.

To conduct a TA experiment, also the polarization of the pump and probe pulses has to be considered and adjusted properly. The fundamental laser output is usually polarized horizontally, but the polarization can be altered due to the applied NLO

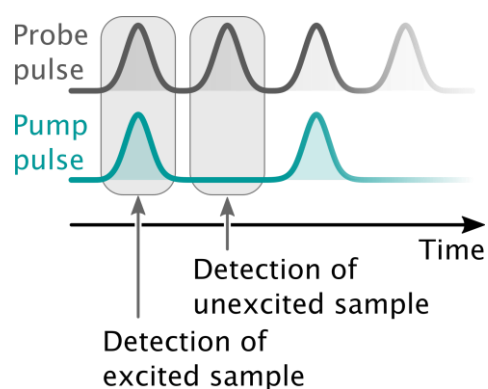


Figure 2.7. Applied chopping scheme: Every second pump pulse is blocked for referencing to the absorbance of the unexcited sample.

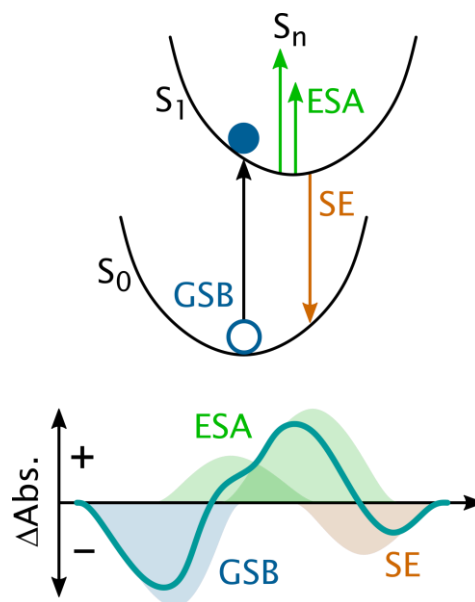


Figure 2.8. Origin of difference absorption signals in TA experiments and resulting difference spectrum with positive excited state absorption (ESA) and negative ground state bleach (GSB) and stimulated emission (SE) contributions.

wavelength conversion processes. To suppress contributions of anisotropy effects, the relative polarization between the pump and probe pulse is typically adjusted to the magic angle (54.7°) by a half-wave plate.

Around the zero point in time, the acquired TA data sets are superimposed with the so-called coherent artifact. This is due to the interaction of the pump pulse and the solvent and has to be subtracted from the raw data. The shape of the artifact can also be affected by the experimental setting and alignment. The coherent artifact itself can be recorded in a solvent measurement for further analysis. Its temporal width reveals the actual time-resolution of the experiment and is therefore associated with the instrumental response function (IRF).^[28] Furthermore, the data sets have to be processed to compensate for the group velocity dispersion (GVD). Since the propagation velocity is wavelength-dependent, the probe pulse is chirped and the signals around the zero point in time are thus distorted.

For kinetic analyses of the processed data sets, different approaches are feasible.^[28,29] Mostly, global fitting is applied, which means that the monitored wavelength range is fitted simultaneously. In global lifetime analysis (GLA), the acquired TA spectrum is approximated by a sum of exponential functions. The respective exponents correspond to lifetime components τ_i that reflect the observed signal progression. The number of lifetimes must be estimated and is usually based on a meaningful kinetic model. To avoid over-parametrization, the least number of lifetime components is preferred. Data fitting via GLA results in the decay associated spectra (DAS) of the determined lifetime components, showing the wavelength-dependent amplitudes. A positive amplitude indicates the decay of a positive signal or the increase of a negative while the opposite is true for a negative amplitude. Apart from GLA, the data can be fitted with a very large number of lifetimes, which is referred to as lifetime distribution analysis (LDA). This approach is not restricted by a given kinetic model and therefore provides a more unbiased perspective. Lifetime density maps (LDM) are obtained that display the temporal and spectral distribution of contributing lifetime components. Both GLA and LDA were applied in this work to analyse the recorded TA spectra. Analyses were performed with the kinetic fitting software OPTIMUS.^[30]

2.3.2 TIME-CORRELATED SINGLE PHOTON COUNTING

The fluorescence decay of a fluorophore molecule generally occurs on the nanosecond time scale and can be observed by means of time-correlated single photon counting (TCSPC). Similar to the pump/probe technique, this method requires a pulsed light source for sample excitation. Yet, no probe pulse is required, but the emitted photons are counted by a single photon detector with sufficient time-resolution. Basically, the time span between excitation and the emission of a photon is measured repetitively and the detected photons are summed up. Hence, a histogram of the counted photons is acquired which represents the fluorescence decay curve. The applied self-assembled TCSPC setup (Figure 2.9) is equipped with a photomultiplier tube (PMT, PicoQuant GmbH) for detection and bears two alternative light sources for excitation in different wavelength ranges.

On the one hand, a 80 MHz Ti:Sapphire laser system type Tsunami (SpectraPhysics) can be used with a fundamental wavelength that is variable from 700 nm to 1000 nm. The second harmonic thereof can also be generated, which is then tunable from 350 nm to 500 nm. The repetition rate of laser excitation can be reduced by a pulse picker, consisting of an acousto-optic modulator (AOM). On the other hand, pulsed light emitting diodes (LED) are available for excitation in the UV (310 nm, 330 nm, 340 nm and 360 nm, PicoQuant GmbH). The repetition rate for LED excitation is set by the LED controller device. In either case, the repetition rate must be adjusted, to avoid reexcitation of the sample, before the excited state decay is entirely over. Typically, repetition frequencies of a few MHz are applied. Furthermore, the excitation energy must be adjusted, so that only 1% of the excitation events results in the detection of a photon. Otherwise, a pile-up effect could occur due to the dead time of the detector electronics.

As shown in Figure 2.9, a trigger signal is branched off the excitation pathway to start data recording. The signal is either obtained from a photodiode (PD) in the case of laser excitation or from the LED controller. The impact of a photon on the PMT detector marks the stop of a single measurement. The detection events are recorded by a TimeHarp Single PCIe counter card, which enables data acquisition with 25 ps time-resolution. As a wavelength-selective detection is not feasible with the applied equipment, coloured glass filters are used to define the detected spectral range and

to minimize the effect of scattered light. The emitted photons are collected in a 90° geometry, within a darkened sample holder housing.

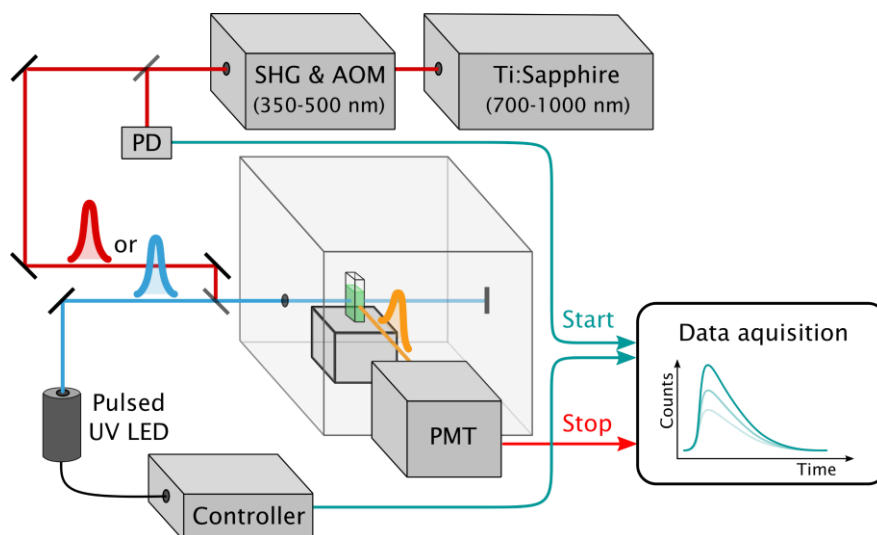


Figure 2.9. Schematic depiction of the applied time-correlated single photon counting (TCSPC) setup. Excitation of the sample is either conducted with a pulsed Ti:Sapphire laser or with pulsed LEDs. The laser output is coupled to a module for frequency doubling and adjustment of the repetition rate by an acousto-optic modulator (AOM). PD - photodiode, PMT - photomultiplier tube, SHG - second harmonic generation.

Similar to TA data, the recorded traces are convoluted with the experimental IRF and have to be processed. The IRF is recorded by collecting the scattered excitation light of a non-fluorescent sample in a separate measurement. Deconvolution of the IRF and data analysis is then carried out with the software FluoFit Pro 4.6 (PicoQuant GmbH). The fluorescence decay curves are fitted multi-exponentially, where the least number of exponential components is chosen, to avoid overfitting. The goodness of fit is assessed by means of the χ^2 criterion and successful data analysis yields the corresponding fluorescence lifetimes τ_i , together with their amplitudes.

2.3.3 STOPPED-FLOW SPECTROSCOPY

Apart from techniques for investigation of light-initiated dynamics, time-resolved optical spectroscopy also holds several standard methods to follow the course of diverse other processes. The stopped-flow technique provides versatile possibilities to resolve conformational changes of proteins or nucleic acids in the microsecond-second time regime. In principle, any process can be addressed, that relies on the

interaction of several components. For example, ligand binding dynamics or cation-mediated folding of biomolecules can be monitored, by rapid mixing of the corresponding components and the subsequent detection of the initiated process in a time-resolved manner (Figure 2.10).

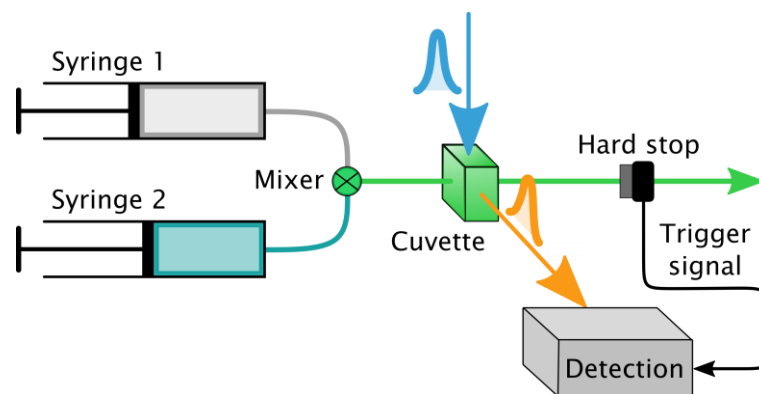


Figure 2.10. Schematic depiction of a stopped-flow device with 2 syringes. The solutions are injected into a mixing chamber prior to the cuvette. The hard stop blocks the flow of the mixed solution and transmits a trigger signal to the connected detection device.

The component solutions are supplied in separate syringes and pushed through a mixing chamber into a cuvette. This flow is then blocked by a hard stop, which marks the starting point of the dynamics. A trigger signal is transmitted from the hard stop to the detection unit to start data acquisition.

Stopped-flow experiments can be combined with different spectroscopic techniques, such as absorption, circular dichroism (CD), IR or fluorescence spectroscopy. The choice of the technique depends on the features of the investigated system and the availability of a suitable read-out. Due to the exceptional sensitivity, fluorescence-monitored stopped-flow spectroscopy is rather convenient, but this requires a distinct emission which changes throughout the observed process and can therefore be used as a reporter signal.

Typically, a series of measurements is conducted, e.g. with varying concentration or temperature. The obtained time-dependent signals are subjected to kinetic modelling analyses to elaborate on the underlying mechanism. Herein, the software Dynafit⁴^[31] was used, that enables simultaneous non-linear fitting of multiple datasets to the kinetic equations of a model of choice. The corresponding expressions for the time-dependent concentrations are derived from the differential equation system of the kinetic model for each reactant.

For model evaluation, the determined root mean square deviation (RMSD) values can be considered, although this might not be unequivocal when comparing several models. Therefore, additional statistical model analyses are provided that allow for the estimation of the actual probability of a tested model compared to others. The Akaike information criterion (AIC) as well as the Bayesian information criterion (BIC) represent an estimation of a model quality where an increased number of free parameters is penalized in order to devalue too complex models.^[32,33] The penalty is more severe for the BIC, which thus clearly favours an increased simplicity. For model comparison, the differences (Δ AIC and Δ BIC) to the best fit model are calculated. By careful and comparative evaluation of multiple tested models, a biased kinetic analysis can be circumvented.

2.4 PHOTORESPONSIVE BIOMOLECULAR SYSTEMS

To introduce a light-driven change of a biologic effect, different approaches are currently being pursued. Besides the design of artificially modified biomolecules in photopharmacology, the large field of optogenetics offers a fundamentally different approach for application in neuroscience. Natural light-sensitive receptors such as microbial opsins are specifically inserted into neurons to attain a light-stimulated neuronal response.^[34,35] The photopharmacological approach, on the other hand, provides virtually unlimited access to develop photoresponsive biomolecular systems. Apart from the use of photoswitches, which is the main focus herein, also photolabile protecting groups^[36,37] (PPG) are widely applied in photopharmacology. The biologic activity of e.g. a small molecular substrate or a large biomolecule can be altered by attachment of a suitable PPG and after photoinduced cleavage the original activity is retained. This methodology allows a fast and efficient release of the bioactive molecule, but this process is irreversible and produces undesirable side products. In this respect, photoswitches are superior to PPGs as potential photoresponsive components. Although it could be more challenging to implement a photoswitch into a biomolecular structure successfully, the photoswitch interconversion is unimolecular and can be reversibly operated.

2.4.1 ORGANIC PHOTOSWITCHES

Photochromic compounds, or photoswitches, represent outstanding photochemical tools that enable a reversible interconversion between two or more structurally isomeric states with different absorption spectra by exposure to light of specific wavelengths. The term photochromism originates from the greek words *phos* (light) and *chroma* (colour) and thus refers to the light-induced change of colour. Besides the different spectroscopic properties, the photo-induced change of molecular structure can be accompanied by significant

changes of chemical features like chirality, polarity, redox potential, or reactivity in general. This way, various environmental responses can be created and controlled by smart implementation of photoswitches into macromolecular assemblies.

For successful application, a promising photochromic compound should enable a rapid photoconversion with a high quantum efficiency and a pronounced switching turnover. The change of molecular properties should be as pronounced as possible. At the same time, the switch should be photoresistant and the mode of operation must be suitable for the desired target system.

How a photoswitch can be operated is dictated by its photophysical properties and the possible interconversion pathways. Thermal as well as photochemical interconversion are the main driving forces for photoswitches, but also other factors like the solvent, ionic strength or electric fields can affect the isomer distribution.^[38] Under dark conditions, photoswitches exist in a thermodynamic equilibrium between the possible isomeric states (Figure 2.11). The ground state distribution in general depends on the relative energies, but for most photoswitches one isomer clearly represents the energetic minimum of the system. Through continuous irradiation to

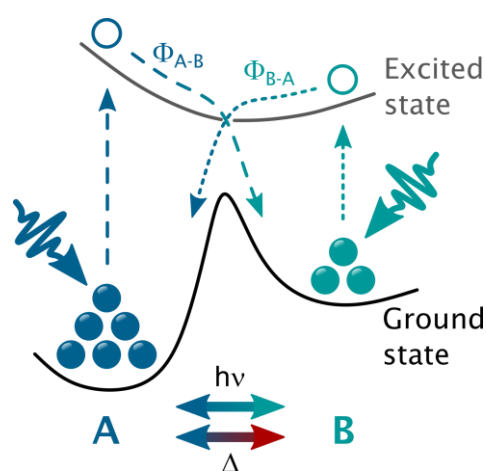


Figure 2.11. Illustration of the ground and excited state energetics of a photoswitch with two isomers A and B. Interconversion might occur thermally in the ground state or photochemically in the excited state.

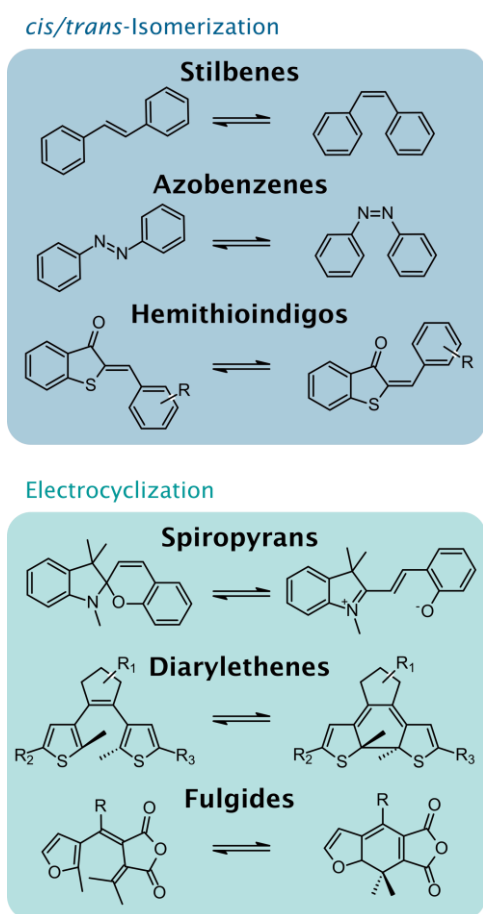


Figure 2.12. Overview of several prominent organic photoswitch classes, divided by their isomerization mechanisms.

induce photoisomerization, the distribution can be shifted and a photostationary state (PSS) is accumulated. The efficiency of the photoconversion is given by the quantum yield ϕ , which corresponds to the ratio of the number of molecules that undergo the photoreaction and the total amount of absorbed photons.^[39]

For so-called T-type switches, the initial distribution is recovered thermally in the dark, which implies that only one wavelength is required to drive the system away from the thermodynamic equilibrium. If no thermal isomerization occurs, the photoswitch system is bistable and must be operated by P-type switching with two different irradiation wavelengths. Furthermore, the different isomers should exhibit well separated absorption bands and high extinction

coefficients ϵ , so that they can be addressed effectively.

By means of molecular design, the switching and absorption properties can be optimized for the requirements of the target system. Especially for biochemical applications, UV light should be avoided to prevent the target system from photodamage. Ideally, the required wavelength should be within the phototherapeutic window (~650-850 nm), because this spectral range is hardly absorbed by biologic samples and enables an increased penetration depth into cellular tissue.

Most organic photoswitch families, can be subdivided by their isomerization mechanisms.^[40,41] Prominent examples are shown in Figure 2.12. Following a *cis/trans*-isomerization mechanism, the structure of stilbenes, azobenzenes, or hemithioindigos changes upon photoactivation, although the electronic molecular framework does not change. In contrast, the photoisomerization of switches that

undergo a 6π -electrocyclic reaction is accompanied by the cleavage or formation of a covalent bond. The photoisomers of e.g. spiropyrans, diarylethenes or fulgides therefore represent constitutional isomers and typically exhibit significantly different physicochemical features. Each of the listed families exhibits unique advantages to develop photochromically gated systems and energy conversion pathways.^[42–44]

Azobenzenes are well-investigated on different levels and remain the most widely applied photochromic compounds.^[45–48] Derivatives thereof typically exhibit a remarkable photostability, high switching turnover, negligible tendency for decomposition and a certain tunability of the spectral features by addition of functional groups.^[49] Moreover, their synthesis via azo coupling is relatively simple and renders a great diversity of compounds easily accessible. They have been successfully used in numerous biomolecular environments already without losing their photoswitching capacities.^[9,50,51] Recently, also heteroaryl-azobenzenes are attracting attention since they provide versatile novel properties to explore.^[52]

2.4.2 SPIROPYRAN-MEROCYANINE SWITCHES

Among the different classes of organic photoswitches, spiropyrans are an explicitly versatile group in a sense that the photoisomerization entails a drastic shift of the molecular properties. Therefore, profound effects can be exerted on their environment. In contrast to the ring-closed, orthogonally connected, and unpolar spiropyran structure (Figure 2.13), the ring-opened merocyanine exhibits a planarized π -conjugated framework with a pronounced charge displacement between the formally cationic indolinium nitrogen to the anionic phenolate oxygen. The charged merocyanine structure is mesomeric resonance-stabilized and might even be represented by its neutral quinoid form. Due to the double bond bridge, the merocyanine form can exist in different *cis* (C)/*trans* (T)-states. In principle eight isomers are possible, but only those with a central T-element are considered as stable. Typically, the TTC isomer represents the dominant form in solution, followed by TTT.

Already discovered in the 1950s,^[53–55] spiropyran compounds were investigated extensively under various conditions.^[56] The basic framework of spiropyran is formed by the 1',3',3'-trimethylspiro(2H-1-benzopyran-2,2'-indoline) structure, or simplified benzo-inolino-pyrano-spiran (BIPS, Figure 2.12). To obtain water-soluble derivatives,

ionic groups are attached to the indoline-nitrogen (Figure 2.13, R₁).^[57,58] The thermodynamic distribution of photoisomers is significantly affected by the applied solvent. Especially in aqueous media, spiropyrans show a very complex behaviour. The merocyanine isomer is known to be sensitive towards hydrolytic decomposition, which significantly depends on the relative stabilization of the merocyanine form. The substituents at the chromene moiety (Figure 2.13, R₂), have a direct effect on the strength of the C_{spiro}-O-bond and thus on the equilibrium distribution between the photoisomers.

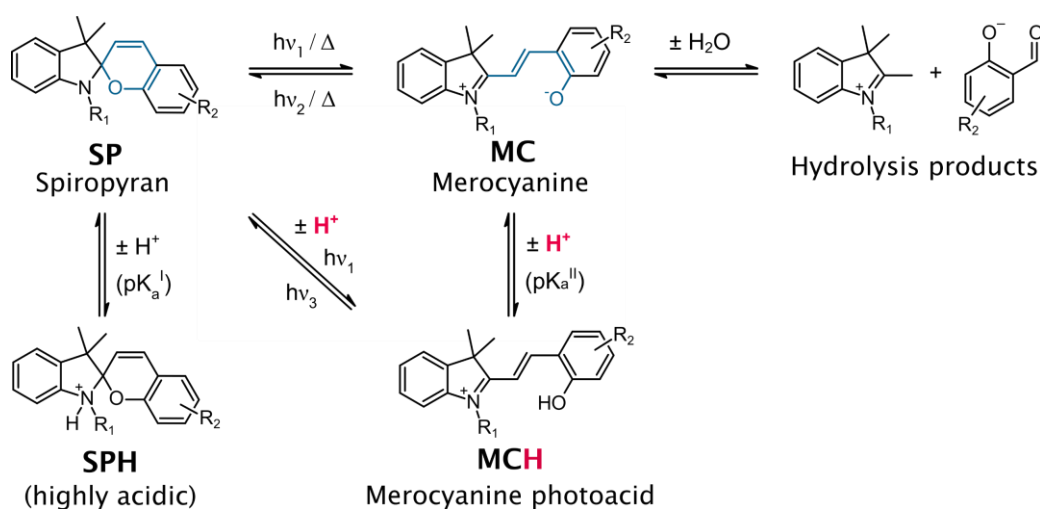


Figure 2.13. General behaviour of the spiropyran (SP) - merocyanine (MC) photowitch system in aqueous solution. The MC isomer is sensitive to hydrolytic decomposition. Upon acidification, both photoisomers are protonated at the indicated positions, where the MCH form is capable of photoprotonolytic ring-closure.

The chromene substitution pattern also has a huge impact on the photodynamic properties of BIPS derivatives. For the parent unsubstituted BIPS compound, photoreaction pathways involving singlet states only are reported.^[59,60] A similar behaviour is found for a BIPS derivative with a cationic pyridinium fragment integrated into the chromene moiety.^[57] Upon cleavage of the C_{spiro}-O-bond, an initial *cisoid*-merocyanine species (CCC) is formed that unfolds via sequential double bond isomerizations towards the stable TTC or TTT structure. The most prominent 6-nitro-BIPS derivative, however, undergoes ring-opening throughout the triplet manifold after a rapid ISC at the ring-closed structure.^[61-63] A long-lived merocyanine triplet state has been identified that decays on a nanoseconds-to-microseconds time scale in organic solvents. Interestingly, for the 6,8-dinitro-derivative, no triplet contribution

was found, but a singlet pathway has been assigned.^[64] As to the ring-closure reaction, the parallel excitation of the most stable TTC and TTT merocyanines has to be taken into account. For nitro-^[65] as well as dinitro-compounds,^[66,67] discriminable photodynamics were observed for both isomers.

Particularly in aqueous solution, the protonation of the photoisomers must be considered carefully (Figure 2.13). While the highly acidic SPH (pK_a^I) is only formed at $pH < 1$, the pK_a^{II} value of the phenolic site of MCH strongly depends on the substituents R_2 . For the parent BIPS compound a pK_a^{II} value of 7.8 is reported,^[68] whereas the pK_a^{II} of 6-nitro-BIPS is drastically lowered to 3.7.^[58] Protonation furthermore alters the photoswitching properties since the stable MCH species is mostly formed by thermal ring-opening. In any case, the MCH species enables photoinduced ring-closure via proton dissociation, which makes it a reversible photoacid. This pH-dependent photochromic reactivity is increasingly studied to develop smart systems, responsive to multiple orthogonal stimuli,^[69,70] and to address proton-coupled reactions.^[71,72]

2.4.3 PHOTOSWITCHES IN BIOMOLECULAR ASSEMBLIES

Photopharmacology makes use of photoresponsive molecular components to enable a non-invasive light-regulation of bioactivity.^[8-10] The use of molecular photoswitches enables a reversible manipulation of the biologic function of a desired target system. There are several possibilities to engage photoswitches for biochemical tasks. They can be integrated into the backbone of proteins or used for amino acid crosslinking to modulate the structure and thus the activity of the target. Additionally, photoswitchable linkers are used to tether ligands, agonists or blockers to enzymes or channel proteins.^[73,74] In a non-covalent manner, photoswitches can also be applied to regulate environmental conditions to alter enzyme activity.^[50]

Besides proteins as the dominant class of pharmacological targets, also nucleic acids have been modified with photoswitches successfully.^[75] Tertiary structure motifs of DNA or RNA can be disrupted by inclusion of photoswitches into the phosphate backbone.^[76] Moreover, the hybridization of double strands can be controlled by substitution of nucleobases with photoswitches.^[77,78]

A very promising and convenient approach to realize light-dependent bioactivity is the derivatization of small molecular metabolites with photoswitchable moieties.^[8] The different photoisomers can thus adopt specific pharmacokinetic properties like binding affinity or cell permeability. For instance, azobenzene has been incorporated successfully into the structures of receptor ligands^[11] allosteric modulators^[79] and also antibiotics.^[12]

2.5 RNA APTAMERS

The multitude of RNA types, responsible for countless cellular functions, is due to its structural diversity. Single-stranded RNA has the ability to form specific tertiary structures with compactly folded regions. Through base pairing of complementary segments and self-assembly, stems may be formed as well as loops, bulges, junctions, or hairpins. Today, even more sophisticated motifs like pseudoknots^[80] or G-quadruplexes^[81,82] are known. Remarkably, interactions between adjacent nucleobases can not only be established on their Watson-Crick faces but also on their so-called Hoogsteen edges (for purine bases) as well as the sugar edges. In addition, different orientations of the glycosidic bonds can result in *trans* or *cis* base pairs. Based on this variety, twelve distinguishable classes of base pair families were identified, that may be visualized by the Leontis-Westhof nomenclature.^[83] Although specific RNA architectures are well conserved, RNA is not supposed to be considered as static but can be highly dynamic.^[84] This is essential for understanding fundamental mechanisms of action of RNA-based regulation. The folding process itself and its energetic landscape are of undeniable importance for the biologic activity of RNA.

2.5.1 NATURAL RIBOSWITCHES

RNA switches (riboswitches) represent exceptionally interesting regulatory elements, since they are capable of modulating gene expression by binding to small molecular ligands without the need for protein interaction.^[85,86] They consist of an aptamer domain, located in the 5'-untranslated region of single stranded mRNA, and an adjacent expression platform which carries a particular genetic code. As depicted for an exemplary riboswitch in Figure 2.14, the aptamer domain forms a sophisticated

tertiary structure which is responsible for the recognition of a specific ligand (blue domain).

Upon ligand binding, a conformational change involving the aptamer domain as well as the interface region to the expression platform (grey domain) is induced that alters the accessibility of the downstream gene. In case of the depicted riboswitch, translation initiation is regulated through sequestration of the ribosomal binding site (RBS) which is located on the interface region. The ribosome cannot associate anymore to its start codon and translation of the following gene is turned off upon ligand binding – this is referred to as an off-switch. Hence, riboswitches represent *cis*-regulatory elements, as they control the expression of the gene sequence located on the same RNA strand as the regulatory unit. Besides translational control, riboswitches are engaged in numerous regulatory processes on different levels of gene expression, such as transcription, RNA degradation or self-cleavage and also post-translational RNA splicing.^[87]

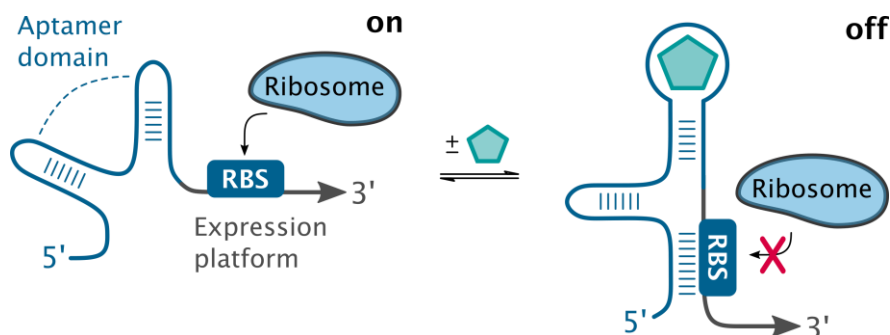


Figure 2.14. Illustration of riboswitch function. Shown as an example is a translational switch that regulates gene expression by sequestration of the ribosomal binding site (RBS) upon ligand (cyan pentagon) binding. The conformational RNA change involves the joining region between aptamer domain (blue) and gene expression platform (grey).

Natural riboswitches have evolved over millions of years and are highly adapted to their specific cellular environment. Therefore, they can exhibit elaborate regulation mechanisms. Their function sensitively relies on the present ligand concentration and other factors like the pH value or the availability of ions. Even riboswitches are known that exclusively depend on the surrounding Mg^{2+} concentration.^[88] In general, numerous riboswitches were found so far, mainly in bacteria, with diverse cellular metabolites as ligands. Typically, natural riboswitches or the enzymes that they encode for are involved in the cellular metabolism of the respective ligand molecules.

A great variety of riboswitches as well as their regulatory tasks and conformational characteristics were addressed by the pioneering work of R. Breaker.^[89,90] Among others, several purine-sensing riboswitches are known, like the adenine,^[91] guanine,^[92] or adenosine triphosphate^[93] (ATP) riboswitches. Moreover, amino acids like the lysine^[94] or glycine^[95] serve as riboswitch ligands, as well as cofactors such as flavin mononucleotide^[96] (FMN) or S-adenosyl methionine^[97] (SAM).

2.5.2 ARTIFICIAL RNA APTAMERS

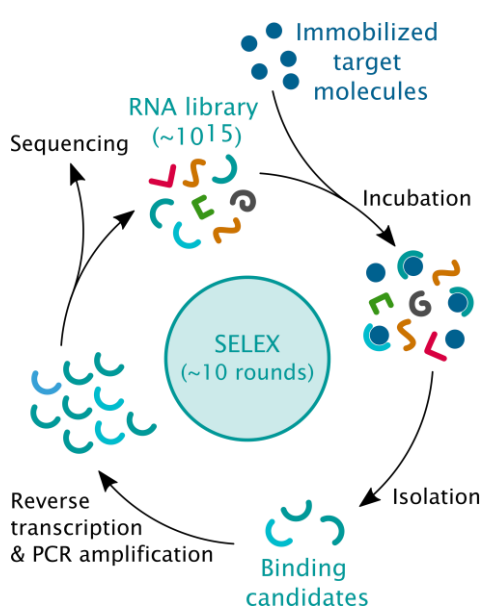


Figure 2.15. Principle of the systematic evolution of ligands by exponential enrichment (SELEX) process.

In order to explore engineered riboswitch architectures, either natural ones can be modified by e.g. exchanging the expression platform, or artificial riboswitches can be created by *de novo* design. Potential RNA aptamer sequences that specifically bind to a target molecule can be generated *in vitro* by a repetitive selection process called systematic evolution of ligand by exponential enrichment (SELEX, Figure 2.15).^[98,99]

The target molecule is immobilized and incubated on a column together with a randomized RNA pool with a total number of about 10^{15} different sequences.

Due to the enormous variety of sequences, a certain binding probability is given for some of the candidates. Those binding aptamers are subsequently isolated and then reversely transcribed and amplified by polymerase chain reaction (PCR). At this point, a small amount of the amplified DNA pool is split for sequencing analyses but most of the pool is mainly transcribed again into RNA again and used for another round of selection. Since the applied reverse and forward transcription processes are slightly error-prone, mutations are introduced to the binding candidates in every single round. This is typically repeated for 10-12 rounds of SELEX which iteratively leads to a

substantial increase in specificity of aptamer sequences and to an enrichment of high affinity binding candidates. The parallel analysis of the obtained aptamer pools of each SELEX round in combination with the development of next generation sequencing (NGS) techniques, enables robust and detailed insights into the enrichment trajectories of specific aptamer candidates.^[100]

The enrichment of aptamer candidates during the selection is essentially influenced by the experimental conditions like buffer medium, pH value and salt concentration as well as the exact SELEX protocol. Especially the washing and elution steps are critical factors and the stringency of the protocol is progressively increased throughout the multiple rounds of selection.^[100] By rigorous separation of weak binders, high affinity aptamers can be enriched that bind to the target molecule with K_D values in the low nanomolar or even picomolar range.

An exceptionally high affinity is a prerequisite for diverse applications of synthetic aptamers, also apart from the design of artificial riboswitches e.g. as biosensors in environmental or clinical diagnostics. The ciprofloxacin (CFX) aptamer R10K6 binds to several representatives of the fluoroquinolone antibiotic family, and thus provides a promising design platform for aptasensors as analytic tools.^[101] Therefore, detection systems mainly make use of electrochemical or optical response changes upon target binding.^[102] In the latter respect, fluorogenic RNA aptamers are interesting tools, for which ligand binding is accompanied by a pronounced increase in emission.^[103] Such aptamers like the Spinach^[104], the Malachite green^[105] or the Mango^[106] aptamer furthermore show great potential for RNA imaging and tracking^[107,108]. However, besides a high ligand affinity also an extraordinary specificity for ligands is observed frequently for synthetic aptamers. The theophylline aptamer as one of the most prominent examples, is able to discriminate between theophylline and caffeine by a 10 000-fold decrease in affinity, although the compounds only differ in one single methyl group.^[109,110]

2.5.3 ENGINEERED RIBOSWITCHES

The most interesting but also most difficult to implement potential application of an artificial aptamer is as the functional aptamer domain of an engineered riboswitch. An exceptional affinity or specificity is by far not sufficient for turning an aptamer into

a riboswitch, but it has to meet additional requirements. As it is the case for natural riboswitches, the ligand binding is supposed to induce a conformational rearrangement of the aptamer domain, that is pronounced enough to mediate a change in the regulation of an adjacent expression platform. Thus, the conformational characteristics of the aptamer and of the dynamic ligand binding process are decisive for engineering. In this respect, also mechanistic features must be taken into account, depending on the aspired regulatory task.

Only a few *in vitro* selected aptamer candidates could be applied so far for successful *in vivo* riboswitch engineering, including the theophylline (Theo) aptamer,^[110] the neomycin (Neo) aptamer,^[111] the TC aptamer,^[112] and also the recently selected paromomycin^[113] and CFX^[114] aptamers. An overview of different regulatory mechanisms carried out in prokaryotes or eukaryotes is provided in Figure 2.16.^[115] In prokaryotes, conditional translation initiation by sequestration of the RBS consisting of the Shine-Dalgarno (SD) sequence and the AUG start codon (Figure 2.16A). This was e.g. realized by installing the Theo aptamer immediately 5' of the RBS and the reporter gene.^[116] In the ligand-bound state, the distance to SD is increased which allows the ribosomal subunit 30S to initiate translation.

Using a distinguishable mRNA architecture, translational control was exerted in eukaryotes (Figure 2.16B) also with the Theo^[117] as well as the Neo^[111] and TC^[118] aptamers. Here, the aptamer can be installed in between the binding site for the ribosomal subunit 40S on the 5'-end (blue sphere) and the AUG start codon.^[119] If the ligand is bound to the aptamer, a stable conformation is adopted that blocks the scanning ribosome and translation initiation is inhibited or the AUG start codon is sequestered. The roadblock formation might be an outstanding mechanism of artificial riboswitches, as in some cases the regulatory potential is assumed to rely on the stability of the ligand-bound state rather than on a pronounced conformational adjustment.

For transcriptional control (Figure 2.16B) the striking conformational switch upon ligand recognition can involve an extended interface region between aptamer and expression platform. Due to ligand binding an anti-terminator stem of the nascent mRNA chain is transformed into a terminator stem, that forces the RNA polymerase (RNAP) to cease transcription. Transcriptional control was executed in prokaryotic cells with the Theo^[120] as well as the TC^[121] aptamer. It could be shown, that aptamer

domains and termination or anti-termination platforms can be combined in a modular manner.^[122] Besides conditional translation or transcription, engineered riboswitches were furthermore applied for several other cellular tasks like pre-mRNA splicing (Figure 2.16D), which was realized with the TC aptamer.^[123] Moreover, self-cleaving ribozymes were designed with various aptamer domains attached to the core structures of hammerhead ribozymes.^[109,115] Hitherto, also RNA degradation and viral replication were successfully controlled by artificial riboswitches.^[119]

Despite the numerous implementations of engineered riboswitches, the criteria that make an artificial aptamer a functional *in vivo* riboswitch are still under debate. In particular the dynamic folding and binding characteristics of aptamers must be considered for the *in vitro* selection of potentially active candidates. The SELEX process generates high affinity binding sequences to a given ligand. An increased simplicity of accumulated RNA structures is therefore favoured naturally. Moreover, the folding landscape can be essentially affected by the presence of metal cations. The concentrations of Na⁺ and K⁺ ions play an important role, e.g. in stabilizing structural motifs like quadruplexes.^[124] Yet, divalent Mg²⁺ cations occupy a special position among the relevant cations, due to its ability to compensate for the negatively charged phosphate backbone of nucleic acids.^[125] They stabilize tertiary structure elements and thus allow RNA to fold into compact structures. The applied Mg²⁺ concentration therefore dictates the conformational variety of enriched aptamer candidates in the SELEX process. Common protocols often provide for concentrations between 5 and 10 mM Mg²⁺; although elevated Mg²⁺ concentrations are assumed to favour the enrichment of

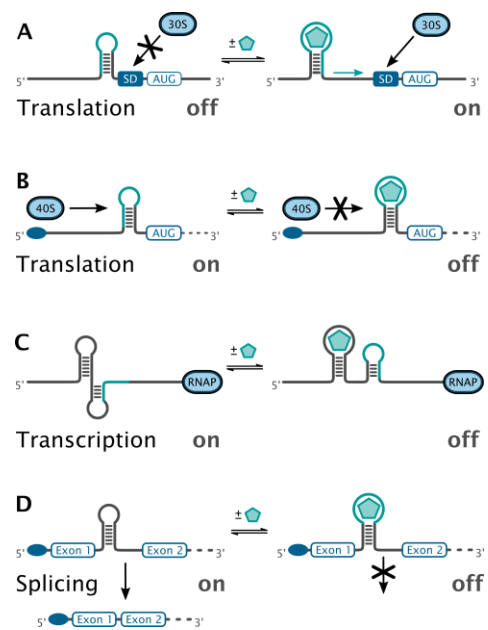


Figure 2.16. Examples of engineered riboswitch regulation mechanisms. **Translational control by A)** sequestration of the Shine-Dalgarno (SD) sequence in prokaryotes or by **B)** roadblock formation in eukaryotes. **C)** Transcriptional control by formation of a stable terminator stem. **D)** Conditional mRNA splicing.

Theoretical Framework

aptamers of poor structural complexity.^[126] In addition, structures might be accumulated that are mostly preformed, which is considered a hindrance for riboswitch function, too. However, the application of lower Mg^{2+} concentrations is suggested to result in the enrichment of structures with increased structural complexity which in turn can be associated with an increased potential functionality.^[127] In view of possible *in vivo* riboswitch applications, especially the physiological Mg^{2+} concentration range from roughly 0.5 to 1.5 mM is of importance.

3 AIM OF THIS WORK

The overall goal of this work is to investigate the photopharmacological application potential of both photoswitches and artificial RNA aptamers. Especially spiropyran photoswitches are studied here in aqueous solution as well as azobenzenes. The key question of the aptamer investigations is which parameters are critical for an artificial aptamer to function as an engineered *in vivo* riboswitch. Ultimately, the two research projects should be combined, as illustrated in Figure 3.1, to develop an RNA aptamer – photoswitch ligand pair that allows for reversible light-regulated ligand binding.

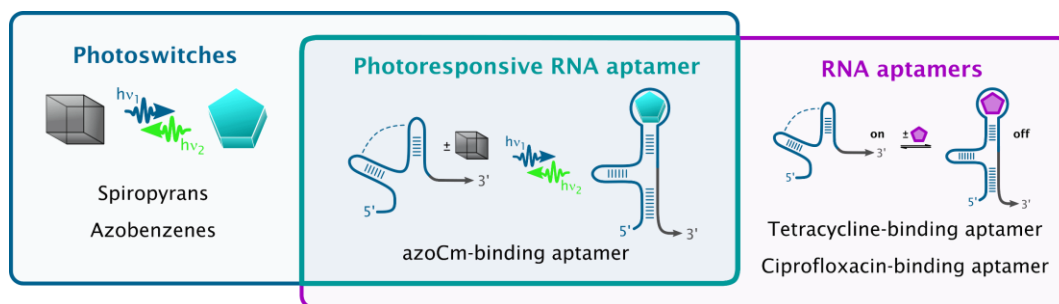


Figure 3.1. Illustration of the main projects of this work. The characteristics of photoswitches as well as artificial RNA aptamers are investigated with regard to a potential biochemical use and both systems are finally combined to a photoresponsive RNA aptamer.

The subject of this thesis is located within the framework of the collaborative research center (CRC) 902 “molecular principles of RNA-based regulation”, funded by the *Deutsche Forschungsgemeinschaft* (DFG). The photoswitch subproject has been worked on together with the group of Prof. Dr. Alexander Heckel. The focus was put on the characterization of spiropyran and azobenzene photoswitches, which were synthesized by Dr. Thomas Halbritter. Based on previous publications,^[57,128] especially spiropyran derivatives of the parent BIPS compound with an integrated pyridine moiety (Py-BIPS) are studied. Moreover, water-soluble derivatives of the prominent 6-nitro-BIPS and the 6,8-dinitro-BIPS compound are added to the list of investigated spiropyranes. The main task was to investigate their photophysical properties in aqueous solution in view of biomolecular applicability by means of elaborate spectroscopic experiments.

The RNA aptamer samples were synthesized and supplied by the group of Prof. Dr. Beatrix Süß and the related group of Dr. Julia Weigand, from the technical university Darmstadt. The artificial TC-binding aptamer has been a long-standing project within the CRC 902. During her doctoral thesis, Dr. Ute Förster investigated the ligand binding kinetics of the system via stopped-flow spectroscopy^[129,130] and Dr. Andreas Reuss later elaborated on the influence of Mg²⁺ ions on the conformation of the aptamer.^[131,132] To gain more detailed insights into the conformational changes during the prefolding and ligand-binding of the TC aptamer, the task of the present work was to investigate the microenvironments of distinct structural motifs of the aptamer spectroscopically. Therefore, fluorescent 2-aminopurine labels were installed at the positions of interest instead of the corresponding nucleobases. The labelled RNA samples were produced and supplied by Dr. Marc Vogel.

The CFX-binding aptamer was selected more recently by Dr. Florian Groher and Dr. Jeannine Schneider.^[101,114] Interestingly, several high affinity aptamer candidates were found in the same SELEX experiment, which drastically differ in their potential riboswitch activities. The most abundant aptamer (original name R10K6) showed no translational riboswitch activity in a GFP reporter assay that was executed in parallel to the SELEX. Only one of those aptamers (original name 10A) could be used as a functional *in vivo* riboswitch. Moreover, the inactive candidate was much more enriched during the selection than the active, which seems to be a common issue of conventional SELEX protocols. Hence, the aim of this project was to elaborate on the differences of inactive aptamers and *in vivo* riboswitches comparatively. As both aptamers exhibit quite similar ligand affinities, other factors might be essential for making an aptamer also an active riboswitch. Especially, the underlying ligand binding kinetics were of interest here and had to be addressed spectroscopically.

As the final goal of the collaborative project, the knowledge about the implementation of photoswitches and about RNA aptamer characteristics should be combined to design a photoresponsive aptamer-ligand system. Together with the Heckel group as well as the Süß group, the roadmap was to design a photochromic small molecular ligand and to generate an aptamer that specifically binds to only one of the respective photoisomers. Since antibiotics provide excellent starting points for the selection of aptamers,^[100] the compound chloramphenicol (Cm) was chosen as potential ligand and Dr. Thomas Halbritter successfully integrated an azobenzene

moiety into its molecular structure (azoCm). Afterwards, Dr. Thea Lotz from the Süß lab conducted SELEX experiments with azoCm as ligand. To generate aptamers, that selectively bind to one azoCm photoisomer, the SELEX protocol was modified with an irradiation step. After incubation with the aptamer pool and elution of the non-binding aptamers, the column was exposed to UV light to isomerize the immobilized ligand. Among the collected aptamers that unbound upon isomerization, some promising candidates were found that should enable light-controlled ligand binding. In parallel, Dr. Sabrina Wahl (formerly Steinwand) characterized the photochromic properties of the ligand during her doctoral thesis^[133] and already investigated the binding behaviour of some of the obtained aptamer candidates. In continuation of this work, optimized aptamer candidates are investigated regarding their photoinduced binding-unbinding abilities.

4 EXPERIMENTAL RESULTS

In this chapter, the acquired results and main conclusions of each subproject are explained. The results have been published in parts throughout the doctoral thesis and reference is made to the respective publications at the appropriate place. In section 4.1, the photoswitch project is addressed. The results about the photo- and thermochromism of a methylated MePy-BIPS derivative and two Nitro-BIPS derivatives in neutral aqueous solution are published in reference [I]. Furthermore, the photoacidic and highly acidochromic behaviour of a non-methylated Py-BIPS compound is presented in reference [II]. The proton-release mechanisms of the protonated merocyanine photoacid forms of Py-BIPS as well as Nitro- and Dinitro-BIPS are addressed by extensive ultrafast TA studies, published in reference [III].

The investigations of the TC aptamer are unpublished so far and will therefore be discussed in detail, in section 4.2.1. The RNA aptamer ligand binding characteristics for the CFX aptamer are presented in section 4.2.2 and published in reference [IV]. Last, in section 4.3 a photoresponsive RNA aptamer is presented that selectively binds to only one photoswitch isomer of a derivatized antibiotic (published in reference [V]).

The applied methods and experimental settings are provided in the corresponding publications in chapter 7. Only for the TC aptamer project, the used materials and methods are listed at the end of section 4.2.1.

4.1 PHOTOSWITCHES IN AQUEOUS SOLUTION

The class of spiropyran-merocyanine photoswitches is very exceptional among the great variety of photochromic compounds. The photoinduced interconversion between SP and MC (Figure 4.1, top) is accompanied by a substantial change of molecular properties like colour, molecular geometry, polarity, and charge displacement, which is highly advantageous for application in a macromolecular assembly. In continuation of previous studies^[57,128] on the design and characterization of spiropyran photoswitches for biochemical use, extensive comparative studies of the compounds **1-4** (Figure 4.1) were carried out. Regarding their molecular structures,

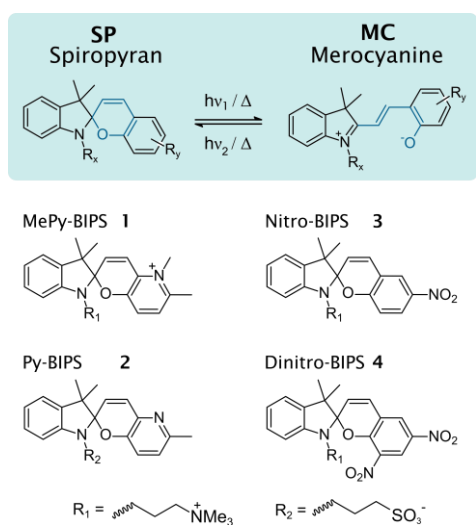


Figure 4.1. Photochromic interconversion of SP and MC (top) and merocyanine isomer structures of the investigated Py- and Nitro-BIPS compounds **1-4** (bottom).

the presented spiropyran switches can be subdivided by the nature of their chromene moieties into the class of Py-BIPS compounds **1** and **2** and the class of Nitro-BIPS derivatives **3** and **4**. The Py-BIPS compounds have a pyridine ring in common that is incorporated into their chromene parts, but they differ in the substitution pattern on the pyridine-nitrogen. Py-BIPS **2** bears no substituent at its pyridine-nitrogen, while MePy-BIPS **3** exhibits a methylated pyridinium moiety. Consequently, they differ in the charge of the respective nitrogen. They

furthermore differ in the polar headgroup of the alkylic residue attached to the indoline nitrogen. Compound **2** is the only compound that carries an anionic sulfonate group instead of a cationic trimethyl ammonium group, since a selective methylation of only the nitrogen on the residue is not feasible as a final step in synthesis. However, both polar groups meet the requirements to increase the water solubility of the compounds, without interfering with their photochromic properties.

The water-soluble compound **3** is a derivative of the most widely used 6-Nitro-BIPS spiropyran chromophore. By installing the same cationic residue as that of compound **1** the polarity and thus the solubility of the parent 6-Nitro-BIPS scaffold could be substantially enhanced.^[58] Similarly, the water-soluble derivative **4** of the 6,8-Dinitro-BIPS compounds could be synthesized and is studied here in detail.

4.1.1 PHOTOCROMISM OF WATER-SOLUBLE SPIROPYRANS

Properties of Py-BIPS Derivatives in Neutral Aqueous Solution

(References [I,II])

In neutral aqueous solution the absorption properties of MePy-BIPS **1**^[I] and Py-BIPS **2**^[II] are rather similar and reflect the typical characteristics of spiropyran photoswitches. In both cases, the ring-closed SP isomer exhibits a minor absorption

band in the UV region around 300-350 nm (Figure 4.2), while the MC isomer shows a pronounced absorption band in the vis range roughly centred around 530 nm. Both compounds undergo photoinduced ring-opening upon UV irradiation of SP as well as ring-closure upon exposure of MC to vis light.

However, the photophysical properties of compound **1** differ remarkably from that of compound **2**, due to the formal additional positive charge. MePy-BIPS **1** almost exclusively exists in its stable ring-closed form in the dark and upon UV irradiation a photostationary state (PSS) with roughly 12% MC is accumulated. In contrast, for Py-BIPS **2** the ring-opened isomer is significantly stabilized, so that an equilibrium distribution containing even 48% of MC is established under dark conditions. Photochemically, a PSS with an MC content as high as 55% can be generated.

Since the rate coefficients of the thermal interconversion reactions of compound **1** are very small, the system is practically bistable and can be operated by photoactivation only, according to P-type switching.^[40] In a photofatigue experiment with alternating UV and vis irradiation cycles an almost constant switching amplitude is observed over 25 cycles (Figure 4.3, upper panel). Only a slight decrease of the maximum MC fraction can be noted, which is ascribed to UV-induced photodegradation of SP. Hydrolytic decomposition of MC is only a minor issue for compound **1**, due to the low content of the ring-opened isomer.

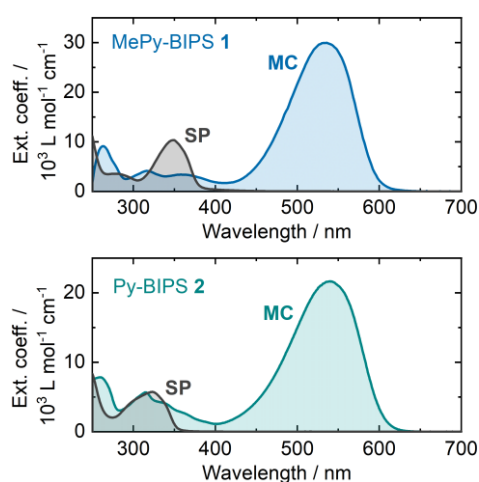


Figure 4.2. Absorption spectra of the pure photoisomers SP and MC of MePy-BIPS **1** (top) and Py-BIPS **2** (bottom).

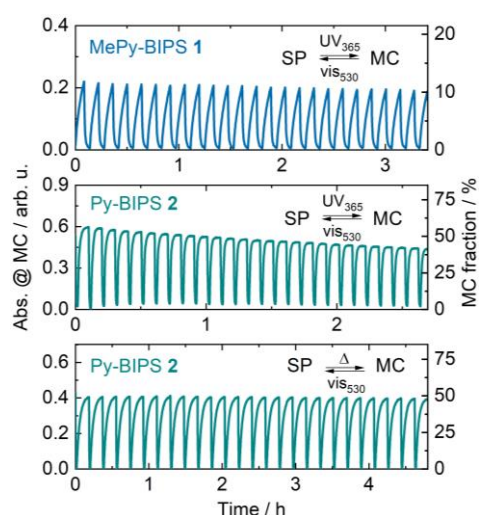


Figure 4.3. Cyclic photofatigue studies of compounds **1** (upper panel) and **2** (lower panels) with shown photoswitch operation modes.

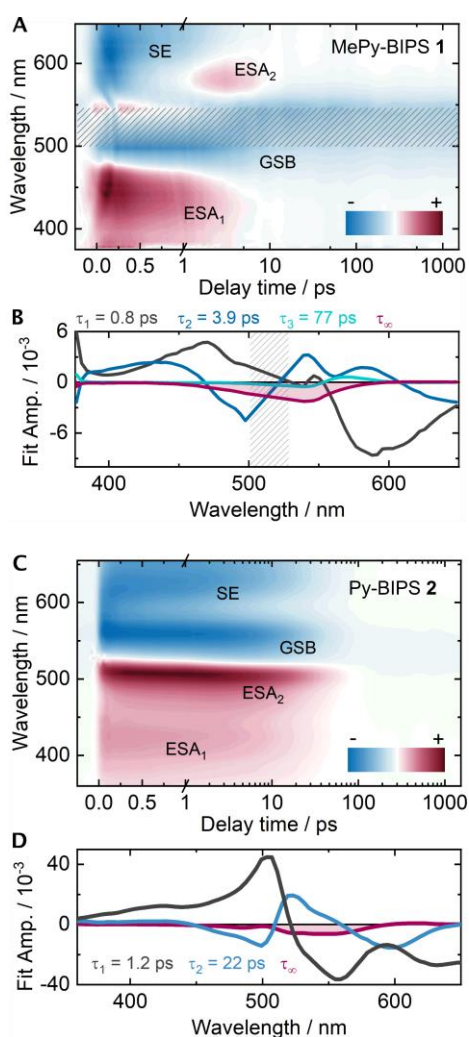


Figure 4.4. **A)** TA spectrum of the MC isomer of MePy-BIPS **1** and **B)** DAS of the lifetime components determined by GLA. **C)** TA spectrum of the MC isomer of Py-BIPS **2** and **D)** DAS of the lifetime components determined by GLA.

merocyanine forms of **1** and **2** (Figure 4.4) are assumed to be mechanistically similar in neutral solutions. In both TA experiments, two ESA signals of MC* are observed, but those of **1** are shifted bathochromically for about 30 nm compared to **2**. The ESA₂ signal of compound **1** is significantly superimposed by the prominent GSB signal (the gray area was excluded due to scattered light) and therefore appears as a split signal. Both MC samples also show an SE signal which fits the fluorescence emission observed for compound **2**. Although merocyanines are generally known to fluoresce,

The photoswitch systems **2** can be operated in two different modes, because of the substantial stabilization of MC. On the one hand, P-type switching can be carried out with alternating UV and vis irradiation. In a corresponding cyclic switching experiment, a significant reduction of the exceptional turnover is observed that is due to the UV-induced photolytic decomposition of SP (Figure 4.3, middle panel). On the contrary, the system can be operated in T-type mode since the initial equilibrium distribution is restored within few minutes without the application of harmful UV light. When ring-opening is carried out thermally, the remarkable switching turnover of 48% is virtually retained throughout the monitored 25 cycles (Figure 4.3, lower panel).

The ring-closure isomerization must be induced photochemically for both herein presented Py-BIPS derivatives, to obtain a pure SP sample. The corresponding photodynamics of the

no steady-state emission was detected for compound **1**, supposedly due to the low MC content in solution.

By kinetic analysis via GLA, two lifetime components are determined to model the dynamics of the signals associated with the excited states (ESA and SE) of both compounds. As illustrated in Figure 4.5, the sub-ps

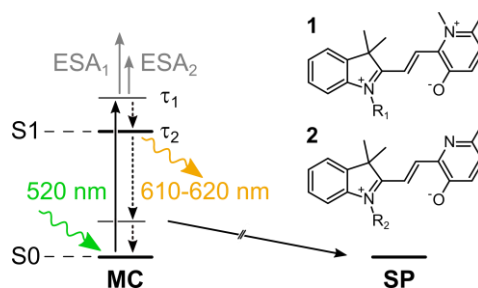


Figure 4.5. Photoreaction mechanism scheme for the ring-closure reactions of the Py-BIPS-type merocyanines **1** and **2**.

lifetimes τ_1 are assigned to initial relaxation processes within the excited S1 state. For the following decay of the vibrationally relaxed MC* state, a lifetime of 3.9 ps is determined for compound **1** and a 22 ps lifetime for compound **2** (τ_2). Thus, the MC* decay of the methylated Py-BIPS **1** is accelerated by factor of almost 6 compared to the unmethylated derivative **2**. Besides the observed radiative relaxation, non-radiative decay into the MC ground state is assumed to be the major deactivation channel in both cases. Just as for the previously reported Py-BIPS compound,^[57] ring-closure is suggested to occur from a vibrationally hot MC ground state.

The photoinduced ring-opening dynamics of Py-BIPS derivatives in water are quite comparable to that of the original BIPS compound.^[56,57,59,60,134] The excited SP singlet species decays within 1-2 ps towards the merocyanine ground state through a conical intersection of the respective potential energy surfaces. Upon excitation and C_{spiro}-O-bond cleavage, a transient *cisoid*-MC species is generated that still adopts an orthogonal structure just as SP. The *cisoid* intermediate sequentially converts into a stable MC form via *cis/trans*-isomerizations around the central bridge of three partial double bonds.

Properties of Nitro-BIPS Derivatives in Neutral Aqueous Solution

(Reference [1])

The parent 6-nitro-BIPS compound represents the most extensively investigated spiropyran compound and derivatives thereof have been applied in different biochemical contexts so far. The photoswitch already served as a reversible intercalator into DNA helices^[135] or to engineer channel proteins.^[136] Even the *in vitro* selection of artificial RNA aptamers has been carried out successfully.^[137] The

Experimental Results

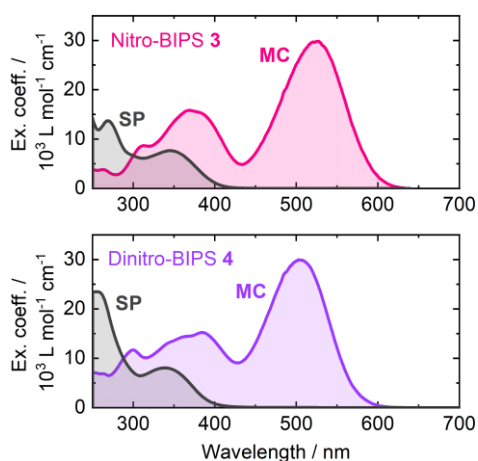


Figure 4.6. Absorption spectra of the pure photoisomers SP and MC of Nitro-BIPS **3** (top) and Dinitro-BIPS **4** (bottom).

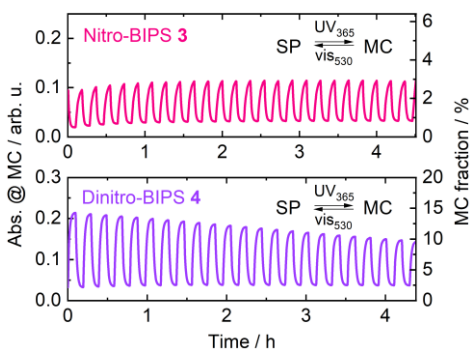


Figure 4.7. Cyclic photofatigue studies of compounds **3** (top) and **4** (bottom) with shown photoswitch operation modes.

photochromic characteristics of 6-nitro-BIPS as well that of 6,8-dinitro-BIPS were subjected to numerous studies, although the exact photodynamics and isomerization sequences are not yet thoroughly understood.

Compared to the original BIPS or the MePy-BIPS derivative **1**, the ring-opened MC isomer is significantly stabilized in aqueous solution for Nitro-BIPS **3**. Regarding Dinitro-BIPS **4**, the effect of the two electron-withdrawing nitro groups is so strong that it even crystallizes in the shape of MC. Therefore, an initially pure MC sample is obtained upon dissolving **4** in water, but the content rapidly decreases thermally. For both compounds a transient thermal equilibrium of 26% is established within 4-5 hours. However, due to an increased sensitivity towards hydrolytic decomposition, the MC amount of **3** and **4** is reduced to final values of 8% and 12%, respectively.

The absorption spectra of the Nitro-BIPS derivatives in water (Figure 4.6) are noticeably different from those of the Py-BIPS derivatives. Both photoisomers exhibit prominent absorption bands in addition to the S1 bands. Regarding the SP spectra, the bands below 300 nm are more pronounced than those around 350 nm. The additional bands of the MC isomers appear around 350-400 nm. The absorbance in this range even exceeds that of the superimposed SP. This makes the ring-opening reaction highly dependent on the incident excitation wavelength since both isomerization directions are induced simultaneously to different extents.

By 260 nm irradiation, exceptional PSS distributions with 36% and 38% of the MC isomer can be obtained for **3** and **4**, respectively. This way, P-type switching can be

exercised in combination with 530 nm excitation light to induced ring-closure. However, the application of 365 nm is more convenient, but the reachable amount of MC in the PSS is drastically lower. Corresponding cyclic switching experiments with alternating illumination at 365 nm and 530 nm are displayed in Figure 4.7. As to compound **3**, only 3% of MC can be accumulated by UV irradiation, but the switch is highly fatigue-resistant (Figure 4.7, top). For compound **4**, an initial maximum amount of 14% MC is obtained that successively declines due to hydrolytic decomposition (Figure 4.7, bottom).

The photodynamics of 6-Nitro-BIPS derivatives were addressed by numerous theoretical^[62,138] as well as experimental studies^[65,139–144] so far. Different to BIPS and the Py-BIPS derivatives, the ring-opening reaction in organic solvents is suggested to proceed mainly on the triplet manifold after a rapid ISC in the ring-closed geometry ($^1\text{SP}^* \rightarrow ^3\text{SP}^*$). Ring-opening subsequently produces an intermediate perpendicular *cisoid*-MC* state that is relatively long-lived and decays on a nanoseconds^[145] to microseconds^[142] time scale in organic solvents. In the excited triplet state a dynamic equilibrium with a *trans*-MC* species is assumed. Relaxation into the ground state subsequently yields a stable ring-opened isomer (mainly TTC) that might undergo further isomerizations thermally.

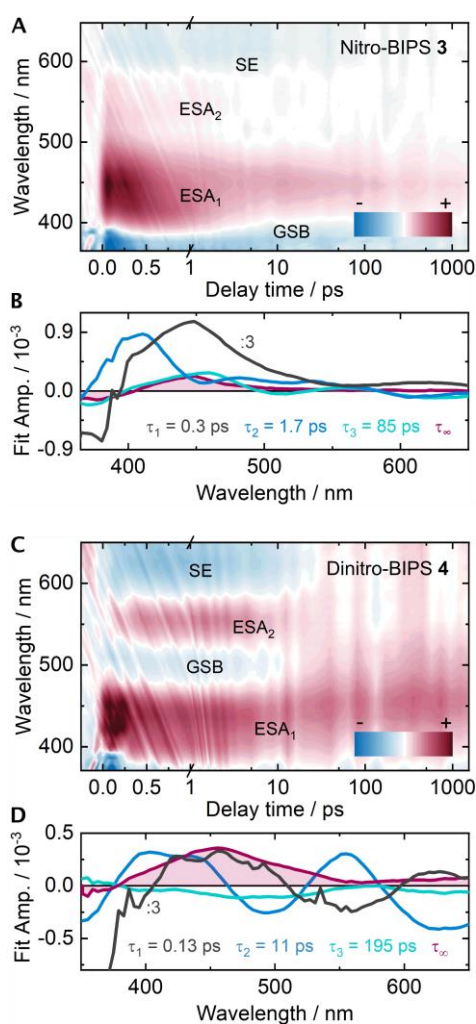


Figure 4.8. **A)** TA spectrum of the ring-opening reaction of Nitro-BIPS **3** and **B)** DAS of the lifetime components determined by GLA. **C)** TA spectrum of the ring-opening reaction of Dinitro-BIPS **4** and **D)** DAS of the lifetime components determined by GLA.

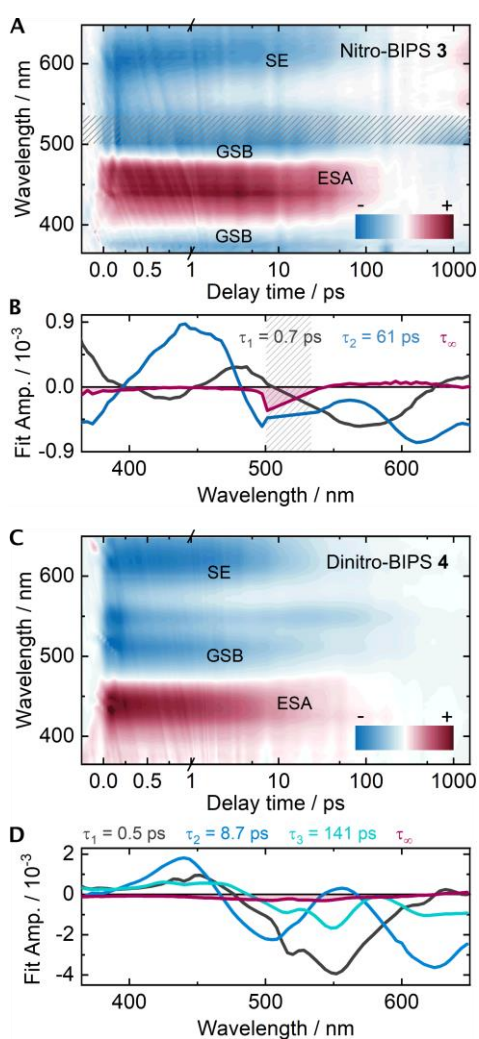


Figure 4.9. **A)** TA spectrum of the ring-opening reaction of Nitro-BIPS **3** and **B)** DAS of the lifetime components determined by GLA. **C)** TA spectrum of the ring-opening reaction of Dinitro-BIPS **4** and **D)** DAS of the lifetime components determined by GLA.

In the TA experiment of compound **3** in neutral aqueous solution (Figure 4.8A) similar characteristics as reported for organic solvents can be noticed. The determined lifetimes τ_1 and τ_2 , probably model a relaxation within the excited $^1\text{SP}^*$ state followed by conversion into $^3\text{SP}^*$. The amplitude of τ_3 with two maxima around 450 nm (ESA_1) and 550 nm (ESA_2) is in good agreement with the reported signature of the *cisoid*- MC^* species. This implies a drastic acceleration of the decay of the respective intermediate to 85 ps. At the end of the measured time window, the infinite lifetime only shows a residual positive signal around 450 nm that supposedly reflects the distinguishable dynamics of the *trans*- MC^* species.

Concerning Dinitro-BIPS, a similar series of isomerizations takes place in the ring-opening reaction, although only singlet states are assumed to be involved.^[146] In the TA map of the SP isomer of compound **4** in water (Figure 4.8C) an ultrafast conversion of the initial SP^* state into a *cisoid*- MC^* species, characterized by ESA_1 and ESA_2 , can be confirmed. The sub-picosecond lifetime τ_1 is found to model this transition. After the depletion of the *cisoid*- MC^* state with the lifetime τ_2 a broad absorption band around 450-500 nm maintains until 1.5 ns (τ_∞) that already indicates the formation of a ground state MC species. However, the absorption is still shifted with respect to the steady-

state absorption band, so the MC species can be expected to undergo further *cis/trans*-isomerization towards the TTC form.

In general, MC isomers with a central *trans*/T-element are considered as stable. The TTC isomer represents the energetically most favoured form, followed by TTT. In a ring-closing experiment, the parallel excitation of multiple MC isomers must be considered carefully. For both Nitro-BIPS^[65,138,147] as well as Dinitro-BIPS^[66,67,146], discriminable photo-reaction pathways are reported for TTC and TTT.

The ring-closure dynamics of the Nitro-BIPS derivative **3** (Figure 4.9A) is dominated by the TTC isomer. The associated ESA and SE signals slightly shift spectrally with the lifetime τ_1 , due to an initial relaxation within the excited S1 state TTC*. The respective state decays via conversion into the spiropyran geometry with the lifetime component τ_2 . The infinite lifetime reveals a residual positive signal around 600 nm, that is indicative of the TTT isomer that is either excited simultaneously or formed in the excited state. To small extent, the TTC isomer is suggested to transform into TTT unidirectionally.^[138,147]

The TA contour plot of the ring-closure of the dinitro compound **4** is displayed in Figure 4.9C. Similar to compound **3**, an initial relaxation within the S1 state occurs that is modelled by an ultrafast lifetime τ_1 . Yet, lifetime τ_2 of the TTC* state is significantly shortened for Dinitro-BIPS **4**. The parallel excitation of TTC and TTT is clearly noticeable in the shape of the peculiar GSB. The two minima of the GSB decay on different time scales which hints at distinguishable repopulation dynamics of two isomers. The recovery of the higher energy GSB minimum is captured by τ_2 but that of the lower energy minimum is modelled by a longer additional lifetime τ_3 .

4.1.2 PH-GATED PHOTOCHROMISM OF PY-BIPS

(Reference [II])

In addition to the common phenolic protonation site of the ring-opened merocyanine isomer, the Py-BIPS derivative **2** is equipped with an additional protonation site at the pyridine-nitrogen. Therefore, it shows a refined acidochromic behaviour in aqueous solution. Both photoisomers can exist in different protonated states that adopt inherent photophysical characteristics. By means of pH-dependent

UV/vis switching studies, the absorption spectrum of each protonated state could be assigned, and the possible interconversion pathways were investigated (Figure 4.10).

In the basic regime, both isomers SP and MC are non-protonated and capable of thermal and photochemical conversion as discussed before for neutral solutions. With a pK_a value of 6.8, the pyridine-nitrogen of the ring-opened isomer is protonated first upon addition of a strong acid. In this intermediate pH range from roughly 6.8 to 4.8 interconversion occurs between HMC and SP and is therefore accompanied by proton dissociation or association. Only at lower pH values, also the ring-closed isomer exists in its protonated state HSP. Strikingly, the pK_a value of the respective protonation site is lowered to 4.8 compared to the ring-opened isomer.

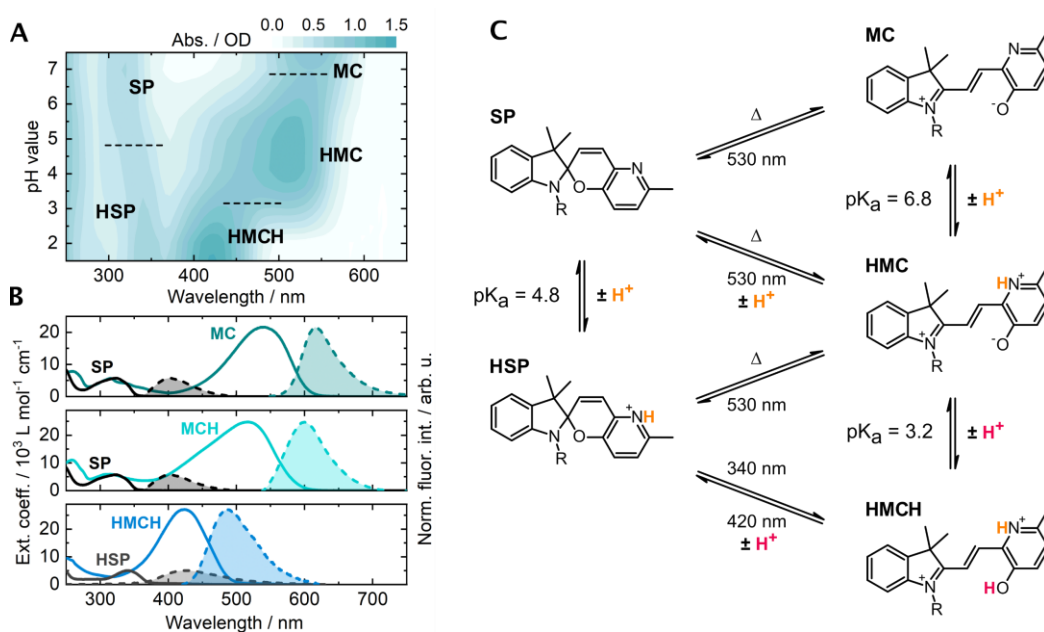


Figure 4.10. Acidochromism of the Py-BIPS derivative **2**. **A)** pH titration UV/vis absorption study. The individual absorption bands correspond to the indicated (non-)protonated species of both photoisomers. **B)** Absorption and scaled fluorescence spectra of the pure photoisomer states, measured at pH 7.4 (top), pH 5.5 (middle) and pH 1 (bottom). **C)** Schematic reaction model of the behaviour of compound **2** in the acidic pH range extracted from systematic pH-dependent switching experiments.

The interconversion abilities of both protonated states HSP and HMC are almost similar to the non-protonated states. Therefore, switching can be carried out in T- or P-type mode with an approximate turnover of almost 50% regardless of the protonation state down to a pH value of 3.2. Upon further acidification also the phenolic site of the ring-opened isomer is protonated (HMCH). Thermal

interconversion is halted under these conditions, but the switch system can still be operated photochemically with an even higher turnover of roughly 60%.

In summary, the Py-BIPS derivative **2** represents a highly pH-dependent photochromic system that exhibits very auspicious switching properties throughout a broad pH range. In addition to the discriminable absorption bands, specific fluorescence signals are observed for the individual protonated states (Figure 4.10B). Hence, the compound serves as fluorescent pH sensor for aqueous solutions. The reversible on-off functionality also makes it an attractive probe for super-resolution microscopy techniques that make use of photoswitch fluorophores.

Light-Controlled Reversible pH Regulation

The most astonishing feature of the Py-BIPS compound **2** is certainly the photoacidity of the protonated MC isomers. Since the HMC \rightarrow SP as well as the HMCH \rightarrow HSP conversion reactions engage the dissociation of a proton, a dual photoacid is provided by compound **2**. It could thus be applied for light-regulation of proton-coupled processes under certain pH conditions. Furthermore, pH jumps induced upon photo-isomerization should be feasible.

The increased proton concentration impedes the detection of a pH jump induced by HMCH \rightarrow HSP conversion. In contrast, a light-driven reversible pH regulation can be realized using the HMC \rightarrow SP isomerization in the less acidic to neutral pH range (Figure 4.11). As the applied buffer concentration apparently affects the pH conditions, diluted PBS buffer (1/100) was used in the experimental procedure. Depending on the amount of compound **2** that is dissolved, the buffer pH value drops, due to the deprotonation of the sulfonic acid residue. The pH can be manually adjusted in this sample preparation phase.

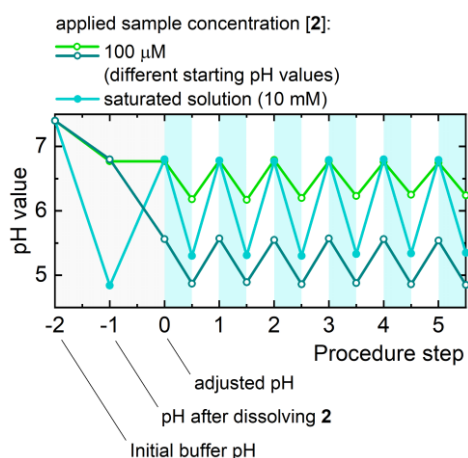


Figure 4.11. Light-regulated pH switching with different concentrations of Py-BIPS **2** in diluted PBS buffer. Prior to the cyclic experiment the buffer pH value can be adjusted manually. Photoswitching is then carried out by alternating irradiation with 530 nm (cyan areas) and thermal recovery in the dark (empty areas).

Starting from an equilibrium distribution of SP and HSP at the adjusted pH value (Figure 4.11, procedure step 0), a pH drop of roughly 0.6-0.7 units can be induced by irradiation of a 100 μ M solution of **2** with visible light.^[11] Remarkably, the initial pH value is restored within few minutes under exclusion of light. This can be readily repeated over several cycles. For a saturated solution of **2**, with an approximate concentration of 10 mM, a more pronounced reproducible pH jump of 1.5 units could be detected. The lower limit for successful pH regulation is provided by the pK_a value of HSP. Therefore, the initial pH value can be adjusted down to a value of ~ 4.5 . Interestingly, pH switching beyond the neutral point with an upper limit of ~ 7.5 could be exercised.

Similar pH regulation experiments were already performed using the light-induced proton dissociation reaction of the phenolic proton of merocyanines in a pH range of $\sim 4-5$.^[148-150] For unsubstituted BIPS-type compounds the respective protonation site exhibits a pK_a value of 7.8. It is striking that the incorporation of the pyridinium moiety shifts the pK_a to 3.2, which is even lower than the value of 3.7 found for Nitro BIPS.^[58] Therefore, an electron-withdrawing effect of the pyridinium motif can be noted.

The use of photoswitches with isomers of different acidities as photoacids provides great opportunities for photoacid development since they enable a reversible control over their acidic state. Especially photoacidic merocyanines represent switches, that can be operated as metastable photoacids, regardless of the mechanism of proton-release.^[151] Yet, depending on the application it is essential to know about the mechanistic details and the time scale of proton-transfer.

Neither for Nitro-BIPS nor for Py-BIPS derivatives, the underlying proton-dissociation mechanism have been investigated so far. It is not clear whether the proton is released upon optical excitation in advance to ring-closing or as a consequence of ring-closing. In the case of compound **2**, this is in principle true for both possible proton-release reactions. The individual mechanisms of the proton-release reactions of the photoacidic states HHMC and HMC of **2** are addressed in the following. To gain a general understanding about the photoacidity of merocyanines, the proton-release dynamics of Nitro-BIPS and Dinitro-BIPS are comparatively investigated.

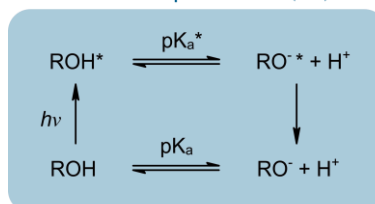
4.1.3 PROTON-TRANSFER DYNAMICS OF MEROCYANINE PHOTOACIDS (Reference [III])

Photoacidic compounds enable the conversion of an optical stimulus into a distinct chemical response – namely proton-transfer. They therefore represent a fascinating photochemical tool to address one of the most fundamental processes in nature in a remote fashion. The concept of photoacidity can in principle rely on discriminable mechanisms, as illustrated in Figure 4.12.

In the original sense, a photoacid (PA) is defined as a compound whose acidity is significantly enhanced upon light-induced electronic excitation. Typical organic molecule representatives for this type of reactivity are aryl-OH compounds (ROH), like phenols or naphthols. The so-called Förster cycle model^[152,153] (Figure 4.12, top) is a purely thermodynamic and simplified approach to describe this phenomenon. The excited state is characterized by its pK_a^* value that is several units lower than the ground state pK_a . Proton-dissociation thus occurs within the excited state lifetime of ROH* which produces the corresponding conjugate base in its excited state (RO^{-*}). This entails that the released proton thermally reassociates upon excited state relaxation.

The second mechanism is based on the formation of an acid in its ground state subsequently to a light-induced reaction. The photoreactive starting material is then referred to as photoacid generator (PAG). Accordingly, numerous types of dissociation or isomerization photoreactions can be applied for photoacid generation and the acidity is ultimately determined by the pK_a value of the product.^[154,155] Typical PAGs are mostly irreversible but allow for a pronounced increase of the proton concentration in solution upon irradiation.

Excited state photoacid (PA)



Photoacid generator (PAG)

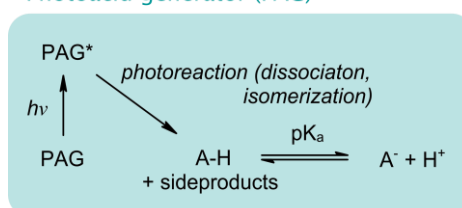


Figure 4.12. Generalized photoreaction mechanism schemes of excited state photoacids (PA) and photoacid generators (PAG).

Photoacid Generation by HMC of Py-BIPS 2

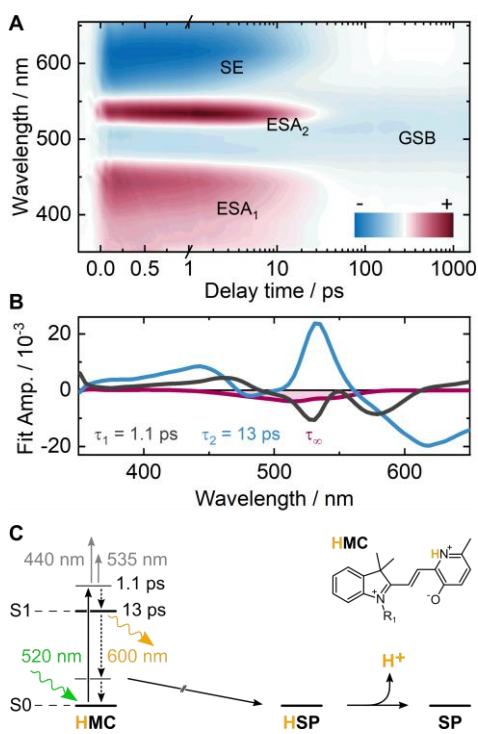


Figure 4.13. **A)** TA spectrum of the HMC isomer of Py-BIPS **2** in aqueous solution at pH 5.5 and **B)** DAS of the lifetime components determined by GLA. **C)** Photoreaction and proton-release mechanism scheme of HMC as a PAG.

Upon conversion of HMC to the ring-closed SP state of compound **2**, the pK_a of the respective site is altered. To find out, whether the proton already dissociates within the excited state or at a later stage of the photoreaction, UV/vis-TA experiments were performed at pH 5.5. The TA spectrum of HMC (Figure 4.13A) shows two separate ESA signals, just as the spectra of the non-protonated MC forms of compound **1** and **2**. Interestingly, the ESA₂ signal is shifted to higher wavelength for the compounds that bear a substituent at the pyridine-nitrogen (**1** and HMC of **2**, Figure 4.4) compared to the unsubstituted (MC of **2**).

In the kinetic analysis of the dataset by GLA, two lifetime components were determined to model the decay dynamics. The corresponding amplitudes

reflect analogous contributions as in the cases of the before discussed Py-BIPS MC forms of **1** and **2** and are furthermore in accordance with the previously reported Py-BIPS compound.^[57] Therefore, a similar relaxation pathway can be assumed for the HMC isomer of compound **2**. An initial cooling within the S1 state HMC* occurs during the first picosecond (τ_1). The following excited state decay is captured by the lifetime component $\tau_2 = 13$ ps, which is in between the excited state lifetimes found for the unsubstituted and the methylated Py-BIPS derivative. Hence, a clear trend for an accelerated excited state decay from the unsubstituted via the protonated to the methylated Py-BIPS MC form can be noted at this point. The residual GSB after 1.5 ns (τ_∞) is indicative of the photoconversion to the ring-closed structure.

The absence of signals that could be attributed to an intermediate excited ring-opened species points to a direct decay into the ground state at the HMC structure. If

the deprotonated MC* would be formed from HMC* via proton dissociation, the same excited state signature should be observed as upon direct excitation of MC of compound **2**. The proton is therefore evidently not released within the excited state. After relaxation into the HMC ground state the ring-closed structure is suggested to be formed in its protonated state HSP and the proton subsequently dissociates. Accordingly, the HMC isomer must be considered as a PAG rather than an excited state PA. Delayed by the formation of the acidic HSP, proton-dissociation is then dictated by the lowered pK_a value and the diffusive motion away from the conjugate base SP.

Typically, non-protonated N-heterocyclic functionalities show a photobasic reactivity. Compounds like quinoline,^[156] acridine^[157] and also pyridine^[158] derivatives can exhibit a lowered pK_a^* value in the excited state and consequently acquire a proton from the solvent upon irradiation. Interestingly, this behaviour does not apply to the non-protonated MC isomer of compound **2** since the formation of HMC* was not observed. However, the reactivity of N-protic sites may vary with the molecular scaffolds that they are incorporated in and the applied conditions.

Proton-Transfer Dynamics of HMCH of Py-BIPS **2**

The pyridinol-oxygen of the ring-opened isomer of compound **2** is protonated with a ground state pK_a of 3.2. At low pH values, the O-protic site of HMCH enables light-induced proton-dissociation. The corresponding photodynamics are addressed by UV/vis-TA experiments, shown in Figure 4.14A. Directly upon excitation, a prominent GSB signal is visible as well as the ESA₁ and the minor SE₁ signal, that are attributed to HMCH*. The respective excited state signals decay with a lifetime $\tau_1 = 1.1$ ps, which is accompanied by the formation of a discriminative excited species indicated by ESA₂ and SE₂. Since the latter signals perfectly match the spectral signature of HMC* and the determined excited state lifetime thereof (τ_2) is in agreement with the one found in the HMC TA measurement at pH 5.5 (Figure 4.13B). Consequently, an excited state proton-release is evidently observed here. The photoacidic phenolate site of HMCH thus functions as an excited state PA, in contrast to the pyridinium site acting as PAG. Thus, the Förster cycle model is applicable for the photoprotolytic reaction of the HMCH isomer (Figure 4.15).

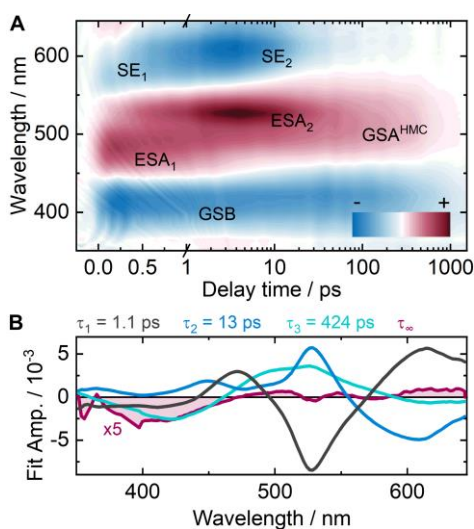


Figure 4.14. A) TA spectrum of the HMCH isomer of Py-BIPS **2** in aqueous solution at pH 1 and **B)** DAS of the lifetime components determined by GLA.

After the depletion of ESA_2 and SE_2 (HMC*), only the GSB maintains until almost 1.5 ns in the TA spectrum, as well as a broad positive signal around 520 nm. The positive signal originates from the HMC ground state absorption (GSA). The simultaneous decay of the GSA signal and the GSB signal with the lifetime τ_3 hints at the recovery of the HMCH ground state via reprotonation. Therefore, the entire Förster cycle can be assigned here and is completed roughly within the detected time frame of 1.5 ns.

The thermodynamic Förster model furthermore allows for an estimation of the excited state pK_a^* .^[159] By correlating the proton-dissociation free-energies in the ground and excited states with the transition energies, a pK_a drop of 8.7 is obtained. With a ground state pK_a of 3.2, this estimation yields a pK_a^* of -5.5. Such exceptionally strong PAs that adopt negative pK_a^* values, are denoted as super-photoacids. The photoacidic capacities of HMCH are therefore comparable to other well-known representatives, like 5,8-dicyano-2-naphthol (DC2N, $pK_a^* = -4.5$)^[160–162] or N-methyl-6-hydroxyquinolinium (NM6HQ, $pK_a^* = -7$).^[163–165] In general, aromatic compounds with electron-withdrawing substituents show an enhanced photoacidity, due to the increased stabilization of the negative charge of the conjugate base. Unsubstituted PAs like the parent phenol or 1-naphthol (1N) are significantly less acidic with positive pK_a^* values of 3^[166] and 0.5,^[160] respectively. The most extensively investigated PA is the polycyclic 8-hydroxypyrene-1,3,6-trisulfonic acid (HPTS), which exhibits a pK_a^* of 1.3.^[167] In the case of HMCH, the phenolate charge is well-delocalized within an extended electronic π -system, where even two additional positive charges are found.

On an ultrafast time scale, the proton-dissociation proceeds via a direct excited state proton-transfer (ESPT) of an ROH-type PA (R = aryl) to an adjacent water molecule in a two-step sequence.^[168–170] Upon proton abstraction, a contact ion pair is formed by the conjugate base anion RO^* and a solvated proton. The contact ion pair

is assumed to be spectrally similar to the free RO^* . Subsequently, the ion pair distance increases because of the diffusive motion of the proton away from RO^* or by proton-hopping via Grotthuss mechanism in water.^[171] This process can be fully reversible within the excited state lifetime of the PA, where the reverse direction is described by the diffusion-assisted recombination model.

The photoprotonolytic reaction of HMCH appears to be very efficient since the excited state signals associated with HMCH^* thoroughly convert into that of the excited conjugate base HMC^* . The determined lifetime component that models this transition can thus be translated into a proton-transfer rate $k_{\text{pt}} = \sim 9.1 \times 10^{11} \text{ s}^{-1}$ for the formation of the contact ion pair. Additional TA experiments in organic solvents confirmed, that the super-photoacid HMCH is also capable of transferring its proton to protic solvents like methanol and ethanol, with a lifetimes of 1.7 and 1.9 ps, respectively. The efficiency of the ESPT process is yet lower than in water and competing deactivation channels are suggested to be more pronounced. Only for the aprotic solvent acetonitrile, no indications for a successful proton-transfer were observed.

Proton-Transfer Dynamics of Nitro-BIPS 3

The TA spectrum recorded upon excitation of MCH of compound **3** at pH 1 is shown in Figure 4.16A. Similar to the protonated Py-BIPS merocyanine isomer presented before, the initially appearing MCH^* signals ESA_1 and SE_1 decay in parallel to the formation of the conjugate base MC^* signals ESA_2 and SE_2 . The assignment is complicated by the fact that the respective ESA bands appear in the same spectral range, but the SE features clearly reveal the transition from MCH^* to MC^* (compare Figure 4.9A). Therefore, an excited state proton-dissociation of compound **3** can be confirmed here.

A lifetime component of 0.4 ps describes an initial relaxation with the HMCH^* state, which subsequently decays with a 2.1 ps lifetime as illustrated in the photoreaction mechanism scheme in Figure 4.16C. However, the proton-transfer is

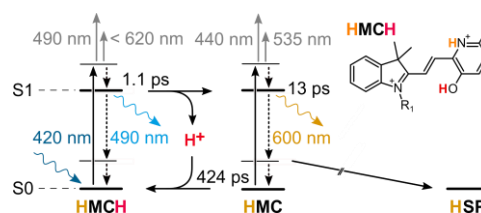


Figure 4.15. Photoprotonolytic reaction scheme according to the Förster cycle of the protonated merocyanine photoacid HMCH of Py-BIPS **2**.

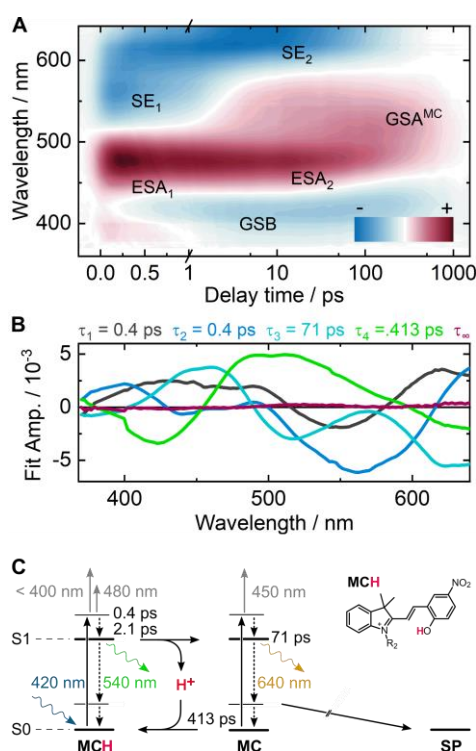


Figure 4.16. **A)** TA spectrum of the MCH isomer of Nitro-BIPS **3** in aqueous solution at pH 1 and **B)** DAS of the lifetime components determined by GLA. **C)** Photoprotolytic reaction scheme of the protonated merocyanine photoacid MCH.

assumed to proceed already during the initial vibrational relaxation, since SE₂ is formed at very early delay times. Modelling the transition from SE₁ to SE₂ with only one exponential component yields a lifetime of 1.6 ps. This corresponds to a rate constant $k_{pt} = 6.3 \times 10^{11} \text{ s}^{-1}$ for the contact ion pair formation step.

The lifetime component obtained for the following MC* decay τ_3 is slightly slower than the one found upon direct excitation of the deprotonated MC (Figure 4.9B). The population of the MC ground state is indicated by the formation of the GSA signal in parallel to the depletion of the MC*-associated ESA₂ and SE₂ signals. The final ground state reprotonation process is modelled by a lifetime of 413 ps, which is interestingly

very similar to the lifetime found for the HMCH isomer of Py-BIPS **2**. Therefore, the reprotonation is assumed to be solvent-controlled and mainly driven by diffusion. The almost negligible amplitude of the infinite lifetime confirms the accomplishment of the entire photoprotolytic cycle within the observed 1.5 ns.

According to the Förster cycle approximation, a substantial pK_a drop of 7.9 units is estimated to be induced by excitation. With the resulting pK_a^* value of -4.2, the MCH isomer of compound **3** can be classified as a strong super-photoacid. Similar to the HMCH isomer of Py-BIPS **2**, Nitro BIPS **3** is also capable of ESPT to the protic solvents methanol and ethanol. Competing deactivation channels are assumed to be favoured in organic solvents, where radiative decay of MCH* and more importantly internal conversion, enhanced by the nitro group, have to be considered.^[144] Nevertheless, similar lifetimes of 2.4 ps were determined for MCH* decay in both organic solvents, which is only slightly longer than the lifetime in aqueous solution. In the aprotic

solvent acetonitrile, however, the absence of a distinct SE₂ signal and the presence of an ESA band that decays on the same time scale as the associated SE band provide evidence for the exclusion of an ESPT.

Proton-Transfer Dynamics of Dinitro-BIPS 4

Compared to Nitro-BIPS **3**, Dinitro-BIPS **4** bears an additional nitro group in *ortho*-position to the photoacidic hydroxy group, which fundamentally affects the ESPT dynamics. The TA spectrum in acidic aqueous solution (Figure 4.17A) reveals drastically accelerated overall photodynamics. Most strikingly, a dominant recovery of the MCH ground state is manifested by a rapid depletion of the GSB signal. The photoprotolytic cycle seems to be only a minor deactivation channel, indicated by the fact that the ultrafast ESA₁/ESA₂ signal decay leaves two weak positive signals

around 460 nm and 550 nm behind. Those correspond to the conjugate base MC*, just as the weak SE signal that is formed simultaneously. An extraordinarily short lifetime of 0.8 ps is obtained for the MCH* state and the 9.4 ps lifetime determined for MC* is in accordance with the 8.7 ps found upon direct excitation of MC.

The acceleration of the observed dynamics is due to the stabilization of the acidic proton by the adjacent oxygen of the nitro group. This pre-existing hydrogen bond facilitates proton-abstraction and the nitro group acts as proton-acceptor in an excited state intramolecular proton-transfer (ESIPT). *Ortho*-nitro benzyl compounds are known to undergo photoinduced ESIPT processes, where typically an α -H-atom of an alkylic residue is transferred.^[172] The proton-transfer to the nitro group produces a protonated *aci*-nitro species, which in the case of MCH of compound **4** converts back the ground state rapidly via proton recombination.

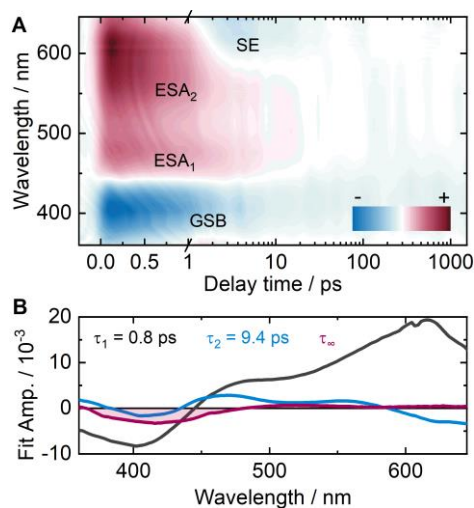


Figure 4.17. A) TA spectrum of the MCH isomer of Dinitro-BIPS **4** in aqueous solution at pH 1 and **B)** DAS of the lifetime components determined by GLA.

The 0.8 ps lifetime component found for the MCH* decay corresponds to an upper limit of $\sim 1.3 \times 10^{12} \text{ s}^{-1}$ for the proton-transfer rate, which is the highest value among the investigated merocyanine PAs. Upon excitation a pK_a drop of -8.3 units is estimated, based on the Förster cycle model. This implies an excited state pK_a^* value of -4.4, which is in a similar range as those determined for compound **2** and **3**.

Free-Energy - Reactivity Correlation

The TA spectroscopic studies of the compounds **2-4** reveal an ultrafast excited state photoacidity for the O-protic site of merocyanines. The investigated derivatives exhibit comparable photoinduced pH decreases of roughly 8-9 units. Extraordinarily low pK_a^* values of -5.5, -4.2 and -4.4 are estimated for the compounds **2**, **3** and **4**, respectively, by using the Förster cycle approach. The findings are further analyzed by a semi-empirical correlation, to rationalize the relationship between the thermodynamics of excited state acidity and the observed proton-transfer rates. The large body of literature about ESPT dynamics confirms the robustness of the free-energy – reactivity correlation, given in equation 4.1.^[173–176] The proton-transfer rate k_{pt} can be expressed as a transition state rate constant, depending on the effective activation free-energy change in the excited state ΔG^\ddagger :

$$k_{\text{pt}} = k^* \cdot \exp\left(-\frac{\Delta G^\ddagger}{RT}\right) \quad (4.1)$$

R is the gas constant, T is the absolute temperature and $(k^*)^{-1}$ represents the intrinsic frequency factor of the transfer process. The free-energy change ΔG^\ddagger can be derived by Marcus theory for electron-transfer reactions but adapted for proton-transfer.^[177] Marcus theory gives a major role to solvent alignment and reorganization energetics in charge transfer processes. The proton-transfer is suggested to proceed along a solvent coordinate with a specific activation barrier. Furthermore, according to the modified bond-energy-bond-order (BEBO) model, the proton-transfer is considered as concerted bond-rupture and bond-formation along an existing hydrogen bond to the solvent.^[178] The free-energy change ΔG^\ddagger is then estimated by equation 4.2:

$$\Delta G^\ddagger = \frac{\Delta G_0}{2} + \Delta G_0^\ddagger + \frac{\Delta G_0^\ddagger}{\ln 2} \ln\left(\cosh\left[\frac{\Delta G_0 \ln 2}{2\Delta G_0^\ddagger}\right]\right) \quad (4.2)$$

The solvent-dependent free-energy of the charge-exchange process is given by ΔG_0^\ddagger when the total free-energy change ΔG_0 of the proton-transfer is equal to zero.

$$\Delta G_0 = RT \ln 10 \Delta pK_a \quad (4.3)$$

The correlation of the proton-transfer rates and the estimated pK_a^* values is depicted in Figure 4.18 together with the Marcus BEBO fit function including multiple com-

parable excited state (super-)photoacids. Several phenol,^[166] 1N,^[175,179] 2N and hydroxy quinoline (HQ) derivatives were added with pK_a^* values around zero and below. For ESPT to water, the pK_a^* values ought to be corrected for the electrostatic contribution $pK_{a,el} = R_D/2.3a$, where a charge of -1 is assumed for the conjugate base anion and the contact radius a is fixed at 6.5 Å.^[180] In the fit routine, a frequency factor of roughly $5 \times 10^{12} \text{ s}^{-1}$ is determined, which is in well agreement with reported values.^[175] When treated as a free parameter, an activation free-energy of $\Delta G_0^\ddagger = 3.5 \text{ kcal mol}^{-1}$ is found.

With their pK_a^* values around -4 to -5, the investigated merocyanine super-photoacids are located on the high exothermic branch of the free-energy – reactivity correlation function. They are significantly more acidic than most phenols and naphthols and drastically more acidic than the prominent HPTS compound. Remarkably, only some representatives of the structurally related quinone cyanine (QCy) family exhibit similar or even stronger photoacidic properties.^[181] Similar to the herein studied Py-BIPS compound **2**, the QCy derivatives exhibit an extended conjugation of an N-heterocyclic π -system that forms a push-pull effect, stabilizing the negative charge of the conjugate base anion. This substantially enhances the photoacidity of the O-protic site. Especially, the QCy9 compound is outstanding in this respect, with the highest proton-transfer rate of $\sim 10^{13} \text{ s}^{-1}$ reported to date.^[182]

Since the results for the merocyanine excited state photoacids are well in line with the literature-based correlation, the ESPT process is suggested to rely on the solvent coordination network in proximity to the photoacidic site. It must be noted that the

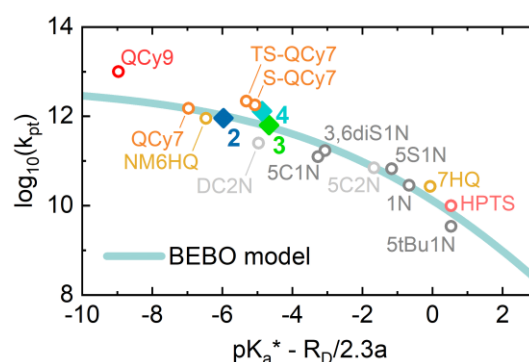


Figure 4.18. Free-energy - reactivity correlation. The proton-transfer rates are plotted versus the estimated pK_a^* values corrected by the electrostatic contribution for ESPT to water.

polar alkylic residues of the investigated merocyanines might contribute to a pre-organization of the solvent molecules, but a direct proton-transfer to the sulfonate group of compound **2** can be excluded. Yet, an enhancing effect of the sulfonate groups is also assumed for the compounds S-QCy and TS-QCy.^[181] As different proton-transfer rates were observed in organic protic solvents, also a proton-transfer to highly coordinated traces of water in the samples that might form solvent clusters seems unlikely.

4.2 ANTIBIOTIC-BINDING RNA APTAMERS

It is still a key question in synthetic biology which factors are vital to turn an artificial aptamer into an active riboswitch. The main focus of the following studies is the investigation of RNA aptamer ligand binding characteristics in order to contribute to the general understanding of RNA-based regulation mechanisms. The TC as well as the CFX aptamer served as model systems to shed light on different aspects of RNA folding and ligand binding.

4.2.1 FOLDING OF THE TC-BINDING APTAMER

Tetracycline (TC) is a well-established therapeutic agent that affects prokaryotic translation by inhibiting ribosomal A-site occupation.^[183] The antibiotic exhibits a low toxicity and a good cellular uptake is ensured, which makes it an excellent starting point for *in vitro* selection of RNA aptamers. Berens et al.^[112] found the first TC-binding aptamers that were structurally optimized and shortened to obtain the minimal motif,^[118,184] illustrated in Figure 4.19. The TC aptamer is highly suitable for spectroscopic investigations since the almost non-existent fluorescence of the free ligand is drastically enhanced upon aptamer binding. Therefore, it represents a fluorogenic RNA aptamer which is very advantageous for biochemical assays or RNA imaging techniques, used in the context of microscopy for example. The substantial fluorescence enhancement relies on the increased rigidity of TC within the binding pocket, that reduces the efficiency of non-fluorescent vibrational relaxation.^[130]

Unlike the majority of artificial aptamers, the TC aptamer can be applied as ligand-sensing domain of engineered riboswitches and it has already been successfully used

in vivo for diverse regulatory tasks.^[119] Following a mechanism, where the TC aptamer forms a ligand-stabilized roadblock for the scanning ribosome, translational control was realized as well as conditional splicing.^[123] Furthermore, TC-dependent translation initiation by sequestration of the ribosomal binding site was successfully exercised in yeast cells^[185] and also self-cleaving hammerhead ribozymes^[186] were designed, based on the TC aptamer.

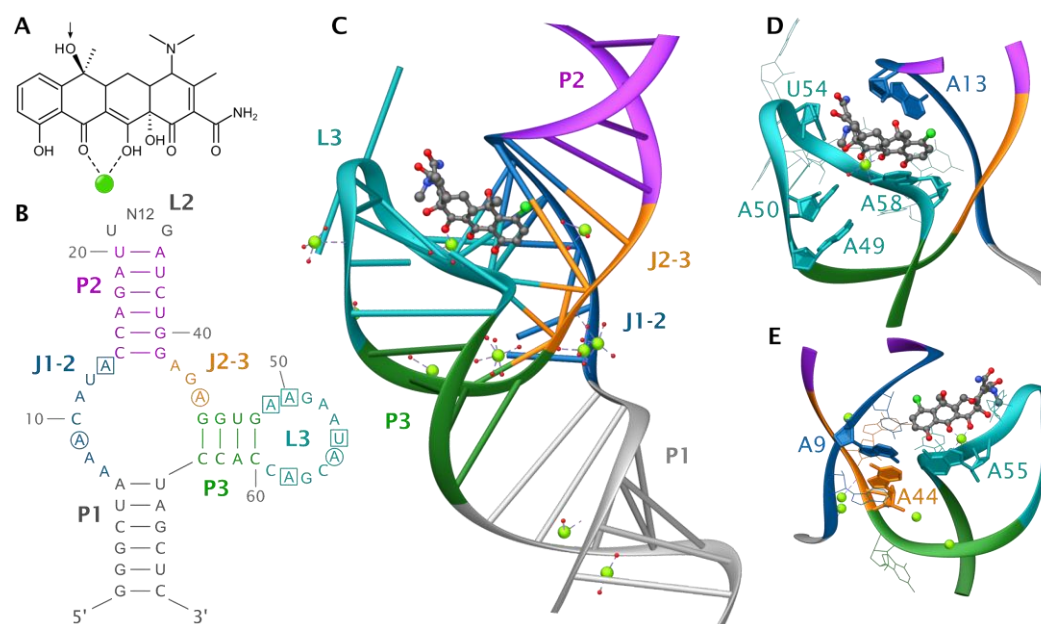


Figure 4.19. **A)** Molecular structure of TC with the chelation site for a divalent Mg^{2+} cation (green sphere). The $R_{6\beta}$ -OH group of TC is indicated by an arrow. **B)** Secondary structure of the TC aptamer. The squares and circles indicate the highlighted nucleobases in D and E, respectively. **C)** Tertiary structure of the ligand-bound state of the TC aptamer based on the reported crystal structure^[187] (PDB: 3EGZ). The ligand TC is depicted as ball and stick model and the incorporated Mg^{2+} ions are shown as green spheres along with coordinated water molecules shown as small red spheres. **D)** Close-up of the binding pocket. The nucleobases in proximity to the ligand are highlighted. **E)** Close-up of the triple helix motif.

The aptamer consists of three stems (P1, P2 and P3), connected by two joining regions (J1-2 and J2-3), and two loops (L2 and L3). The core motif is relatively small and consists of 69 nucleotides, where the lower part of the stem P1 and the loop L2 may vary in the numerous reported studies as those regions are not essential for ligand recognition. The ligand TC is bound as a Mg^{2+} ion chelate complex and is clamped within the binding pocket by loop L3 and the upper part of J1-2. TC stacks upon the nucleobase A58 and mainly together with A49, A50 and A13 the binding pocket interaction network is established (Figure 4.19D). The base A13 is oriented

perpendicular to TC and closes the clamp on top of the ligand by forming two H-bonds to the R_{6β}-OH group of TC (Figure 4.19A). However, the core of the aptamer structure is based on an irregular triple helix of the junctions J1-2, J2-3 and the loop L3.^[187] Stabilized by the base triplet A9, A44 and A55 (Figure 4.19E), this motif is vital for the formation of the ligand-bound conformation. To fold into this compact state and to compensate for the negatively charged phosphate backbone, several Mg²⁺ ions are incorporated in the immediate vicinity of the triple helix motif.

The aptamer was found to be preformed to a significant extent and an extraordinarily low dissociation constant of 770 pM^[184] was determined at 10 mM Mg²⁺. Based on EPR studies of spin-labeled TC aptamer variants, two mainly competing folds were identified in absence of TC.^[188] While one of them shows high structural similarity to the ligand-bound state already, the other exhibits a more opened conformation at the joining region J1-2. The latter undergoes a structural adjustment of the respective region upon ligand binding and is not observed anymore when TC is present.

The ligand binding kinetics were addressed by Förster et al.^[130] by means of stopped-flow studies, monitoring the TC fluorescence increase upon ligand binding in a time-resolved fashion. Starting from an entirely prefolded aptamer conformation, the ligand binding proceeds in a two-step sequence that is interpreted as an initial association of TC towards the binding pocket, followed by a structural reorganization of the aptamer to accommodate the ligand. Comparison with the observed kinetics of point mutated aptamer variants furthermore revealed that the association step is mainly driven by interactions of TC with the bases A13 (J1-2) and A50 (L3), located on opposite halves of the binding pocket (Figure 4.19D). The following accommodation step proceeds virtually irreversible, indicating an energetically favoured structural adjustment. Here, the establishment of H-bonds between TC and A13 presumably plays an important role.

The *in vitro* selection of the TC aptamer, as well as following characterization studies, were carried out at Mg²⁺ concentrations far above the physiological range, where the aptamer is suggested to be preformed and binding-competent. Yet, the folding landscape of the aptamer shows a pronounced Mg²⁺-dependence in the lower concentration range which was elaborated by Reuss et al.^[131] In the absence of Mg²⁺, the aptamer exists as an ensemble of only partially folded conformations, not being

able to bind the ligand. A minimum Mg^{2+} concentration of 0.5 mM is required for preformation of binding competent folds. Ligand binding itself further stabilizes the aptamer structure, but additional Mg^{2+} ions are acquired during the binding process to establish the final complex. At Mg^{2+} concentrations above 1.5 mM, the conformational distribution is entirely shifted towards binding-competent structures.

Especially when discussing *in vivo* regulation mechanisms of engineered riboswitches, the conformational features under physiological conditions must be considered carefully. Therefore, the aim of the present study is to shed light on the effect of Mg^{2+} on the folding of crucial structural elements of the TC aptamer and to determine characteristic differences between the prefolded and ligand-bound state.

The 2ApFold Approach

The rational use of fluorescence labels is an excellent approach for addressing dynamic properties of biomolecules. Concerning conformational RNA studies, especially the nucleobase analogue 2-aminopurine (Ap) is a well-suited label since it is relatively non-invasive to the overall tertiary structure when replacing a purine base. Its inherent fluorescence is quenched due to π -stacking interactions and therefore reports on environmental changes very sensitively.^[189]

Time-resolved detection of the fluorescence change of an Ap label, attached to carefully chosen positions, even allows for global interpretations about the folding dynamics of structural motifs. The term 2ApFold approach was coined by Micura et al.,^[190] who used this methodology to investigate the folding behaviour of e.g. the adenosine deaminase A-riboswitch,^[191] the thiamine pyrophosphate riboswitch^[192] and the preQ₁ class-I riboswitch.^[193]

In this work, a systematic study of Ap-labelled variants of the TC core aptamer is presented that is supposed to provide a comprehensive description of the Mg^{2+} -induced structural changes during prefolding and the ligand binding process. Five single labelled aptamer samples are investigated, where Ap replaces the nucleobase positions shown in Figure 4.20. Due to the lower synthetic effort, split aptamer variants are used here where loop 2 is missing and the two single stranded halves of the aptamer are hybridized prior to experimental use. The secondary structure of the employed samples is provided in the Appendix (Figure A1). The respective loop may vary without significant effects and is thus irrelevant for proper folding of the TC core

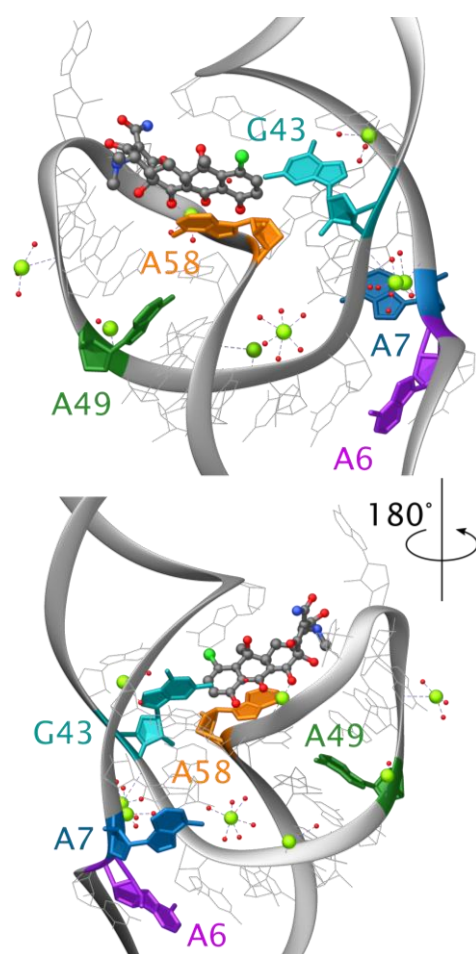


Figure 4.20. Nucleobase positions A6, A7, G43, A49 and A58 that were substituted individually with fluorescent Ap labels.

aptamer.^[115] The herein applied sequence numbering corresponds to the one used in previous literature.^[130,131]

The base A58 (L3) forms a direct contact with the ligand since TC stacks upon it in the ligand bound state. A49 (L3) and G43 (J2-3) are located on the two opposite halves of the binding pocket and thus report on the folding of the core structure. The positions A6 and A7 were chosen to investigate the establishment of the turn motif at the transition from the stem P1 to the joining region J1-2. Furthermore, A7 and G43 are integrated in the surrounding of the triple helix and should indirectly report on this motif.

To determine the Mg^{2+} -dependent conformational changes during preformation and ligand binding, a series of fluorescence titrations was conducted with each of the labelled aptamer variants. The emission of Ap was monitored upon stepwise addition of

Mg^{2+} both in presence and in absence of TC. Without Mg^{2+} , the aptamer is unfolded and not capable of ligand binding, which is the starting point of the titration experiments. In absence of TC, an entirely prefolded and binding-competent aptamer structure is formed upon addition of Mg^{2+} whereas the ligand bound state is established in the presence of TC. Yet, it is important to note, that the folding sequences do not necessarily progress via similar Mg^{2+} -stabilized prefolded states. If TC is present, a ligand-stabilized intermediate bound state is formed at medium Mg^{2+} concentrations around 0.5 mM.^[131]

The obtained Mg^{2+} -dependent emission data for the variants G43Ap, A49Ap and A58Ap with labels in proximity to the binding pocket are displayed in Figure 4.21. The shown curves of both titration series, with and without TC, are normalized to the initial emission value of Ap. When TC is present, its emission increase upon Mg^{2+} addition (gray lines) confirms the binding of the ligand. The corresponding curves are shaped similarly for all variants, with a steep initial increase up to roughly 0.5 mM Mg^{2+} .

The Ap label of the variant G43Ap is located near the triple helix motif and is stacked between the neighbouring bases A42 and A57 from the loop L3. During the transition from unfolded to the prefolded state in absence of TC, an overall decrease of Ap emission of 35% is observed, that successively takes place almost over the entire Mg^{2+} range up to 5 mM. This is indicative of a cation-induced compacting of the aptamer. Yet, the decrease of Ap emission is twice as pronounced in the presence of TC. After a significant drop at low Mg^{2+} concentrations (< 0.5 mM), virtually no signal change occurs anymore above 1.5 mM Mg^{2+} . The different Ap emission changes hint at distinguishable environments of the G43 position in the prefolded and the bound state. In the prefolded state, the triple helix motif is thus not entirely formed even at saturating Mg^{2+} concentrations. This is in agreement with the assumption, that the prefolded state adopts a more open conformation in the region of J1-2 and J2-3 and the two halves of the binding pocket are more distant to one another.^[130,188] This might further indicate that the missing interaction in the prefolded state is the stacking with A57 from the adjoining loop L3.

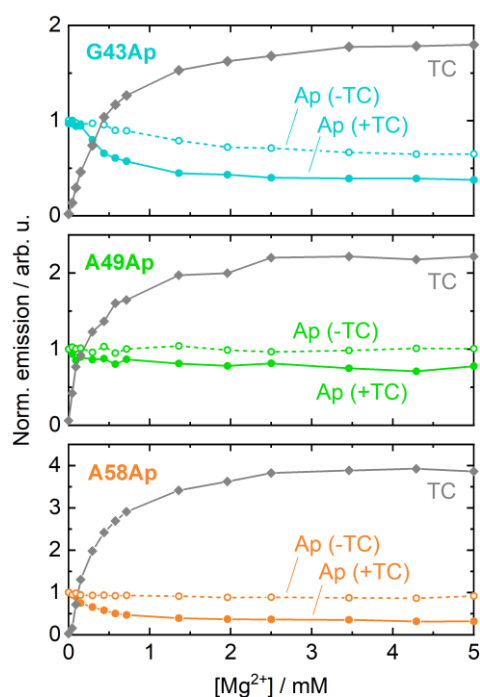


Figure 4.21. Fluorescence-monitored Mg^{2+} titration data in presence (solid lines) and absence of TC (dashed lines) for the variants G43Ap (top), A49Ap (middle) and A58Ap (bottom). Ap emission (coloured lines) was collected at 365 nm and TC emission (grey lines) at 520 nm.

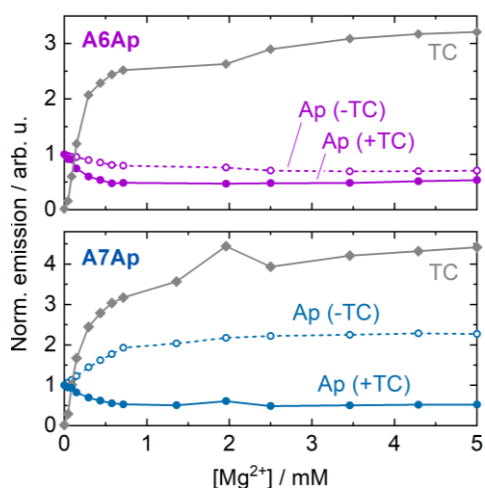


Figure 4.22. Fluorescence-monitored Mg^{2+} titration data in presence (solid lines) and absence of TC (dashed lines) for the variants A6Ap (top) and A7Ap (bottom). Ap emission (coloured lines) was collected at 365 nm and TC emission (grey lines) at 520 nm.

the low Mg^{2+} range in presence of TC. This means that the surrounding of A58 does not drastically change upon prefolding and the only additional interaction that A58 encounters in the bound state is the direct stacking contact with the ligand.

The label positions A6Ap and A7Ap are used as local probes for the formation of the kink below the joining region J1-2 and the triple helix motif. The crystal structure of the bound state reveals a Watson-Crick base pairing between A6 and U64 which forms the top of the stem P1. The Ap emission of A6Ap decreases already in the 0-1 mM Mg^{2+} range and levels off above for both titration series (Figure 4.22, top). The decrease is more pronounced in presence of TC. Hence, the prefolded and the bound state are established already at a similarly low Mg^{2+} threshold, but they differ structurally in the upper part of P1. Most strikingly, the kink motif between A6 and A7 observed for the ligand bound structure must be drastically different in the prefolded state, since the recorded Ap emission changes of A7Ap showed opposite responses in presence and in absence of TC. While the emission drops upon ligand binding, it increases by more than double upon exclusive prefolding. Therefore, the A7 position lacks interactions in the Mg^{2+} -stabilized prefolded state, that can be found in the unfolded state. It can be concluded at this point that formation of the kink and triple

For variant A49Ap, the emission signal does practically not change at all in absence of TC. The stacking interactions with the purine bases G48 and A50 are therefore assumed to be established already without Mg^{2+} . The slight decrease of Ap emission in presence of TC is not very defined and might merely account for a more compact conformation of the binding pocket region in the ligand bound state.

Since TC stacks upon the A58 base, the label emission of the A58Ap variant directly reports on ligand binding. Again, no signal change is observed during preformation but a drop of 70% occurs in

helix motifs are highly involved in the conformational adjustments during ligand binding.

Mg²⁺-Dependent Conformational Dynamics

To reveal the conformational dynamics in a time-resolved fashion, the Ap emission changes during aptamer folding were recorded in stopped-flow mixing experiments. Therefore, the aptamer was supplied together with TC as one solution, which was mixed with different Mg²⁺ concentrations to monitor emission changes during the transition from the unfolded to the Mg²⁺-stabilized ligand-bound state.

The recorded Ap fluorescence traces of the Mg²⁺-dependent measurement series for the variants A58Ap, G43Ap and A7Ap are shown in Figure 4.23, provided with experimental concentration conditions. The Mg²⁺-dependent traces of A58Ap reveal a biphasic signal progression and apparently delayed binding kinetics at low Mg²⁺

concentrations in the physiological range. The 0.5 mM Mg²⁺ curve only slightly decreases during the first 10-30 ms, indicating that the A58 surrounding is relatively unaffected by the initial Mg²⁺-driven prefolding of the binding-competent conformation. The following emission drop is then ascribed to ligand capture and the establishment of the TC-A58 stacking interaction. At 1.5 mM Mg²⁺, the Ap emission decrease is still delayed, but significantly faster. For G43Ap, the trace at 0.5 mM Mg²⁺ resembles the biphasic progression of the respective curve of the A58Ap variant, although the initial decrease is more defined. In contrast, the kinetics of G43Ap are almost accelerated to saturating levels at 1.5 mM Mg²⁺. In both cases, however, the

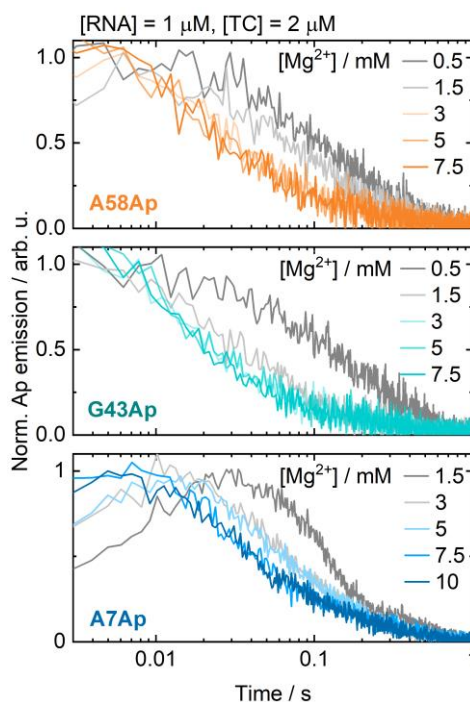


Figure 4.23. Fluorescence-detected stopped-flow experiments with A58Ap (top), G43Ap (middle) and A7Ap (bottom). Shown is the Ap emission change during Mg²⁺-induced formation of the ligand bound state from the unfolded state.

kinetics become completely independent of Mg^{2+} at concentrations above 1.5 mM. The overall decrease of Ap emission is in accordance with the observations from the time-integrated Mg^{2+} titration experiments in presence of TC (Figure 4.21).

The stopped-flow traces of A7Ap show a remarkable rise and decay behaviour at relatively high Mg^{2+} levels. The pronounced initial increase is supposedly due to the preformation of the aptamer and resembles the detected increase in the titration series in the absence of TC (Figure 4.22, bottom). The following signal decrease originates from the establishment of the interaction framework of the A7 position in the bound state and also confirms the decrease in the steady-state experiment in presence of TC. Both steps seem to be accelerated at increasing Mg^{2+} concentrations up to 7.5 mM, where saturation is reached. This strongly hints to one or more distinct metal binding sites in the triple helix region, that are highly involved in the conformational adjustment upon ligand binding. The crystal structure (Figure 4.19E) reveals at least three Mg^{2+} ions in the proximity to the triple helix motif in the final ligand-bound structure. Furthermore, the fluorescence traces show a less steep decrease at later times after 100-200 ms, which hints at a slower final folding step occurring in the region of A7.

To estimate the influence of Mg^{2+} on the individual sequential folding steps, kinetic modeling is performed by fitting the acquired datasets to several meaningful mechanisms. By means of non-linear regression with the software Dynafit4,^[31] the fluorescence stopped-flow traces are approximated with the time-dependent concentration functions of the involved reaction components. Those are derived from the differential equation system based on the corresponding kinetic model and all of the single traces are fitted simultaneously. The obtained fit qualities are then subjected a comparative model evaluation analysis by determination of the Akaike information criterion (AIC) and the Bayesian information criterion (BIC).^[32,33] Both criteria reflect the probability of a certain model compared to other applied models, considering the fit qualities as well as the number of parameters required. High numbers of variable parameters are penalized to avoid over-fitting the datasets. This penalty is more pronounced for the BIC, compared to the AIC. Commonly, the difference values ΔAIC and ΔBIC to the most probable model are calculated, so that values close to zero indicate suitable kinetic models.

Since the RNA samples are provided without Mg^{2+} in the stopped-flow experiments and folding into a binding-competent state is only induced upon mixing with Mg^{2+} . Each of the tested models therefore comprises the addition of Mg^{2+} as a first step followed by ligand binding. An initial ligand binding is also tested as well as a third order reaction of RNA, TC and Mg^{2+} , but those mechanisms are discarded as they completely failed to describe the data.

Starting with a Mg^{2+} -induced prefolding step, numerous different models with increasing complexity and varying combinations of reversible and irreversible steps are applied. After exclusion of unsuitable mechanisms, eight remaining models A-H are compared, which are provided in the Appendix (Table A1). In addition, the determined rate constants of all models are given together with the RMSD values of the corresponding fits and the ΔAIC and ΔBIC criteria (Table A2-4). When comparing the applied models, it turned out that a structural adjustment step must be introduced after ligand binding, to obtain adequate fit qualities. The most suitable models thus represent three-step models with an initial Mg^{2+} -driven RNA prefolding step, followed by ligand binding which in turn induces a final conformational reorganization of the aptamer. The essential models 1,2 and 3 (D, E, and H, Table A1) for the three TC aptamer variants are shown in Table 4.1 and will be discussed in the following paragraphs.

Table 4.1. Selected mechanistic models applied in the kinetic analysis of the fluorescence stopped-flow data of the three TC aptamer variants A58Ap, G43Ap and A7Ap.

Model	Folding mechanism scheme
1	$RNA + M \xrightleftharpoons[k_{-1}]{k_1} RNA_M^* + TC \xrightarrow{k_2} TC@RNA_M^* \xrightarrow{k_3} TC@RNA_M$
2	$RNA + M \xrightarrow{k_1} RNA_M^* + TC \xrightleftharpoons[k_{-2}]{k_2} TC@RNA_M^* \xrightarrow{k_3} TC@RNA_M$
3	$RNA + M \xrightleftharpoons[k_{-1}]{k_1} RNA_M^* + TC \xrightarrow{k_2} TC@RNA_M^* + M \xrightarrow{k_3} TC@RNA_M$

It has to be noted that the actual role of Mg^{2+} can hardly be modelled by single folding steps, especially as multiple Mg^{2+} cations are supposed to assist in TC aptamer folding. Nevertheless, kinetic modelling should provide a robust estimation of the

cation-dependence of individual steps of the folding sequence. The initial association of Mg^{2+} (M) that results in the formation of a metal-stabilized prefolded state (RNA_M^*) is considered as the only reversible step in model 1. In contrast, the respective step is irreversible in model 2, but the ligand binding step is reversible. The subsequent structural adjustment step from an intermediate bound state ($TC@RNA_M^*$) to the final complex ($TC@RNA$) is unimolecular for both models. Model 3 is similar to model 1 with a reversible prefolding step, only that the final adjustment step is considered bimolecular and implies the addition of another Mg^{2+} ion.

The two aptamer variants A58Ap and G43Ap with labels in the binding pocket region show very similar dynamics. The obtained respective fit parameters and model criteria are summarized in the Table 4.2 and 4.3. For both variants, model 1 is found to describe the data best as the corresponding fits exhibit the lowest RMSD values. In comparison to the other models, ΔAIC and ΔBIC values of zero were determined, which is why this model is to be judged as the most probable one. Hence, the initial prefolding step is Mg^{2+} -dependent and shows a significant contribution of a back reaction. The determined rates k_{-1} and k_2 are higher for G43Ap compared to A58Ap, which might hint at a more unstable conformation at this label position. It is remarkable that the metal association rates k_1 are in general some orders of magnitude smaller than the ligand binding rates k_2 . The Mg^{2+} -induced prefolding therefore represents the rate-limiting step in the binding sequence. However, the final structural adjustment is found to be independent of Mg^{2+} . It proceeds faster for A58Ap with a rate $k_3 = 2.5 \text{ s}^{-1}$, while that of G43Ap is 2.1 s^{-1} . Since A58 forms a direct ligand contact, this suggests that the conformational reorganization upon binding starts from the binding pocket and then propagates towards the triple helix region, where G43 is located.

Model 2 with a reversible ligand binding step clearly failed as the model of choice for both A58Ap and G43Ap, since large ΔAIC and ΔBIC values around 140 are obtained and the RMSD values are worse than those of model 1. For A58Ap, the additional back rate k_{-2} approaches zero and is thus negligible, whereas the contribution of the back rate seems more pronounced for G43Ap. A mechanism comprising reversible prefolding as well as ligand binding steps is also discarded for both aptamer variants due to over-parametrization and poor fit qualities.

The reversible ligand binding step in model 2 was applied, as the TC binding dynamics are reported to follow a two-step mechanism with a reversible first and an irreversible second step. Yet, it has to be stressed that different processes are monitored using the Ap emission reporter signal, than upon detection of the TC emission. The reversible TC binding step observed by Förster et al.^[130] might thus partially reflect the reversible prefolding step found herein. As TC is assumed to first associate to the bases A13 and A50 on the upper parts of the two halves of the binding pocket, which is enabled by the Mg²⁺-assisted prefolding of the binding pocket. Interestingly, the forward ligand binding rate of 13.1 $\mu\text{M}^{-1}\text{s}^{-1}$ determined by Förster et al. is on the same order of magnitude as the rates k_2 found herein.

Table 4.2. Results of the kinetic modelling analysis of the fluorescence stopped-flow data of the TC aptamer variant A58Ap, corresponding rate constants and obtained non-linear fit quality criteria. The models 1-3 refer to the tested folding mechanisms shown in Table 4.1.

Model	k_1 / $\mu\text{M}^{-1}\text{s}^{-1}$	k_{-1} / s^{-1}	k_2 / $\mu\text{M}^{-1}\text{s}^{-1}$	k_{-2} / s^{-1}	k_3 / s^{-1}	RMSD	ΔAIC	ΔBIC
1	0.036 ± 0.003	35 ± 5	11.3 ± 0.3	--	2.5 ± 0.1	0.04601	0	0
2	0.019 ± 0.001	--	14.9 ± 0.4	$<10^{-9}$ $\pm \text{n.d.}^{[a]}$	3.2 ± 0.1	0.0467	144	144
3	36 $\pm \text{n.d.}$	$>10^3$ $\pm \text{n.d.}$	0.96 ± 0.02	--	280 ^[b] $\pm \text{n.d.}$	0.191	13861	13861

^[a] n.d. (not determined), the rate constant approaches zero and its error value is very large,

^[b] for model 3, the third step is bimolecular and the rate k_3 is considered as a second order constants in units of $\mu\text{M}^{-1}\text{s}^{-1}$.

Table 4.3. Results of the kinetic modelling analysis of the fluorescence stopped-flow data of the TC aptamer variant G43Ap, corresponding rate constants and obtained non-linear fit quality criteria. The models 1-3 refer to the tested folding mechanisms shown in Table 4.1.

Model	k_1 / $\mu\text{M}^{-1}\text{s}^{-1}$	k_{-1} / s^{-1}	k_2 / $\mu\text{M}^{-1}\text{s}^{-1}$	k_{-2} / s^{-1}	k_3 / s^{-1}	RMSD	ΔAIC	ΔBIC
1	0.029 ± 0.002	57 ± 8	20 ± 1	--	2.1 ± 0.1	0.0446	0	0
2	0.015 ± 0.001	--	23.3 ± 0.9	9.7 ± 0.6	4.1 ± 0.2	0.04525	142	142
3	0.06 ± 0.01	129 ± 20	12.6 ± 0.3	--	0.0005 ^[a] ± 0.0002	0.05089	783	783

^[a] for model 3, the third step is bimolecular and the rate k_3 is considered as a second order constants in units of $\mu\text{M}^{-1}\text{s}^{-1}$.

In the fitting routine, each of the involved species is assigned a response value, that accounts for the signal change caused by that species. These responses are in general

optimized iteratively and then fixed, so that the number of free parameters includes only the kinetic rates. It is striking that the response of the prefolded state RNA_M^* is almost zero in the cases of A58Ap and G43Ap. This is in accordance with the initially flat stopped-flow curves (Figure 4.23) and indicates that the microenvironment of the respective two nucleobases is not directly affected by prefolding. The response of the following formation of the intermediate bound state TC@RNA_M^* is determined to be roughly 50% of the absolute signal decrease, just as the final structural adjustment step. This is indicative of a significant participation of A58 and G43 in the reorganization of the aptamer structure to accommodate the ligand. Last, model 3 which comprises the addition of another Mg^{2+} ion during the final step apparently also fails to describe the dynamics of A58Ap as well as G43AP.

The fluorescence stopped-flow traces of the variant A7Ap show a peculiar rise and decay progression. This points to a folding sequence that implies opposed signal response steps that must be taken into account in the kinetic analysis. In contrast to G34Ap and A58Ap, the obtained model fit results for A7Ap (Table 4.4) reveal that model 3 scores the lowest RMSD value and information criteria and is thus the most adequate description. That is to say that the final structural adjustment step is assumed to involve the addition of another Mg^{2+} ion in proximity to A7 near the triple helix region.

Table 4.4. Results of the kinetic modelling analysis of the fluorescence stopped-flow data of the TC aptamer variant A7Ap, corresponding rate constants and obtained non-linear fit quality criteria. The models 1-3 refer to the tested folding mechanisms shown in Table 4.1.

Model	k_1 / $\mu\text{M}^{-1}\text{s}^{-1}$	k_{-1} / s^{-1}	k_2 / $\mu\text{M}^{-1}\text{s}^{-1}$	k_{-2} / s^{-1}	k_3 / s^{-1}	RMSD	ΔAIC	ΔBIC
1	0.011 ± 0.001	9 ± 2	14.5 ± 0.2	--	3.5 ± 0.1	0.04398	316	316
2	0.009 ± 0.001	--	17.7 ± 0.2	$<10^{-9}$ $\pm \text{n.d.}^{[a]}$	3.98 ± 0.05	0.04403	327	327
3	0.034 ± 0.003	28 ± 3	4.7 ± 0.1	--	0.014 ^[b] ± 0.001	0.04258	0	0

^[a] n.d. (not determined), the rate constant approaches zero and its error value is very large,

^[b] for model 3, the third step is bimolecular and the rate k_3 is considered as a second order constants in units of $\mu\text{M}^{-1}\text{s}^{-1}$.

The reversible Mg^{2+} -addition step is assigned to the initial fluorescence increase, so RNA_M^* is provided with a positive response value in the kinetic fitting routine.

Remarkably, the respective prefolding step has a pronounced impact on the surrounding of A7Ap, but only a minor one for G43Ap or A58Ap. The increase in emission is probably caused by the loss of a stacking interaction and hints to the formation of the kink between A6 and A7.

The prefolding equilibrium of A7Ap is shifted towards the binding-competent state RNA_M^* , compared to G43Ap and A58. Moreover, the following ligand association rate k_2 is significantly smaller and the response value of TC@RNA_M^* converged towards zero for different initial values. The A7 base thus seems to be unaffected by ligand association. Finally, the Mg^{2+} -dependent conversion into the ligand-bound state TC@RNA_M proceeds with the second order rate k_3 . The implicated structural adjustment in the environment of A7 results in the signal decrease, which is reflected by a negative response value whose amount is twice as high as the initial increase.

The presented stopped-flow data reveal a holistic idea of the conformational preformation and ligand binding characteristics of the TC aptamer with focus on the Mg^{2+} -dependence of individual folding steps. The determined kinetic models for the three investigated aptamer variants are summarized in Figure 4.24. A three-step mechanism is assigned for any of the label positions, confirming a preceding prefolding of the aptamer that requires the addition of Mg^{2+} ions. The respective association rates of all three variants are quite similar, although it remains unclear how many metal cations are actually involved in this step.

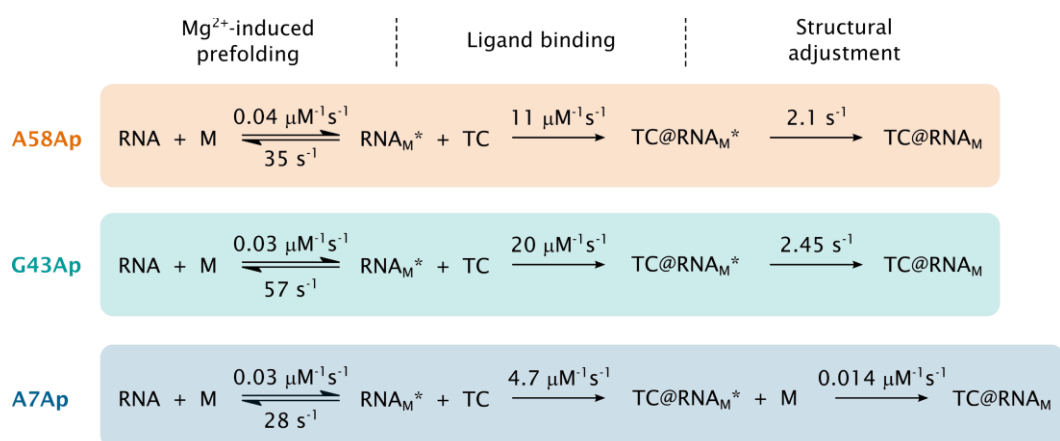


Figure 4.24. Proposed mechanisms and rate constants for sequential folding and ligand binding steps, determined by kinetic analysis of the fluorescence stopped-flow data. The sequence comprises an initial Mg^{2+} -induced prefolding step of a binding-competent conformation, followed by ligand binding which in turn induces a structural adjustment of the aptamer.

The increased back rate of G43Ap, compared to A7Ap and A58Ap, hints at a looser conformation in the surrounding of junction J2-3. In agreement with that, the prefolded state is suggested to adopt a more opened conformation of J1-2, which is in equilibrium with a closed one similar to the ligand bound state.^[188] The prefolded state is thus characterized by an approximation of the two halves of the binding pocket,^[130] but the triple helix motif is not yet entirely established.

The increase in A7Ap emission during prefolding points to an opening of the tertiary structure above A6 on the top of the stem P1 and a pre-arrangement of the triple helix. Regarding the subsequent ligand binding, G43Ap exhibits the highest rate constant k_2 , even higher than that of A58AP which forms a direct contact to the ligand in the bound state. Yet, when TC approaches the binding pocket from the top it is thus supposed to encounter the nucleobases A50 and A13 at first.^[130] As the nucleobases A13 and A12 of J1-2 and the bases A42 and G43 of J2-3 form single hydrogen bond base pairs in the ligand bound state,^[187] respectively, it seems plausible that those joining regions are involved in the initial ligand association step. The high ligand binding rate k_2 of G43Ap furthermore compensates for its increased metal dissociation rate k_{-1} , which hints at a stabilization of the respective aptamer region by TC.

To conclude, the herein presented investigations of the folding behaviour of the well-known TC aptamer provides important additional insights into the Mg^{2+} -dependence of functional aptamer tertiary structures. In accordance to the reported model, the degree of preformation of a binding-competent conformation is essentially affected on the available Mg^{2+} concentration.^[131] The conformational transition from non-binding to prefolded occurs roughly around 0.5 mM Mg^{2+} and the formation of an entirely binding-competent state is accomplished around 1.5 mM Mg^{2+} . As these thresholds correspond to the limits of the physiological range, the results confirm the presence of functional conformations already at low Mg^{2+} levels, which is essential for biologic applications. Hence, the cation-dependence of the conformational landscape of functional RNAs is a critical parameter that must be taken into account in the investigation and design of RNA-based regulation mechanisms.

Besides static structural aspects, dynamic conformational adjustments are fundamental regarding riboswitch activity. For the TC aptamer, a Mg^{2+} -dependent prefolding step prior to ligand binding could be identified that involves the binding pocket region as well as the triple helix motif. The results furthermore give an

excellent example for a structural adjustment that is induced by the ligand binding event and that propagates from the binding site to more distant regions. In response to ligand recognition, indications a following structural adjustment of the A7 position at the base of the triple helix motif were observed here. Most strikingly, the surrounding of A7 is suggested to lock into the final conformation in a Mg^{2+} -mediated fashion. Kinetic modeling revealed that a binding model with a cation-dependent final binding step is the most adequate description of the data. Although a robust estimation about the actual number of acquired cations throughout the folding sequence can hardly be made, the results significantly contribute to the understanding of the dynamic folding process of the TC aptamer as a model system for a successfully engineered functional RNA.

Materials and Methods

The RNA samples were stored in highly purified water at $-20^{\circ}C$. Prior to each experimental use, the RNA was prepared using the following folding procedure: the aqueous RNA solutions were heated to $95^{\circ}C$ for 5 min and snap-cooled on ice for 5 min. Next, buffer was added (20 mM sodium cacodylate, 80 mM KCl, pH 6.8) and the samples were equilibrated for 20 min. For the Mg^{2+} -dependent fluorescence titrations, 1 μM RNA was provided and 3 μM TC was added for the titrations in presence of the ligand. The Mg^{2+} solution contained similar buffer components except for RNA and ligand. The samples were prepared in 4 x 10 mm quartz glass cuvettes (Hellma Analytics, Müllheim, Germany) The titrations were conducted with a FP-8500 spectrofluorometer (Jasco, Groß-Umstadt, Germany) with an excitation wavelength of 310 nm (slit width 5 nm) and a PMT voltage of 700 V.

Stopped-flow measurements were carried out with a SFM-20 device (Bio-Logic Science Instruments, Seyssinet-Pariset, France) with Berger Ball mixer and a cuvette (FC08) with a volume of 20 μL and a light path of 0.8 mm attached. The stopped-flow device was coupled to a FP-8500 spectrofluorometer with a glass-fibre module (OBF-832, Jasco). The detected PMT signal was transferred to a transient recorder board (PCI-6052E, National Instruments, Austin, USA) using an A/D-adapter (BNC-2110, National Instruments). Data acquisition was controlled with the Bio-Kine 32 software (Version 4.42, Bio-Logic Science Instruments). For every single mixing experiment, 33 μl of the two sample solutions were injected into the mixing compartment via

syringes. The injection was stopped by a hard-stop valve which determined the start of the observed binding dynamics. The excitation wavelength for the measurements was 310 nm and fluorescence emission was detected at 370 nm in a 90° angle. The sample concentrations in the cuvette were 2 μM RNA, 4 μM TC, and the Mg²⁺ concentrations varied between 0.5-10 mM. 20-30 traces were averaged, baseline-corrected and normalized prior to the kinetic model analysis, which was carried out with the DynaFit4 software (Biokin Ltd., Watertown, USA).^[31]

4.2.2 REGULATORY POTENTIALS OF CFX-BINDING APTAMERS

(Reference [IV])

The *de novo* design of high affinity aptamers for specific target molecules by *in vitro* selection offers great opportunities for countless biochemical tasks in the wide field of life sciences. Further engineering of artificial aptamers into active *in vivo* riboswitches even opens the door for creating novel genetic circuits and RNA-based therapeutic approaches. However, the targeted design of engineered riboswitches using artificial aptamers is still enormously challenging.^[115,194] Only very few *in vitro* selected aptamers could be applied as functional riboswitches so far such as the Theo,^[109] Neo,^[111] TC^[185,186,195] and the recently selected CFX^[114] and paromomycin^[113] aptamers.

In order to determine decisive criteria, that distinguish inactive aptamers from *in vivo* active riboswitches, three CFX-binding aptamer candidates that exhibit different regulatory potentials are investigated here comparatively. The compound CFX (Figure 4.25C) is a broadband antibiotic from the fluoroquinolone group, that inhibits bacterial topoisomerases. The compound is well-characterized on a pharmacological level^[196] and it is very suitable for analytical purposes, due to its fluorescent emission. Similar to other antibiotics, it has been applied for *in vitro* selection of specifically binding RNA aptamers. An aptamer termed R10K6 with an extraordinary ligand affinity was identified, that could be applied as aptasensor for fluoroquinolone derivatives in clinical or environmental diagnostics.^[101]

Further analysis of the aptamer pools over the multiple rounds of SELEX by next-generation sequencing (NGS) revealed detailed and reliable insights into the characteristics and abundancies of enriched sequences. Based on this, auspicious

candidates were screened in parallel for their *in vivo* riboswitch abilities by cloning the corresponding sequences into the 5'-UTR of a GFP reporter gene following the protocol developed by the Suess group.^[197] Most interestingly, two aptamers with very similar dissociation constants in the low nanomolar range were obtained that showed drastically different enrichment trajectories throughout the SELEX experiment.^[114] It turned out that the most abundant candidate R10K6 showed almost no regulatory performance in contrast to the 80-fold less abundant candidate 10A. The inactive candidate R10K6 is the precursor of the herein investigated aptamer **A**. The less abundant candidate 10A, here denoted as **preRS**, showed a ligand-dependent 2.2-fold regulation change in yeast cells. By introducing randomized nucleobase variations, a candidate with a pronounced gain of function (GOF) was created,^[114] which is herein referred to as the active riboswitch **RS**. It is even capable of a 7.5-fold change in GFP expression in yeast cells and exhibits a similarly low dissociation constant. The predicted secondary structures of the three aptamers, based on in-line probing analyses, are depicted in Figure 4.25.

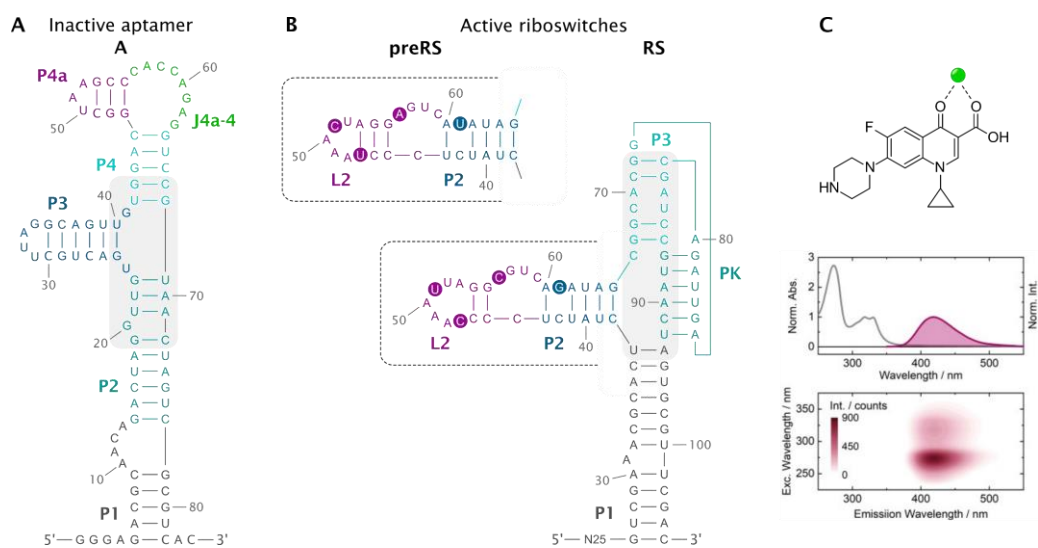


Figure 4.25. Secondary structures of **A)** the investigated inactive aptamer **A** and **B)** the *in vivo* active riboswitches **preRS** and **RS**. The depicted structures are based on in-line probing experiments.^[114] The binding pocket regions are highlighted (grey boxes). **C)** Molecular structure of the ligand CFX with shown metal binding site (top). The graphs show the normalized absorption and emission spectra of CFX (middle) and an excitation wavelength-dependent CFX emission contour plot (bottom).

Although they were obtained from one SELEX experiment, the aptamer **A** and the riboswitch **preRS** do not show pronounced similarities regarding sequence or

structure, except for a three-way junction in core of the RNAs, which is assumed to form the basis of the binding pocket (Figure 4.25, gray boxes). The aptamer **A** forms a basic stem consisting of the individual stems P1, P2 and P4, the branching stems P3 and P4a and a joining region J4a-4. The active riboswitches exhibit a more complex structure with a pseudoknot (PK) connecting the stems P1 and P3 directly at a junction towards stem P2 with the loop L2. Because the riboswitch **RS** was derived from **preRS**, they only differ in 4 nucleobases located within P2 and L2.

The comparable binding affinities of the three presented aptamer candidates are apparently not sufficient for predicting riboswitch engineering potential, as their regulatory capacities vary drastically. Therefore, the ligand binding characteristics of the inactive aptamer **A** and the active riboswitches **preRS** and **RS** are compared in view of conformational as well as kinetic aspects.

The inherent fluorescence of the ligand CFX can readily be used as optical reporter signal for the binding process since it is quenched upon binding to any of the three candidates. The fluorescence emission of CFX, observed upon excitation at 330 nm, is centred at 420 nm (Figure 4.25C). Besides the minor absorption band at 330 nm there is a second more pronounced band at 270 nm. The excitation wavelength-dependent emission contour plot shows, that fluorescence is observed upon excitation at both absorption bands, yet an excitation at the low energy absorption band is preferred for the spectroscopic studies, to avoid parallel excitation of the RNAs.

Mg²⁺-Dependent Aptamer Binding Affinities

The potential influence of Mg²⁺ on the conformational landscape of RNA aptamers must be investigated carefully, since a high ligand affinity even at low Mg²⁺ levels is a precondition for potential riboswitch function. As the results of the TC aptamer (section 4.2.1) confirmed, the prefolding as well as the ligand binding process can involve distinct interactions with divalent cations. The Mg²⁺-dependences of the three candidates **A**, **preRS** and **RS** were addressed by means of fluorescence titration experiments at defined Mg²⁺ levels. The top panel of Figure 4.26 (top panel) shows the normalized CFX emission decreases observed upon addition of RNA at 5 mM Mg²⁺ which corresponds to the SELEX conditions. Following a Hill analysis of the data, K_D values of 19, 130 and 226 nM were determined for **A**, **preRS** and **RS**,

respectively. The aptamer **A** therefore exhibits the highest ligand affinity, in spite of the lowest regulatory potential.

Additional titration studies were carried out at 0.5, 1.5, 3 and 10 mM and in the absence of Mg^{2+} . Without Mg^{2+} present, none of the candidates showed a reasonable binding curve, indicating that the availability of minimal amounts of cations is necessary for each of them to fold properly. The determination of the K_D values at defined Mg^{2+} levels revealed an exceptional cation-dependence of **A** in contrast to **preRS** and **RS** (Figure 4.26, bottom). At a Mg^{2+} concentration of

0.5 mM the aptamer **A** only binds weakly with an approximate K_D value of 1.4 μ M. The affinity substantially increases to a nanomolar K_D value at 1.5 mM. Thus, a pronounced conformational shift towards a binding-competent conformation involving distinct metal binding sites occurs exactly within the physiological range. Additionally, at even higher cation concentrations the K_D value of **A** continuously decreases which might point to a Mg^{2+} -driven increasing compacting of the tertiary structure. In comparison to **A**, the affinities of the active riboswitch candidates **preRS** and **RS** are relatively unaffected by Mg^{2+} . Their K_D values show a very similar behaviour and only vary slightly above a concentration of 0.5 mM. Consequently, the binding-competent state exists already at low cation levels and no significant further structural adjustment occurs upon increasing the cation excess.

The regulatory potential of **preRS** and **RS** is certainly partly due to the low dependence Mg^{2+} , although small amounts of divalent cations are required to form their binding-competent states. The affinity of the aptamer **A** varies greatly within the limits of the physiological Mg^{2+} range, but it is nevertheless capable of ligand binding. The behaviour of **A** can be compared well with that of the TC aptamer.^[131] In spite of its Mg^{2+} -dependence, the TC aptamer is highly functional *in vivo*. The inactivity activity of **A** can therefore hardly be attributed to its cation-dependency alone.

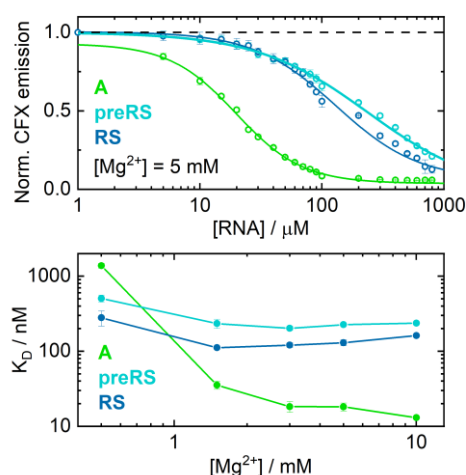


Figure 4.26. Mg^{2+} -dependent binding affinities of the candidates **A** (green), **preRS** (cyan) and **RS** (blue). Fluorescence titration at 5 mM Mg^{2+} (top) and Mg^{2+} -dependent K_D values (bottom).

Fluorescence-Detected Ligand Binding Kinetics

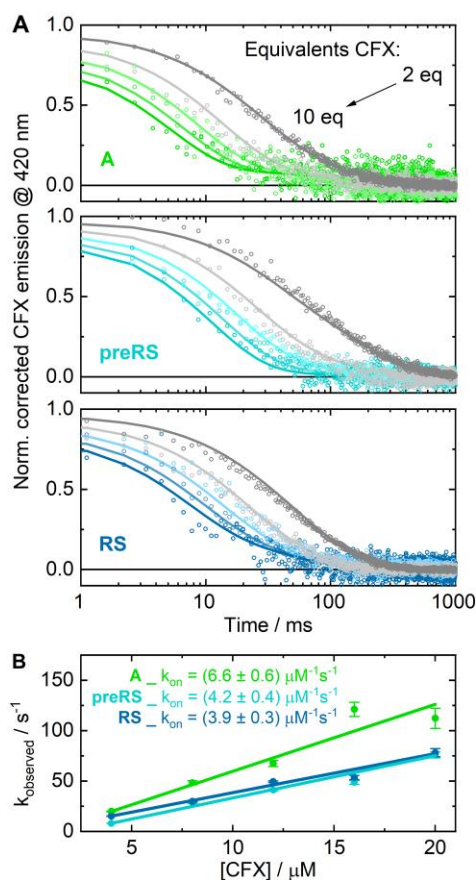


Figure 4.27. A) Stopped-flow traces that show the time-resolved decrease of CFX emission upon binding by the aptamer candidates **A** (top), **preRS** (middle) and **RS** (bottom). The solid lines represent the most suitable model fits as discussed in the text. **B)** Association rates k_{on} determined by monoexponential fitting of the stopped-flow traces.

Rather than the K_D value, which is derived from equilibrium conditions, dynamic properties of the ligand binding process are supposed to reveal fundamental differences between the inactive aptamer **A** and the active riboswitches **preRS** and **RS**. To monitor the binding event, the CFX emission is measured in real time with millisecond resolution by stopped-flow mixing experiments. During the mixing of the ligand and the corresponding aptamer candidates, the SELEX buffer conditions with 5 mM Mg^{2+} were retained. According to the cation fluorescence titrations, each of the candidates should exist in its binding-competent fold and a structural preformation should only play a minor role. Nevertheless, it is important to consider a distribution of multiple interconvertible aptamer conformations where only one is capable of binding. Such a preceding conformational

selection mechanism is found frequently for the binding kinetics of aptamers.^[198,199] The ligand stabilizes a specific RNA conformation significantly by binding.^[200] If the preformation proceeds on a slower time scale it can even be rate limiting for ligand binding.

The recorded stopped-flow traces (Figure 4.27A) show accelerated binding kinetics upon mixing with increasing equivalents (eq) of CFX for each of the RNA candidates. The ligand binding occurs on similar time scales, yet the ligand binding of **A** seems to be faster than of **preRS** or **RS**. As the ligand is supplied in excess, first

order conditions prevail. The observed ligand binding rate k_{observed} can therefore be obtained by mono-exponential curve fitting. Based on the k_{observed} values, the overall binding rate k_{on} is estimated by linear regression (Figure 4.27B). For aptamer **A** the highest rate is determined, followed by almost similar values for **preRS** and **RS**. The first order rates show a linear increase in any case, which hints at an induced fit mechanism. This furthermore confirms the exclusion of preformation contributions to the observed kinetics. However, there are no firm criteria to rule out a conformational search.^[201]

A simple first order ligand binding in one irreversible step is certainly not a realistic description of the actual ligand binding mechanism. To determine the exact mechanism, the acquired datasets were subjected to kinetic modeling analyses. Several reaction models with varying complexity were tested including different sequences of reversible and irreversible steps. For each aptamer candidate, the datasets of all concentrations were fitted simultaneously with the expressions for the time-dependent concentrations derived from the sets of differential equations for the corresponding models. Similar to the kinetic analysis of the TC stopped-flow data, the resulting fit qualities were then comparatively evaluated by a statistical model selection analysis based on the ΔAIC and ΔBIC criteria.^[31–33] Both criteria estimate the probability of a certain model compared to others, taking the obtained fit quality into account as well as the complexity of the respective model in order to avoid overfitting.

The kinetic modeling analysis revealed two-step binding models as the most adequate descriptions for each of the three RNA candidates. The binding process is therefore governed by an initial association of the ligand to the preformed binding pocket followed by a structural reorganization to accommodate the ligand. The determined most probable mechanisms and corresponding rate constants are illustrated in Figure 4.28. The association step is considered reversible for each of the candidates, but the mechanisms differ significantly in the reversibility of the accommodation step.

Only for the inactive aptamer **A**, a fully reversible binding sequence is assigned as most suitable mechanism. It is striking, that second binding step is significantly accelerated for **preRS** and virtually irreversible for **RS**. For the potential riboswitch **preRS**, a kinetic model with an irreversible as well as a reversible second step seems

to reflect the observed binding process properly. Yet, for the reversible model a back rate several orders of magnitude lower than the forward rate was determined, which makes its contribution almost negligible. For candidate **RS** with the highest regulatory potential, both information criteria explicitly confirm an irreversible second step as best description. Not only that the structural adjustment step of **RS** is found to be irreversible, but there is also a clear tendency of an increasing forward rate of the second step from **A** to **preRS** to **RS**. Consequently, an evident correlation between regulatory activity and an acceleration of the accommodation step can be noted.

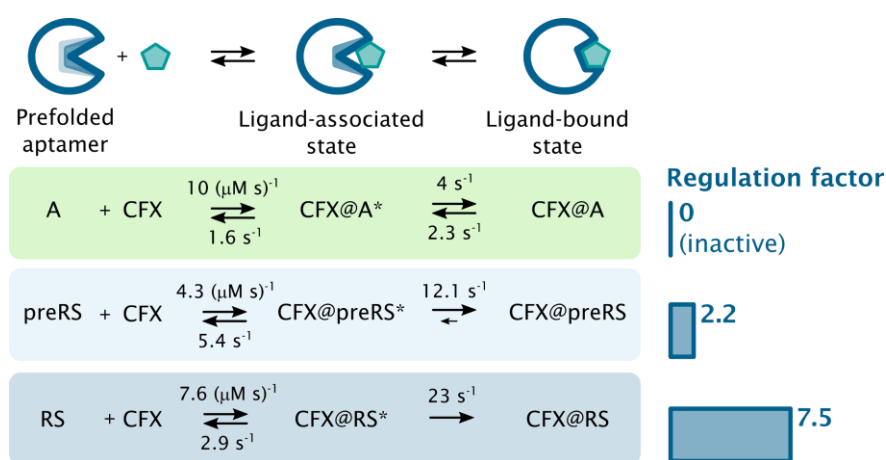


Figure 4.28. Determined kinetic ligand binding models of aptamer **A** and the riboswitches **preRS** and **RS**. A decreasing contribution of a back reaction rate of the second binding step correlates with an increasing regulation factor, observed in a *in vivo* GFP expression assay.

Interestingly, also the rates of the initial ligand association step differ significantly when comparing the inactive **A** and the active candidates **preRS** and **RS**. The first step seems to be much more favoured and exhibits a significantly smaller dissociation rate for aptamer **A**. Since the association step is assumed to be mostly driven by electrostatic interactions, this different behaviour might also be due to the fact that the structure of **A** contains a significantly higher number of metal cations.

A nearly irreversible and therefore highly favoured accommodation step is found frequently for functional aptamer binding kinetics. This step is assumed to rely on a conformational adjustment of the RNA and a tightening of the binding pocket. As this is determined to be the most striking kinetic difference between the inactive **A** and the active candidates **preRS** and **RS**, the irreversibility is suggested to be indicative of a ligand-induced rearrangement of the RNA that is pronounced enough to enable

riboswitch functionality. A virtually irreversible binding furthermore results in an increased lifetime of bound state. This might be a critical factor for in *in vivo* activity because of the essential interplay of the ligand binding kinetics and the time scale of the addressed cellular regulation mechanism. Similar observations are reported for the TC aptamer, where the effect is even stronger than for **RS**.^[130] Regarding the Theo aptamer, a conformational preformation step precedes the ligand binding process and the dissociation rate is found to be almost negligible, too.^[199] Moreover, a reduced back rate is also reported for the Neo aptamer^[202] where additional structural data of active and inactive aptamers are available.^[203] The highest activity is observed for the aptamer N1 that is structurally more complex than less active variants thereof. The increased complexity is furthermore associated with a more drastic ligand-induced conformational rearrangement of N1.

Besides synthetic aptamers, analogous binding kinetics are as well reported for the aptamer domains of natural riboswitches. An initial association followed by a highly favoured structural adjustment was found for the family of purine riboswitches.^[204–206] Similar trends were also observed for the TPP riboswitch^[192,207] or the FMN riboswitch.^[208] Ultimately, a conformational switch of the aptamer that is manifested as a rapid final binding step to accommodate the ligand is assigned as the essential characteristic that natural as well as artificial functional aptamers have in common.

The determined correlation of regulatory potential and ligand binding kinetics could have additional implications for the *in vitro* selection of aptamers and could explain the underrepresentation of functional aptamer candidates in an enriched SELEX pool. First, although the application of Mg^{2+} concentrations far above the physiological range might enhance an enrichment of high affinity aptamers, it is suggested to impede the accumulation of potentially *in vivo* active candidates. At low Mg^{2+} levels, aptamers of increased structural complexity can be obtained, whose K_D values are not substantially dependent on the present cation concentration.^[126] Second, an irreversible binding step and the corresponding increased lifetime of the bound state must be considered during the selective elution of aptamers during the SELEX. The stringency and the waiting times in the elution protocol could be optimized so that it is more probable to obtain functional candidates. An improved SELEX approach is developed in the Süss lab, which is referred to as capture-SELEX.^[113,209] In this variation, the RNA is immobilized instead of the ligand by a

complementary docking strand. The elution is then carried out with the target molecule, implying that the RNA strands are supposed to unbind from the docking strand. Hence, a dynamic structural rearrangement step is introduced to the selection protocol.

4.3 A LIGHT-RESPONSIVE AZOCM-BINDING APTAMER

(Reference [VI])

Ultimately, the expertise gained from the detailed investigations of photochromic compounds and the characterization of novel RNA aptamers is combined to design a light-responsive aptamer that specifically senses only one isomer of a photochromic ligand. For the design strategy of the ligand, an azobenzene molecular scaffold is chosen as photochromic unit, due to its promising photophysical properties like a high quantum yield and fatigue resistance as well as high switching turnover. Since the use of antibiotics is suggested to be advantageous for the enrichment of high affinity aptamers during the SELEX process, the azobenzene chromophore is synthetically merged with the molecular structure of the antibiotic chloramphenicol^[210] (Cm) as illustrated in Figure 4.29A.

The nitro phenyl group of Cm was converted into one half of an azobenzene moiety and an additional amino propyl anchor group for immobilization was installed on the opposite half (amino-azoCm). The free ligand azoCm, however, bears only a terminal carboxyl group. The *trans*-isomer of the azoCm derivative is efficiently convertible into its *cis*-form by use of 365 nm light and the reverse reaction is induced by 420 nm (Figure 4.29B). The ligand azoCm is highly promising for in cell applications. It is stable in HeLa cell extracts for days and highly photoresistant. Over multiple repeated switching cycles a switching turnover of 75% is maintained (Figure 4.29C, bottom). The *cis*-isomer exhibits a thermal half-life time of ~27 days under dark conditions. An activation energy of 109 kJ/mol is determined for the *cis*- to *trans*-azoCm conversion by an Arrhenius measurement series at different temperatures. Further toxicity tests reveal that azoCm exerts no significant effect on cell growth in bacteria, yeast and also human cell lines (HeLa cells).

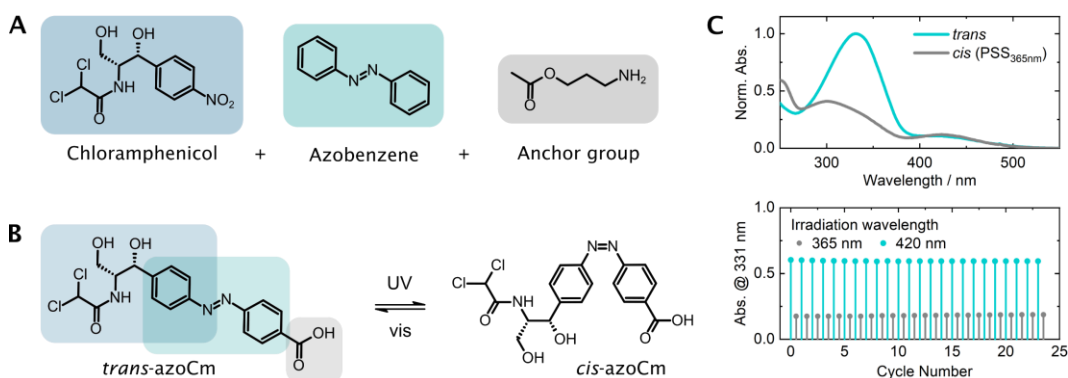


Figure 4.29. A) Molecular design route for the chloramphenicol-azobenzene (azoCm) compound with an anchor group for immobilization. **B)** Structures of the *cis*- and *trans*-photoisomers of azoCm. **C)** Spectroscopic studies of the ligand azoCm: The top panel shows the absorption spectra of *trans*-azoCm and of the photostationary state (PSS) obtained upon continuous irradiation at 365 nm. The PSS contains about 80% of *cis*-azoCm. The lower panel shows a photofatigue experiment over multiple cycles of alternating irradiation.

In vitro Selection Against azoCm

The goal of the *in vitro* selection against azoCm was to obtain aptamer candidates that selectively bind to the thermodynamically stable *trans*-isomer and that reversibly unbind upon photoisomerization. To achieve this, several SELEX protocols were combined and modified systematically. In total, three selections were carried out with different RNA libraries and elution procedures. Two selections were conducted with established RNA libraries that were successfully applied already.^[112,114] For the first affinity SELEX an RNA pool was used, that consisted of a 1:1 mixture of different N64 sequences (64 nucleotides). One part of the mixture was a completely randomized N64 pool while the other contained a predefined hairpin motif, flanked by two randomized N26 regions.

In the second SELEX, a randomized N74 RNA pool was applied. This resulted in a more pronounced enrichment than the first SELEX after 6 rounds. The enriched pool of round 6 was split and subsequently two different selection procedures were conducted in parallel for four more rounds. One of the selection protocols was continued regularly but the other was modified with an illumination step to isomerize the ligand (Figure 4.30A).

After incubation of the RNA pool with immobilized *trans*-azoCm, non-binding RNAs were discarded. Then the column was irradiated with 365 nm under exclusion of all other light sources to induce the photoconversion of the ligand in each round. Those aptamers, that unbind upon *trans*- to *cis*-conformational change were eluted

during illumination and then applied for the reselection rounds. Interestingly, sequencing analyses of the SELEX pools revealed the conservation of a motif of 13 nucleotides (CCTACGGGAAAGG) in three of the candidates. One of them stems from the N64 1:1 SELEX and two from the light branch of the N74 SELEX.

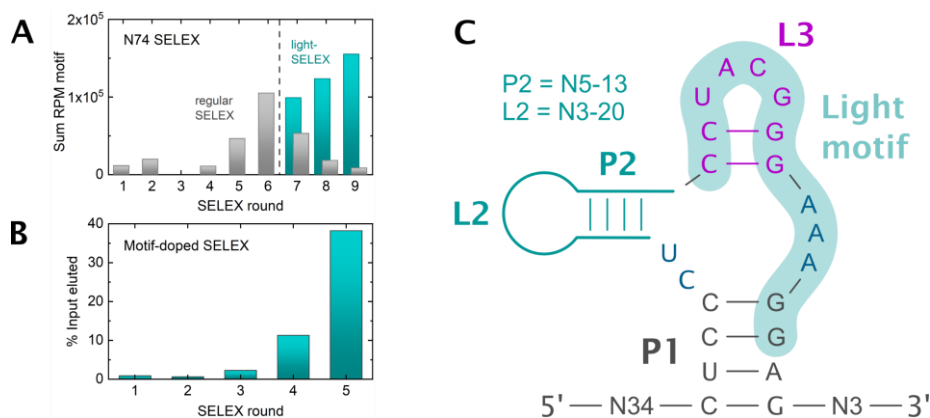


Figure 4.30. Illustration of the SELEX results. **A)** Sum of reads per million (RPM) of the light-motif sequence in the regular and light branch of the N74 SELEX. **B)** Fraction of loaded RNAs that could be eluted with an azoCm solution. **C)** Conserved structural motif determined by LocARNA analysis of the motif-doped SELEX pools.^[211,212] The mutated light-motif is embedded within the common structure motif. The lengths of stem P2 and loop L2 are variable, as indicated.

Additional DEEP sequencing analyses were performed to track the enrichment of this light-motif during the selection rounds of the N74 SELEX. The total read count, normalized to reads per million (RPM), of the light-motif sequence is shown in Figure 4.30A, to visualize the enrichment processes in both SELEX branches. The respective motif was continuously enriched in the light-branch, whereas its abundance declined in the regular branch.

In the following, the light-motif sequence was applied for the third *in vitro* selection engaging a motif-doped RNA library. Therefore, the light-motif was provided with randomized flanking regions to obtain a total length of 50 nucleotides. Additionally, a 6% mutation rate was allowed for the light-motif to eventually find even optimized variants thereof. The motif-doped SELEX showed a steep enrichment trajectory so that 38% of the RNA input could be eluted by washing with a ligand solution in round 5 (Figure 4.30B). By sequencing 96 individual candidates, it was found that no particular aptamer dominated the pool, but the motif itself was mostly conserved. The adjacent nucleobases thus seemed to be not essential for the ligand properties. Since the light-motif sequence could still be integrated in a superordinate structure motif,

the pool was also examined for matching secondary structure motifs by use of the prediction tool LocARNA.^[211,212] Indeed, a three-way junction motif was determined, that embeds the light-motif sequence as displayed in Figure 4.30C. The branching hairpin consisting of P2 and L2 is of variable size, while the stem P1 and the stem-loop motif L2 are conserved.

Ligand Binding Studies of Aptamer B2-1 and azoCm

From the different enriched SELEX pools, four aptamer candidates were chosen for further selective ligand binding studies. In a column binding assay, the candidates were tested for their ligand isomer specificity. Especially the binding and affinity properties of aptamer B2-1 (P2 = N10, L2 = N5) from the motif-doped SELEX appeared rather promising. Therefore, isothermal titration calorimetry (ITC) measurements were performed to determine the photoisomer-dependent K_D values of B2-1. The ITC binding curves for both ligand isomers are

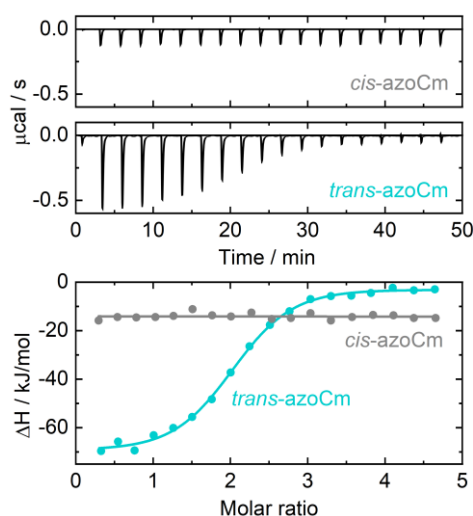


Figure 4.31. Isothermal titration calorimetry (ITC) studies of *cis*- and *trans*-azoCm and the aptamer B2-1.

depicted in the upper panels of Figure 4.31 and the derived enthalpy changes ΔH in the lower panel. For *cis*-azoCm no reasonable binding curve was observed at all, but due to the experimental conditions a minimum millimolar K_D value can be estimated. In contrast, for *trans*-azoCm an exceptional K_D value of 545 nM is obtained, which confirms an auspicious selectivity for this photoisomer. The difference in K_D values corresponds to an at least ~ 1800 -fold discrimination between the ligand states.

The candidate B2-1 could only serve as reversible photoresponsive aptamer if it also detaches from the ligand, upon switching from *trans*- to *cis*-azoCm. The capability of photoswitching of azoCm in presence of B2-1, was confirmed by UV/vis irradiation experiments. However, to investigate the structural response of the RNA to the switching event, circular dichroism (CD) spectroscopy is a suitable technique. It allows for observing conformational changes of biomolecules like RNA, due to their

Experimental Results

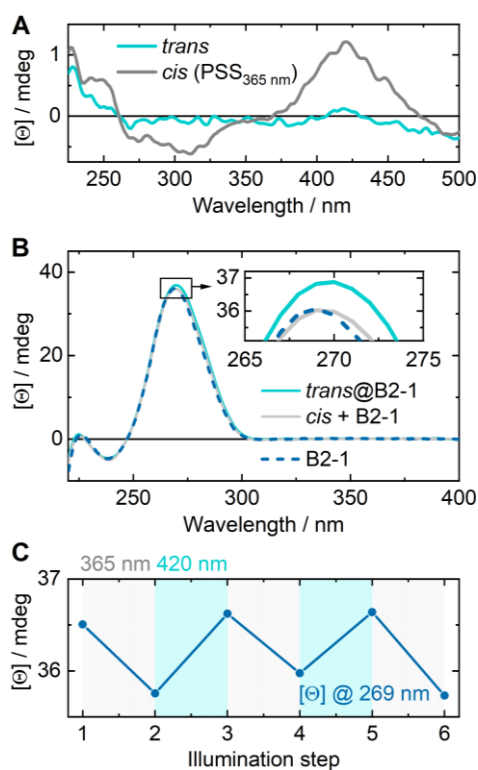


Figure 4.32. Circular dichroism (CD) studies. **A)** CD spectra of *trans*- (cyan) and *cis*-azoCm (grey). **B)** CD spectra of the pure aptamer B2-1 (dashed blue line), its ligand bound state *trans*@B2-1 (cyan line) and the dissociated state (*cis* + B2-1, grey line) obtained upon switching from the *trans*- to *cis*-isomer with 365 nm. **C)** CD signal change at 269 nm during a cyclic switching experiment with alternating illumination steps using 365 nm and 420 nm.

chirality and the associated differences in absorption of left and right circularly polarized light. To determine contributions of the ligand, at first switching experiments were performed with azoCm under similar conditions as the following RNA measurements (Figure 4.32A). The spectrum of free state of aptamer B2-1 (Figure 4.32B, dashed blue line) shows a dominant positive amplitude around 270 nm and a minor negative signal around 245 nm. The observed signature is indicative of RNA hairpin structure motifs.^[213,214] For the binding studies, *trans*-azoCm was provided in excess to ensure that the majority of present aptamers are bound to the ligand. The spectrum of the bound state *trans*@B2-1 exhibits an increased positive amplitude around 270 nm and the signal is shifted bathochromically with respect to the free aptamer. This hints at a noticeable conformational adaption of the aptamer to the ligand. Upon irradiation of the sample with 365 nm to convert the ligand into its *cis*-form, the spectrum of the free aptamer was nearly restored, which strongly points to a dissociation of the ligand. Only a slight bathochromic shift is still observed.

To confirm a reversible light-controlled ligand binding, the sample was irradiated alternately with 365 nm to induce *trans*- to *cis*-isomerization and with 420 nm to trigger the reverse reaction. The CD signal maximum of B2-1 at the individual irradiation steps over 3 switching cycles is displayed in Figure 4.32C. The signal clearly decreases and increases reversibly due to the repeated photo-isomerization of the ligand. The observed signal change makes approximately 3% of the absolute

amplitude so the overall tertiary structure of the aptamer is only adjusted to a small extent. Though, the adaption of the RNA to the ligand by e.g. the tightening of the binding pocket is not suggested to cause a drastic signal modulation anyway. Hence, the presented reversible signal change can evidently be associated with the binding and unbinding of azoCm and aptamer B2-1.

5 CONCLUSION

In this work, the potential of molecular photoswitches as light-sensitive components for photopharmacological applications is elaborated as well as that of artificial RNA aptamers as regulatory switch units for riboswitch engineering. Different essential aspects of both fields of application are investigated, and the two approaches are finally connected by the design of a synthetic light-controlled RNA aptamer that responds to the isomerization of its photoswitch ligand.

Molecular photoswitches such as azobenzenes and spiropyrans have proven to be promising photochemical tools to create light-driven biochemically usable effects in a reversible manner. While azobenzenes represent the mostly applied class of photoswitches, the huge photopharmacological potential of spiropyrans is yet to unfold. To further explore this potential, prominent water-soluble spiropyrans are studied here in view of their practical photoswitch properties and photoreaction dynamics. The Py- and Nitro-BIPS derivatives **1-4** investigated here show refined photo- and thermochromic behaviour in aqueous solution. Especially the Py-BIPS compound **2** is very promising for diverse applications in a biochemical context. Compared to the other investigated compounds, a much higher merocyanine content of roughly 50% is accumulated thermally within minutes. In so-called T-type switching mode, with alternating photoinduced ring-closure to a pure spiropyran sample and thermal equilibrium recovery, this elevated switching amplitude is retained over multiple cycles without significant decomposition. Since the pronounced absorption band of the merocyanine around 540 nm is well separated from that of the spiropyran, it can be addressed selectively with high extinction. In addition, the fact that the use of harmful UV light can be avoided is very promising for potential photopharmacological use.

Compound **2** furthermore shows fascinating pH-dependent properties. Upon acidification, several protonated states are formed that adopt inherent photophysical features. First, the pyridine-nitrogen is protonated, where the pK_a value of the ring-opened form HMC is two units higher (6.8) than that of the closed form HSP (4.8). This difference allows for a light-stimulated reversible regulation of the pH value in a

Conclusion

range from roughly 4.5 to 7.5. Depending on the applied concentration, a pK_a drop of up to 1.5 units can be attained by light-induced ring-closure. By means of transient absorption studies, a photoacid generator reactivity of HMC could be confirmed. Accordingly, the respective proton is released subsequently to ring-closure, due to the altered pK_a value and the reassociation thereof depends on the isomerization state of the compound.

With a pK_a of 3.2, also the phenolate-oxygen of compound **2** is protonated to form HMCH. This protic site corresponds to the commonly applied photoacidic moiety of merocyanines. The first time-resolved studies of this photoinduced proton release presented here, reveal an excited state photoacid reactivity of HMCH as well as of such protonated merocyanines in general. The phenolic proton is transferred to the water with lifetimes around 1-2 ps and due to the negative estimated excited state pK_a^* values these protonated merocyanines must be classified as super-photoacids. Merocyanine photoacids can thus be employed as ultrafast triggers for proton-mediated processes, which are among the most fundamental reactions in nature.

Concerning potential pharmacological targets, RNA should have a bright future ahead since it is easy to synthesize and provides access to different levels of cellular regulation mechanisms. Especially, RNA aptamers that are capable of binding ligand molecules with extraordinary high affinity and specificity are highly interesting for riboswitch engineering. Artificial aptamers are readily available by *in vitro* selection but only few of those function as active riboswitches when applied *in vivo*. In addition, functional aptamers appear to be underrepresented in an enriched SELEX pool. The results herein reveal the importance of the aptamer conformational dynamics during ligand binding for the regulatory potential. The Mg^{2+} -dependent binding studies of the well-known and highly active TC aptamer show that divalent cations are not only vital for proper prefolding of the aptamer but can also be involved in the ligand binding and RNA structure adaption. Upon association of TC to the binding pocket, a conformational adjustment propagates through the aptamer core to the distant triple helix region where Mg^{2+} is suggested to be required to fold into the final bound state. This subtle structural change seems to be sufficient for the functionality of the TC aptamer in diverse riboswitch constructs applied for different regulatory tasks.

From the three investigated CFX aptamers, only the inactive aptamer A exhibits a pronounced Mg^{2+} -dependence in the physiological range, just as the TC aptamer.

Hence, the influence of Mg^{2+} on RNA folding alone is no firm criterion to predict the regulatory potential of aptamers. Yet, low Mg^{2+} concentrations should be applied already during the selection, to obtain aptamers that are able to cope with physiological conditions and not to enrich highly preformed structures of poor complexity. The dynamic ligand binding studies reveal a clear correlation between the regulatory potential of the three aptamer candidates and the reversibility of the final structure adaption step. It is concluded that an accelerated and irreversible RNA adaption is indicative of a conformational change that is pronounced enough to enable riboswitch activity. This is further confirmed by the reported ligand binding kinetics of artificial aptamers like the TC or theophylline aptamer and also that of natural riboswitches. These findings should also have far reaching implications for optimizations of selection protocols for functional aptamers.

Finally, a light-responsive aptamer-ligand system is developed, with an azobenzene-derivatized antibiotic as photochromic ligand azoCm. By a systematic sequence of in vitro selections and the successful implementation of an illumination step to isomerize the ligand, aptamers could be obtained that specifically bind to the *trans*-azoCm form. ITC binding affinity studies further confirm this selectivity and additional CD studies provide evidence for a light-induced reversible dissociation of *cis*-azoCm. Therefore, a successful and straightforward design route for a light-responsive RNA aptamer is presented here. The fusion of a photoswitch as light-sensitive probe and an artificial RNA aptamer target holds great potential for the development of diverse light-stimulated biologic regulation pathways.

6 BIBLIOGRAPHY

- [1] A. Einstein, *Ann. Phys.* **1905**, *17*, 132–148.
- [2] D. M. Chapin, C. S. Fuller, G. L. Pearson, *J. Appl. Phys.* **1954**, *25*, 676–677.
- [3] T. Maiman, *Nature* **1960**, *187*, 493–494.
- [4] A. H. Zewail, *J. Phys. Chem. A* **2000**, *104*, 5660–5694.
- [5] L. Möckl, D. C. Lamb, C. Bräuchle, *Angew. Chem. Int. Ed.* **2014**, *53*, 13972–13977.
- [6] G. Mourou, D. Strickland, *Opt. Commun.* **1985**, *55*, 447–449.
- [7] A. Ashkin, *Proc. Natl. Acad. Sci. USA* **1997**, *94*, 4853–4860.
- [8] J. Broichhagen, J. A. Frank, D. Trauner, *Acc. Chem. Res.* **2015**, *48*, 1947–1960.
- [9] M. M. Lerch, M. J. Hansen, G. M. van Dam, W. Szymanski, B. L. Feringa, *Angew. Chem. Int. Ed.* **2016**, *55*, 10978–10999.
- [10] K. Hüll, J. Morstein, D. Trauner, *Chem. Rev.* **2018**, *118*, 10710–10747.
- [11] L. Laprell, E. Repak, V. Franckevicius, F. Hartrampf, J. Terhag, M. Hollmann, M. Sumser, N. Rebola, D. A. DiGregorio, D. Trauner, *Nat. Commun.* **2015**, *6*, 1–11.
- [12] W. A. Velema, J. P. Van Der Berg, M. J. Hansen, W. Szymanski, A. J. M. Driessen, B. L. Feringa, *Nat. Chem.* **2013**, *5*, 924–928.
- [13] F. Crick, *Nature* **1970**, *227*, 561–563.
- [14] T. R. Cech, *Cold Spring Harb. Perspect. Biol.* **2012**, *4*, 1–5.
- [15] U. Sahin, A. Muik, E. Derhovanessian, I. Vogler, L. M. Kranz, M. Vormehr, A. Baum, K. Pascal, J. Quandt, D. Maurus, S. Brachtendorf, V. Lörks, J. Sikorski, R. Hilker, D. Becker, A. K. Eller, J. Grützner, C. Boesler, C. Rosenbaum, M. C. Kühnle, U. Luxemburger, A. Kemmer-Brück, D. Langer, M. Bexon, S. Bolte, K. Karikó, T. Palanche, B. Fischer, A. Schultz, P. Y. Shi, C. Fontes-Garfias, J. L. Perez, K. A. Swanson, J. Loschko, I. L. Scully, M. Cutler, W. Kalina, C. A. Kyratsous, D. Cooper, P. R. Dormitzer, K. U. Jansen, Ö. Türeci, *Nature* **2020**, *586*, 594–599.
- [16] W. Winkler, A. Nahvi, R. R. Breaker, *Nature* **2002**, *419*, 952–956.
- [17] A. Nahvi, N. Sudarsan, M. S. Ebert, X. Zou, K. L. Brown, R. R. Breaker, *Chem. Biol.* **2002**, *9*, 1043–1049.
- [18] L. Tuerk, C. Gold, *Science* **1990**, *249*, 505–510.

Bibliography

- [19] D. W. Ball, *The Basics of Spectroscopy*, SPIE Press, Bellingham, Washington USA, **2001**.
- [20] A. E. Siegmann, *Lasers*, University Science Books, Mill Valley, California USA, **1986**.
- [21] S. Mukamel, *Phys. Rep.* **1982**, *93*, 1–60.
- [22] J. R. Lakowitz, *Principles of Fluorescence Spectroscopy*, Springer US, **2006**.
- [23] M. Born, R. Oppenheimer, *Ann. Phys.* **1927**, *84*, 457–484.
- [24] J. Franck, E. G. Dymond, *Trans. Faraday Soc.* **1926**, *21*, 536–542.
- [25] E. Condon, in *Sel. Sci. Pap. E.U. Condon*, Springer New York, New York, **1991**, pp. 1–19.
- [26] M. Kasha, *Discuss. Faraday Soc.* **1950**, *9*, 14–19.
- [27] W. Demtröder, *Laser Spectroscopy*, Springer Science & Business Media, Berlin, **2007**.
- [28] J. S. Beckwith, C. A. Rumble, E. Vauthey, *Int. Rev. Phys. Chem.* **2020**, *39*, 135–216.
- [29] I. H. M. Van Stokkum, D. S. Larsen, R. Van Grondelle, *Biochim. Biophys. Acta - Bioenerg.* **2004**, *1657*, 82–104.
- [30] C. Slavov, H. Hartmann, J. Wachtveitl, *Anal. Chem.* **2015**, *87*, 2328–2336.
- [31] P. Kuzmic, *Anal. Biochem.* **1996**, *237*, 260–273.
- [32] H. Akaike, *IEEE Trans. Automat. Contr.* **1974**, *19*, 716–723.
- [33] J. I. Myung, Y. Tang, M. A. Pitt, *Methods Enzymol.* **2009**, *454*, 287–304.
- [34] L. Fenno, O. Yizhar, K. Deisseroth, *Annu. Rev. Neurosci.* **2011**, *34*, 389–412.
- [35] K. Deisseroth, *Nat. Methods* **2011**, *8*, 26–29.
- [36] A. P. Pelliccioli, J. Wirz, *Photochem. Photobiol. Sci.* **2002**, *1*, 441–458.
- [37] C. G. Bochet, *J. Chem. Soc. Perkin 1* **2002**, *2*, 125–142.
- [38] H. Dürr, H. Bouas-Laurent, *Photochromism: Molecules and Systems*, Amsterdam, **2003**.
- [39] J. Polster, *Reaktionskinetische Auswertung Spektroskopischer Messdaten*, Springer Vieweg, Wiesbaden, **1995**.
- [40] H. Bouas-Laurent, H. Dürr, *Pure Appl. Chem.* **2001**, *73*, 639–665.
- [41] B. L. Feringa, W. R. Browne, *Molecular Switches*, Wiley-VCH Weinheim, **2011**.
- [42] R. Göstl, A. Senf, S. Hecht, *Chem. Soc. Rev.* **2014**, *43*, 1982–1996.
- [43] D. Bléger, S. Hecht, *Angew. Chem. Int. Ed.* **2015**, *54*, 11338–11349.

- [44] M. Kathan, S. Hecht, *Chem. Soc. Rev.* **2017**, *46*, 5536–5550.
- [45] H. M. D. Bandara, S. C. Burdette, *Chem. Soc. Rev.* **2012**, *41*, 1809–1825.
- [46] J. Wachtveitl, T. Nägele, B. Puell, W. Zinth, M. Krüger, S. Rudolph-Böhner, D. Oesterhelt, L. Moroder, *J. Photochem. Photobiol., A* **1997**, *105*, 283–288.
- [47] T. Nägele, R. Hoche, W. Zinth, J. Wachtveitl, *Chem. Phys. Lett.* **1997**, *272*, 489–495.
- [48] A. A. Beharry, G. A. Woolley, *Chem. Soc. Rev.* **2011**, *40*, 4422–4437.
- [49] O. Sadovski, A. A. Beharry, F. Zhang, G. A. Woolley, *Angew. Chem. Int. Ed.* **2009**, *48*, 1484–1486.
- [50] W. Szymanski, J. M. Beierle, H. A. V Kistemaker, W. A. Velema, B. L. Feringa, *Chem. Rev.* **2013**, *113*, 6114–6178.
- [51] A. S. Lubbe, W. Szymanski, B. L. Feringa, *Chem. Soc. Rev.* **2017**, *46*, 1052–1079.
- [52] C. E. Weston, R. D. Richardson, P. R. Haycock, A. J. P. White, M. J. Fuchter, *J. Am. Chem. Soc.* **2014**, *136*, 11878–11881.
- [53] R. Heiligman-Rim, Y. Hirshberg, E. Fischer, *J. Chem. Soc.* **1961**, *297*, 156–163.
- [54] R. Heiligman-Rim, Y. Hirshberg, E. Fischer, *J. Phys. Chem.* **1962**, *66*, 2465–2470.
- [55] R. Heiligman-Rim, Y. Hirshberg, E. Fischer, *J. Phys. Chem.* **1962**, *66*, 2470–2477.
- [56] L. Kortekaas, W. R. Browne, *Chem. Soc. Rev.* **2019**, *48*, 3406–3424.
- [57] J. Kohl-Landgraf, M. Braun, C. Özçoban, D. P. N. Gonçalves, A. Heckel, J. Wachtveitl, *J. Am. Chem. Soc.* **2012**, *134*, 14070–14077.
- [58] M. Hammarson, J. R. Nilsson, S. Li, T. Beke-Somfai, J. Andréasson, *J. Phys. Chem. B* **2013**, *117*, 13561–13571.
- [59] N. P. Ernsting, T. Arthen-Engeland, *J. Phys. Chem.* **1991**, *95*, 5502–5509.
- [60] M. Rini, A. K. Holm, E. T. J. Nibbering, H. Fidder, *J. Am. Chem. Soc.* **2003**, *125*, 3028–3034.
- [61] A. K. Chibisov, H. Görner, *Phys. Chem. Chem. Phys.* **2001**, *3*, 424–431.
- [62] Y. Sheng, J. Leszczynski, A. A. Garcia, R. Rosario, D. Gust, J. Springer, *J. Phys. Chem. B* **2004**, *108*, 16233–16243.
- [63] C. Lenoble, R. S. Becker, *J. Phys. Chem.* **1986**, *90*, 62–65.
- [64] J. Buback, M. Kullmann, F. Langhojer, P. Nuernberger, R. Schmidt, F. Würthner, T. Brixner, *J. Am. Chem. Soc.* **2010**, *132*, 16510–16519.
- [65] C. J. Wohl, D. Kuciauskas, *J. Phys. Chem. B* **2005**, *109*, 22186–22191.

Bibliography

- [66] M. Kullmann, S. Ruetzel, J. Buback, P. Nuernberger, T. Brixner, *J. Am. Chem. Soc.* **2011**, *133*, 13074–13080.
- [67] J. Buback, P. Nuernberger, M. Kullmann, F. Langhojer, R. Schmidt, F. Würthner, T. Brixner, *J. Phys. Chem. A* **2011**, *115*, 3924–3935.
- [68] Z. Shi, P. Peng, D. Strohecker, Y. Liao, *J. Am. Chem. Soc.* **2011**, *133*, 14699–14703.
- [69] L. Kortekaas, J. Chen, D. Jacquemin, W. R. Browne, *J. Phys. Chem. B* **2018**, *122*, 6423–6430.
- [70] L. Kortekaas, O. Ivashenko, J. T. Van Herpt, W. R. Browne, *J. Am. Chem. Soc.* **2016**, *138*, 1301–1312.
- [71] N. Abeyrathna, Y. Liao, *J. Am. Chem. Soc.* **2015**, *137*, 11282–11284.
- [72] L. A. Tatum, J. T. Foy, I. Aprahamian, *J. Am. Chem. Soc.* **2014**, *136*, 17438–17441.
- [73] P. Gorostiza, E. Isacoff, *Mol. Biosyst.* **2007**, *3*, 686–704.
- [74] S. Berlin, S. Szobota, A. Reiner, E. C. Carroll, M. A. Kienzler, A. Guyon, T. Xiao, D. Trauner, E. Y. Isacoff, *eLife* **2016**, *5*, e12040.
- [75] A. S. Lubbe, W. Szymanski, B. L. Feringa, *Chem. Soc. Rev.* **2017**, *46*, 1052–1079.
- [76] J. Thevarpadam, I. Bessi, O. Binas, D. P. N. Gonçalves, C. Slavov, H. R. A. Jonker, C. Richter, J. Wachtveitl, H. Schwalbe, A. Heckel, *Angew. Chem. Int. Ed.* **2016**, *55*, 2738–2742.
- [77] C. Brieke, F. Rohrbach, A. Gottschalk, G. Mayer, A. Heckel, *Angew. Chem., Int. Ed.* **2012**, *51*, 8446–8476.
- [78] T. Goldau, K. Murayama, C. Brieke, S. Steinwand, P. Mondal, M. Biswas, I. Burghardt, J. Wachtveitl, H. Asanuma, A. Heckel, *Chem. - A Eur. J.* **2015**, *21*, 2845–2854.
- [79] M. Stein, S. J. Middendorp, V. Carta, E. Pejo, D. E. Raines, S. A. Forman, E. Sigel, D. Trauner, *Angew. Chem. Int. Ed.* **2012**, *51*, 10500–10504.
- [80] D. P. Giedroc, C. A. Theimer, P. L. Nixon, *J. Mol. Biol.* **2000**, *298*, 167–185.
- [81] J. U. Guo, D. P. Bartel, *Science* **2016**, *353*, aaf5371.
- [82] B. Luke, J. Lingner, *EMBO J.* **2009**, *28*, 2503–2510.
- [83] N. B. Leontis, E. Westhof, *RNA* **2001**, *7*, 499–512.
- [84] P. Brion, E. Westhof, *Annu. Rev. Biophys. Biomol. Struct.* **1997**, *26*, 113–137.
- [85] H. Schwalbe, J. Buck, B. Fürtig, J. Noeske, J. Wöhnert, *Angew. Chem. Int. Ed.* **2007**, *46*, 1212–1219.
- [86] R. R. Breaker, *Mol. Cell* **2011**, *43*, 867–879.

- [87] A. Serganov, E. Nudler, *Cell* **2013**, *152*, 17–24.
- [88] M. J. Cromie, Y. Shi, T. Latifi, E. A. Groisman, *Cell* **2006**, *125*, 71–84.
- [89] M. Mandal, R. R. Breaker, *Nat. Rev. Mol. Cell Biol.* **2004**, *5*, 451–463.
- [90] R. R. Breaker, *Cold Spring Harb. Perspect. Biol.* **2012**, *4*, a003566.
- [91] J.-F. Lemay, J. C. Penedo, R. Tremblay, D. M. J. Lilley, D. A. Lafontaine, *Chem. Biol.* **2006**, *13*, 857–868.
- [92] R. T. Batey, S. D. Gilbert, R. K. Montange, *Nature* **2004**, *432*, 411–415.
- [93] P. Y. Watson, M. J. Fedor, *Nat. Chem. Biol.* **2012**, *8*, 963–965.
- [94] A. Serganov, L. Huang, D. J. Patel, *Nature* **2008**, *455*, 1263–1267.
- [95] L. Huang, A. Serganov, D. J. Patel, *Mol. Cell* **2010**, *40*, 774–786.
- [96] A. Serganov, L. Huang, D. J. Patel, *Nature* **2009**, *458*, 233–237.
- [97] C. D. Stoddard, R. K. Montange, S. P. Hennelly, R. P. Rambo, K. Y. Sanbonmatsu, R. T. Batey, *Structure* **2010**, *18*, 787–797.
- [98] C. Tuerk, L. Gold, *Science* **1990**, *249*, 505–510.
- [99] A. D. Ellington, J. W. Szostak, *Nature* **1990**, *346*, 818–822.
- [100] F. Groher, B. Suess, *Methods* **2016**, *106*, 42–50.
- [101] J. Jaeger, F. Groher, J. Stamm, D. Spiehl, J. Braun, E. Dörsam, B. Suess, *Biosensors* **2019**, *9*, 1–10.
- [102] P. Hong, W. Li, J. Li, *Sensors* **2012**, *12*, 1181–1193.
- [103] J. Ouellet, *Front. Chem.* **2016**, *4*, 1–12.
- [104] K. Y. Han, B. J. Leslie, J. Fei, J. Zhang, T. Ha, *J. Am. Chem. Soc.* **2013**, *135*, 19033–19038.
- [105] V. S. Yerramilli, K. H. Kim, *ACS Synth. Biol.* **2018**, *7*, 758–766.
- [106] A. Autour, S. C. Y. Jeng, A. D. Cawte, A. Abdolazadeh, A. Galli, S. S. S. Panchapakesan, D. Rueda, M. Ryckelynck, P. J. Unrau, *Nat. Commun.* **2018**, *9*, 1–12.
- [107] E. V. Dolgosheina, S. C. Y. Jeng, S. S. S. Panchapakesan, R. Cojocar, P. S. K. Chen, P. D. Wilson, N. Hawkins, P. A. Wiggins, P. J. Unrau, *ACS Chem. Biol.* **2014**, *9*, 2412–2420.
- [108] R. J. Trachman, L. Truong, A. R. Ferré-D’Amaré, *Trends Pharmacol. Sci.* **2017**, *38*, 928–939.
- [109] A. Wrist, W. Sun, R. M. Summers, *ACS Synth. Biol.* **2020**, *9*, 682–697.
- [110] G. R. Zimmermann, R. D. Jenison, C. L. Wick, J. Simorre, A. Pardi, *Nat. Struct. Biol.* **1997**, *4*, 644–649.

Bibliography

- [111] J. E. Weigand, M. Sanchez, E. Gunnesch, S. Zeiher, R. Schroeder, B. Suess, *RNA* **2008**, *14*, 89–97.
- [112] C. Berens, A. Thain, R. Schroeder, *Bioorg. Med. Chem.* **2001**, *9*, 2549–2556.
- [113] A. Boussebayle, D. Torca, S. Ollivaud, J. Braun, C. Bofill-Bosch, M. Dombrowski, F. Groher, K. Hamacher, B. Suess, *Nucleic Acids Res.* **2019**, *47*, 4883–4895.
- [114] F. Groher, C. Bofill-Bosch, C. Schneider, J. Braun, S. Jager, K. Geißler, K. Hamacher, B. Suess, *Nucleic Acids Res.* **2018**, *46*, 2121–2132.
- [115] A. Wittmann, B. Suess, *FEBS Lett.* **2012**, *586*, 2076–2083.
- [116] B. Suess, B. Fink, C. Berens, R. Stentz, W. Hillen, *Nucleic Acids Res.* **2004**, *32*, 1610–1614.
- [117] I. Harvey, P. Garneau, J. Pelletier, *RNA* **2002**, *8*, 452–463.
- [118] B. Suess, S. Hanson, C. Berens, B. Fink, R. Schroeder, W. Hillen, *Nucleic Acids Res.* **2003**, *31*, 1853–1858.
- [119] B. Suess, J. E. Weigand, *RNA Biol.* **2008**, *5*, 1–6.
- [120] M. Wachsmuth, S. Findeiß, N. Weissheimer, P. F. Stadler, M. Mörl, *Nucleic Acids Res.* **2013**, *41*, 2541–2551.
- [121] P. Ceres, J. J. Trausch, R. T. Batey, *Nucleic Acids Res.* **2013**, *41*, 10449–10461.
- [122] P. Ceres, A. D. Garst, J. G. Marcano-Velázquez, R. T. Batey, *ACS Synth. Biol.* **2013**, *2*, 463–472.
- [123] J. E. Weigand, B. Suess, *Nucleic Acids Res.* **2007**, *35*, 4179–4185.
- [124] R. J. Trachman, A. Autour, S. C. Y. Jeng, A. Abdolazadeh, A. Andreoni, R. Cojocar, R. Garipov, E. V. Dolgosheina, J. R. Knutson, M. Ryckelynck, P. J. Unrau, A. R. Ferré-D'Amaré, *Nat. Chem. Biol.* **2019**, *15*, 472–479.
- [125] A. S. Petrov, J. C. Bowman, S. C. Harvey, L. D. Williams, *RNA* **2011**, *17*, 291–297.
- [126] J. M. Carothers, J. A. Goler, Y. Kapoor, L. Lara, J. D. Keasling, *Nucleic Acids Res.* **2010**, *38*, 2736–2747.
- [127] J. M. Carothers, S. C. Oestreich, J. H. Davis, J. W. Szostak, *J. Am. Chem. Soc.* **2004**, *126*, 5130–5137.
- [128] C. Özçoban, T. Halbritter, S. Steinwand, L.-M. Herzig, J. Kohl-Landgraf, N. Askari, F. Groher, B. Fürtig, C. Richter, H. Schwalbe, B. Suess, J. Wachtveitl, A. Heckel, *Org. Lett.* **2015**, *17*, 1517–1520.
- [129] U. Förster, *Untersuchung der Konformation und Dynamik von RNA mit Hilfe fluoreszierender Farbstoffmoleküle* **2010**, Dissertation, Goethe University, Frankfurt/Main.

- [130] U. Förster, J. E. Weigand, P. Trojanowski, B. Suess, J. Wachtveitl, *Nucleic Acids Res.* **2012**, *40*, 1807–1817.
- [131] A. J. Reuss, M. Vogel, J. E. Weigand, B. Suess, J. Wachtveitl, *Biophys. J.* **2014**, *107*, 2962–2971.
- [132] A. J. Reuss, *Functional Dynamics of Ribonucleic Acids* **2016**, Dissertation, Goethe University, Frankfurt/Main.
- [133] S. Steinwand, *Conform. Control Org. Mol. by Azobenzene-Based Photoswitches – A Spectrosc. Study* **2016**, Dissertation, Goethe University, Frankfurt/Main.
- [134] S. Prager, I. Burghardt, A. Dreuw, *J. Phys. Chem. A* **2014**, *118*, 1339–1349.
- [135] J. Andersson, S. Li, P. Lincoln, J. Andréasson, *J. Am. Chem. Soc.* **2008**, *130*, 11836–11837.
- [136] A. Kocer, M. Walko, W. Meijberg, B. L. Feringa, *Science* **2005**, *309*, 755–758.
- [137] D. D. Young, A. Deiters, *ChemBioChem* **2008**, *9*, 1225–1228.
- [138] C. Walter, S. Ruetzel, M. Diekmann, P. Nuernberger, T. Brixner, B. Engels, *J. Chem. Phys.* **2014**, *140*, 224311.
- [139] T. Tamaki, M. Sakugari, K. Ichimura, K. Aoki, *Chem. Phys. Lett.* **1989**, *161*, 23–26.
- [140] A. K. Chibisov, H. Görner, *J. Phys. Chem. A* **1997**, *101*, 4305–4312.
- [141] A. K. Chibisov, H. Görner, *Chem. Phys.* **1998**, *237*, 425–442.
- [142] H. Görner, *Phys. Chem. Chem. Phys.* **2001**, *3*, 416–423.
- [143] A.-K. Holm, M. Rini, E. T. J. Nibbering, H. Fidder, *Chem. Phys. Lett.* **2003**, *376*, 214–219.
- [144] H. Fidder, M. Rini, E. T. J. Nibbering, *J. Am. Chem. Soc.* **2004**, *126*, 3789–3794.
- [145] C. Lenoble, R. S. Becker, *J. Phys. Chem.* **1986**, *90*, 62–65.
- [146] J. Buback, M. Kullmann, F. Langhojer, P. Nuernberger, R. Schmidt, F. Würthner, T. Brixner, *J. Am. Chem. Soc.* **2010**, *132*, 16510–16519.
- [147] S. Ruetzel, M. Diekmann, P. Nuernberger, C. Walter, B. Engels, T. Brixner, *J. Chem. Phys.* **2014**, *140*, 1–10.
- [148] Z. Shi, P. Peng, D. Strohecker, Y. Liao, *J. Am. Chem. Soc.* **2011**, *133*, 14699–14703.
- [149] N. Abeyrathna, Y. Liao, *J. Am. Chem. Soc.* **2015**, *137*, 11282–11284.
- [150] V. K. Johns, Z. Wang, X. Li, Y. Liao, *J. Phys. Chem. A* **2013**, *117*, 13101–13104.
- [151] Y. Liao, *Acc. Chem. Res.* **2017**, *50*, 1956–1964.

Bibliography

- [152] T. Förster, *Naturwissenschaften* **1949**, *36*, 186–187.
- [153] J. F. Ireland, P. A. H. Wyatt, *Adv. Phys. Org. Chem.* **1976**, *12*, 131–221.
- [154] C. J. Martin, G. Rapenne, T. Nakashima, T. Kawai, *J. Photochem. Photobiol., C* **2018**, *34*, 41–51.
- [155] N. Zivic, P. K. Kuroishi, F. Dumur, D. Gigmes, A. P. Dove, H. Sardon, *Angew. Chem. Int. Ed.* **2019**, *58*, 10410–10422.
- [156] E. W. Driscoll, J. R. Hunt, J. M. Dawlaty, *J. Phys. Chem. A* **2017**, *121*, 7099–7107.
- [157] E. T. Ryan, T. Xiang, K. P. Johnston, M. A. Fox, *J. Phys. Chem. A* **1997**, *101*, 1827–1835.
- [158] G. Favaro, U. Mazzucato, F. Masetti, *J. Phys. Chem.* **1973**, *77*, 601–604.
- [159] Z.R. Grabowski, W. Rubaszewska, *J. Lumin.* **1981**, *24*, 559–562.
- [160] I. Carmeli, D. Huppert, L. M. Tolbert, J. E. Haubrich, *Chem. Phys. Lett.* **1996**, *4*, 109–114.
- [161] D. Huppert, L. M. Tolbert, S. Linares-Samaniego, *J. Phys. Chem. A* **1997**, *5639*, 4602–4605.
- [162] L. M. Tolbert, J. E. Haubrich, *J. Am. Chem. Soc.* **1990**, *112*, 8163–8165.
- [163] T. G. Kim, M. R. Topp, *J. Phys. Chem. A* **2004**, *108*, 10060–10065.
- [164] J. L. Pérez-Lustres, F. Rodriguez-Prieto, M. Mosquera, T. A. Senyushkina, N. P. Ernsting, S. A. Kovalenko, *J. Am. Chem. Soc.* **2007**, *129*, 5408–5418.
- [165] E. A. Gould, A. V. Popov, L. M. Tolbert, I. Presiado, Y. Erez, D. Huppert, K. M. Solntsev, *Phys. Chem. Chem. Phys.* **2012**, *14*, 8964–8973.
- [166] S. Kaneko, S. Yotoriyama, H. Koda, S. Tobita, *J. Phys. Chem. A* **2009**, *113*, 3021–3028.
- [167] R. Simkovitch, D. Huppert, *J. Phys. Chem. A* **2015**, *119*, 1973–1982.
- [168] A. Weller, *Z. Elektrochem.* **1952**, *56*, 662.
- [169] M. Eigen, *Angew. Chem. Int. Ed.* **1964**, *3*, 1–19.
- [170] N. Agmon, *J. Phys. Chem. A* **2005**, *109*, 13–35.
- [171] N. Agmon, *Chem. Phys. Lett.* **1995**, *50*, 456–462.
- [172] J. Kohl-Landgraf, F. Buhr, D. Lefrancois, J. M. Mewes, H. Schwalbe, A. Dreuw, J. Wachtveitl, *J. Am. Chem. Soc.* **2014**, *136*, 3430–3438.
- [173] K. Adamczyk, M. Prémont-Schwarz, D. Pines, E. Pines, E. Nibbering, *Science* **2009**, *326*, 1690–16994.
- [174] M. Ekimova, F. Hoffmann, G. Bekçioğlu-Neff, A. Rafferty, O. Kornilov, E. T. J. Nibbering, D. Sebastiani, *J. Am. Chem. Soc.* **2019**, *141*, 14581–14592.

- [175] M. Prémont-Schwarz, T. Barak, D. Pines, E. T. J. Nibbering, E. Pines, *J. Phys. Chem. B* **2013**, *117*, 4594–4603.
- [176] N. Agmon, *Int. J. Chem. Kinet.* **1981**, *13*, 333–365.
- [177] R. A. Marcus, *J. Am. Chem. Soc.* **1969**, *91*, 7224–7225.
- [178] A. O. Cohen, R. A. Marcus, *J. Phys. Chem.* **1968**, *72*, 4249–4256.
- [179] E. Pines, D. Pines, T. Barak, B.-Z. Magnes, L. M. Tolbert, J. E. Haubrich, *Ber. Bunsenges. Phys. Chem.* **1998**, *102*, 511–517.
- [180] E. Pines, G. R. Fleming, *J. Phys. Chem.* **1991**, *95*, 10448–10457.
- [181] I. Presiado, N. Karton-lifshin, Y. Erez, R. Gepshtein, D. Shabat, D. Huppert, *J. Phys. Chem.* **2012**, *116*, 7353–7363.
- [182] R. Simkovitch, S. Shomer, R. Gepshtein, M. E. Roth, D. Shabat, D. Huppert, *J. Photochem. Photobiol. A Chem.* **2014**, *277*, 90–101.
- [183] C. M. T. Spahn, C. D. Prescott, *J. Mol. Med.* **1996**, *74*, 423–439.
- [184] M. Müller, J. E. Weigand, O. Weichenrieder, B. Suess, *Nucleic Acids Res.* **2006**, *34*, 2607–2617.
- [185] S. Hanson, K. Berthelot, B. Fink, J. E. G. McCarthy, B. Suess, *Mol. Microbiol.* **2003**, *49*, 1627–1637.
- [186] K. Beilstein, A. Wittmann, M. Grez, B. Suess, *ACS Synth. Biol.* **2015**, *4*, 526–534.
- [187] H. Xiao, E. E. Edwards, A. R. Ferré-D'Amaré, *Chem. Biol.* **2008**, *15*, 1125–1137.
- [188] D. Wunnicke, D. Strohbach, J. E. Weigand, B. Appel, E. Feresin, B. Suess, S. Mu, **2011**, 182–188.
- [189] J. M. Jean, K. B. Hall, *Proc. Natl. Acad. Sci.* **2001**, *98*, 37–41.
- [190] A. Haller, M. F. Soulière, R. Micura, *Acc. Chem. Res.* **2011**, *44*, 1339–1348.
- [191] R. Rieder, K. Lang, D. Graber, R. Micura, *ChemBioChem* **2007**, *8*, 896–902.
- [192] K. Lang, R. Rieder, R. Micura, *Nucleic Acids Res.* **2007**, *35*, 5370–5378.
- [193] M. Frener, R. Micura, *J. Am. Chem. Soc.* **2016**, *138*, 3627–3630.
- [194] C. Berens, B. Suess, *Curr. Opin. Biotechnol.* **2015**, *31*, 10–15.
- [195] M. Vogel, J. E. Weigand, B. Kluge, M. Grez, B. Suess, *Nucleic Acids Res.* **2018**, *46*, e48.
- [196] R. Davis, A. Markham, J. A. Balfour, *Drugs* **1996**, *51*, 1019–1074.
- [197] C. Schneider, B. Suess, *Methods* **2016**, *97*, 44–50.
- [198] E. Duchardt-Ferner, J. E. Weigand, O. Ohlenschläger, S. R. Schmidtke, B. Suess, J. Wöhnert, *Angew. Chem. Int. Ed.* **2010**, *49*, 6216–6219.

Bibliography

- [199] F. M. Jucker, R. M. Phillips, S. A. McCallum, A. Pardi, *Biochemistry* **2003**, *42*, 2560–2567.
- [200] A. Umuhire Juru, N. N. Patwardhan, A. E. Hargrove, *ACS Chem. Biol.* **2019**, *14*, 824–838.
- [201] F. Paul, T. R. Weikl, *PLoS Comput. Biol.* **2016**, *12*, 1–17.
- [202] H. Gustmann, A. J. Segler, D. B. Gophane, A. J. Reuss, C. Gr, M. Braun, J. E. Weigand, S. T. Sigurdsson, J. Wachtveitl, *Nucleic Acids Res.* **2019**, *47*, 15–28.
- [203] J. E. Weigand, S. R. Schmidtke, T. J. Will, E. Duchardt-Ferner, C. Hammann, J. Wöhnert, B. Suess, *Nucleic Acids Res.* **2011**, *39*, 3363–3372.
- [204] S. D. Gilbert, C. D. Stoddard, S. J. Wise, R. T. Batey, *J. Mol. Biol.* **2006**, *359*, 754–768.
- [205] J. Buck, B. Furtig, J. Noeske, J. Wohnert, H. Schwalbe, *Proc. Natl. Acad. Sci.* **2007**, *104*, 15699–15704.
- [206] J. K. Wickiser, M. T. Cheah, R. R. Breaker, D. M. Crothers, *Biochemistry* **2005**, *44*, 13404–13414.
- [207] D. Burnouf, E. Ennifar, S. Guedich, B. Puffer, G. Hoffmann, G. Bec, F. Disdier, M. Baltzinger, P. Dumas, *J. Am. Chem. Soc.* **2012**, *134*, 559–565.
- [208] J. K. Wickiser, W. C. Winkler, R. R. Breaker, D. M. Crothers, *Mol. Cell* **2005**, *18*, 49–60.
- [209] A. Boussebayle, F. Groher, B. Suess, *Methods* **2019**, *161*, 10–15.
- [210] D. H. Burke, D. C. Hoffman, A. Brown, M. Hansen, A. Pardi, L. Gold, *Chem. Biol.* **1997**, *4*, 833–843.
- [211] S. Will, T. Joshi, I. L. Hofacker, P. F. Stadler, R. Backofen, *RNA* **2012**, *18*, 900–914.
- [212] C. Smith, S. Heyne, A. S. Richter, S. Will, R. Backofen, *Nucleic Acids Res.* **2010**, *38*, 373–377.
- [213] O. C. Uhlenbeck, P. N. Borer, B. Dengler, I. Tinoco, *J. Mol. Biol.* **1973**, *73*, 483–496.
- [214] D. J. Williams, K. B. Hall, *Biochemistry* **1996**, *35*, 14665–14670.

7 PUBLICATIONS

The supporting information files for the individual publications are available on the corresponding journal websites using the associated digital object identifier (DOI) numbers.

(* - these authors contributed equally)

7.1 DECLARATION OF THE OWN CONTRIBUTION FOR EACH PUBLICATION

Reference [I], pages 106-119

Thermal, Photochromic and Dynamic Properties of Water-Soluble Spiroyrans

C. Kaiser*, T. Halbritter*, A. Heckel, J. Wachtveitl,

ChemistrySelect **2017**, 2, 4111-4123.

(DOI: 10.1002/slct.201700868)

- Performance of steady-state absorption and fluorescence spectroscopic experiments and analysis of the acquired data.
- Execution and analysis of time-resolved transient absorption experiments.
- Writing of the manuscript together with T. Halbritter.

Reference [II], pages 120-128

Pyridine-Spiropyran Derivative as a Persistent, Reversible Photoacid in Water

T. Halbritter*, C. Kaiser*, J. Wachtveitl, A. Heckel,

J. Org. Chem. **2017**, 82, 8040-8047.

(DOI: 10.1021/acs.joc.7b01268)

- Performance of steady-state absorption and fluorescence spectroscopic experiments and analysis of the acquired data.
- Execution of pH-switching experiments under various conditions.

- Interpretation of the data together with co-authors.
- Writing of the manuscript together with T. Halbritter.

Reference [III], pages 129-143

Proton-Transfer Dynamics of Photoacidic Merocyanines in Aqueous Solution

C. Kaiser, T. Halbritter, A. Heckel, J. Wachtveitl,

Chem. Eur. J. **2021**, *27*, 9160-9173.

(DOI: 10.1002/chem.202100168)

- Performance of steady-state absorption and fluorescence spectroscopic experiments.
- Execution of time-resolved TA experiments and analysis of the acquired datasets.
- Interpretation of the data together with co-authors.
- Writing of the manuscript in coordination with co-authors.

Reference [IV], pages 144-155

What Defines a Synthetic Riboswitch? - Conformational Dynamics of Ciprofloxacin Aptamers with Similar Binding Affinities but Varying Regulatory Potentials

C. Kaiser, J. Schneider, F. Groher, B. Suess, J. Wachtveitl,

Nucleic Acids Res. **2021**, *49*, 3661-3671.

(DOI: 10.1093/nar/gkab166)

- Performance of steady-state absorption and fluorescence spectroscopic experiments for characterization of the dye molecule.
- Execution of time-resolved fluorescence experiments and analysis of acquired datasets.
- Execution of time-resolved fluorescence-monitored ligand binding studies and kinetic analysis of acquired datasets.
- Interpretation of the results and writing of the manuscript together with the co-authors.

Reference [V], pages 156-168

A Light-Responsive RNA Aptamer for an Azobenzene Derivative

T. S. Lotz, T. Halbritter, C. Kaiser, M. M. Rudolph, L. Kraus, F. Groher, S. Steinwand, J. Wachtveitl, A. Heckel, B. Suess,

Nucleic Acids Res. **2019**, *47*, 2029-2040.

(DOI: 10.1093/nar/gky1225)

- Reproduction of photoswitching experiments of S. Wahl (formerly Steinwand).
- Performance and analysis of circular dichroism studies to investigate the behaviour of selected RNA aptamers in presence of the photoswitch ligand.
- Interpretation of the data together with co-authors.
- Writing of the manuscript section concerned with the spectroscopic investigations.

Not referenced, pages 169-180

The Interplay of Nanoconfinement and pH from the Perspective of a Dye-Reporter Molecule

R. Brilmayer*, M. Bodrecht*, C. Kaiser, H. Breitzke, B. Kumari, J. Wachtveitl, G. Buntkowsky, A. Andrieu-Brunsen,

ChemNanoMat **2020**, *6*, 1843-1853.

(DOI: 10.1002/cnma.202000423)

- Performance of steady-state absorption and fluorescence spectroscopic experiments for characterization of the dye molecule.
- Execution of time-resolved fluorescence experiments and analysis of acquired datasets.
- Determination of the fluorescence quantum yield with an integrating sphere.
- Writing of the manuscript section concerned with the spectroscopic characterization of the dye molecule.

7.2 Kaiser et al., *ChemistrySelect* 2017, 2

Reference [1]

Thermal, Photochromic and Dynamic Properties of Water-Soluble Spiropyrans

C. Kaiser*, T. Halbritter*, A. Heckel, J. Wachtveitl,

ChemistrySelect **2017**, 2, 4111-4123.

(DOI: 10.1002/slct.201700868)

Biological Chemistry & Chemical Biology

Thermal, Photochromic and Dynamic Properties of Water-Soluble Spiroopyrans

Christoph Kaiser[†],^[a] Thomas Halbritter[†],^[b] Alexander Heckel,^{*,[b]} and Josef Wachtveitl^{*,[a]}

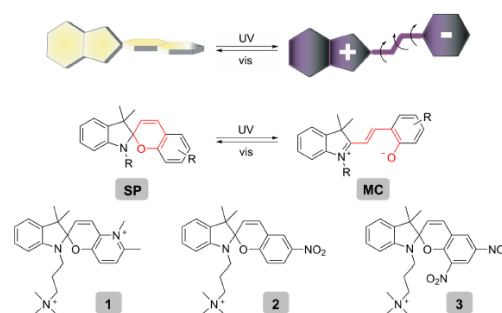
Numerous studies in biological and material sciences have used nitro-BIPS, dinitro-BIPS as well as Py-BIPS as versatile photo-switches. Still, the photochemical picture of this class of compounds is far from complete. We present photometric steady-state and ultrafast time-resolved pump/probe spectroscopic measurements on water-soluble derivatives of these three spiroopyrans. Our experiments reveal significant differences between the nitro-substituted spiroopyrans and Py-BIPS. In contrast to the high resistance of Py-BIPS towards hydrolysis

over weeks, the two nitro-BIPS derivatives decompose over hours. The fluorescence properties of Py-BIPS are unique in showing an emission of the spiro photoisomer. The ring-opening and -closing reaction of Py-BIPS is accomplished within picoseconds, whereas nitro-derivatives photoisomerize on longer time scales. These long-lived transients indicate either the contribution of triplet states or the involvement of multiple merocyanine isomers in the reaction pathway.

Introduction

Photochromic compounds undergo unimolecular, bidirectional reversible structural and chemical changes after irradiation with light. If applied correctly, light can be operated as a harmless and selective external trigger to control material properties or even biological processes if the target photoswitch is soluble in aqueous solution. In contrast to azobenzenes^[1–8] which undergo photoinduced *cis/trans* isomerization, spiroopyrans,^[9–12] diarylethenes,^[13] fulgides^[14–16] and fulgimides^[17,18] exist in an opening and closed isomeric form. Spiroopyrans possess an indoline and a chromene moiety and can be switched reversibly between the closed-ring, nonpolar spiroopyran (SP) structure and the open-ring merocyanine (MC) which adopts a zwitterionic or a quinoidal mesomeric resonance structure. Furthermore, MC is known to exist as different *cis* (C) / *trans* (T) isomers due to its central ethylene bridge (Scheme 1, top and middle) with the two adjacent bonds. In principle eight different conformations are imaginable, but due to steric reasons only those four with *trans* conformation in the middle are stable.^[12]

The corresponding main absorption bands of both photoisomers are well separated and typically account for a yellow SP and a reddish MC form. The photochromic features as well as the thermodynamically favored state considerably depend



Scheme 1. Reversible photochromic reaction between the closed spiroopyran (SP) and the open-ring merocyanine (MC, TTC conformation) isomer of the BIPS compound (top and middle). The three water-soluble spiroopyran derivatives (1–3) investigated in this study (bottom).

on the particular substituents attached to the indoline and chromene moieties.

Spiroopyrans are widely used in material sciences^[19–21] and thus, have been subjected to numerous experimental steady-state and also ultrafast time-resolved studies in organic solvents.^[10,22–24] Moreover, theoretical studies have been carried out^[25,26] also under simulation of aqueous conditions.^[27] Since spiroopyrans are getting more and more into the focus for the control of biological systems,^[28–30] it is necessary to understand their switching behavior and photodynamics in aqueous conditions thoroughly, as these features may differ significantly because of the increased solute polarity. The obtained results could help tuning the photoresponsive properties to design enhanced spiroopyran photoswitches for diverse applications.

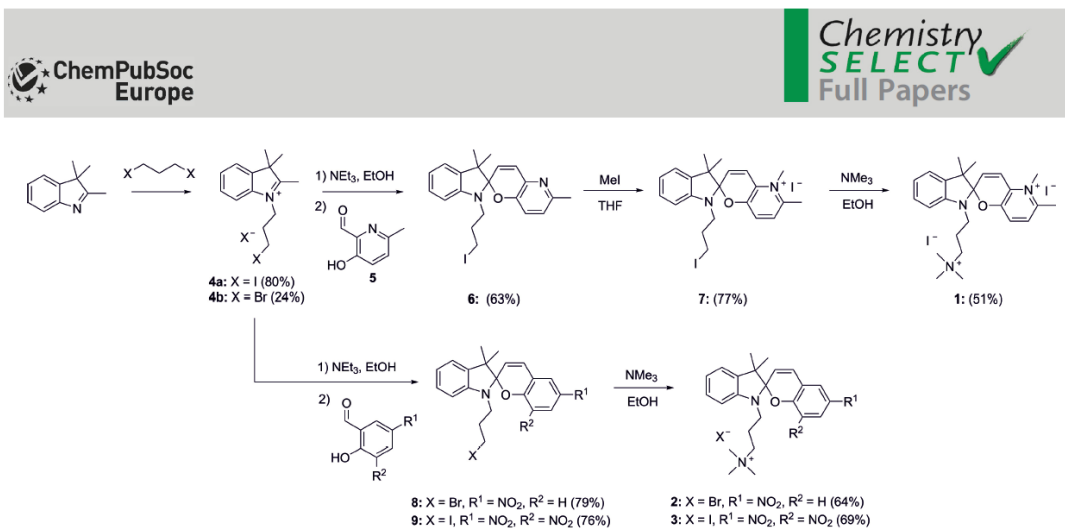
The best-studied and mostly applied spiroopyran derivative is the nitro-substituted 1',3',3'-trimethylspiro[2H-1-benzopyran-2,2'-indoline] (nitro-BIPS), which has been introduced to various

[a] C. Kaiser,[†] Prof. Dr. J. Wachtveitl
Institute of Physical and Theoretical Chemistry
Goethe-University Frankfurt, Max-von-Laure-Str. 7
60438 Frankfurt (Germany)
E-mail: wweitl@theochem.uni-frankfurt.de

[b] T. Halbritter,[†] Prof. Dr. A. Heckel
Institute of Organic Chemistry and Chemical Biology
Goethe-University Frankfurt, Max-von-Laure-Str. 7
60438 Frankfurt (Germany)
E-mail: heckel@uni-frankfurt.de

[*] C. Kaiser and T. Halbritter contributed equally to this article.

Supporting information for this article is available on the WWW under <https://doi.org/10.1002/slct.201700868>



Scheme 2. Overview of the synthesis of the water-soluble Py-BIPS derivative **1** (upper row) and the nitro-BIPS derivatives **2** and **3** (lower row).

biological environments like RNA,^[28] DNA,^[31] and proteins so far.^[32] Nitro-BIPS has been found to undergo hydrolysis under aqueous conditions^[33–35] and shows loss of switching efficiency in the presence of DNA.^[36] In previous work we could show that different spiropyran derivatives which we called “Py-BIPS” 3,3,5,6-tetra-methyl-spiro[2H-indole-2,2'-[2H]pyrano[3,2-b]pyridinium]-1-(2-hydroxypropyl) iodide are stable under aqueous conditions and are well suited for applications in the context of nucleic acids.^[29,37]

We synthesized water-soluble Py- (**1**), nitro- (**2**) and dinitro-BIPS (**3**) derivatives with a trimethylammonium substituent on the indolene ring (Scheme 1, bottom).

The photophysical properties should give a first hint about the influence of the chromene part on the photochromic behavior of spiropyrans in aqueous conditions. Hence, we performed photoswitching and thermal relaxation studies as well as fluorescence measurements in order to characterize the steady state properties of the most promising spiropyrans Py-BIPS **1**, nitro-BIPS **2** and dinitro-BIPS **3**.

To ascertain the photochemical pathways upon optical excitation of the **SP** and **MC** isomers, we executed time-resolved pump/probe studies in the vis- and mid-IR-range. Thereby we could prove that the photodynamics of Py-BIPS **1** in aqueous solution is very similar to those of the original Py-BIPS compound.^[38] To the best of our knowledge, the ultrafast dynamics of nitro-BIPS derivatives has not yet been investigated in aqueous solutions. Thus, we also performed transient absorption experiments with nitro-BIPS **2** and dinitro-BIPS **3** to provide an insight into their dynamic features in water and to allow for comparisons to their behavior in organic solvents.

Results and Discussion

Synthesis

Scheme 2 summarizes the synthetic routes to the spiropyran derivatives **1**, **2**, and **3**. To obtain the two new spiropyran

derivatives **1** and **3**, 2,3,3-trimethyl-3H-indole was first alkylated with 1,3-diiodopropane on the nitrogen and then deprotonated with NEt₃ under temporary formation of an enamine, followed by an aldol condensation with the respective aldehydes to form compounds **6** and **9**. The afforded spiropyran **6** was methylated with iodomethane to yield compound **7**. The spiropyran derivatives were stirred in a trimethylamine solution to obtain the water-soluble derivatives **1**, **2**, **3** (see Supporting Information for details). Py-BIPS **1** exhibits an extraordinary solubility of 52 mM in PBS buffer (pH 7.4), which is higher than that of the original Py-BIPS compound (28 mM) with a hydroxypropyl substituent on the indolene nitrogen.^[38] Nitro-BIPS **2** shows a comparably high solubility of 57 mM in water.^[37] In contrast, the solubility of compound **3** was found to be drastically lower (450 μM).

Photochromic Properties

The material properties as well as the spectroscopic characteristics of spiropyran compounds are substantially affected by their particular substitution pattern especially on the chromene part. Py-BIPS **1** appears as colorless solid as the closed-ring **SP** isomer is thermodynamically favored in the solid state as well as in aqueous solution.

Nitro-BIPS **2** is also colorless as a solid. However, the relative stabilization of the zwitterionic **MC** form is increased in solution, owing to the presence of the electron-withdrawing nitro group. As to dinitro-BIPS **3**, the open-ring **MC** isomer is stabilized to such an extent that it exists as a dark purple merocyanine solid. Dissolving dinitro-BIPS **3** in aqueous PBS buffer (pH 7.4) results in an initially pure **MC** sample where the fraction of the open-ring isomer immediately starts to decline due to hydrolysis and thermal equilibration (see following sections). To this end, a freshly prepared solution of dinitro-BIPS **3** was immediately irradiated with visible light to prevent hydrolysis. The absorption spectra of the closed **SP** photoisomers of the three compounds exhibit absorption bands in

the near UV region around 350 nm, which refer to $S_0 \rightarrow S_1$ transitions within the chromene moieties. The **SP** extinctions below 300 nm increase in the order from compound **1** to compound **3** (Figure 1).

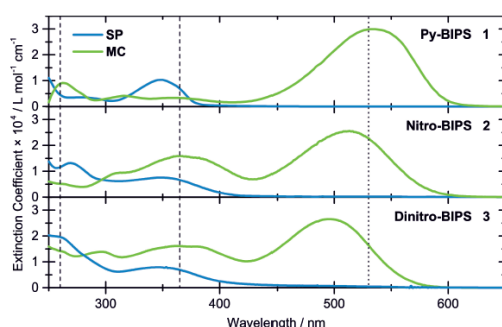


Figure 1. Steady-state absorption spectra of both photoisomers **SP** (black lines) and **MC** (red lines) of compound **1** (upper panel), **2** (middle panel) and **3** (lower panel). The spectra for compound **1** were taken from an RP-HPLC run in TEAA-buffer (pH 7.4) with 10% MeCN. For compounds **2** and **3**, the spectra were obtained by the published method of Hammarsen et al. (PBS buffer, pH 7.4).^[34] The dashed lines indicate the UV wavelengths (260 nm and 365 nm) applied to induce the ring-opening in steady-state experiments and the dotted line the vis wavelength (530 nm) applied for the ring-closure.

Figure 1) to induce the ring-opening reaction. The maximum fraction of **MC** of the nitro-BIPS compounds that can be accumulated is apparently higher upon 260 nm irradiation due to the increased **SP** extinction with respect to **MC**, whereas 365 nm irradiation yields a minor fraction. Concerning compound **1**, an inverse behaviour was observed as the **SP** isomer is predominantly activated at 365 nm. However, at this point it has to be noted that the compositions of the PSDs are in general severely affected by multiple effects. On the one hand the compositions are dictated by the above mentioned ratio of the **SP**/**MC** extinction coefficients ϵ and by the thermal isomerization rates on the other hand (see following sections). The equilibrium can thus be envisioned rather as photothermal than as purely photostationary. If the photo- and thermo-chromic rates affecting the PSD are comparable, the composition also depends on the incident radiation power. Apart from that, irradiation with 530 nm to induce the ring-closure yields virtually 100% **SP** for all three substances, at least if sufficient power is provided. As the **MC** absorption band in the vis range is well separated from the **SP** band, exclusively the open-ring isomer is activated.

The quantum yields of the ring opening reactions were determined following equation (1) for both UV wavelengths as well as for the ring closure reaction upon 530 nm irradiation (Table 1). Here, the quantum yield is represented by the ratio of

Table 1. Molar extinction coefficients of the S_1 absorption bands of both photoisomers of compounds 1–3 (λ_{max}), photostationary distributions (PSD) upon continuous UV irradiation as well as quantum yields Φ for the ring-opening reaction at different excitation wavelengths (260 nm, 365 nm) and for the ring-closure reaction (530 nm).							
Compound	ϵ_{SP} [L mol ⁻¹ cm ⁻¹]	ϵ_{MC} [L mol ⁻¹ cm ⁻¹]	PSD _{260 nm} ^[a] [% MC]	PSD _{365 nm} ^[b] [% MC]	$\Phi_{260 nm}$ ^[a] [%]	$\Phi_{365 nm}$ ^[b] [%]	$\Phi_{530 nm}$ ^[c] [%]
1	10340 ± 90 (348 nm)	29900 ± 300 (528 nm)	4	12	3.9 ± 0.3	2.1 ± 0.1	11.9 ± 0.1
2	7600 ± 500 (350 nm)	25600 ± 1700 (512 nm)	38	3	8.3 ± 0.6	0.3 ± 0.1	4.4 ± 0.4
3	7930 ± 60 (347 nm)	26540 ± 140 (496 nm)	36	14	4.6 ± 0.3	1.5 ± 0.2	3.4 ± 0.1

[a] The output of the 260 nm photodiode was 1.35 mW for all experiments. [b] The output of the 365 nm LED was 5.3 mW for experiments with **1** and **2** and 2.5 mW for **3**. [c] The output of the 530 nm LED was 1.7 mW for **1** and **2** and 1.2 mW for **3**.

While the **SP** isomers have virtually no absorption above 450 nm, the open-ring **MC** isomers exhibit pronounced $S_0 \rightarrow S_1$ absorption bands in the visible range from 450 nm to 600 nm. In contrast to compound **1**, the absorption properties of the **MC** isomers of nitro-BIPS **2** and dinitro-BIPS **3** are significantly altered. Both derivatives exhibit an additional $S_0 \rightarrow S_2$ absorption band, which not only superimposes with the **SP** absorption band but also exceeds its extinction in the near UV. Thus, the initiation of the ring-opening photoreaction by UV irradiation is necessarily accompanied by a simultaneous activation of the **MC** isomer to a certain degree accounting for photostationary distributions (PSD) that strongly depend on the incident wavelength (Table 1). In view of a biological application, wavelengths beyond the near UV range should be avoided since they are harmful to biomolecules and organisms.

In this study, we used two wavelengths 260 nm and 365 nm for steady-state investigations (indicated by dashed lines in

the number of molecules N that actually undergo photoisomerization upon photon absorption and the total number of photons N_i absorbed by those molecules. Further details concerning the calculation are given in the Supporting Information.

$$\phi = \frac{N}{N_i} \quad (1)$$

The quantum yield of the ring closure reaction of compound **1** is considerably higher than the value of the opening reaction, where comparable quantum yields were found for both UV wavelengths applied. In contrast to that, the quantum yield for the ring closure reactions of nitro-BIPS **2** and dinitro-BIPS **3** are significantly lower. The ring-opening of compounds **2** and **3** apparently adopts a higher quantum yield upon 260 nm irradiation since this $S_0 \rightarrow S_2$ excitation results in a more

efficient isomerization pathway than the $S_0 \rightarrow S_1$ excitation with 365 nm (see Table 1).

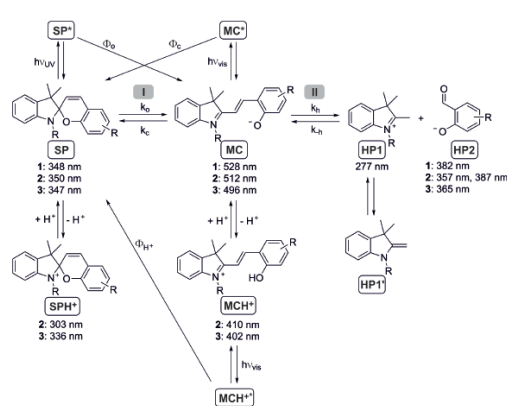
Since an increased photoresistance is of major importance for the application of photochromic compounds, the photolytic degradation properties of the three investigated substances were determined by different experimental procedures. First, the resistance towards prolonged UV irradiation was monitored photometrically in continuous illumination studies with 365 nm. In contrast to both nitro-compounds **2** and **3**, whose absorption spectra merely changed due to the hydrolytic decomposition after the PSD was accomplished (see Supporting Figure 25 and 26), compound **1** was completely decomposed within 6 hours (see Supporting Figure 24). The subsequent disappearance of the **SP** and **MC** absorption bands due to the photodegradation was accompanied by the emergence of a new absorption feature at 309 nm. By means of a MS-MS analysis of the decomposed sample a photolysis product could be identified, which appears as an indole scaffold with a carbonyl group in its 2-position and the trimethylammonium-propyl side chain still attached to the nitrogen. The formation of this species could be accomplished via addition of oxygen to a reactive open-ring intermediate which was already reported for related spiropyran compounds.^[39]

Additionally, cyclic photofatigue measurements with alternating irradiation with 365 nm and 530 nm were carried out to estimate the resistance towards repeated switching between both photoisomers (see Supporting Figures 27–29). The time-dependent evolution of the **MC** absorption band was monitored as it is regarded as a measure for the turnover of the photoreaction. Herein, a reduction of the maximum **MC** fraction was recorded for both compounds **1** and **3** throughout the measurement, resulting in a decline to half of the starting value after about 35 cycles. Concerning compound **1**, this degradation is caused by the above mentioned photolysis upon exposure to UV light, whereas the reduction of the switching amplitude of compound **3** is due to the sensitivity of the **MC** isomer of nitro-BIPS derivatives towards hydrolysis, as will be discussed in the following section. However, it has to be mentioned that the comparability of such photofatigue studies is seriously affected by the exact experimental conditions, i.e. the applied power of the LEDs and the irradiation time for each wavelength. Regarding compound **2** the acquirable turnover with a 365 nm LED was apparently small. For this reason the hydrolytic decomposition was only a minor effect and a constant value for the maximum switching amplitude with less than 3% **MC** could be maintained for more than 20 switching cycles.

Thermal Properties

Apart from their photochromic properties, spiropyran compounds also exhibit thermochromic features as the distribution of isomers depends on their relative thermodynamic stability and can therefore be shifted with varying temperatures. Additionally, even solvato- and acidochromic processes have to be considered especially in aqueous media. A summarizing overview of the possible photoinduced and thermal reaction

pathways is provided by Scheme 3. The thermal interconversion between the two isomers (equilibrium I) is accompanied



Scheme 3. Kinetic system of equilibrium reactions between **SP**, **MC**, **MCH⁺**, **SPH⁺** and the hydrolysis products (**HP1** and **HP2**) with corresponding rate constants and quantum yields of additional photoinduced reactions. The maxima of the associated major absorption bands are provided below the corresponding structures.

by the apparent drawback of the aqueous environment: the hydrolytic decomposition of **MC** due to the nucleophilic attack of water to the ethylene carbon next to the phenolate fragment (equilibrium II).^[34]

The thermal **SP/MC** equilibrium is also affected by the pH value of the solution since both isomers can be protonated, forming **SPH⁺** (pKa typically around 0.5) and **MCH⁺** (pKa typically around 3), respectively.^[34,37] The protonated merocyanine is capable of photoinduced ring-closure.^[40,41] This allows for its application as a photoacidic compound with the advantage of being resistant towards hydrolysis. Moreover, a pure **MC** sample can be generated for at least a few minutes by shifting the equilibrium completely towards **MCH⁺** (stirring at 50 °C for one hour at pH 1 after addition of HCl) followed by quick neutralization of the buffered solution with NaOH (1 M).

To evaluate the compositions of thermally equilibrated, non-irradiated mixtures in neutral solutions the interaction of the thermal equilibria I and II (Scheme 3) has to be taken into account. Thus, the contents of **SP**, **MC** and the hydrolysis products (**HP1**, **HP2**) at distinct times are dictated by the respective rate constants k_o , k_c , k_h and k_{h+} . Py-BIPS **1** appears remarkably stable towards hydrolysis, since the thermal equilibrium is mostly shifted in the direction of the closed **SP** isomer and contains less than 2% of **MC**. In this case, the values for the thermal reaction rates were determined via temperature-dependent equilibration studies. Here it has to be noted that a slightly increased hydrolysis rate at higher temperatures was neglected in the determination of the k_o and k_c values (Table 2). This yielded an lower bound for closing rate k_c which is nine times higher than upper bound of k_o . An estimate of the rate k_h was obtained from fitting the increase of the HP absorption

Table 2. Rate constants for reversible thermal isomerization processes and hydrolysis at room temperature.

Compound	k_o [s^{-1}]	k_c [s^{-1}]	k_h [s^{-1}]	k_b [s^{-1}]
1	$\sim 1 \times 10^{-5}$	$\sim 9 \times 10^{-5}$	$\sim 3 \times 10^{-7}$	$< 10^{-8}$
2	$\sim 5 \times 10^{-5}$	$\sim 8 \times 10^{-5}$	$\sim 5 \times 10^{-5}$	$\sim 4 \times 10^{-6}$
3	$\sim 4 \times 10^{-5}$	$< 10^{-7}$	$\sim 1 \times 10^{-4}$	$\sim 1 \times 10^{-5}$

band at 400 nm exponentially (see Supporting Figure 31). In comparison to k_o and k_c , the rate of hydrolytic decomposition k_h is two orders of magnitude smaller, while the upper limit of the back reaction rate k_b is suggested to be another order of magnitude lower. By means of a photometric long-term measurement of a sample that was kept in the dark, a degradation half-life time of the SP absorption band of more than 30 weeks was determined.

Unlike compound **1**, the hydrolytic decomposition of compounds **2** and **3** is significantly accelerated due to a decreasing stability of the MC isomers towards hydrolysis as well as an increased amount of MC that is established thermally in buffered solution. In order to unravel the thermal reaction rates of both Nitro-BIPS derivatives, the time-dependent evolution of the concentration of the open-ring MC was monitored, starting from a pure SP sample. As a freshly prepared solution of dinitro-BIPS **3** consists of MC exclusively, the sample had to be pre-irradiated by vis-light to yield a SP sample, which was afterwards allowed to equilibrate in the dark. The detected time-courses revealed an initial rise of the corresponding absorption band due to the accumulation of MC yielding a temporary maximum fraction of approximately 26% for nitro-BIPS **2** and dinitro-BIPS **3** within 4.5 hours (see Supporting Figure 31). This is followed by a subsequent decay caused by hydrolytic decomposition of the emerging open-ring isomer which affords a final equilibrium containing 8% MC for compound **2** and 12% for compound **3**.

Hence, the recorded trace is modeled by the biexponential function $y(t)$ shown in equation 2, where k_{rise} and k_{decay} comprise the interaction of the four thermal rate constants k_o , k_c , k_h , and k_b given in Scheme 3.

$$y(t) = y_0 + A_1 e^{-k_{rise} t} - A_2 e^{-k_{decay} t} \quad (2)$$

From fitting the obtained datasets biexponentially, the values for the particular thermal reaction rates of the kinetic system were derived via application of the Laplace transform method (Table 2).^[42] In order to apply this method, a kinetic model was assumed that treats the formation of MC from the hydrolysis products as a first order reaction. This causes the inaccuracy of the k_b values being represented as unimolecular rate constants although the respective reaction is apparently second order. As opposed to compound **1**, the k_c/k_o ratio is significantly reduced from 5 to approximately 1.6 for compound **2** and is close to zero for compound **3** since the thermal ring closure is drastically decelerated in the latter case. Instead, the hydrolysis rates k_h are noticeably increased by two orders of magnitude compared to **1**, where the value for compound **3**

is even twice as high as for **2**. The fact that the thermal rate for the reverse reaction k_b of **3** is on a similar scale as k_h justifies the increased fraction of MC in the final equilibrium.

Fluorescence Properties

Apart from their exceptional photochromic features, spiropyran compounds or rather their open-ring MC isomers are known to fluoresce.^[43,44] Therefore, the emission properties of the three investigated BIPS derivatives were monitored by means of excitation wavelength-dependent fluorescence contour plots (Figure 2) that were measured under identical experimental conditions.

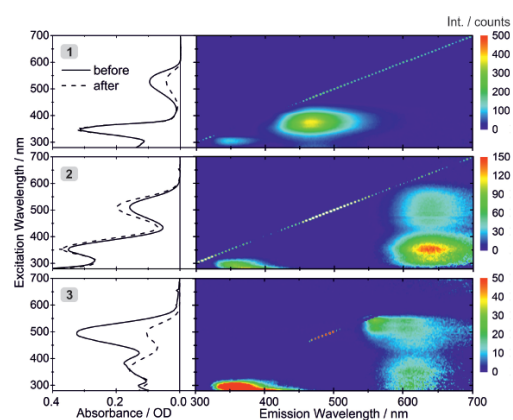


Figure 2. Corrected excitation wavelength-dependent fluorescence contour plots of compound **1** (upper panel), **2** (middle panel) and **3** (lower panel). The absorption spectra of the samples before and after the measurements are attached on the left.

The excitation started at 280 nm and the wavelengths were increased up to 700 nm in 5 nm steps. Moreover, the absorption spectra attached to the contour plots reveal the composition of the measured samples before and after the experiments which take up to 1.5 hours. Concerning compound **1** and **2**, the samples were pre-irradiated with 365 nm to obtain distributions containing both SP and MC. As to derivative **3**, a freshly prepared pure MC sample was measured. During the measurement time, the sample compositions change due to thermal equilibration and because of the fact that the varying excitation supposedly induces photoisomerization processes.

The two-dimensional fluorescence plots of the nitro-BIPS compounds **2** and **3** display emission signals from 580 nm to 700 nm and between 550 nm and 680 nm, respectively, that can be ascribed to fluorescence of the MC isomers. The overall emission intensity of nitro-BIPS **2** is significantly higher than of dinitro-BIPS **3**. Obviously, an excitation in the S_1 absorption band in the visible range yields fluorescence emission just as S_2 excitation in the near UV where the latter is apparently more

effective for compound **2**. Moreover, the emission signal of nitro-BIPS **2** upon excitation between 430 nm and 580 nm is rather unstructured and blurred while the corresponding signal for compound **3** exhibits distinguishable maxima. In contrast to an excitation in the hypsochromic edge of the steady-state S_1 absorption band, which apparently results in a weak emission signal at 610 nm, an excitation in the bathochromic edge yields an even more pronounced emission at 565 nm. This points to a selective excitation of different MC isomers, that are present in solution and adopt varying relaxation pathway properties (see following sections).

Regarding the fluorescence spectra, again a fundamental discrepancy between the Py-BIPS derivative **1** and the nitro-BIPS derivatives **2** and **3** is observed. Interestingly, the contour plot of compound **1** reveals an emission signal maximizing at 470 nm that cannot be ascribed to the MC photoisomer. This might be assigned to the SP isomer since the emission signal represents the mirror image of the S_1 absorption band of the closed form. This would imply a Stokes shift of 122 nm for the suggested SP emission. The assignment to the SP isomer was furthermore verified by measurement of the fluorescence of the salicylaldehyde precursor (compound **5**, Scheme 2) which afforded a similar emission signal at 470 nm (see Supporting Information Figure 32). The fluorescence of the MC isomer of Py-BIPS **1** is not observable in the contour plot, although a significant fraction of MC was present in the sample. Nevertheless, a very weak emission of the open-ring isomer at 630 nm was detected in a separate experiment upon excitation at 520 nm.

The additional emission signal around 360 nm upon excitation with 300 nm which is present in all of the two-dimensional fluorescence plots, is suggested to correspond to one of the hydrolysis products (HP), because the signal gained intensity with increasing time. Thus, the emission properties of the indolium HP1 (Scheme 3) were tested but no distinct fluorescence could be observed. Only after addition of NaOH (1 M) – in order to generate HP1' – the very same intense fluorescence emission at 360 nm was detected (see Supporting Information Figure 33).

Transient Absorption Measurements

Py-BIPS 1

Time-resolved pump/probe measurements in the visible range have been performed in PBS-buffered solution on the femto-second to nanosecond timescale in order to shed light on the ultrafast photodynamics triggered upon excitation of the SP or MC isomer. The obtained transient absorption (TA) spectra for both photoisomerizations of compound **1** are collected in Figure 3 A,C. The datasets were subjected to a global lifetime analysis (GLA) routine that is based on fitting the TA data with a sum of exponential decay functions to determine contributing rate constants. The GLA results in decay associated spectra (DAS) that display the wavelength dependent amplitudes of the ascertained lifetimes τ (Figure 3B,D).^[45,46]

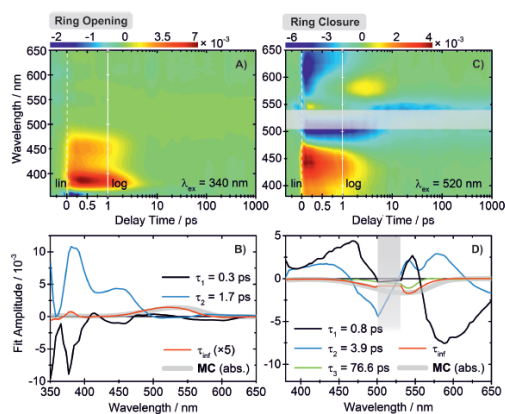


Figure 3. A) Transient absorption spectrum of the ring-opening reaction of compound **1** upon excitation with 340 nm and B) corresponding DAS. C) Transient absorption spectrum of the ring-closing reaction with D) related DAS. The gray bars indicate the wavelength range that was excluded from the kinetic analysis due to increased scattering around the excitation wavelength. Delay time zero (0 ps) and the change from linear to logarithmic scale (1 ps) are marked by white lines.

The transient map of the ring-opening reaction (Figure 3A) exhibits two pronounced excited state absorption (ESA) signals at 380 nm and 450 nm, which refer to transitions from the SP S_1 (^1SP) state into particular higher excited S_n states. Additionally, the ground state absorption of the emerging merocyanine photoproduct is observable in the transient map from 1 ps onward as a slight positive absorption difference signal around 520 nm which is retained until the end of the measured time span.

According to the kinetic analysis, three time constants were required to describe the dynamics adequately as shown in the related DAS (Fig. 3B). The fast time constant $\tau_1 = 0.3$ ps reflects vibrational cooling processes in the excited singlet state of the closed-ring isomer as it captures the spectral shift of the ESA signals towards shorter wavelengths. Since the decay of both ESA signals is modeled by the positive amplitude of $\tau_2 = 1.7$ ps between 360 nm and 500 nm, this time constant is ascribed to the lifetime of the ^1SP state.

The weakly negative amplitude of τ_2 between 500 nm and 550 nm monitors the increase of the MC ground state absorption, which is also apparent from the residual absorption after 1 ns that is reflected by τ_{inf} . On account of this, a direct transition from the S_1 state of the closed-ring SP into the ground state of the opened MC structure is suggested via a conical intersection (CI) where the potential energy surfaces of both geometries are degenerate. Starting from the CI also a repopulation of the spiropyran ground state occurs rather efficiently since the quantum yield of the ring opening was estimated to be only around 3%. Interestingly, the maximum of the amplitude of τ_{inf} is shifted hypsochromically with respect to the steady-state spectrum, indicating that further *cis/trans* isomerizations in the MC ground state structure occur on

longer timescales yielding the final spectrum. These results coincide well with the photodynamics suggested for a previously investigated Py-BIPS derivative, where a time constant of 1.6 ps was found for the opening reaction.^[38] This includes, that the effect of the varied substituent on the indoline moiety does not affect the photodynamics significantly. Moreover, similar dynamic properties were reported for the original BIPS compound in organic solvents.^[12]

Concerning the ring-closure reaction it should generally be noted, that at least two different MC ground state structures have to be taken into account that contribute to the spectral envelope of the MC steady-state absorption spectrum. Depending on the separating energy barriers they can interconvert thermally. The most stable and prevailing configuration was found to be MC-TTC, followed by -TTT whereat the exact ratio of their amounts present in solution is dictated by the nature of the solvent (and the substitution pattern).^[23,47,48] These multiple isomers can therefore be excited in parallel and are suggested to undergo different photodynamics.

The TA spectrum of the ring-closure reaction (Figure 3C) is dominated by a ground state bleach (GSB) signal around 520 nm, a stimulated emission (SE) feature at 620 nm and three ESA signals. The most pronounced ESA features below 480 nm as well as the signal at 545 nm evolve directly after excitation whereas the third positive signal at 575 nm appears delayed and reaches its maximum after 3 ps. At this point it remains unclear whether the two minor ESA signals actually appear separately or they represent one positive signal but are superimposed with the surrounding strong negative features.

Following the lifetime analysis of the dataset, four time constants were extracted to describe the observed photodynamics (Figure 3D). The decay of the broad ESA feature below 480 nm is captured by $\tau_1 = 0.8$ ps over the whole corresponding spectral range whereas the constant $\tau_2 = 3.9$ ps models a slower contribution below 465 nm which results in a hypsochromic shift of the respective ESA-band. Between 465 nm and 500 nm, the positive amplitude of τ_1 is to be regarded as an increase of the negative GSB. The decrease of the ESA signal at 550 nm is also reflected by τ_1 where this positive absorption difference evolves into a negative one, characterized by τ_2 . As τ_1 also models the bathochromic shift of the SE signal above 560 nm, this time constant is assigned to vibrational relaxation within the MC S_1 state. Besides the decrease of the SE, the negative amplitude of τ_1 also describes the emergence of the ESA at 575 nm, whereas the decay of this signal is reflected by τ_2 . Since τ_2 obviously captures the decay of the characteristic features associated to the S_1 state, it is ascribed to the respective lifetime. The third constant $\tau_3 = 76.6$ ps exhibits a similar amplitude as the infinite time constant and reflects the decrease of the remaining bleach of the MC ground state. However, the blue shift of the GSB after 100 ps as well as the slightly negative amplitude of τ_3 around 600 nm, indicating the emergence of a positive feature at late delay times, could hint at the occurrence of isomerization processes in the excited MC state or upon the before mentioned excitation of different MC isomers whose photodynamics may proceed on different timescales. Basically, it has to be assumed

that the ring-closure occurs via an intermediate MC species adopting a certain kind of *cisoid*-structure (supposedly TCC) which is formed in its excited state via different isomerization sequences upon excitation.

Since the formation of the ring-closed SP photoproduct could not be observed directly in the vis-probe experiment also a vis-pump/IR-probe measurement was executed (Figure 4 A)

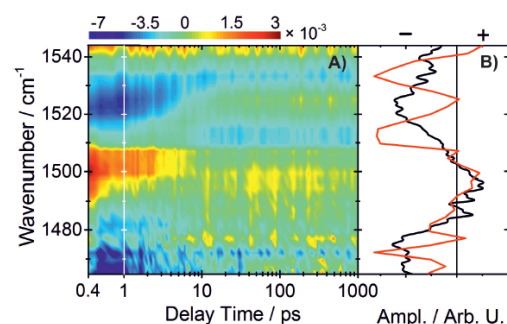


Figure 4. A) Transient absorption spectrum of the ring-closure reaction of compound 1 upon excitation with 520 nm obtained from an IR-probe experiment. B) Comparison of the scaled amplitudes of the time slice after 1 ns (red line) and a steady-state FTIR difference spectrum (black line).

in order to assess vibrational modes of SP. The obtained transient map exhibits negative absorption difference signals at 1535 cm^{-1} , 1510 cm^{-1} and at 1470 cm^{-1} representing bleached vibrational modes of the excited open-ring isomer. At early delay times, the spectrum is dominated by spectrally shifting features that reveal vibrational cooling processes. Following the kinetic analysis, two fast time constants $\tau_1 = 1.5$ ps and $\tau_2 = 4.4$ ps were determined to model the vibrational relaxation processes.

The emergence of the closed SP structure was identified by the positive signal at 1500 cm^{-1} evolving with the time constant $\tau_3 = 30$ ps. This vibrational mode was ascertained by means of a FT-IR difference spectrum of the closing reaction (Figure 4B, black line) that adopts a similar positive amplitude as the time slice of the TA spectrum after 1 ns (Figure 4B, red line).

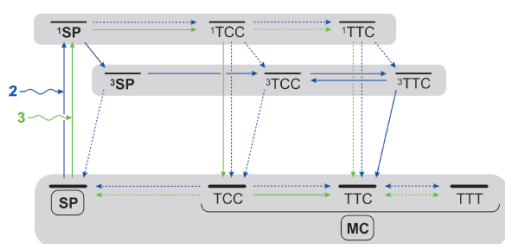
Though, at higher wavenumbers there are considerable differences between both spectra in Figure 4b, since the FT-IR difference spectrum exhibits a negative amplitude above 1505 cm^{-1} whereas a bipartite negative band with an intermittent slightly positive feature at 1525 cm^{-1} is present after 1 ns. As this arising positive band is not assigned to SP, since it is not modelled by τ_3 , this observation provides another indication for the presence of multiple MC isomers that undergo varying isomerization pathways. Hence, a particular MC isomer already accomplishes ring-closure with the time constant τ_3 , while another MC isomer would be formed short time after excitation which either subsequently proceeds towards the closed form on longer timescales or relaxes back

into the merocyanine ground state. The emergence of the associated feature at 1525 cm^{-1} would therefore be a result of the superposition with the broad initial negative signal that vanishes after 10 ps. It should also be noted that eventually a **MC** isomer is activated that is not capable of photoinduced ring-closure at all but merely re-establishes a stable **MC** conformation. Furthermore, the ring-closure of the open-ring *cisoid* precursor is supposed to be accomplished through the ground state potential energy surface (PES). According to theoretical investigations the energy barrier is significantly smaller than in the excited state.^[27,48] This could reason that a similar time-constant for ring-closure was not observed in the *vis*-probe measurement. Additionally, also the interconversion between different **MC** isomers prior to the ring-closure could occur on the ground state level.

Nitro-BIPS 2 and dinitro-BIPS 3

State of the art. The photodynamics of nitro- as well as dinitro-BIPS derivatives have been investigated extensively in various organic solvents but not yet in aqueous solution. In previous studies there is a general agreement about the contribution of triplet states to the ring-opening reaction pathway of 6-nitro-BIPS compounds since the attachment of a nitro-group enhances the intersystem crossing (ISC) rates significantly.^[11,24,47–52] Though, the assignment of the suggested excited states and the extracted mechanistic models were not unequivocal, also because the photodynamics may be drastically altered in different solvents.^[53]

The reported findings concerning the ring-opening reaction of nitro-BIPS and dinitro-BIPS-related derivatives are summarized in a schematic overview of suggested pathways (Scheme 4). A basic mechanism is assumed that includes at



Scheme 4. Comparison of estimated reaction pathways in the ring opening reaction of nitro-BIPS derivatives (**2**, blue) and dinitro-BIPS derivatives (**3**, green). The solid arrows represent dominant pathway and the dashed arrows display possible side reaction pathways including relaxation via radiative emission or internal conversion.

least two detectable **MC** species that are formed within the first nanosecond upon relaxation of the promoted ^1SP state. The cleavage of the $\text{C}_{\text{spiro}}\text{-O}$ -bond gives rise to an initial *cisoid*-merocyanine which still adopts a **SP**-like perpendicular structure but unfolds subsequently via internal rotation.^[11,24,50]

According to TD-DFT calculations, this open-ring transition state is structurally related to the **TCC** isomer, although the exact geometry might differ slightly in the excited state.^[48] Furthermore, the **TCC** species is regarded as the precursor of the second observed isomer which is preferentially the most stable conformation **TTC**. This isomer may further interconvert into other stable ground-state structures such as the slightly less stable **TTT** on expanded timescales.

As to nitro-BIPS compounds (Scheme 4, blue arrows), the ring-opening itself can be accomplished throughout the singlet or the triplet manifold, where the latter possibility is supposed to be the dominant pathway. Here, an initial ISC at the ring-closed structure is required which results in the population of a short-lived ^3SP state. The existence of a **SP** triplet state was proven indirectly by means of cryo-phosphorescence experiments.^[24] Starting from the transient **TCC** species, one or even more **MC** intermediates with partial *trans*-geometry (mainly **MC-TTC**) can be formed also via singlet or triplet route. The estimated triplet pathway for the ring-opening following Scheme 4 (blue solid arrows) is favoured, where an equilibrium between the triplet states ^3TCC and ^3TTC is suggested.^[11,24] ISC transitions from the energetically higher singlet manifold towards the triplet energy surface could also occur at the **TCC** as well as the **TTC** geometry. Moreover, both of them may yield ground state configurations via internal rotation, although the unstable **TCC** isomer is assumed to undergo ring-closure rather than *cis/trans* isomerization. At this point it has to be mentioned, that also other isomerization sequences are reasonable, like a primary isomerization around the central double bond upon ring-opening yielding **CTC** which converts into **TTC**. Though, this pathway is rather unlikely due to significantly higher barriers.^[48]

Regarding dinitro-BIPS derivatives, again a mechanism is assumed, that involves a *cisoid* intermediate (**MC-TCC**) that may proceed towards multiple possible ground state structures – preferably the energetically most favorable **TTC** (Scheme 4, green arrows).^[10] The $\text{TCC} \rightarrow \text{TTC}$ isomerization is suggested to occur preferably from a vibrationally hot TCC^* on the electronic ground state level, although it is not clear yet whether this state is populated from the relaxation of a ^1TCC state or directly from the ^1SP state via conical intersection. Although indications were found that are consistent with a triplet route similar to nitro-BIPS compounds, this pathway was excluded for dinitro-derivatives since significantly shorter time constants were determined.

Experimental results. We performed femtosecond time-resolved UV-pump/*vis*-probe studies to evaluate similarities and differences in the photodynamics of compound **2** and **3** in aqueous PBS buffered solution. The recorded TA spectra and the related DAS of the ring-opening reaction are depicted in Figure 5, whereat the comparison of the transient maps instantly reveals several conatural absorption difference features. In accordance to previous findings, prominent ESA signals in the range from 390 nm to nearly 500 nm are monitored, that persist until the end of the measured time window for both compounds. Moreover, these positive features spectrally shift with increasing time and their progression is

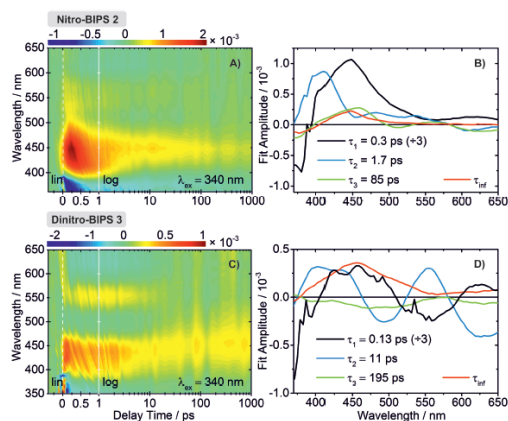


Figure 5. A) Transient absorption spectra of the ring-opening reaction upon excitation of the SP isomer with 340 nm of compound **2** and B) corresponding DAS. C) Transient absorption spectra of compound **3** and D) associated DAS.

obviously affected by multiple contributing time constants, which is also apparent from the related DAS (Figure 5B,D).

The associated transients (Figure 6) indicate, that the decay of the broad ESA band at 450 nm of **3** proceeds similarly but

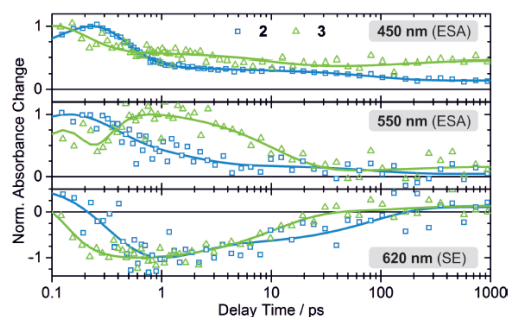


Figure 6. Comparison of particular transients found in the ring-opening reactions of compounds **2** (blue) and **3** (green). The obtained data points are represented by squares (**2**) and triangles (**3**) and the fit is indicated by solid lines.

faster than that of **2**, also because the transient of **2** initially rises and reaches its maximum amplitude a few hundred femtoseconds after excitation. In both cases a rapid initial intensity decrease of these ESA signals just as their blue shift is modeled by the ultrafast time constants τ_1 . Therefore, those time constants are presumably related to vibrational cooling processes in the ^1SP states. While τ_1 of compound **2** captures a depletion of positive signals on the entire spectral range above 400 nm, the corresponding τ_1 of compound **3** adopts a

negative amplitude between 510 nm and 600 nm. This indicates the population of a particular state correlated to the ESA signal around 550 nm that is clearly delayed, as illustrated by the associated transient (Figure 6). Supposedly, the respective signature is attributed to the emergence of an initial open-ring merocyanine (TCC, Scheme 4) in its excited state. If a vibrationally hot ground state configuration would be responsible for this ESA signal, it would rather blue shift with increasing time and its absorption maximum would evolve into the steady-state MC spectrum.

Regarding compound **2**, a similar transient at 550 nm is displayed, although the corresponding feature is formed earlier. In contrast to derivative **3**, where the successive decay of the ESA at 550 nm is modeled only by $\tau_2 = 11$ ps, the decay of the ESA of compound **2** is captured by two time constants $\tau_2 = 1.7$ ps and $\tau_3 = 85$ ps (Fig. 5B), just as the evolution of the ESA band at 450 nm. This hints at the contribution of two discriminable excited state species.

In organic solvents, similar transients around 450 nm were detected in nitro- and dinitro-BIPS studies, which were assigned to a *cisoid* MC species (TCC, Scheme 4). In contrast to dinitro-BIPS, where this transient decays on the ps timescale (e.g. 34 ps in chloroform)^[10], the corresponding ESA of nitro-BIPS is rather long-lived and decays in the ns to μs range^[50] (e.g. 8 μs in acetonitrile)^[11]. In the latter case, the signal is ascribed to the triplet state of the open-ring intermediate, since its rise as well as its decay are effectively quenched in oxygen-saturated solution.^[11,24] The assigned absorption spectrum of this triplet species exhibits another minor band at 550 nm and is suspected to be overlaid by the spectrum of the short-lived ^3SP precursor. At later delay times, the difference absorption features are superimposed with the emerging positive absorption bands of a vibrationally hot MC-TTC isomer around 400 nm and 500–600 nm.

Since our observations concerning compound **2** coincide quite well with the reported spectral characteristics of the suggested triplet pathway (Scheme 4), the most probable explanation is the ultrafast formation of a ^3SP state with the time constant τ_2 that converts into a longer-lived triplet MC state (^3TCC) modeled by τ_3 . The absence of any fluorescent emission from the ^1SP state renders an ultrafast ISC into the triplet manifold fairly plausible. This mechanism further implies that the triplet lifetime τ_3 of the intermediate ^3TCC is essentially shortened by some orders of magnitude in aqueous solution. An acceleration of the triplet decay was already reported for increasing solvent polarities.^[11]

Another mechanism that should be regarded for compound **2** is the singlet pathway for the ring-opening step via direct transition from the ^1SP state into an excited ^1TTC state that further evolves into the corresponding triplet state with the time constant τ_2 . The latter possibility would explain the contribution of the time constant τ_2 to the decay of the negative SE signal above 580 nm, as stimulated emission is supposed to occur from a singlet MC state exclusively. However, for both compounds it cannot be ruled out that the observed negative signals above 580 nm as well as the minor negative features around 500 nm could arise from the SE and

the GSB of small amounts of MC that are present in the measured sample, respectively. This is supported by analogous negative signals that are detected in the ring-closure experiments upon excitation of MC (Figure 7 A,C).

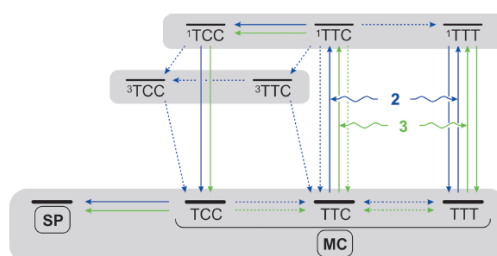
Concerning compound **3**, the similar ESA bands around 450 nm and 550 nm also hint at the formation of an excited TCC intermediate. The associated time constant τ_2 adopts a sinusoidal amplitude and is in good agreement with the time constant ascribed to the ^3TCC triplet state of compound **2**. Therefore, the assumption of an accelerated triplet pathway cannot be ruled out at this point, although the ring-opening of dinitro compounds is supposed to occur only via singlet route.^[10] Relaxation of the ^1TCC state is supposed to yield a vibrationally hot TTC^* state that proceeds towards the TTC isomer in its ground state. The formation of the TTC ground state could be monitored by the time constant $\tau_3 = 195$ ps, since the negative amplitude between 400 nm and 550 nm reflects the MC steady-state spectrum quite good. Though, the increase of absorption above 580 nm captured by τ_3 eventually signifies the population of an excited TTC isomer or even additional excited species. The residual absorption after 1 ns is revealed by τ_{inf} , which also exhibits a shoulder around 500 nm, that could correspond to the ground state absorption of the TTC isomer of compound **3**. Besides that, the infinite time constants of both compounds exhibit similar maxima around 450 nm, indicating the emergence of analogous configurations on longer timescales.

Nitro-BIPS 2 and Dinitro-BIPS 3 – Ring-Closure.

State of the art. The mechanism of the photoinduced ring-closure of nitro- and dinitro-BIPS derivatives is rather complex, just as the ring-opening pathway, since multiple different MC species and isomerizations have to be taken into account. The triplet pathway is again suggested to contribute to the overall dynamics of nitro-BIPS, since a ^3TTC state was found that adopted the same time constant as upon excitation of SP.^[11,24] However, the triplet route was regarded as a minor side reaction and a pathway on the singlet PES was claimed to be the dominant pathway.^[48]

Again, at least two MC isomers have to be considered that are present in solution and adopt different ring-closure pathways (Scheme 5). For nitro-BIPS compounds, the diverging photodynamics of particular isomers (TTC and TTT) were distinguished by time-resolved measurements employing spectrally varying excitation pulses within the MC steady-state absorption band. Hence, different MC ground-state structures could be addressed preferentially.^[26,47,54]

The absorption band of the TTT isomer is found in the red edge of the steady-state MC absorption band while the TTC absorption dominates the blue region. It was claimed, that in acetonitrile there are three competing decay channels for the mainly excited short-lived TTC isomer of nitro-BIPS within the first nanosecond.^[54] First, a relaxation into the ground state via radiative emission could occur. Second, a partial conversion into the longer-lived MC-TTT was identified by an evolving positive absorption feature around 600 nm and the observation



Scheme 5. Comparison of estimated reaction pathways in the ring-closure reaction of nitro-BIPS derivatives (**2**, blue) and dinitro-BIPS derivatives (**3**, green). The solid arrows represent dominant pathways and the dashed arrows display possible side reaction pathways including relaxation via radiative emission or internal conversion.

of coherent vibrational modes. The reverse $\text{TTT} \rightarrow \text{TTC}$ isomerization was excluded though and the main channel for relaxation of the ^1TTT state is claimed to be fluorescent emission.^[26] The third decay channel is the formation of another isomer – supposedly TCC – in its excited state that proceeds towards the ring-closed SP. This intermediate species was also detected in toluene where it was ascribed to an absorption band around 650 nm.^[47] For nitro-BIPS derivatives only the TTC isomer is suggested to be capable of photoinduced ring-closure.

Furthermore, theoretical studies revealed the TCC intermediate as the precursor of the ring-closed SP, which verifies the assignment as the third detected species. The ring-closure itself is suggested to occur on the ground state PES, as this pathway benefits from the smallest activation energy barrier.^[48]

Concerning dinitro-BIPS, TTC and TTT can be thermally interconverted in their ground states whereas an excited-state equilibration between them was ruled out, due to a considerable barrier separating the isomers.^[22,55] Nevertheless, both isomers are supposed to be capable of ring-closure following different singlet pathways, although the TTT isomer is suggested to preferably relax back into its ground state. In a first step, the excited MC-TTC is expected to convert into TCC. Afterwards the ring-closure is accomplished on the ground-state PES yielding SP.^[10,48] As to the ring-closing reaction of the TTT isomer, an initial isomerization around the central double bond seems to be more likely.^[55] This results in the TCT isomer which can then be interconverted into the SP precursor TCC.

Experimental results. For our ultrafast time-resolved investigations of the ring-closure of compounds **2** and **3** (Figure 7), the pump wavelength was tuned to 520 nm. This is approximately in the center of the MC absorption band of compound **2** and slightly shifted towards the red edge for compound **3**. Hence, the simultaneous excitation of multiple MC isomers has to be assumed, although the photochemistry of TTC should dominate the observed dynamics.

As revealed by the transient maps (Figure 7 A,C), the only positive signals observed, refer to ESA of the ^1TTC state, eventually superimposed with that of the ^1TTT state. Moreover,

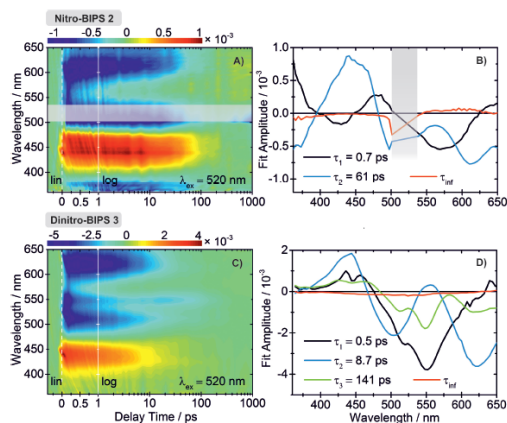


Figure 7. A) Transient absorption spectrum of the ring-closure reaction upon excitation of the MC isomer with 520 nm of compound **2** and B) corresponding DAS. C) Transient absorption spectrum of compound **3** and D) associated DAS.

both spectra exhibit pronounced negative SE features above 580 nm and GSB signals around 500 nm to 550 nm. Regarding compound **2**, the wavelength range from 505 nm to 530 nm had to be excluded from the kinetic analysis due to scattered light from the pump-pulses. This was not necessary for the measurement of compound **3**. However, the overall dynamics of compound **3** appears to be accelerated compared to that of compound **2**, which is also evident from selected transients (Figure 8).

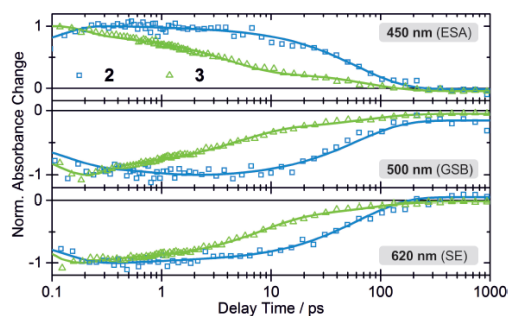


Figure 8. Comparison of particular transients found in the ring-closure reactions of compounds **2** (orange) and **3** (purple). The obtained datapoints are represented by squares (**2**) and triangles (**3**) and the estimated fit is indicated by solid lines.

According to the GLA of the ring-closure reaction of nitro-BIPS **2**, three time constants were determined (Figure 7b). The fastest $\tau_1 = 0.7$ ps reflects a spectral shift of all signals associated with the first excited state and is therefore assigned

to vibrational cooling processes in ^1TTC . The decay of the respective ESA, GSB and SE signals is reflected by the lifetime $\tau_2 = 61$ ps. After 100 ps the absorption difference above 550 nm increases again which is captured by τ_{ref} additionally. This hints at the formation of further MC isomers, where two possible decay channels of ^1TTC could be suggested – the conversion into ^1TTT as well as the population of an excited ^1TCC state (Scheme 5). The emergence of an isomer in its ground-state is not likely since the corresponding absorption band would be too redshifted with respect to the steady-state spectra.

Concerning dinitro-BIPS **3**, the assumption of a simultaneous excitation of at least TTC and TTT is supported by the peculiar GSB signal of derivative **3** whose two minima at 500 nm and 550 nm indicate the contributions of two isomers. In the kinetic analysis, again an ultrafast time constant $\tau_1 = 0.5$ ps was determined that supposedly models vibrational cooling in the excited singlet state. Moreover, the progression of the observed dynamics is apparently affected by multiple processes. The decay of the bleach signal around 500 nm is mainly captured by $\tau_2 = 8.7$ ps whereas the decay of the 550 nm signal is modelled by the slower component $\tau_3 = 141$ ps. Additionally, the decay of the ESA and the SE signal is described by both of the time constants. These results are again quite conform to the reported findings for dinitro derivatives in organic solvents. In chloroform a time constant of 98 ps is assigned to the TTC isomer, while the decay of the excited TTT is modelled by a significantly slower constant of 830 ps.^[10] Therefore, we ascribe the faster time constant τ_2 that is determined herein, to the lifetime of the ^1TTC state and the slower τ_3 to the ^1TTT state. However, the formation of the ring-closed photoproduct was not observed in the transient maps, since its ground state absorption below 400 nm is absent for both compounds.

By reason of the herein observed photodynamics and the suggested distinguishable relaxation pathways of the TTC and the TTT isomer of the nitro-BIPS derivatives **2** and **3** (Scheme 5), also the before mentioned fluorescence properties can be explained in more detail (Figure 2). Apparently, compound **2** emits fluorescence around 640 nm, whether the sample is excited in the near-UV or in the vis range. In contrast, vis excitation of compound **3** yields a structured emission signal with two maxima whereas near-UV excitation exclusively yields emission at 610 nm. Concerning nitro-BIPS **2**, this hints at a relaxation on the excited state PES upon vertical excitation with near-UV light that proceeds without a significant barrier towards the emitting state. As to dinitro-BIPS **3**, supposedly there is a considerable barrier that can only be overcome if enough energy is supplied. Unlike reported findings in organic solvents^[47,54,56], clearly discriminable emission signals corresponding to different MC isomers of **2** could not be observed in aqueous solution, although at least the two isomers TTC and TTT are suggested to be present. However, the emission signal upon S_1 excitation exhibits a slight red shift with increasing excitation wavelength which is assumed to favor excitation of the TTT isomer. The obtained blurred signal is probably caused by a partial excited state interconversion of the isomers,



crucially different fluorescence quantum yields or particular Stokes-shifts that result in superimposed emission signals.

Regarding the fluorescence plot of compound **3**, there are two distinguishable emission maxima observable around 560 nm and 610 nm upon excitation in the S_1 band. This indicates separate fluorescence signals from the two isomers TTC and TTT that are suggested to be present in solution. The signal around 560 nm is assigned to the TTT isomer, since it emerges upon excitation in the red edge of the steady-state absorption band whereas the signal at 610 nm is related to TTC. Furthermore, the higher intensity of the TTT emission confirms the assumption of a preferred relaxation into its ground state.

Conclusion

Spiropyran and especially nitro-derivatives have been successfully used for various applications in biological and material studies. Since we are interested in using spiropyran as small ligands for riboswitches we studied the photochemistry of the most promising derivatives nitro-BIPS, dinitro-BIPS as well as Py-BIPS. We investigated their photoisomerization properties in terms of steady state as well ultrafast dynamic characterizations. Each of the three investigated water-soluble spiropyran derivatives exhibit reversible photochromic properties in PBS buffered solution, although there is a substantial difference between Py-BIPS **1** and the nitro-BIPS compounds **2** and **3**. We could show that **1** exhibited high water solubility, thermal stability, virtually no hydrolysis and ultrafast reaction pathways for both isomerization directions that include singlet states only. Additionally compound **1** show the most beneficial switching amplitude upon 365 nm irradiation which is harmless and therefore useful for biological application. In contrast to that, the nitro-BIPS compounds show higher switching amplitudes upon 260 nm excitation and the merocyanine is decomposed hydrolytically. A remarkable feature of **2** and **3** was their stability towards photolysis. Though, they adopted an isomerization pathway including triplet states which are eventually critical for potential application, due to possible side reaction caused by their reactivity.

To summarize our findings, all the studied compounds showed many particular advantages for use in biological applications that could be combined to create advanced spiropyran photoswitches. In general, it is necessary to characterize the photochromic properties adequately in view of future applications. Therefore spiropyran provide numerous advantages compared to other photoswitches like azobenzenes or fulgides, although their behavior in aqueous solution is rather complex to understand and accompanied by certain drawbacks.

Supporting Information Summary

The supporting information provides an experimental section where all procedures concerning the spectroscopic steady-state as well as time-resolved measurements are explained and the employed equipment is listed. Furthermore, the synthetic

routes and all corresponding NMR spectra of the synthesized compounds are included. Additionally, the determination of the quantum yields of photoinduced reactions, photodegradation and -fatigue measurements as well as thermal and fluorescence properties are depicted.

Acknowledgements

We thank the Deutsche Forschungsgemeinschaft (DFG) for funding through SFB 902 "Molecular Principles of RNA-based Regulation".

Conflict of Interest

The authors declare no conflict of interest.

Keywords: fluorescence · kinetics · photochromism · spiro compounds · time-resolved spectroscopy

- [1] H. M. D. Bandara, S. C. Burdette, *Chem. Soc. Rev.* **2012**, *41*, 1809–1825.
- [2] J. Broichhagen, J. A. Frank, D. Trauner, *Acc. Chem. Res.* **2015**, *48*, 1947–1960.
- [3] L. Laprell, E. Repak, V. Franckevicius, F. Hartrampf, J. Terhag, M. Hollmann, M. Sumser, N. Rebola, D. A. DiGregorio, D. Trauner, *Nat. Commun.* **2015**, *6*, 1–11.
- [4] R. Göstl, A. Senf, S. Hecht, *Chem. Soc. Rev.* **2014**, *43*, 1982–1996.
- [5] S. Steinwand, T. Halbritter, D. Rastädter, J. M. Ortiz-Sánchez, I. Burghardt, A. Heckel, J. Wachtveitl, *Chem. - Eur. J.* **2015**, *21*, 15720–15731.
- [6] M. Stein, S. J. Middendorp, V. Carta, E. Pejo, D. E. Raines, S. A. Forman, E. Sigel, D. Trauner, *Angew. Chem. Int. Ed.* **2012**, *51*, 10500–10504.
- [7] J. Wachtveitl, T. Nägele, B. Puell, W. Zinth, M. Krüger, S. Rudolph-Böhner, D. Oesterheld, L. Moroder, *J. Photochem. Photobiol. Chem.* **1997**, *105*, 283–288.
- [8] H. Satzger, S. Spörlein, C. Root, J. Wachtveitl, W. Zinth, P. Gilch, *Chem. Phys. Lett.* **2003**, *372*, 216–223.
- [9] V. I. Minkin, *Chem. Rev.* **2004**, *104*, 2751–2776.
- [10] J. Buback, M. Kullmann, F. Langhojer, P. Nürnberg, R. Schmidt, F. Würthner, T. Brixner, *J. Am. Chem. Soc.* **2010**, *132*, 16510–16519.
- [11] H. Görner, *Phys. Chem. Chem. Phys.* **2001**, *3*, 416–423.
- [12] N. P. Ernstring, T. Arthen-Engeland, *J. Phys. Chem.* **1991**, *95*, 5502–5509.
- [13] M. Irie, Diarylethenes for Memories and Switches, *Chem. Rev.* **2000**, *100*, 1685–1716.
- [14] Y. Yokoyama, Y. Kurita, *Mol. Cryst. Liq. Cryst. Sci. Technol. Sect. Mol. Cryst. Liq. Cryst.* **1994**, *246*, 87–94.
- [15] S. Draxler, T. Brust, S. Malkmus, J. A. DiGirolamo, W. J. Lees, W. Zinth, M. Braun, *Phys. Chem. Chem. Phys.* **2009**, *11*, 5019–5027.
- [16] C. Slavov, N. Bellakbil, J. Wahl, K. Mayer, K. Rück-Braun, I. Burghardt, J. Wachtveitl, M. Braun, *Phys. Chem. Chem. Phys.* **2015**, *17*, 14045–14053.
- [17] B. Heinz, S. Malkmus, S. Laimgruber, S. Dietrich, C. Schulz, K. Rück-Braun, M. Braun, W. Zinth, P. Gilch, *J. Am. Chem. Soc.* **2007**, *129*, 8577–8584.
- [18] C. Slavov, C. Boumriřak, C. A. Hammer, P. Trojanowski, X. Chen, W. J. Lees, J. Wachtveitl, M. Braun, *Phys. Chem. Chem. Phys.* **2016**, *18*, 10289–10296.
- [19] R. Klajn, *Chem. Soc. Rev.* **2014**, *43*, 148–184.
- [20] D. Davis, A. Hamilton, J. Yang, L. D. Cremer, D. Van Gough, S. L. Potisek, M. T. Ong, P. V. Braun, T. J. Martinez, S. R. White, J. S. Moore, N. R. Sottos, *Nature* **2009**, *459*, 68–72.
- [21] T. Sendai, S. Biswas, T. Aida, *J. Am. Chem. Soc.* **2013**, *135*, 11509–11512.
- [22] M. Kullmann, S. Ruetzel, J. Buback, P. Nürnberg, T. Brixner, *J. Am. Chem. Soc.* **2011**, *133*, 13074–13080.
- [23] J. Hobbey, V. Malatesta, R. Millini, L. Montanari, Jr. W. O. Neil Parker, *Phys. Chem. Chem. Phys.* **1999**, *1*, 3259–3267.
- [24] A. K. Chibisov, H. Görner, *J. Phys. Chem.* **1997**, *101*, 4305–4312.
- [25] I. Gómez, M. Reguero, M. A. Robb, *J. Phys. Chem. A* **2006**, *110*, 3986–3991.
- [26] C. Walter, S. Ruetzel, M. Diekmann, P. Nürnberg, T. Brixner, B. Engels, *J. Chem. Phys.* **2014**, *140*, 224311.



- [27] S. Prager, I. Burghardt, A. Dreuw, *J. Phys. Chem. A* **2014**, *118*, 1339–1349.
- [28] D. D. Young, A. Deiters, *ChemBioChem* **2008**, *9*, 1225–1228.
- [29] C. Brieke, A. Heckel, *Chem. - Eur. J.* **2013**, *19*, 15726–15734.
- [30] M. Bälter, M. Hammarson, P. Remón, S. Li, N. Gale, T. Brown, J. Andréasson, *J. Am. Chem. Soc.* **2015**, *137*, 2444–2447.
- [31] J. Andersson, S. Li, P. Lincoln, J. Andréasson, *J. Am. Chem. Soc.* **2008**, *130*, 11836–11837.
- [32] A. Koçer, M. Walko, B. L. Feringa, *Nat. Protoc.* **2007**, *2*, 1426–1437.
- [33] T. Stafforst, D. Hilvert, *Chem. Commun. Camb. Engl.* **2009**, 287–288.
- [34] M. Hammarson, J. R. Nilsson, S. Li, T. Beke-Somfai, J. Andréasson, *J. Phys. Chem. B* **2013**, *117*, 13561–13571.
- [35] D. Movia, A. Prina-Mello, Y. Volkov, S. Giordani, *Chem. Res. Toxicol.* **2010**, *23*, 1459–1466.
- [36] H.-A. Wagenknecht, C. Beyer, *Synlett* **2010**, *9*, 1371–1376.
- [37] C. Özçoban, T. Halbritter, S. Steinwand, L. M. Herzig, J. Kohl-Landgraf, N. Askari, F. Groher, B. Fürtig, C. Richter, H. Schwalbe, B. Süß, J. Wachtveitl, A. Heckel, *Org. Lett.* **2015**, *17*, 1517–1520.
- [38] J. Kohl-Landgraf, M. Braun, C. Özçoban, D. P. N. Gonçalves, A. Heckel, J. Wachtveitl, *J. Am. Chem. Soc.* **2012**, *134*, 14070–14077.
- [39] R. Demadrille, A. Rabourdin, M. Campredon, G. Giusti, *J. Photochem. Photobiol. Chem.* **2004**, *168*, 143–152.
- [40] L. A. Tatum, J. T. Foy, I. Arahamian, *J. Am. Chem. Soc.* **2014**, *136*, 17438–17441.
- [41] N. Abeyrathna, Y. Liao, *J. Am. Chem. Soc.* **2015**, *99*, 1–3.
- [42] J. Andraos, *J. Chem. Educ.* **1999**, *76*, 1578–1583.
- [43] K. Horie, K. Hirao, I. Mita, Y. Takubo, T. Okamoto, M. Washio, S. Tagawa, Y. Tabata, *Chem. Phys. Lett.* **1985**, *6*, 499–502.
- [44] L. Wu, Y. Dai, X. Jiang, C. Petchprayoon, J. E. Lee, T. Jiang, Y. Yan, G. Marriott, *PLoS ONE* **2013**, *8*, 6–13.
- [45] I. H. M. Van Stokkum, D. S. Larsen, R. Van Grondelle, *Biochim. Biophys. Acta - Bioenerg.* **2004**, *1657*, 82–104.
- [46] C. Slavov, H. Hartmann, J. Wachtveitl, *Anal. Chem.* **2015**, *87*, 2328–2336.
- [47] C. J. Wohl, D. Kuciauskas, *J. Phys. Chem. B* **2005**, *109*, 22186–22191.
- [48] Y. Sheng, J. Leszczynski, A. A. Garcia, R. Rosario, D. Gust, J. Springer, *J. Phys. Chem. B* **2004**, *108*, 16233–16243.
- [49] S. A. Krysanov, M. V. Alfimov, *Chem. Phys. Lett.* **1982**, *91*, 77–80.
- [50] C. Lenoble, R. S. Becker, *J. Phys. Chem.* **1986**, *90*, 62–65.
- [51] A. K. Holm, O. F. Mohammed, M. Rini, E. Mukhtar, E. T. J. Nibbering, H. Fidder, *J. Phys. Chem. A* **2005**, *109*, 8962–8968.
- [52] A.-K. Holm, M. Rini, E. T. J. Nibbering, H. Fidder, *Chem. Phys. Lett.* **2003**, *376*, 214–219.
- [53] A. K. Holm, O. F. Mohammed, M. Rini, E. Mukhtar, E. T. J. Nibbering, H. Fidder, *J. Phys. Chem.* **2005**, *109*, 8962–8968.
- [54] S. Ruetzel, M. Diekmann, P. Nürnberger, C. Walter, B. Engels, T. Brixner, *J. Chem. Phys.* **2014**, *140*, 224310.
- [55] J. Buback, P. Nürnberger, M. Kullmann, F. Langhojer, R. Schmidt, F. Würthner, T. Brixner, *J. Phys. Chem. A* **2011**, *115*, 3924–3935.
- [56] S. Ruetzel, M. Diekmann, P. Nürnberger, C. Walter, B. Engels, T. Brixner, *Proc. Natl. Acad. Sci.* **2014**, *111*, 4764–4769.

Submitted: April 24, 2017

Accepted: May 3, 2017

7.3 Halbritter et al., *J. Org. Chem.* 2017, 82

Reference [II]

Pyridine-Spiropyran Derivative as a Persistent, Reversible Photoacid in Water

T. Halbritter*, C. Kaiser*, J. Wachtveitl, A. Heckel,

J. Org. Chem. **2017**, *82*, 8040-8047.

(DOI: 10.1021/acs.joc.7b01268)

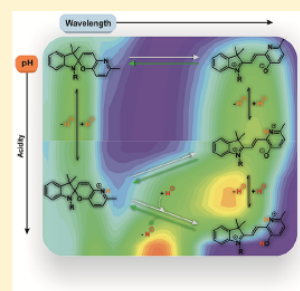
Pyridine–Spiropyran Derivative as a Persistent, Reversible Photoacid in Water

Thomas Halbritter,^{†,§} Christoph Kaiser,^{‡,§} Josef Wachtveitl,^{*,†,§} and Alexander Heckel^{*,†,§}

[†]Institute for Organic Chemistry and Chemical Biology and [‡]Institute for Physical and Theoretical Chemistry, Goethe University Frankfurt, Max-von-Laue-Strasse 7, 60438 Frankfurt (M), Germany

Supporting Information

ABSTRACT: A highly versatile water-soluble pyridine–spiropyran photoswitch is reported which functions as photoacid in a wide pH range. Under neutral conditions, the open-ring merocyanine (MC[−]) exists to 48% and closes quantitatively by irradiation with visible light, while the reverse reaction occurs rapidly in the dark or by irradiation at 340 nm. The different pK_a of the pyridine nitrogen in the closed spiropyran (4.8) and open merocyanine form (6.8) leads to a reversible proton release in a pH range of 3–7. Only negligible hydrolytic decomposition was observed in the pH range from 1 to 12. The application of potentially harmful UV light can be circumvented due to the fast thermal ring-opening except for pH values below 3. Its photoacidic properties make this compound an effective pH-regulating photoswitch in water and enable controlled proton-transfer processes for diverse applications. Additionally, all of the involved protonated states of the compound exhibit discriminative fluorescence features within certain pH ranges, which even expands its utility to a light-controllable, pH-sensitive fluorophore.



1. INTRODUCTION

Proton-transfer reactions are of fundamental importance in nature and can be used to regulate chemical reactivity,^{1–3} photochemical features,^{4–6} biological functions,^{7–9} as well as material properties.^{10,11} Photoacidic compounds release a proton upon optical excitation and can be used to control protonations and deprotonations. With commercially available technology, light as an external trigger can be applied with high precision of location, timing, and dosage.^{12–18} Possible side reactions can be minimized if the wavelengths for operation are cleverly chosen. Recently, we have shown that even processes triggered by near-UV light are possible in living mice.¹⁹

In recent years, effective reversible photoacids have become the focus of current research. Molecular motors,^{20–22} memory hydrogels,^{23,24} as well as acid-catalyzed reactions²⁵ are only a few research areas where photoacids are studied.

In the majority of examples, “photoacid” refers to a compound where the electronically excited state has a lower pK_a compared to the ground state.^{26,27} Therefore, the duration of the proton release is correlated with the lifetime of the excited species. Typically, after pico- to nanoseconds the proton reassociates. Thus, the liberated proton is too short-lived to catalyze a chemical process or to alter a macroscopic property.

Reversible photoswitches are compounds that exist in two photoisomeric states that can be interconverted by light of different wavelengths. In some cases, the isomerization in one of the directions can occur thermally. If the process is fast enough, this can even be an advantage in cases where this isomerization direction would involve UV light or leads to photodegradation.

The two isomeric states can have different acidic properties. In such a case, the proton transfer effect is as persistent as the stability of the photoisomers. There are only very few examples in which such types of persistent photoacids have been shown to work in water (and are hence compatible with biological applications): In a seminal study, Liao et al. presented a “long-lived photoacid” using a spiropyran/merocyanine photoswitch (1, Scheme 1a).^{28,29} They achieved a light-induced pH shift from 5.5 to 3.3 in water. In a follow-up study in which the term “metastable-state photoacid” was used they presented a new system (2, Scheme 1b) that could also operate in a more neutral pH range.³⁰ After light irradiation, the pH of an unbuffered aqueous solution (with 10% DMSO) shifted from 6.0 to 4.3. The process was thermally reversible in the dark over the course of 8–48 h.

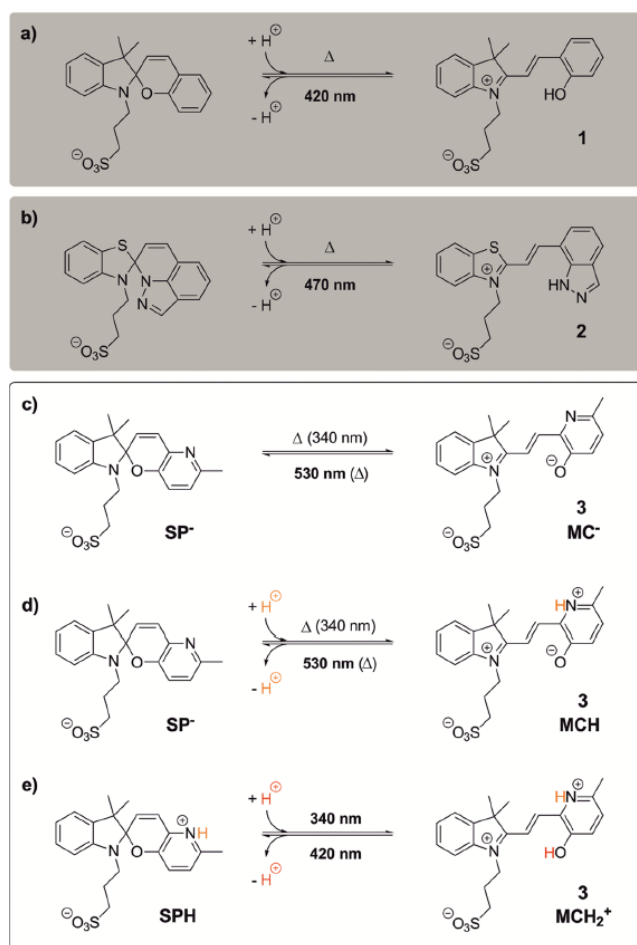
For example, Klajn et al. used the approach of long-lived spiropyran photoacids for the light-controlled self-assembly of nanoparticles.¹⁰ Aprahamian et al. used spiropyran 1 for the proton-induced switching of a hydrazone-based actuator in methanol.³¹

In general, spiropyran are very interesting photoswitches for diverse applications because the two photoisomers differ strongly in many properties, such as, for example, dipole moment and structure.^{32–34} They can be switched reversibly between the closed-ring, nonpolar spiropyran (SP) structure and the open-ring merocyanine (MC), which adopts a zwitterionic or a quinoidal mesomeric resonance structure.

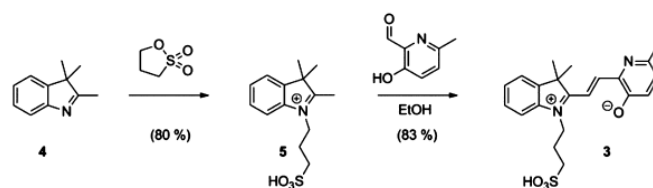
Received: May 23, 2017

Published: July 7, 2017

Scheme 1. (a, b) Metastable-State Photoacids 1 and 2, Respectively, Used in Previous Studies.^{28,30} (c–e) Isomerization Reactions of the Spiropyran/Merocyanine Compound 3 of This Study at pH 7–12 (c), pH 3–7 (d), and pH 1–3 (e)



Scheme 2. Overview of the Synthesis of the Water-Soluble Spiropyran Photoacid 3



Here, it has to be considered that merocyanines can exist as an equilibrium of different *cis-trans* isomers due to the central chain of three double bonds. The TTC (*trans-trans-cis*) isomer is supposed to be the most stable conformation and therefore dominates the visible absorption band of MC.^{35,36}

In many studies, “nitro-BIPS” is used which has an additional nitro group in *para* position of the phenolic OH group in compound 1.^{34,37–40} However, despite its frequent use, the

photochemical properties are suboptimal.⁴¹ We had previously shown that “Py-BIPS”, a spiropyran derivative with a methylpyridinium ring, has many favorable properties. These include, for example, a singlet-only photoswitching mechanism and a high solubility of 28 mM in PBS buffer.^{12–14}

For this study we wondered if the nonmethylated Py-BIPS derivative 3 (Scheme 1c–e) could also photoswitch and found that it functions as a metastable-state photoacid with properties

which are better than the ones of previous examples. The sulfonic acid side chain was installed for water solubility. The compound can exist in five photochromic states depending on the pH value (Scheme 1c–e).

2. RESULTS AND DISCUSSION

Synthesis of Photoacid 3. Scheme 2 depicts the synthetic route for photoacid 3 starting from 2,3,3-trimethylindoline which was alkylated with 1,3-propane sultone followed by an aldol condensation with the corresponding salicylic aldehyde. The obtained merocyanine derivative exhibits a high solubility (10 mM) at pH 7.4 in PBS buffer.

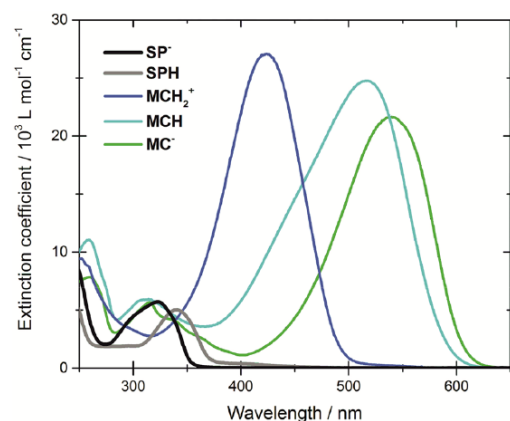


Figure 1. Pure absorption spectra in aqueous medium of the compounds shown in Scheme 1c–e.

Ground-State Properties of Photoacid 3 at Constant pH Values. The ground-state properties as well as the spectroscopic characteristics of compound 3 differ from most common spiropyran derivatives^{12,14,42} since the thermal

equilibrium is substantially shifted to the open-ring form. Even in the solid state, photoacid 3 exists as dark purple merocyanine crystals. Dissolving photoacid 3 in aqueous PBS buffer (pH 7.4) results in an initially pure MC^- sample with a pronounced absorption band at 540 nm (Scheme 1c and Figure 1). The fraction of the open-ring isomer starts to decline due to the thermal equilibration in buffered solution. The MC^- concentration drops from 100% to 48% at pH 7.4 within a few minutes ($k_{close} = 0.32 \text{ min}^{-1}$), and this equilibrium is stable over several days (see Supporting Figure 5), unlike with other spiropyrans in aqueous conditions^{42–44} (for a graphical overview of the (photo)switching properties, see Figure 3e). At pH 7–12, both isomers of photoacid 3 (SP^- and MC^-), however, remain relatively stable. Only in a pH range above 12 does the open-ring form hydrolyze. A freshly prepared solution of photoacid 3 at pH 5.5 leads to a sample consisting mostly of MCH , which bears a proton on its pyridine nitrogen (Scheme 1d) and adopts a major absorption band with a maximum at 515 nm (see Figure 1). From titration experiments, a pK_a value of this protonation step of 6.8 could be estimated. The initial sample composition in this pH regime changes rapidly from 100% to 70% of the MCH isomer ($k_{close} = 0.17 \text{ min}^{-1}$, see also Figure 5c).

At a pH of approximately 4.8, the pyridine nitrogen of the closed-ring isomer gets protonated, resulting in an absorption band at 340 nm assigned to SPH . Below pH 3, an additional absorption band with a maximum at 420 nm emerges that can be assigned to MCH_2^+ (Scheme 1e and Figure 1). When dissolved at a pH of 1, the solution remains a pure solution of MCH_2^+ .

A summarizing overview of the pH-dependent isomers that were detected by the titration experiment and the corresponding reaction pathways is provided in Figure 2. The detected absorption signals assigned to the open-ring isomers are likely a superposition of multiple *cis-trans* isomers that could additionally possess slightly different pK_a values.

Photoswitching and Fluorescence Properties of Photoacid 3 at Constant pH. All of the open-ring species

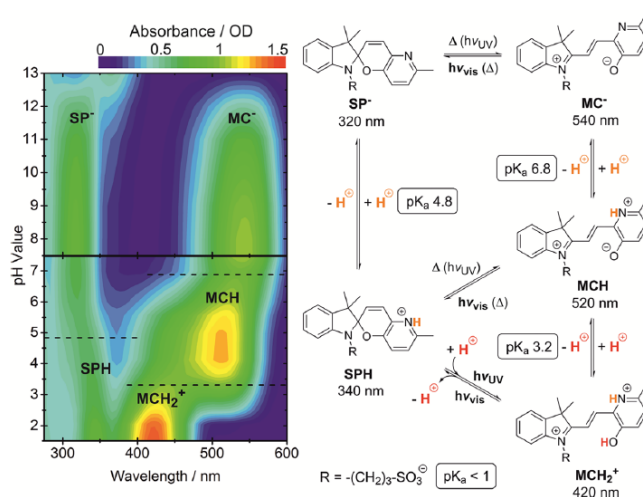


Figure 2. pH-dependent absorption spectra of photoacid 3 obtained from a titration experiment.

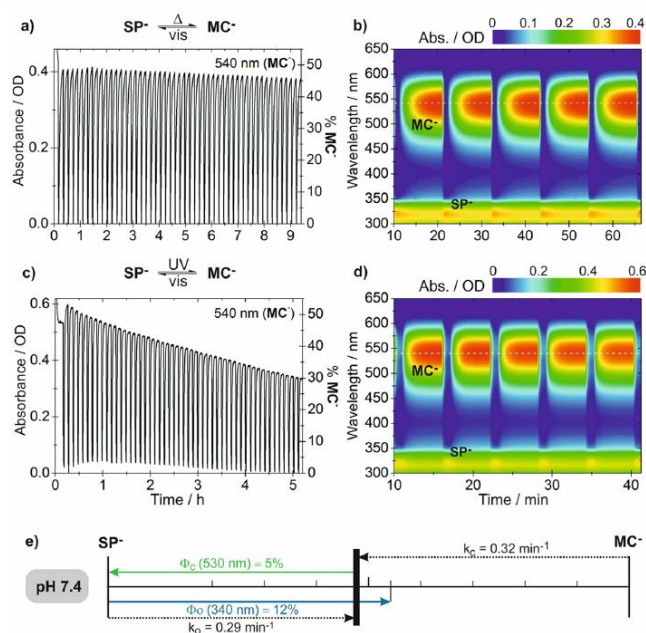


Figure 3. Reversible switching cycles of photoacid 3 in PBS buffer (pH 7.4). (a, b) Irradiation with 530 nm for 1 min (7.3 mW), then 15 min reaction in the dark. (c, d) Irradiation with 530 nm for 1 min (7.3 mW), then with 340 nm for 5 min (0.6 mW). (e) Graphical overview of the (photo)switching properties of photoacid 3 at pH 7.4.

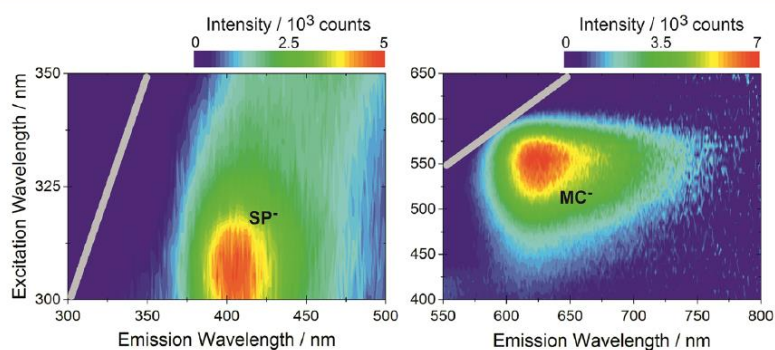


Figure 4. Excitation wavelength-dependent fluorescence contour plots of SP^- (left, $\Phi_f = 3.1\%$) and MC^- (right, $\Phi_f = 8.9\%$) of compound 3 at pH 7.4.

are capable of photoisomerization. Therefore, we studied their photochromic behavior at first under different but constant pH conditions. Irradiation at a pH of 7.4 with 530 nm converts the MC^- isomer quantitatively to the SP^- isomer with a quantum yield of $\Phi_{close} = 5\%$. From the pure SP^- state, isomerization was possible either thermally within minutes (Figure 3a,b, $k_{open} = 0.29 \text{ min}^{-1}$) or by irradiation at 340 nm (Figure 3c,d, $\Phi_{open} = 12\%$). In the former case, photoacid 3 is highly stable over 50 switching cycles. In the latter case, the initial photostationary state contained slightly more MC^- than the thermal equilibrium. However, a gradual photodegradation was observed over the switching cycles. For a graphical overview of the switching behavior, see Figure 3e.

Spiropyran derivatives are known for their fluorescence properties in the open-ring form.^{45–47} Figure 4 shows the fluorescence signals of the SP^- and the MC^- isomers at pH 7.4. The open-ring MC^- has an emission maximum at 625 nm while the ring-closed SP^- fluoresces around 405 nm. The latter is attributed to the pyridine fragment of the molecule.

At a pH of 5.5, a similar photochromic behavior was observed. After irradiation with 530 nm, a quantitative ring-closing reaction to SP^- is detectable ($\Phi_{close} = 7\%$). The ring-opening reaction again occurs thermally and rapidly in the dark, producing the protonated MCH (Figure 5a,b, $k_{open} = 0.22 \text{ min}^{-1}$). The ring-opening reaction was also initiated by irradiation with UV light at 340 nm at pH 5.5 (Figure 5c,d,

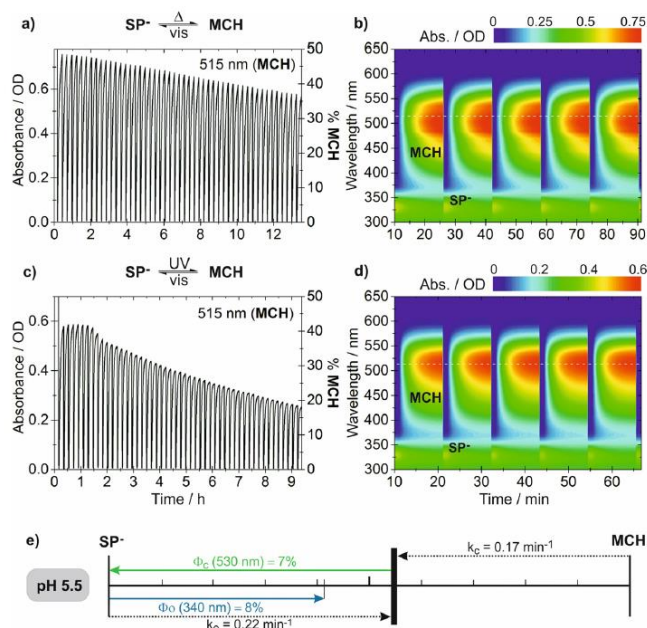


Figure 5. Reversible switching cycles of photoacid 3 in PBS buffer (pH 5.5). (a, b) Irradiation with 530 nm for 5 min (7.3 mW), then 15 min reaction in the dark. (c, d) Irradiation with 530 nm for 5 min (8.5 mW), then with 340 nm for 10 min (0.6 mW). (e) Graphical overview of the (photo)switching properties of photoacid 3 at pH 5.5.

$\Phi_{\text{open}} = 8\%$). The photostationary state contained slightly less MCH than the thermal equilibrium. Photodegradation over 50 cycles was slightly more pronounced compared to pH 7.4.

In a pH range between approximately 5 and 7, the interconversion occurs between MCH and SP^- as depicted in Figure 2. If the solvent acidity increases to pH 3–5, the ring-closed isomer exists in its protonated SPH state. The respective open-ring species also exhibits a fluorescence emission at 610 nm (Figure 6) that is slightly blue-shifted in comparison to MC^- at pH 7.4. The peculiar shape of the observed emission signal with its two maxima hints at the presence of different conformational MCH isomers adopting inherent fluorescent properties.

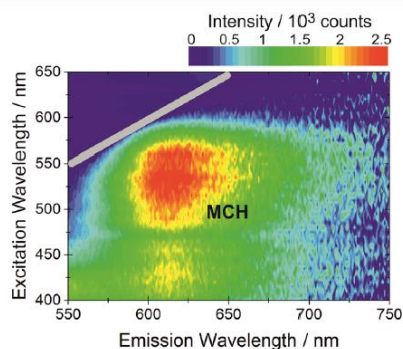


Figure 6. Excitation wavelength-dependent fluorescence contour plot of MCH ($\Phi_f = 3.5\%$) of compound 3 at pH 5.5.

After compound 3 is dissolved at pH 1, MCH_2^+ is initially formed quantitatively and remains if the sample is not exposed to visible light. Furthermore, MCH_2^+ appears to be thermally stable toward hydrolysis. After irradiation at 420 nm, SPH is formed with an absorbance maximum of 340 nm ($\Phi_{\text{close}} = 10\%$) and can be reversibly switched back to the open merocyanine form by irradiation at 310 nm (Figure 7, $\Phi_{\text{open}} = 11\%$, no thermal opening rate detected).

Compared to MC^- and MCH, this second protonation step accounts for a substantially blue-shifted fluorescence signal of MCH_2^+ around 470 nm (Figure 8).

pH Switching Behavior of Photoacid 3. As mentioned previously, the $\text{p}K_a$ of the pyridine nitrogen of compound 3 changes from 4.8 in the closed form to 6.8 in the open form. This should allow for a photoreversible release of a proton, switching between the two photoisomers. As an example, we prepared a $100 \mu\text{M}$ solution of compound 3 in $0.01\times$ PBS (step 1 in Figure 9) and adjusted the starting pH to ca. 6.8 or 5.5 (green and red curve in Figure 9, respectively) with 0.1 M NaOH. Then the solution was irradiated at 530 nm (5 min, 8.5 mW) and left in the dark. These steps were repeated, and the resulting end pH values obtained are shown in Figure 9. pH jumps of 0.6–0.7 units were obtained in every step under these conditions. Then a saturated solution of compound 3 was treated similarly after the initial pH was adjusted to 6.8. In these experiments, a pH jump of 1.5 was obtained. In all cases, a reversible switching performance was observed, and the starting pH value was recovered within 15 min.

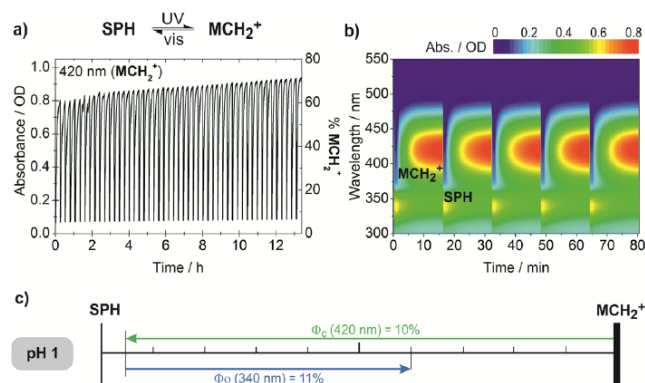


Figure 7. Reversible switching cycles of photoacid 3 in PBS buffer (pH 1). (a) Irradiation with 420 nm for 1 min (11.7 mW), then with 340 nm for 15 min (0.6 mW). (c) Graphical overview of the (photo)switching properties of photoacid 3 at pH 1.

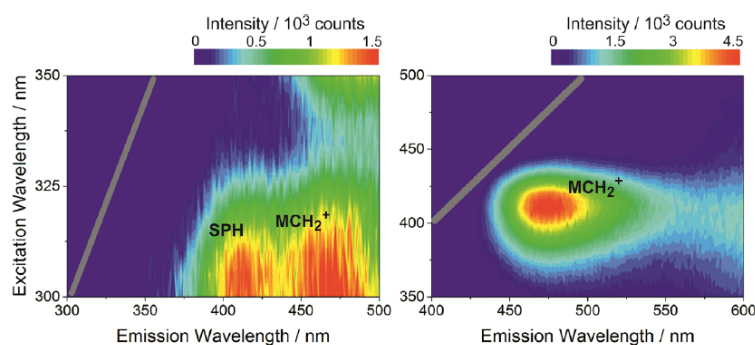


Figure 8. Excitation wavelength-dependent fluorescence contour plot of SPH (left, Φ_f = 2.5%) and MCH₂⁺ (right, Φ_f = 4.5%) of compound 3 at pH 1.

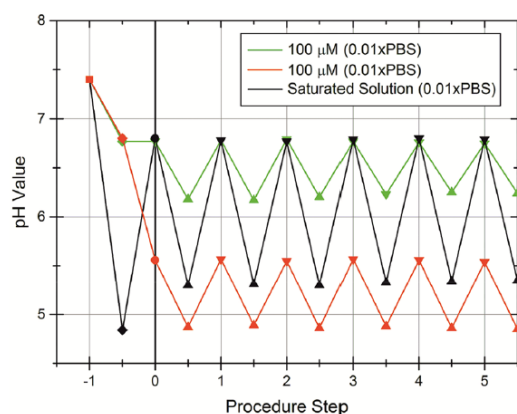


Figure 9. pH regulation experiments with photoacid 3. Key: squares, initial pH value of buffer; diamonds, pH after dissolving compound 3; circles, after addition of HCl or NaOH to adjust pH; down triangles, pH value upon irradiation with 530 nm (5 min); up triangles, pH recovered thermally in the dark (15 min).

3. CONCLUSION

The pH jump that can be obtained is determined by several factors. For a simulation of the effect of different properties on the maximally obtainable pH jump, see Supporting Figures 6–9. In general, the pH jump will become negligible with decreasing starting pH since then the maximally liberated amount of protons will become negligible compared to the one already available in solution. Toward basic starting conditions, the maximally obtainable pH jump will be determined by the difference of the acidic pK_a of MCH and SPH, respectively. A higher concentration of photoacid will lead to a higher pH jump, but the effect levels off. All of these effects will be reduced if the switching amplitude of the photoacid is reduced or, trivially, if buffer salts are present. The acidic pK_a of MCH₂⁺ will only play a role at very high concentrations of photoacid 3 or would play a more pronounced role if it were closer to the one of SPH.

In the case of compound 3, the solubility in water is very high (10 mM). With the three pK_a values being as they are, the actually obtained pH jump behavior is dominated by the ΔpK_a on the pyridine nitrogen. The jumps are relatively high and fully reversible as compound 3—unlike other spiroopyrans—is surprisingly stable toward hydrolysis. Our photoacid can be operated in a comparably broad pH range. This characteristic can be used for a time-resolved and locally controlled

protonation in chemical reactions for biomedical applications, polymerization reactions, and material sciences. Compared to other spiropryan compounds, the switching amplitude is quite high. This can be a problem with spiropryan if they are to be photoswitched in water. Andréasson and Pischel et al. had solved this problem for example applying supramolecular complexation.⁴⁸ In our system the use of UV light can be avoided due to the fast thermal ring-opening reaction. Apart from the changes in acidity the two photoisomers show distinct fluorescence properties. This photoswitchable fluorescence could make compound 3 interesting for biomedical imaging. Conversely, it is possible to use the molecule as a pH sensor, which functions in a pH range from 1 to 12 due to the different absorption and emission signals.

4. EXPERIMENTAL SECTION

Synthesis of Photoacid 3. Scheme 2 shows the synthetic route. 2,3,3-Trimethylindoline 4 (3.00 g, 18.84 mmol, 1.0 equiv) and 1,3-propane sultone (2.30 g, 18.84 mmol, 1.0 equiv) were stirred at 120 °C for 1.5 h. Methanol was added to the reaction mixture and stirred at room temperature for 30 min. Ethyl acetate and cyclohexane were added. The white precipitate was filtered and washed with ethyl acetate. The solid was dried under reduced pressure to afford 3-(2,3,3-trimethyl-3H-indol-1-ium-1-yl)propane-1-sulfonate 5 (4.25 g, 15.12 mmol, 80%) as a white solid. ¹H NMR (500 MHz, DMSO-*d*₆): δ = 8.06–8.04 (m, 1H), 7.83–7.81 (m, 1H), 7.65–7.59 (m, 2H), 4.65 (t, *J* = 8.0 Hz, 2H), 3.51 (bs, 1H), 2.83 (s, 3H), 2.62 (t, *J* = 6.6 Hz, 2H), 2.18–2.12 (m, 2H), 1.53 (s, 6H) ppm. ¹³C NMR (125 MHz, DMSO-*d*₆): δ = 196.5, 141.9, 141.2, 129.3, 129.0, 123.4, 115.5, 54.1, 47.4, 46.6, 23.8, 22.1, 13.8 ppm. ESI-MS (+): *m/z* = 282.20 [M + H]⁺. HRMS: *m/z* calcd for C₁₄H₂₀NO₃S 282.11584 [M + H]⁺, found 282.11627 (Δ*m* = 0.00043, error 1.5 ppm).

3-(2,3,3-Trimethyl-3H-indol-1-ium-1-yl)propane-1-sulfonate (2.00 g, 7.11 mmol, 1.0 equiv) was dissolved in EtOH (20 mL), and 3-hydroxy-6-methylpicolinialdehyde 3 (0.98 g, 7.11 mmol, 1.0 equiv) was added. The reaction mixture was stirred at 80 °C for 8 h. The precipitate was filtered and dried under reduced pressure to afford 3-(3,3,6'-trimethylspiro[indoline-2,2'-pyrano[3,2-*b*]pyridin]-1-yl)propane-1-sulfonic acid (2.37 g, 5.92 mmol, 83%) as a light red solid. ¹H NMR: (500 MHz, DMSO-*d*₆): δ = 8.48 (d, *J* = 15.8 Hz, 1H), 8.12–8.10 (m, 1H), 7.92 (d, *J* = 15.9 Hz, 1H), 7.89–7.88 (m, 1H), 7.67–7.63 (m, 2H), 7.40–7.36 (m, 2H), 4.75 (t, *J* = 7.7 Hz, 2H), 2.65 (t, *J* = 6.9 Hz, 2H), 2.51 (s, 3H), 2.23–2.17 (m, 2H), 1.77 (s, 6H) ppm. ¹³C NMR: (125 MHz, DMSO-*d*₆): δ = 181.6, 154.9, 150.0, 145.5, 143.6, 141.1, 136.6, 129.6, 129.2, 129.1, 126.0, 123.0, 115.6, 112.8, 52.3, 47.7, 46.3, 26.0, 24.7, 23.1 ppm. ESI-MS (+): 401.20 [M + H]⁺. HRMS: *m/z* calcd for C₂₁H₂₅N₃O₄S 401.15295 [M + H]⁺, found 401.15290 (Δ*m* = 0.00005, error 0.1 ppm). Mp: 200 °C dec.

NMR Spectra. For the characterization of the compounds were recorded on Bruker AVIII-HD 500 MHz instruments equipped with a N₂-cooled cryogenic probe head using *d*₆-DMSO as solvent. HRMS spectra were recorded using a Thermo Scientific MALDI LTQ Orbitrap (see the Supporting Information).

Photometric Measurements. The photometric studies with compound 3 were performed with either a Jena Analytik Specord S600 spectrometer or an Ocean Optics DH-mini UV-vis-NIR light source with an USB 4000 fiber spectrometer. For photoswitching experiments, the spectrophotometers were equipped with modular ThorLabs cuvette holders and mounted LEDs with wavelengths of 340, 420, and 530 nm.

pH Measurements. The pH value of the sample solutions was measured with a Mettler Toledo InLab Nano pH electrode. The light-induced pH regulation experiments were performed in 0.01× PBS buffer by use of the above-described spectrometers with ThorLabs LEDs attached.

■ ASSOCIATED CONTENT

5 Supporting Information

The Supporting Information is available free of charge on the ACS Publications website at DOI: 10.1021/acs.joc.7b01268.

¹H and ¹³C NMR spectra of compounds 5 and 3. Data for optical spectroscopy: determination of pure spectra of all particular isomers of compound 3, thermal reaction rates and stability, calculation of photoreaction as well as fluorescence quantum yields. Simulated data: calculations of maximum obtainable pH jumps in dependence of the particular p*K*_a as well as starting pH values for different sample concentrations (PDF)

■ AUTHOR INFORMATION

Corresponding Authors

*Tel: +49 (69) 798-29351. E-mail: wweilt@theochem.uni-frankfurt.

*Tel: +49 (69) 798-42505. E-mail: heckel@uni-frankfurt.de.

ORCID

Josef Wachtveitl: 0000-0002-8496-8240

Alexander Heckel: 0000-0003-3541-4548

Author Contributions

§T.H. and C.K. contributed equally.

Notes

The authors declare no competing financial interest.

■ ACKNOWLEDGMENTS

We thank the Deutsche Forschungsgemeinschaft (DFG) for funding through SFB 902 "Molecular Principles of RNA-based Regulation".

■ REFERENCES

- (1) Hsieh, C.-C.; Jiang, C.-M.; Chou, P.-T. *Acc. Chem. Res.* 2010, 43 (10), 1364–1373.
- (2) Fu, C.; Xu, J.; Boyer, C. *Chem. Commun.* 2016, 52, 7126–7129.
- (3) Cukier, R. I.; Nocera, D. G. *Annu. Rev. Phys. Chem.* 1998, 49 (1), 337–369.
- (4) Pinheiro, A. V.; Parola, A. J.; Baptista, P. V.; Lima, J. C. *J. Phys. Chem. A* 2010, 114 (49), 12795–12803.
- (5) Johns, V. K.; Peng, P.; Dejesus, J.; Wang, Z.; Liao, Y. *Chem. - Eur. J.* 2014, 20 (3), 689–692.
- (6) Xie, X.; Bakker, E. *J. Am. Chem. Soc.* 2014, 136, 7857–7860.
- (7) Ramsey, I. S.; Mokrab, Y.; Carvacho, I.; Sands, Z. a.; Sansom, M. S. P.; Clapham, D. E. *Nat. Struct. Mol. Biol.* 2010, 17 (7), 869–875.
- (8) Li, J.; Liu, Z.; Tan, C.; Guo, X.; Wang, L.; Sancar, A.; Zhong, D. *Nature* 2010, 466 (7308), 887–890.
- (9) Xie, X.; Crespo, G. A.; Mistlberger, G.; Bakker, E. *Nat. Chem.* 2014, 6 (3), 202–207.
- (10) Kundu, P. K.; Samanta, D.; Leizrowice, R.; Margulis, B.; Zhao, H.; Börner, M.; Udayabhaskararao, T.; Manna, D.; Klajn, R. *Nat. Chem.* 2015, 7 (8), 646–652.
- (11) Su, X.; Voskian, S.; Hughes, R. P.; Aprahamian, I. *Angew. Chem., Int. Ed.* 2013, 52 (41), 10734–10739.
- (12) Kohl-Landgraf, J.; Braun, M.; Özçoban, C.; Gonçalves, D. P. N.; Heckel, A.; Wachtveitl, J. *J. Am. Chem. Soc.* 2012, 134 (34), 14070–14077.
- (13) Brieke, C.; Heckel, A. *Chem. - Eur. J.* 2013, 19 (46), 15726–15734.
- (14) Özçoban, C.; Halbritter, T.; Steinwand, S.; Herzog, L.-M.; Kohl-Landgraf, J.; Askari, N.; Groher, F.; Fürtig, B.; Richter, C.; Schwalbe, H.; Suess, B.; Wachtveitl, J.; Heckel, A. *Org. Lett.* 2015, 17 (6), 1517–1520.
- (15) Göstl, R.; Senf, A.; Hecht, S. *Chem. Soc. Rev.* 2014, 43 (6), 1982–1996.

- (16) Lerch, M. M.; Hansen, M. J.; van Dam, G. M.; Szymanski, W.; Feringa, B. L. *Angew. Chem., Int. Ed.* **2016**, *55* (37), 10978–10999.
- (17) Brieke, C.; Rohrbach, F.; Gottschalk, A.; Mayer, G.; Heckel, A. *Angew. Chem., Int. Ed.* **2012**, *51* (34), 8446–8476.
- (18) Szymanski, W.; Beierle, J. M.; Kistemaker, H. A. V.; Veleva, W. A.; Feringa, B. L. *Chem. Rev.* **2013**, *113*, 6114–6178.
- (19) Lucas, T.; Schäfer, F.; Müller, P.; Eming, S. A.; Heckel, A.; Dimmeler, S. *Nat. Commun.* **2017**, *8*, 15162.
- (20) Moo, J. G. S.; Presolski, S.; Pumera, M. *ACS Nano* **2016**, *10* (3), 3543–3552.
- (21) Ray, D.; Foy, J. T.; Hughes, R. P.; Aprahamian, I. *Nat. Chem.* **2012**, *4* (9), 757–762.
- (22) Silvi, S.; Arduini, A.; Pochini, A.; Secchi, A.; Tomasulo, M.; Raymo, F. M.; Baroncini, M.; Credi, A. *J. Am. Chem. Soc.* **2007**, *129*, 13378–13379.
- (23) Feng, W.; Zhou, W.; Zhang, S.; Fan, Y.; Yasin, A.; Yang, H. *RSC Adv.* **2015**, *5* (100), 81784–81789.
- (24) Qian, H.; Aprahamian, I. *Chem. Commun.* **2015**, *51* (56), 11158–11161.
- (25) Ghosh, T.; Slanina, T.; König, B. *Chem. Sci.* **2015**, *6* (3), 2027–2034.
- (26) Förster, T. *Naturwissenschaften* **1949**, *36*, 186–187.
- (27) Ditkovich, J.; Pines, D.; Pines, E. *Phys. Chem. Chem. Phys.* **2016**, *18* (24), 16106–16115.
- (28) Shi, Z.; Peng, P.; Strohecker, D.; Liao, Y. *J. Am. Chem. Soc.* **2011**, *133*, 14699–14703.
- (29) Johns, V. K.; Wang, Z.; Li, X.; Liao, Y. *J. Phys. Chem. A* **2013**, *117* (49), 13101–13104.
- (30) Abeyrathna, N.; Liao, Y. *J. Am. Chem. Soc.* **2015**, *137*, 11282–11284.
- (31) Tatum, L. A.; Foy, J. T.; Aprahamian, I. *J. Am. Chem. Soc.* **2014**, *136*, 17438–17441.
- (32) Minkin, V. I. *Chem. Rev.* **2004**, *104* (5), 2751–2776.
- (33) Klajn, R. *Chem. Soc. Rev.* **2014**, *43* (1), 148–184.
- (34) Ernsting, N. P.; Arthen-Engeland, T. *J. Phys. Chem.* **1991**, *95* (14), 5502–5509.
- (35) Sheng, Y.; Leszczynski, J.; Garcia, A. A.; Rosario, R.; Gust, D.; Springer, J. *J. Phys. Chem. B* **2004**, *108* (41), 16233–16243.
- (36) Buback, J.; Nuemberger, P.; Kullmann, M.; Langhoyer, F.; Schmidt, R.; Würthner, F.; Brixner, T. *J. Phys. Chem. A* **2011**, *115* (16), 3924–3935.
- (37) Young, D. D.; Deiters, A. *ChemBioChem* **2008**, *9* (8), 1225–1228.
- (38) Beyer, C.; Wagenknecht, H.-A. *Synlett* **2010**, *2010*, 1371–1376.
- (39) Görner, H. *Phys. Chem. Chem. Phys.* **2001**, *3* (3), 416–423.
- (40) Kocer, A.; Walko, M.; Meijberg, W.; Feringa, B. L. *Science* **2005**, *309* (5735), 755–758.
- (41) Kaiser, C.; Halbritter, T.; Heckel, A.; Wachtveitl, J. *ChemistrySelect* **2017**, *2* (14), 4111–4123.
- (42) Hammarson, M.; Nilsson, J. R.; Li, S.; Beke-Somfai, T.; Andréasson, J. *J. Phys. Chem. B* **2013**, *117* (43), 13561–13571.
- (43) Piard, J. *J. Chem. Educ.* **2014**, *91*, 2105–2111.
- (44) Stafforst, T.; Hilvert, D. *Chem. Commun.* **2009**, *3*, 287–288.
- (45) Horie, K.; Hirao, K.; Mita, I.; Takubo, Y.; Okamoto, T.; Washio, M.; Tagawa, S.; Tabata, Y. *Chem. Phys. Lett.* **1985**, *119* (6), 499–502.
- (46) Wu, L.; Dai, Y.; Jiang, X.; Petchprayoon, C.; Lee, J. E.; Jiang, T.; Yan, Y.; Marriott, G. *PLoS One* **2013**, *8* (6), No. e64738.
- (47) Wan, S.; Zheng, Y.; Shen, J.; Yang, W.; Yin, M. *ACS Appl. Mater. Interfaces* **2014**, *6*, 19515–19519.
- (48) Nilsson, J. R.; Parente Carvalho, C.; Li, S.; Da Silva, J. P.; Andréasson, J.; Pischel, U. *ChemPhysChem* **2012**, *13* (16), 3691–3699.

7.4 Kaiser et al., *Chem. EUR. J.* 2021, 27

Reference [III]

Proton-Transfer Dynamics of Photoacidic Merocyanines in Aqueous Solution

C. Kaiser, T. Halbritter, A. Heckel, J. Wachtveitl,

Chem. Eur. J. **2021**, 27, 9160-9173

(DOI: 10.1002/chem.202100168)

Proton-Transfer Dynamics of Photoacidic Merocyanines in Aqueous Solution

Special Collection

Christoph Kaiser,^[a] Thomas Halbritter,^[b, c] Alexander Heckel,^[c] and Josef Wachtveitl^{*,[a]}

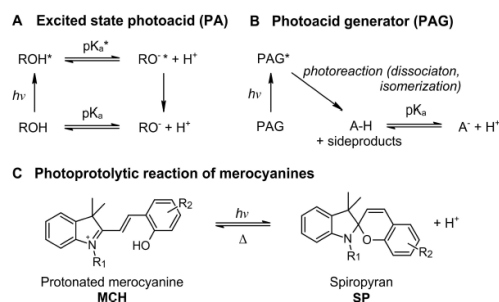
Abstract: Photoacids attract increasing scientific attention, as they are valuable tools to spatiotemporally control proton-release reactions and pH values of solutions. We present the first time-resolved spectroscopic study of the excited state and proton-release dynamics of prominent merocyanine representatives. Femtosecond transient absorption measurements of a pyridine merocyanine with two distinct protonation sites revealed dissimilar proton-release mechanisms: one site acts as a photoacid generator as its pK_a^* value is modulated in the ground state after photoisomerization,

while the other functions as an excited state photoacid which releases its proton within 1.1 ps. With a pK_a drop of 8.7 units to -5.5 upon excitation, the latter phenolic site is regarded a super-photoacid. The 6-nitro derivative exhibits only a phenolic site with similar, yet slightly less photoacidic characteristics and both compounds transfer their proton to methanol and ethanol. In contrast, for the related 6,8-dinitro compound an intramolecular proton transfer to the *ortho*-nitro group is suggested that is involved in a rapid relaxation into the ground state.

Introduction

Photoacids (PAs) turn into strong acids upon irradiation and thus enable light-stimulated proton dissociation. They steadily gain scientific attention, as they provide a convenient way to convert an optical input into a desired chemical response. If chosen properly, photoacids or photobases can in principle exert control over any proton- or pH-driven system with light as an outstanding external stimulus with unrivalled spatiotemporal precision. As a versatile trigger for proton-mediated processes, they can be exploited to regulate protein activity,^[1,2] to design photoelectric circuits^[3,4] and to advance functional materials.^[5–7]

The generic term photoacid originally refers to compounds whose acidity is significantly enhanced when promoted to their electronically excited state (Scheme 1A). This entails an ultrafast proton dissociation or rather an excited state proton transfer



Scheme 1. Generalized proton-release reaction schemes A) of excited state photoacids (PA) following the Förster cycle, and B) of photoacid generators (PAG). C) Typical proton-release reaction of merocyanine-spiropyran photo-switches.

[a] C. Kaiser, Dr. J. Wachtveitl
Institute for Physical and Theoretical Chemistry
Goethe University Frankfurt/Main
Max-von-Laue-Str. 7, 60438 Frankfurt/Main (Germany)
E-mail: wweitl@theochem.uni-frankfurt.de

[b] Dr. T. Halbritter
Current address: Department of Chemistry, Science Institute
University of Iceland
Dunhaga 3, Reykjavik postcode is missing (Iceland)

[c] Dr. T. Halbritter, Dr. A. Heckel
Institute for Organic Chemistry and Chemical Biology
Goethe University Frankfurt/Main
Max-von-Laue-Str. 7, 60438 Frankfurt/Main (Germany)

Supporting information for this article is available on the WWW under <https://doi.org/10.1002/chem.202100168>

This manuscript is part of an Indo-German special collection.

© 2021 The Authors. Chemistry - A European Journal published by Wiley-VCH GmbH. This is an open access article under the terms of the Creative Commons Attribution Non-Commercial License, which permits use, distribution and reproduction in any medium, provided the original work is properly cited and is not used for commercial purposes.

(ESPT) to the solvent. First described as Förster cycle^[8] this mechanism implies that the released proton is short-lived and reassociates thermally when the excited species relaxes back to its less acidic ground state.^[9] An essential feature of a PA is its excited state dissociation constant pK_a^* , which is correlated with the proton transfer rate. The pK_a^* can be estimated by the Förster cycle model, while the proton transfer rates are typically determined by time-resolved spectroscopic techniques. In this context, various kinds of aryl-OH compounds are among the most extensively investigated photoacids. Examples like phenol or 1-naphthol (1N) exhibit lowered but still positive pK_a^* values of 3^[10] and 0.5,^[11] respectively. In this acidity range 8-hydroxy-pyrene-1,3,6-trisulfonic acid (HPTS) also known as pyranine^[12,13] is a prominent representative with a $pK_a^* = 1.3$. The proton transfer process can take up to nanoseconds in aqueous solution for such photoacids with positive pK_a^* values. Though, photoacids that adopt negative pK_a^* values (< -1) were termed

super-photoacids^[14] and are even able to transfer their proton to alcohols within a few picoseconds. In several pioneering studies Tolbert and co-workers reported a series of 1N and 2-naphthol (2N) derivatives, where 5,8-dicyano-2-naphthol (DC2N) was found to be the strongest PA among them with a $pK_a^* = -4.5$.^[11,14–16] Further related and even more photoacidic examples are hydroxyquinolinium compounds, which adopt pK_a^* values of ~ -7 . Topp,^[17] Ernsting^[18] and Solntsev^[19] reported the ESPT dynamics of *N*-methyl-6-hydroxyquinolinium (NM6HQ) and showed that proton dissociation occurs in a solvent-controlled manner within an excited state lifetime of 2–3 ps in aqueous solutions. More recently, Huppert *et al.* investigated several quinone cyanine dyes^[20,21] (QCy), which are typically used as fluorophores for super-resolution microscopy. The highly conjugated dye QCy9 for example, exhibits a pK_a^* value as low as -8.5 and is thus the strongest photoacid studied so far.^[22]

Following a mechanism different from ESPT, a proton-release can also occur as a result of a photoreaction cascade which makes the respective compound a photoacid generator (PAG, Scheme 1B).^[23] After activation, PAGs allow for a high increase in proton concentration, but often irreversibly. They have been successfully utilized to initiate acid-catalyzed reactions^[24] or cationic polymerization,^[25] to create pH jumps^[26] or photoacidic polymers.^[27] They have also been applied as photoresists in microlithography.^[28]

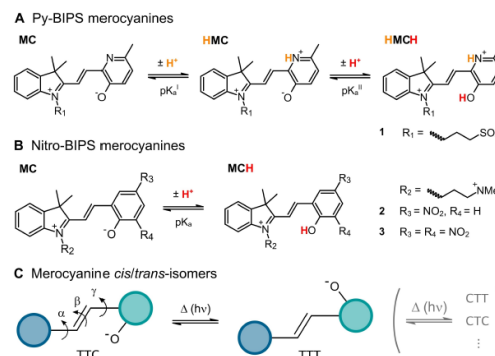
To this end, using photoswitches as photoacidic compounds can be very advantageous since they allow for a reversible operation of their protonation state, regardless of the nature of the photoacid itself. The reassociation of the proton is dictated by the isomerization of the photochromic compound and can be driven either thermally, photochemically or both.^[29] Moreover, the (de-)protonation itself can essentially affect the properties of the respective photoswitch which can be applied to design multistimuli-responsive molecular logic systems.^[30,31] Therefore, merocyanine-based photoacids, in particular benzo-indolino-pyrano-spiran (BIPS)^[32,33] derivatives have been studied extensively for miscellaneous applications.^[3,34–38]

Under acidic conditions, the ring-opened merocyanine form is protonated at its phenolate moiety (Scheme 1C). This proton is released upon photoisomerization towards the spirocyclic structure and the compound thermally reverts to the protonated ring-opened form in the dark.^[39–44] The pK_a value of this protonation site can be tuned by the choice of substituents on the respective phenyl ring (R_2 in Scheme 1C). For an unsubstituted ring a pK_a value of 7.8^[39] is reported, while, for example, attachment of electron-withdrawing functionalities like an NO_2 - or a CN-group in *para*-position drastically lowers the pK_a to 3.7 and 4.4, respectively.^[35] Different proton-release pathways were postulated like an initial *cis/trans* photoisomerization of the protonated merocyanine followed by proton dissociation and ring-closure. Also the formation of a highly acidic spirocyclic protonated on the indoline nitrogen has been discussed.^[31,42] At very low pH values, an intramolecular transfer of the phenolic proton to the indoline nitrogen upon ring closure was suggested, where the latter protic site adopts a pK_a value below 1.6.^[35] Yet, it has not been clarified whether the proton-release

occurs from the excited merocyanine prior to the ring-closing sequence (excited state PA) or as consequence of the photoreaction due to the formation of an acidic photoproduct (PAG).

We previously investigated the photochromic properties of several pyridine derivatives of the parent BIPS compound, which we referred to as Py-BIPS.^[45–47] Originally, the pyridine nitrogen of Py-BIPS-type compounds was methylated and therefore positively charged. More recently, we reported on an unmethylated Py-BIPS derivative, which shows refined photo- and acidochromic behaviour in aqueous solution.^[48] The merocyanine isomer of this compound **1** and its protonated states are shown in Scheme 2A.

Due to the absence of the methyl group, merocyanine **1** exhibits a slightly acidic protonation site on its pyridine nitrogen ($pK_a^1 = 6.8$), in addition to the phenolic site. Interestingly, the incorporation of the pyridine moiety lowers the pK_a^2 value of the phenolic site to 3.2, which is even lower than the values of Nitro-BIPS derivatives. The pK_a of Nitro-BIPS **2** is 3.7^[35] and that of Dinitro-BIPS **3** is 3.9^[49] (Scheme 2B). Upon exposure to light, each of the shown protonated merocyanines is capable of photoinduced ring-closure which is accompanied by proton dissociation. In addition to protonated states, the existence of several *cis/trans*-isomers (the configurations of the three central double bonds are typically denoted by T for *trans* and C for *cis*) should be considered when investigating merocyanine compounds spectroscopically (Scheme 2C).^[52] Eight isomers are possible in principle, but only those with a central T bond are stable ones. It is known that the two most stable isomers – mainly TTC and a minor fraction of TTT – exist in an equilibrated solution. The absorption band of TTT is shifted bathochromically with respect to the dominant TTC isomer. For Nitro-BIPS^[50] as well as Dinitro-BIPS^[51] derivatives distinguishable photoisomerization pathways were assigned for the two main isomers in



Scheme 2. Nomenclature of protonated species of the investigated A) Py-BIPS derivative **1** and B) Nitro-BIPS-type merocyanines **2** and **3**. C) Illustration of merocyanine *cis/trans* (T) isomers, referring to the configurations of the central double bond bridge. Rotation around the angles α , β and γ may occur thermally or photochemically. Among the eight possible isomers, those four with a T configuration at the middle bond are stable and the shown TTC and TTT (to a minor extent) are typically present in solution.

organic solvents, which might also be true for protonated merocyanines in general.

Here we present the first time-resolved investigation of the proton-release dynamics of photoacidic merocyanines by means of UV/vis-transient absorption (TA) spectroscopy in the fs–ns time window. We address the proton-release reactions of both protonation sites of compound **1** and of the phenolic sites of compounds **2** and **3** in order to shed light on the underlying mechanisms. The observed dynamics allow for a clear discrimination between photoacid generation and excited state photoacidity and provide clear evidence that the phenolic protonation site of the photoacidic merocyanines functions as a super-photoacid. Comparison with additional experiments in protic organic solvents give further insights into the ESPT dynamics of excited state PAs and the photoprotolytic cycle in general.

Results and Discussion

Photodynamics of MC and HMC of compound **1**

The compounds **MC** and **HMC** (Scheme 2A) were investigated at pH 7.4 and 5.5, respectively, to ensure the maximal amount of the particular isomers. The photoinduced ring-closure reaction causes the pK_a^1 value of the pyridine nitrogen to shift from 6.8 down to 4.8 for the spiropyran structure. Due to this outstanding side effect of photoswitching, we could realize a light-controlled steady-state pH value regulation of aqueous solution in a pH range roughly from 4.5 to 7. A pH drop of about 1.5 units was monitored upon exposure of an equilibrated **HMC** sample to visible light (520 nm) and the initial pH value was recovered within 5 minutes in the dark.^[48] A comprehensive summary of the photophysical acidochromic properties of compound **1** is provided in the Supporting Information (see Figure S1). However, the fact that a significant persistent pH drop can be observed, implies that a thermal reassociation of the released proton is hindered after photoisomerization to the ring-closed structure. Thus, the observable pH drop apparently relies on the change of acidity of the peculiar *N*-protic site and the reprotonation is only feasible via ring opening. It remains unclear though, whether the proton is released as consequence of ring-closing or due to an increased excited state acidity of **HMC*** (excited states are indicated by asterisks).

The time-dependent spectral evolution during the first 1.5 ns of the ring-closing sequence of **MC** and **MCH** upon excitation with 520 nm at pH 7.4 and 5.5, respectively, is shown in Figure 1. The contour plots display the absorption difference relative to the ground state absorption. Hence, positive signals can be assigned to excited state absorption (ESA) or to the absorption of emerging intermediate species. Negative signals appear because of the ground state bleach (GSB) upon electronic excitation and due to stimulated emission (SE) induced by the probe pulse. In the transient map of **MC** (Figure 1A, left panel), a positive signal at 425 nm (ESA_1) and a more pronounced one around 505 nm (ESA_2) is observed. Both appear directly upon excitation and can thus be ascribed to the

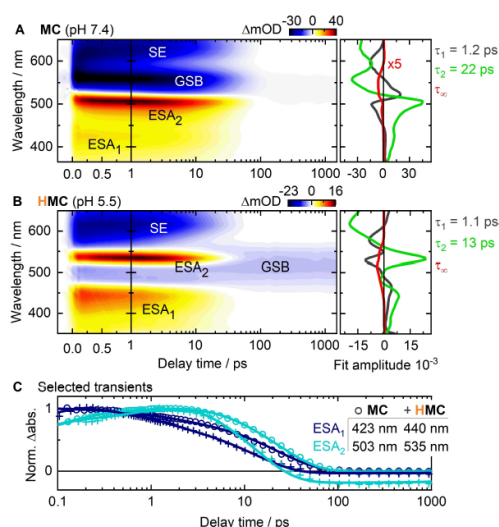
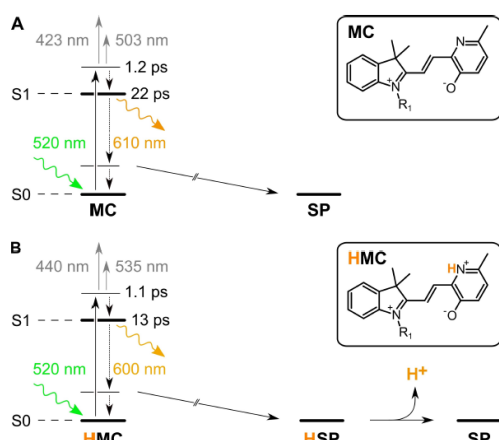


Figure 1. A) TA contour plot of **MC** of compound **1** at pH 7.4 (left panel) and corresponding DAS (right panel). B) TA contour plot of **HMC** of compound **1** at pH 5.5 (left panel) and corresponding DAS (right panel). C) Selected transients showing the time-dependent progression of the signals ESA_1 (blue) and ESA_2 (cyan) for **MC** (circles) and **HMC** (plus signs). Data points are represented by symbols and the fit from GLA by solid lines.

excited S1 state **MC***. Moreover, the negative SE signal around 620 nm resembles the steady-state emission of **MC** and the GSB is visible around 540 nm, where the ground state absorption band is centred (Figure S1). All of the excited state signals (both ESAs and SE) decay on a similar timescale and are almost vanished after 100 ps.

The kinetics observed in the TA spectra were analyzed by fitting the data sets globally with a sum of a given number of exponential lifetime components, which is referred to as global lifetime analysis (GLA).^[52] From this procedure, decay-associated spectra (DAS) are obtained, which show the wavelength-dependent amplitudes of the determined lifetimes (Figure 1A and B, right panels). The reading of the DAS is as follows: a positive amplitude captures the decay of a positive absorption difference signal or a build-up of a negative signal. Inversely, a negative amplitude indicates a decay of a negative or an increase of a positive signal. Analysis of the TA spectrum of **MC** via GLA revealed that two main time constants are sufficient to describe the observed dynamics adequately. An additional infinite time constant τ_{∞} reflects the residual signal at the end of the measurement after 1.5 ns. A schematic depiction of the assumed mechanism is given in Scheme 3A. The determined 1.2 ps lifetime (τ_1) models the solvent reorganization and vibrational relaxation within the S1 state **MC*** as the sigmoidal shape of its DAS captures a slight blue-shift of the ESA signals and a dynamic Stokes shift of the SE. However, the slower constant $\tau_2 = 22$ ps accounts for the decay of the signals



Scheme 3. Photoreaction pathway schemes of Py-BIPS 1. A) Ring-closure dynamics of MC at pH 7.4. B) Ring-closure dynamics of HMC and subsequent proton-release from the HSP ground state at pH 5.5.

associated with the electronically excited state and is therefore ascribed to its lifetime. The large negative contribution of τ_2 around 560 nm indicates that the decay of MC^* mostly recovers the initial MC ground state through SE but also non-radiatively. Last, the infinite time constant τ_∞ reveals that residual GSB is present at the end of the measured time frame due to the formation of the ring-closed photoisomer SP. Interestingly, there is no indication for the formation of a protonated state upon excitation of MC. Thus, the pyridine group plausibly does not acquire a proton from the solvent when excited as one could expect since related compounds like quinoline or acridine are known to be photobases.^{33,54}

Just as the transient map of MC, the spectrum of HMC (Figure 1B, left panel) exhibits two separated ESA signals, although both are shifted to longer wavelengths by about 30 nm. Thus, the GSB appears in between the positive ESA signals. Similarly, the ESAs shift hypsochromically with time. Apart from the GSB, there is a pronounced negative SE signal around 610 nm. Data analysis indicates two main time constants reflecting an analogous spectral evolution as for MC (Figure 1B, right panel). First, the fast time constant $\tau_1 = 1.1$ ps models a rapid relaxation within the S1 state HMC^* , due to an initial motion away from the Franck-Condon region and to solvent reorganization. Then, the decay of the excited state is monitored by τ_2 , which is significantly accelerated compared to MC^* (13 ps vs. 22 ps). At the end of the measured time, again GSB is the only observed residual signal. The significant acceleration of the photodynamics of HMC compared to MC is also evident in view of the transient signal evolution depicted in Figure 1C. Similar dynamics for each of the signals are observed, where it takes approximately 80 ps for the MC^* excited state signals to decay thoroughly and only about 40 ps for MCH^* . In both cases, the more pronounced ESA_2 seems to

increase during the first ps, but this effect can be ascribed to the superposition of the respective ESA and the GSB.

The similarities in the MC and HMC photodynamics hint at analogous ring-closure pathways for both compounds. Furthermore, the observed dynamics is in agreement with the singlet pathway of the previously reported Py-BIPS⁴⁵ compound, where the decay of the excited state is further accelerated to 3.2 ps. These observations account for a distinct correlation between the substitution on the pyridine nitrogen and the excited state lifetime of the ring-open merocyanine. Starting from a mere lone pair on the nitrogen (MC) to a proton (HMC) to a methyl-group (Py-BIPS), the electron density on the N-atom decreases, which enhances the excited state decay. Although the formation of the photoproduct HSP could not be directly monitored here due to limitations of the probe light (broken arrows, Scheme 3), we suggest that ring-closure proceeds similarly to the parent Py-BIPS derivative. Hence, upon excitation of the thermodynamically favoured *trans*-merocyanine, ring-closure occurs via a series of *cis-trans* isomerizations from the vibrationally hot ground state of the ring-open isomer.^{45,55} An indirect indication for these isomerizations is that the remaining GSB signal is slightly shifted with respect to the steady-state absorption band. The planar *trans*-merocyanine converts into a *cisoid* intermediate which already adopts a perpendicular structure and finally establishes the C–O bond.

In our previous study,⁴⁸ a fluorescence quantum yield of ~9% was determined for MC by integrating sphere measurements. Hence, non-radiative decay such as internal conversion or vibrational relaxation occurs with a ~91% probability. Starting from a vibrationally hot MC ground state, ring-closure is assumed to occur with a yield of ~5%, according to steady-state switching experiments. Compared to MC, the excited state decay of HMC is significantly faster and a lower fluorescence quantum yield of ~3.5% was found, which entails a probability of ~96.5% for non-radiative relaxation. Moreover, the quantum yield for photoproduct formation (SPH) is slightly higher at pH 5.5 (~7%) than at pH 7.4 (SP). This points to a favoured establishment of the ring-closed form when the pyridine nitrogen is protonated.

Concerning the proton-release of HMC it appears that the decay of the excited state is not accompanied by the emergence of an intermediate state. Hence, a dissociation of the proton in the excited state can be ruled out, as this would imply the formation of the excited deprotonated MC^* . HMC therefore does not release H^+ within the excited state but directly converts into the ring-closed structure HSP (Scheme 3B). This entails that HMC has to be considered as a reversible PAG rather than an excited state PA. The proton is released subsequently after formation of HSP and the observable pH jump therefore merely results from the altered pK_a value of the respective protic site.

Photo- and ESPT-dynamics of HMCH of compound 1

The TA spectrum of the doubly protonated HMCH in aqueous solution at pH 1 is shown in Figure 2A. Several signals are

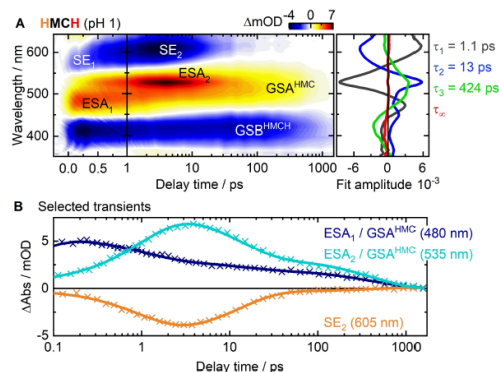


Figure 2. A) TA contour plot of HMCH of compound 1 at pH 1 (left panel) and corresponding DAS (right panel). B) Selected transients showing the time-dependent progression of the signals ESA_1 (blue), ESA_2 (cyan) and SE (orange). Data points are represented by symbols (crosses) and the fit from GLA by solid lines.

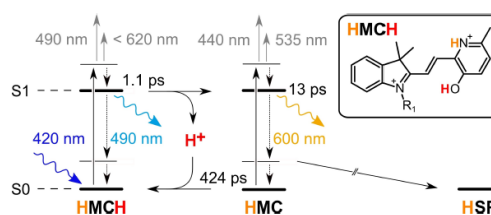
present directly upon excitation – the GSB at 420 nm and two ESA signals around 480 nm (ESA_1) and above 625 nm (not denoted). Moreover, an SE signal is detectable already at early times in between the ESA bands. Besides the GSB, the listed signals correspond to the excited $HMCH^*$ species. The positive amplitude of the time constant $\tau_1 = 1.1$ ps between 450 nm and 500 nm, where ESA_1 is located (Figure 2A, DAS), is indicative of an ultrafast decay of the initial excited species. The pronounced negative amplitude of τ_1 around 530 nm reveals that the decay of ESA_1 is accompanied by the emergence of a second positive signal (ESA_2) at 530 nm. The positive amplitude of τ_1 above 570 nm additionally captures the formation of the main SE_2 signal around 610 nm. Therefore, this time constant corresponds to a transition from $HMCH^*$ to a distinct new transient species. Comparison of the transients between 0.2 and 4 ps (Figure 2B) illustrates that the decay of ESA_1 and the increase of ESA_2 and SE_2 indeed occur with one rate. The spectral signature of the state, evolving with the constant τ_1 (ESA_2 and SE_2), coincides with that of the excited single protonated HMC^* (ESA_2 and SE, see Figures 1B and S2) when the GSB is relaxed. The decay of ESA_2 and SE_2 is described by a similar time constant $\tau_2 = 13$ ps with a DAS that resembles the one found for HMC^* which further confirms the assignment of the HMC^* state. Hence, the release of the phenolic proton of $HMCH^*$ can be directly observed here and evidently occurs in the excited state. This process interestingly takes place on the same timescale as relaxation within the excited state in the cases of MC and HMC. Consequently, the proton is transferred to the solvent rather efficiently even before the $HMCH^*$ state is thoroughly relaxed on the S_1 potential energy surface. Competing deactivation channels for $HMCH^*$ are non-radiative decay and fluorescent emission. A fluorescence maximum at 470 nm was observed in the steady-state spectra and the red edge of

this emission band that extends to roughly 600 nm is detected in the shape of SE_1 .

After the proton transfer and the transition to HMC^* , the decay towards the ring-closed structure progresses analogously to the dynamics observed upon direct excitation of HMC. A simplified photoreaction and proton-release mechanism is provided in Scheme 4. The weaker ESA band of HMC^* at 440 nm is not clearly visible in the contour plot (Figure 2A) due to the superposition with the GSB. Another small, positive signal below 370 nm can be noticed between 1 ps and 10 ps that also corresponds to HMC^* . Furthermore, the amplitudes of τ_1 and τ_2 indicate a rise and decay behaviour of the respective signal. Interestingly, the 13 ps lifetime exhibits no negative amplitude in the range of the GSB, which means that a recombination process of the proton from HMC^* straight to the $HMCH$ ground state is not indicated here.

After roughly 10–30 ps the sharp ESA_2 signal of HMC^* superimposes with an emerging broad positive signal between 450 and 580 nm, which decays on a longer timescale but is almost vanished after 1.5 ns. The slow depletion of this broad signal can be observed in the spectral range where ESA_1 was located (Figure 2B). This broad absorption signal matches the time-integrated absorption spectrum of HMC and can thus be attributed to its ground state absorption (GSA). The positive amplitude of the time constant $\tau_3 = 424$ ps around 500 nm reflects the decay of the respective signal. Since the negative amplitude of τ_3 in the wavelength range of the GSB captures a repopulation of the $HMCH$ ground state, we assign the respective time constant to the thermal reassociation of the proton. This reprotonation process completes the photoprotonolytic Förster cycle roughly within the first nanosecond after excitation. At the end of the monitored time window the remaining bleach signal around 420 nm, described by the infinite time constant, reflects the conversion of some of the molecules into the spiro form.

Similar to HMC, a fluorescence quantum yield of $\sim 3.5\%$ was determined for $HMCH$.^[48] Non-radiative relaxation of $HMCH^*$ certainly represents a considerable decay channel as the amplitude of τ_3 exhibits a ground state recovery contribution. However, the proton dissociation channel is suggested to be the predominant decay pathway, which is further supported by the fact that ESA_1 ($HMCH^*$) seems to thoroughly convert into ESA_2 (HMC^*) with mostly one lifetime. Assuming that radiative relaxation of HMC^* again occurs with $\sim 3.5\%$ probability, non-



Scheme 4. Photoreaction pathway scheme of the excited state proton-release and ring-closure of HMCH of Py-BIPS 1 at pH 1.

radiative decay is again the major channel. Though, an overall quantum yield of SPH formation of ~10% was obtained by steady-state experiments, which is even higher than upon excitation of HMC. If this is due to relative excess energy provided by the high efficiency of the photoprolytic decay channel towards HMC* remains speculative.

The pK_a^* of the excited state can be estimated by applying the Förster cycle, which provides a simplified thermodynamic model for photoprolytic processes. Equation (1) gives the correlation between the free energies ΔG of the proton dissociation processes in the ground and excited state and the transition energies of the acid AH and conjugate base A⁻.^[56,57]

$$E_{AH} - E_{A^-} = \Delta G - \Delta G^* = -RT(\ln K_a - \ln K_a^*) \quad (1)$$

To determine these energies, the transition energy differences between the vibrational ground states of S0 and S1 have to be estimated. Therefore, the most reasonable approach is to average the frequencies of the absorption and emission maxima of the acid (ν_{ROH}) and the conjugate base (ν_{RO^-}) as observed in steady-state experiments. Then the difference of the pK_a values of the ground and excited state is obtained by Equation (2).

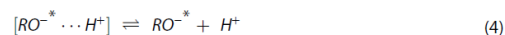
$$pK_a - pK_a^* = N_A h(\nu_{ROH} - \nu_{RO^-}) / 2.3RT \quad (2)$$

Here, N_A is Avogadro's number, h Planck's constant and R the universal gas constant. With a ground state $pK_a = 3.2$ of HMCH this estimation results in a substantial pK_a drop of 8.7. Therefore, an excited state pK_a^* of -5.5 is determined, which makes this merocyanine isomer one of the strongest super-photoacids reported, significantly more acidic than 1N or HPTS. Regarding its pK_a^* value, HMCH is most comparable to the naphthol derivative DC2N^[11] ($pK_a^* = -4.5$) or to the QCy derivatives like, for example, QCy7^[20] ($pK_a^* = -5.7$). The ultrafast proton transfer within less than 1.1 ps and the striking pK_a drop indicate a pronounced enhancement of the acidity of HMCH* upon excitation. The photoacidity basically depends on the charge distribution in the excited state and the stabilization of the negative charge of the deprotonated form. In case of merocyanines, the negative charge is in general highly delocalized due to the expanded conjugation of the molecule and can be displaced from the phenolate oxygen to the indolinium nitrogen. Because of that, the neutral quinoid mesomeric resonance structure of the core chromophore strongly contributes to the stabilization. Moreover, a pronounced redistribution of π -electrons is suggested to take place upon excitation of aromatic photoacids, which facilitates the proton-release process.^[58]

Following theory, the ESPT mechanistically occurs in two consecutive steps.^[59-62] Upon electronic excitation, the proton is transferred from an aromatic photoacid ROH* to an adjacent water or solvent molecule with an intrinsic rate. This creates a solvent stabilized contact ion pair, with a distinct contact radius [Eq. (3)]:



With further increase of the distance between the ions the proton becomes thoroughly solvated or rather is transferred to larger water clusters. This step is apparently dictated by the diffusion of the proton away from the anion into the bulk solvent and is therefore strongly affected by solvent properties and electrostatic interactions. Therefore, the timescale of this diffusive step is typically much longer than that of the initial proton abstraction on contact [Eq. (4)]:



A mathematical treatment engages the Debye-Smolouchowski equation (DSE) that takes the random thermal motion into account as well as the Coulomb potential between the ions.^[63] The back reaction is referred to as diffusion-assisted geminate recombination, which is substantially influenced by the electric field of the conjugate base anion.

In the case of HMCH*, the initial step of the photoprolytic reaction occurs within 1.1 ps in water. This translates into an overall proton transfer rate $k_{pt} = 9.1 \times 10^{11} \text{ s}^{-1}$. The formation of ESA₂ (Figure 2A) is ascribed to the contact ion pair, as this is assumed to adopt identical spectral properties as the deprotonated RO⁻. There are no clear indications for a major contribution of the back reaction since ESA₁ seems to convert entirely into ESA₂. Though, the existence of the equilibrium can be verified since a pH dependent fluorescence emission of HMCH* is observed in the steady state. Interestingly, the initial proton transfer occurs on a similar timescale as solvent relaxation dynamics. The Debye relaxation time of water around a solute molecule is found to be approximately 1 ps^[17] and the proton hopping time from one water molecule to another is roughly 1.5 ps.^[62] Hence, the proton transfer from HMCH* to a water molecule proceeds even faster than the proton transfer in between water molecules via the Grotthuss mechanism. The subsequent diffusion is supposed to occur similarly fast in aqueous solution, although this is influenced by the electric field of the conjugate base anion. Apart from the negative phenolate charge, the deprotonated merocyanine HMC* exhibits two positively charged nitrogen atoms. In addition, the compound bears a flexible negatively charged sulfonic acid residue that could exert enhancing effects on geminate recombination.

To gain more insights into the ESPT dynamics and to verify whether HMCH is capable of transferring its proton to poorer proton acceptors like organic solvents, we conducted additional TA experiments in the protic solvents methanol (MeOH) and ethanol (EtOH) and the aprotic solvent acetonitrile (MeCN) at pH 1. Although, both protic solvents are capable of H-bonding, they are significantly less polar. While water exhibits a dielectric constant ϵ of 78, those of MeOH and EtOH are 33 and 24, respectively. The dielectric constant of MeCN is 37 and is therefore comparable to MeOH. The obtained transient maps in MeOH and EtOH show almost the same spectral signature as

observed in water, although the signals are slightly shifted hypsochromically (see Figures S3 and S4).

The decay of the initially formed ESA_1 and SE_1 of $HMCH^*$ is accompanied by the emergence of ESA_2 and SE_2 within the first ps. The latter two signals are again assigned to the excited state of the conjugate base HMC^* . An ultrafast ESPT of the phenolic proton therefore evidently occurs also in protic organic solvents.

Apart from that, the decay of ESA_1 is slowed down with decreasing proton acceptor capabilities of the solvents. As the formation of ESA_2 and SE_2 is also delayed it can be noted that the ESPT is decelerated in the order from water to MeOH to EtOH. Furthermore, the relative intensities of the ESA_2 signals in the protic solvents compared to ESA_1 are smaller than in water, which hints at a less efficient process. Accordingly, the SE_2 signal is significantly less pronounced, too. In the kinetic analysis of the data sets, a similar number of lifetime components as in water was determined (Figure 3A). The respective lifetimes are of similar orders of magnitude and their amplitudes mostly resemble analogous contributions. Yet, the measurement in aprotic MeCN revealed no emergence of the excited conjugate base signals (see Figure 3B). Only the signals originating from $HMCH^*$ are visible, which decay substantially slower than in water and the protic solvents. Therefore, the lifetime of the excited state $HMCH^*$ is elongated. However, a proton transfer to MeCN can be ruled out, although it is the organic solvent with the highest polarity among the investigated ones.

In the GLA of the MeOH and EtOH measurements, time constants of 1.7 ps and 1.9 ps, respectively, were determined to

describe the proton transfer processes (Figure 3A). Despite the before mentioned hypsochromic shift of the signals, the amplitudes of these time constants are in excellent agreement with the 1.1 ps constant found in aqueous solution. Hence, the ESPT is significantly slower than in water but roughly similarly fast in MeOH and EtOH. The time constants found for the subsequent decay of HMC^* are also slower in MeOH (16 ps) and EtOH (24 ps) than the 13 ps constant in water. The respective time constants exhibit positive contributions in the range of ESA_1 around 490 nm, which are absent in the DAS of the lifetime determined in water. This might indicate that a pronounced fraction of ESA_1 decays on a 10–30 ps timescale and the actual lifetime of the $HMCH^*$ state is prolonged in both protic solvents. The biphasic decay of ESA_1 furthermore shows that a slowed down decay channel competes with proton dissociation. A similar timescale of the ESA decay was also observed in the MeCN measurement. A 10 ps lifetime was determined for the main decay channel of $HCMH^*$ and an additional 33 ps lifetime was found. The latter captures a decay of a positive band around 500 nm as well as the formation of a positive absorption signal above 550 nm and a repopulation of the ground state. The respective lifetime might thus account for the decay of a distinguishable merocyanine isomer, which is excited simultaneously or which is formed in the excited state through isomerization. Although the photodynamics are suggested to be dominated by the TTC isomer (Scheme 2C), the observed signals may be superimposed with those of the TTT isomer. The lifetime components τ_2 found in MeOH and EtOH therefore supposedly represent mixed lifetimes that comprise additional decay dynamics of $HMCH^*$. In any case, the biphasic decay of ESA_1 , modelled by τ_1 and τ_2 implicates competing deactivation pathways that lower the efficiency of proton dissociation.

The lifetimes τ_2 furthermore exhibit negative amplitudes below 475 nm and thus model a recovery of the $HMCH$ ground state, in contrast to the corresponding lifetime found in water. Hence, in organic solvents a proton recombination quenching of HMC^* seems to occur, which could be assisted by the negatively charged sulfonate residue. In aqueous solution this process might occur too, but significantly less pronounced. As in water, the formation of the broad GSA of HMC (450–550 nm) can be observed in both TA maps of the protic solvents (Figures S3 and S4) after the ESA_2 decay. The relative intensity of this long-term feature decreases significantly in the order from water to MeOH to EtOH, which provides another evidence that the efficiency of the photolytic decay of $HMCH^*$ also decreases in that order. In contrast to the measurement in water, the depletion of this signal is not completed at the end of the accessible time window after 1.5 ns. The HMC ground state is therefore still present in both protic solvents.

However, to fit the data sets adequately by GLA, a third lifetime component had to be engaged, that captures a partial decay of the HMC ground state towards $HMCH$. This lifetime τ_3 exhibits a much smaller relative amplitude than the corresponding 424 ps lifetime determined for reprotonation in water and it is accelerated to 320 ps in MeOH and 254 ps in EtOH. The amplitudes of τ_3 in the protic solvents exhibit a minor

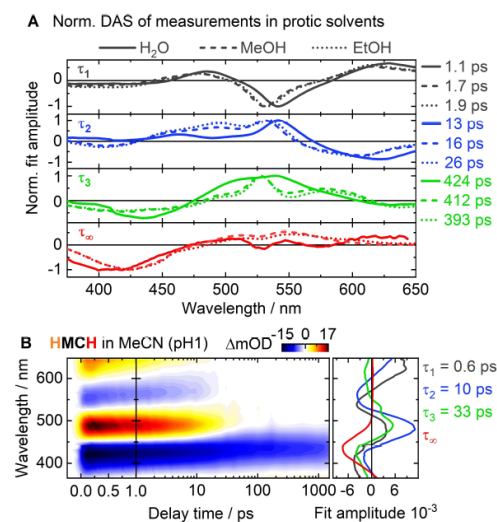


Figure 3. A) Comparison of the determined DAS of the TA measurements of $HMCH$ of compound 1 in H₂O (solid lines), MeOH (dashed lines) and EtOH (dotted lines). B) TA contour plot of $HMCH$ of compound 1 at pH 1 in MeCN (left panel) and corresponding DAS (right panel).

contribution to the decay of ESA_2 and a slower decay component of the SE_2 signal. This hints at a non-exponential long-term decay of the excited conjugate base. An accelerated reprotonation process seems plausible, if it is due to geminate recombination, as the solvation of the free proton is less favoured in both organic solvents than in water. Here, again the sulfonate residue supposedly plays an important role in arranging the nearby solvation shell of the photoacid. An exclusively diffusion-driven reprotonation process, following the DSE model, should be much slower in the protic solvents, since the diffusion coefficients of the proton are significantly smaller than in water. Thus, the electrostatic potential of the negatively charged and flexible residue supposedly affects the diffusion of the proton and assists to the recombination. Moreover, the amplitudes of τ_3 reveal a decay contribution in the red flank of the overall GSA signal (575 nm) in the protic solvents. The blue region of the signal around 550 nm is still present after 1.5 ns, which is captured by the infinite lifetimes. This might again be ascribed to the presence of two merocyanine conformers, where one undergoes the reprotonation process faster than the other. Upon excitation, the main TTC-merocyanine converts into a ground state *cisoid* structure which either undergoes ring-closure or reverts back to the initial *trans*-configuration and adopts a red-shifted absorption band.^[64] Hence, the decay of the red flank of the GSA signal might account for the *cisoid*-form which favours the reprotonation process due to its particular geometry.

As additional model-free data evaluation method, lifetime distribution analyses (LDA) were performed on each data set. The obtained lifetime density maps (LDM) for the three solvents are depicted and further compared in the Supporting Information (see Figure S6). The LDMs represent the time-dependent distribution of lifetime components, obtained from fitting the data sets with a high number of lifetimes (> 100). In contrast to the GLA, this analysis is thus not biased by a kinetic scheme and a given set of contributing lifetimes. It therefore provides a better representation of the actual timescales of the assigned processes. The reading of the LDM contour plots, however, is similar as for the DAS. A positive amplitude indicates the decay of a positive signal or the increase of a negative one and vice versa.

Proton-transfer dynamics of Nitro-BIPS derivative 2

TA experiments were conducted with the protonated form of the extensively applied 6-nitro-BIPS derivative 2 (Scheme 2B). In acidified aqueous solution, the spiro-merocyanine equilibrium is shifted to the energetically favoured protonated merocyanine MCH and thermal conversion to the ring-closed isomer is not observed anymore. The photophysical properties in neutral aqueous solution as well as the ultrafast dynamics are reported elsewhere.^[47] A brief description of the steady-state behaviour in the neutral and acidic pH range may be found in the Supporting Information, together with the absorption and emission spectra of the MC and MCH states (Figure S7). The ground state pK_a value of compounds 2 is 3.7.^[35] Thus, the TA

measurements were carried out at pH 1 to accumulate the pure protonated state.

The transient map of Nitro-BIPS 2, shown in Figure 4A, reveals initial signals that can clearly be assigned to the excited S1 state MCH*. Around 560 nm the negative signal SE_1 appears directly upon excitation, as well as a prominent positive signal (ESA_1) and a minor ESA band below 425 nm (not denoted). The latter overlaps with the GSB around 410 nm, which also emerges instantaneously upon excitation. The minor ESA below 425 nm vanishes after around 1 ps just as the signal SE_1 , which is accompanied by the formation of the even more pronounced SE_2 around 610 nm. This spectral evolution already hints at the formation of the excited conjugate base, as SE_2 fits the steady-state emission thereof.^[47] The prominent ESA_1 prevails until roughly 100 ps but evolves into a broad positive signal between 450 nm and almost 600 nm. Here, the interpretation is not unequivocal at first, due to the superposition of multiple signals. Yet, in comparison with the reported TA data of the deprotonated MC^[47] the assignment becomes clear. The deprotonated form exhibits an SE signal between 575 nm and 650 nm and one pronounced ESA signal around 450 nm, both lasting until approximately 100 ps. The similarity of this spectral signature and the observed signal of MCH (ESA_1) indicate that both the acid and the conjugate base exhibit ESA signals around 450 nm, impeding a precise discrimination in the spectrum in Figure 4A.

The ESA_1 transient at 485 nm (Figure 4B) reveals an initial ultrafast decrease within the first 700 fs, followed by a slower depletion of the signal. According to the DAS (Figure 4A, right panel), a sub-ps lifetime was found ($\tau_1 = 0.4$ ps), which is ascribed to an initial cooling process within the excited S1 state MCH*, as it models a slight shift of the corresponding signals. The lifetime $\tau_2 = 2.1$ ps captures the decay of the minor ESA below 425 nm as well as the decay of SE_1 and the subsequent formation of SE_2 . In the wavelength range around ESA_1 the

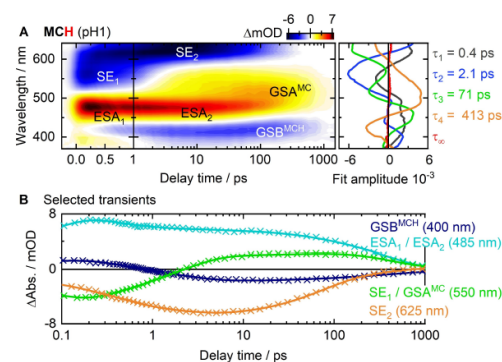
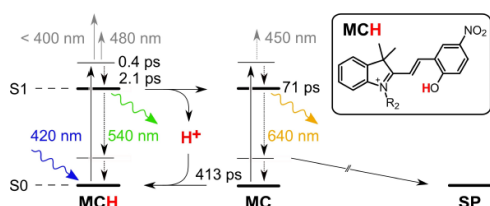


Figure 4. A) TA contour plot of MCH of compound 2 at pH 1 (left panel) and corresponding DAS (right panel). B) Selected transients showing the time-dependent progression of the signals GSB (blue), ESA_1 and ESA_2 (cyan), SE_1 and GSA^{MC} (green) and SE_2 (orange). Data points are represented by symbols (crosses) and the fit from GLA by solid lines.

amplitude of this lifetime is almost zero. However, we assign τ_2 to the proton-release process, as illustrated in Scheme 5, primarily because it accounts for the transition from SE_1 (MCH^*) to SE_2 (MC^*). Yet, as the signal SE_2 already emerges within the first 0.5 ps, the proton transfer is supposed to start during the vibrational relaxation process. If the transition from SE_1 to SE_2 is just fitted with one lifetime component, a lifetime of 1.6 ps is determined, which therefore reflects the mean value of the proton transfer lifetime component. This estimation results in a proton transfer rate $k_{pt} = 6.3 \times 10^{11} \text{ s}^{-1}$. However, compared to compound 1 the quantum yield of the ESPT process is suggested to be similarly high, since the SE_1 signal is entirely converted into SE_2 . The minor ESA below 400 nm shows similar decay dynamics as SE_1 which also speaks against a large contribution of additional competing dynamics.

The subsequent decay of ESA_2 and SE_2 , that correspond to MC^* , is modelled by time component $\tau_3 = 71 \text{ ps}$ (positive amplitude around 450 nm and negative amplitude above 575 nm). Therefore, it can be attributed to the lifetime of the respective state and a lifetime in the same order of magnitude and with a similar DAS was found upon direct excitation of MC .^[47] The negative amplitude of τ_3 between 490 nm and 575 nm accounts for the emergence of another positive signal (ESA_2) whose decay is modelled by the broad positive amplitude of $\tau_4 = 413 \text{ ps}$ in this range. This absorption band is related to the MC ground state. As τ_4 features a negative amplitude below 450 nm it also captures a repopulation of the MCH ground state. Hence, τ_4 describes the reprotonation process, which completes the photoprolytic cycle on the same timescale as observed for compound 1. Interestingly, the reprotonation in the ground state proceeds with almost similar lifetimes for both merocyanine derivatives 1 and 2, as the pK_a values of the acid ground states are rather similar. This is indicative of a diffusion-driven recombination with the solvated proton. Apparently, the alkyl residue attached to the indoline nitrogen does not affect the reprotonation in aqueous solution, as the two compounds exhibit differently charged functional groups.

Based on the steady-state absorbance and fluorescence data (Figure S7), again the excited state pK_a^* of MCH^* could be obtained. With a $pK_a = 3.7$, the Förster cycle estimation yields a pK_a drop of 7.9 units and a $pK_a^* = -4.2$. This is only slightly less acidic than the Py-BIPS PA 1 discussed before and Nitro-BIPS 2 has to be considered a super-photoacid as well. The attachment



Scheme 5. Photoreaction pathway scheme of the excited state proton-release and ring-closure of MCH of Nitro-BIPS 2 at pH 1.

of the NO_2 -group exerts a smaller electron-withdrawing effect on the phenolic oxygen than the incorporated nitrogen of Py-BIPS and the charge displacement upon optical excitation is less pronounced.

The photoprolytic reaction of MCH of compound 2 was also measured in the solvents MeOH, EtOH and MeCN. The TA spectra of MCH in MeOH (Figure 5A) and EtOH (Figure S8) show very similar features and monitor clear indications for a proton transfer to the solvent. In the protic solvents, the signal SE_1 of MCH^* is longer lived and SE_2 of MC^* is significantly less pronounced which is indicative of the proton transfer. A time constant of $\tau_1 = 2.4 \text{ ps}$ was found for the proton transfer in both protic solvents as it models the transition from SE_1 to SE_2 (Figure 5B). It also captures a partial decay of the superimposed ESA_1/ESA_2 signal and the decay of the minor ESA below 400 nm, that also corresponds to MCH^* . The following decay of the ESA_1/ESA_2 feature seems significantly accelerated compared to water and it evolves into the broad absorption signal of the MC ground state, which is also less pronounced. The decay of the ESA signal is captured by two more lifetime components. While the main decay is modelled by a 17 ps (18 ps) in MeOH (EtOH), a considerable contribution decays with a significantly longer lifetime of 290 ps (298 ps). The corresponding amplitudes are in good agreement for both protic solvents. The amplitude of the 71 ps lifetime found in water for the particular ESA decay is rather resembled by the slower lifetime components than the faster ones, regarding the minimum in the near-UV and the region above 500 nm (Figure 5B). However, both the fast and the slow components show contributions to the formation of the broad GSA signal and the decay of SE_2 but at different

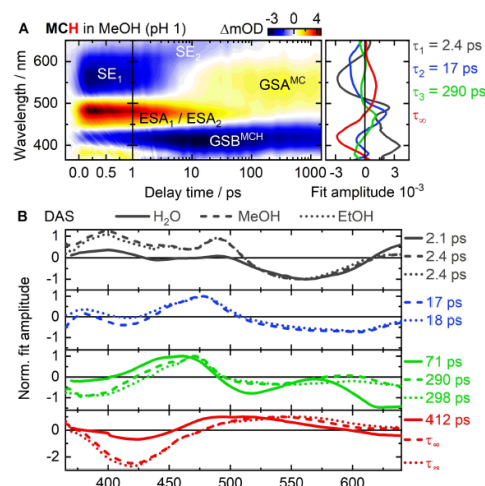


Figure 5. A) TA contour plot of MCH of compound 2 in MeOH (left panel) and corresponding DAS (right panel). B) Comparison of the DAS determined through GLA for the three solvents H_2O (solid lines), MeOH (dashed lines) and EtOH (dotted lines). The lifetime components are sorted by highest agreement.

wavelength ranges. Therefore, the respective two lifetimes are supposedly attributed to different *cis-trans* merocyanine isomers that undergo the discriminable relaxation pathways.

Especially concerning Nitro-BIPS derivatives, different isomerization sequences have been reported for particular conformers in various solvents.^[64] Ruetzel et al. found that in MeCN the TTC isomer converts into the TTT in the excited state unidirectionally within 200 fs and both forms decay on different timescales afterwards.^[50] An SE signal around 625 nm was assigned to the TTC isomer while that of the TTT form is shifted bathochromically by 30 nm. Therefore, we ascribe the lifetime τ_2 , which models the decay of the blue region of SE₂ to the TTC conformer. The longer lifetime τ_3 with a smaller relative amplitude then presumably corresponds to TTT which represents the isomer, typically existing to a smaller extent. After 1.5 ns, there is still a pronounced positive signal around 550 nm, which is in good accordance with the reported ground state absorption of the TTC isomer. This, as well as a prominent residual fraction of the MCH bleach signal, is reflected by the infinite time constants determined in both protic solvents (Figure 5B). Their amplitudes are in good agreement with the 412 ps lifetime component determined in water. Hence, the ground state reprotonation seems to be essentially slower than in water and also than in the case of compound 1. Here again, this might be influenced by the alkyl residue attached to the indoline nitrogen. Compound 2 bears a positively charged functionality, which is supposed to exert a repulsive effect on the released proton and therefore hinders a diffusion-assisted recombination.

The essentially reduced efficiency of the photoprolytic decay of MCH* in MeOH and EtOH hints at the existence of other major reaction channels than in water. Besides fluorescence relaxation also non-radiative decay into the ground state may occur. Internal conversion is reported to be a considerable pathway for Nitro-BIPS derivatives, also because of the enhancing effect of the nitro group.^[65] Moreover, the contribution of triplet states to the photodynamics of Nitro-BIPS is well-known,^[64] although no distinct indications were found here. Non-radiative decay is suggested to yield a vibrationally hot ground state which undergoes further cooling. This cooling process causes the observed bathochromic shift of the GSB signal after 100 ps (Figure 5A). However, the remaining bleach after 1.5 ns resembles the ground state absorption spectrum quite well.

In the measurement in MeCN (Figure S11) similar MCH-associated signals were detected as in the protic solvents, like an ESA around 480 nm and SE around 570 nm and both decay on a similar timescale within 10–20 ps. As no emergence of signals that could be assigned to the excited conjugate base was observed, a proton transfer can be ruled out. Though, a positive absorption signal from 500 nm to 625 nm appearing after 20 ps is detected, which accounts for a deprotonated merocyanine ground state absorption. This could either arise from small amounts of water within the measured sample that the proton is transferred to or to residual amounts of non-protonated merocyanine that undergoes the isomerization observed by Ruetzel et al. The GLA revealed a vibrational

relaxation of MCH* with a lifetime of 1.1 ps. Interestingly, a lifetime of 7.5 ps was determined here for the MCH* decay of the main isomer (TTC), which is essentially faster than the lifetimes reported for the non-protonated Nitro-BIPS analogue.

Proton-transfer dynamics of Dinitro-BIPS derivative 3

For the Dinitro-BIPS derivatives 3 (Scheme 2B), the ring-opened MC isomer is even more stabilized than for the nitro compound 2. In aqueous solution, compound 3 is therefore more prone to hydrolysis. Though, the photoswitching properties are quite comparable to compound 2 just as the excited state dynamics of the unprotonated MC isomer.^[47] With a pK_a value of 3.9,^[49] the protonated MCH state is formed upon acidification, which is thermally stable at pH 1 and shows fluorescence emission around 495 nm. A brief summary of the behaviour in aqueous solution may be found in the Supporting Information, with corresponding absorption and emission spectra of the MC and MCH states (Figure S7). Based on these spectra, again the pK_a* value can be estimated for compound 3 by use of the Förster cycle approximation. The resulting pK_a drop of 8.3 units is even more pronounced than that of the nitro compound 2. Ultimately, a pK_a* value of –4.2 is determined for MCH of compound 3 is, which makes it a super-photoacid.

The TA measurement of MCH of the Dinitro-BIPS derivative 3 at pH 1 revealed an essentially different behaviour than the before presented PAs 1 and 2. The TA spectrum (Figure 6A) displays two ESA signals centred around 470 nm and 600 nm, where the latter is more intense by a factor of roughly 2.5. Those positive signals as well as the GSB at 400 nm decay almost completely within 1 ps. This implies, that the compound mainly relaxes back into its ground state non-radiatively upon optical excitation. After roughly 30 ps, all observed signals virtually decay to zero, as the transients in Figure 6B illustrate.

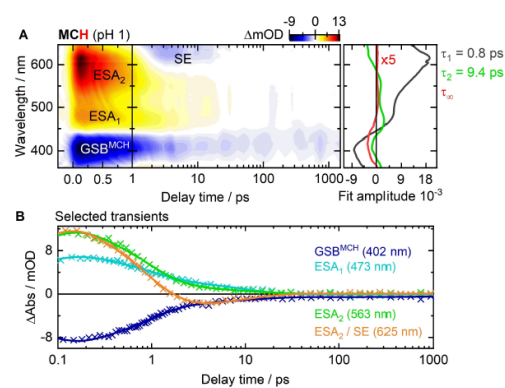


Figure 6. A) TA contour plot of MCH of compound 3 in MeOH at pH 1 (left panel) and corresponding DAS (right panel). B) Selected transients showing the time-dependent progression of the signals GSB^{MCH} (blue), ESA₁ (cyan), ESA₂ (green) and ESA₂ and SE₂ (orange).

However, a small portion of the GSB signal remains until the end of the measurement. The ESA features decay with a 0.8 ps time constant and leave two small blue-shifted positive signals around 460 nm and 550 nm behind. After approximately 1.5 ps, a small negative SE signal is noticeable above 600 nm which decays with the same time constant (9.4 ps) as the respective minor positive signals. These signals and the corresponding lifetime are assigned to the conjugate base MC^* , as they are in good agreement with the reported spectral signature, although the weak ESA around 550 nm could not be observed upon direct excitation of MC at pH 7.4 due to the superimposed prominent bleach signal.^[47] The reported lifetime of the excited MC^* state is 8.7 ps, which further confirms this assignment. The amplitude of the lifetime determined here exhibits a small contribution to the ground state recovery, which indicates a proton-recombination induced quenching process. The 0.8 ps thus models the transition from MCH^* to MC^* and is associated with the proton transfer rate $k_{pt} = 1.3 \times 10^{12} \text{ s}^{-1}$. After the depletion of the MC^* signals, there is almost no residual signal observable. Only the infinite time constant reveals a weak positive residual signal around 520 nm that corresponds to the conjugate base ground state. An additional lifetime component for the reprotonation process could not be determined.

The peculiar photodynamics of compound **3**, compared to compounds **1** and **2**, apparently arise from the additional nitro group in *ortho*-position to the acidic hydroxyl group of MCH . With a partially negative charge on both oxygen atoms of the nitro group, it may stabilize the hydroxyl proton already in the ground state and react as proton acceptor upon excitation. The photodynamics of *o*-nitro benzyl (*o*NB) compounds is known to involve an initial excited state intramolecular proton transfer (ESIPT) but typically from an alkyl α -H-atom to the nitro group.^[66–68] This results in the formation of the tautomeric *aci*-nitro form ($=NO_2H$) through parallel singlet and triplet pathways, which is frequently exploited for the subsequent removal of photolabile protecting groups.^[69,70] Regarding compound **3**, an ultrafast ESIPT to the 8-nitro group might therefore be an considerable reaction channel, although no distinguishable spectroscopic characteristics of this species are observed here. However, since MCH^* of compound **3** mostly decays into its ground state, the *o*NB group might facilitate the proton-induced recombination quenching of the MC^* state via transient *aci*-nitro formation.

Similar to Nitro-BIPS derivatives, the presence of the TTC and TTT isomer has been reported for the non-protonated dinitro-analogues.^[71] The TTC form also represents the most stable one with a main absorption band around 560 nm, while the TTT absorbance is shifted to longer wavelengths. An interconversion between the two conformers is not supposed to be a significant reaction pathway. In this study, we found no indications for discriminable isomers and the photodynamics are suggested to be dominated by the TTC isomer.

Correlation between free-energy and ESPT rates

The determined photoacidic characteristics of the three investigated compounds are summarized in Table 1. It is noticeable that the ground state pK_a values are in a similar range. This entails, that the electron distribution at the phenolate moiety is influenced in a comparable way. The attachment of the electron withdrawing nitro substituents and the incorporation of the pyridine ring evidently lower the pK_a value to a similar extent and the estimated pK_a changes upon optical excitation are quite similar, too. Compound **1** yet exhibits the lowest pK_a^* value and thus the most pronounced charge displacement in the excited state.

The relationship of the extracted proton transfer rate constants and the estimated pK_a^* values can be further rationalized by a semi-empirical correlation, which is based on the Marcus theory for electron transfer processes^[72] yet modified for proton transfer. This gives a major role to the alignment of solvent molecules in the vicinity of the dissociating proton.^[73,74] Accordingly, the proton transfer process is described by a solvent coordinate along an pre-existing hydrogen bond. The rate k_{pt} is then expressed as a function of the intrinsic solvent-dependent activation free-energy change ΔG^\ddagger of the reaction [Eq. (5)]:

$$k_{pt} = k^* \cdot \exp\left(-\frac{\Delta G^\ddagger}{RT}\right) \quad (5)$$

Here, $(k^*)^{-1}$ represents the frequency factor of the transfer reaction, R is the gas constant, and T the absolute temperature. The free energy change ΔG^\ddagger is estimated by the Marcus bond-energy-bond-order (BEBO) model [Eq. (6)]:^[75]

$$\Delta G_0 = \frac{\Delta G_0}{2} + \Delta G^\ddagger + \frac{\Delta G_0^\ddagger}{\ln 2} \ln\left(\cosh\left[\frac{\Delta G_0 \ln 2}{2\Delta G_0^\ddagger}\right]\right) \quad (6)$$

The free-energy of the charge-exchange with the solvent is given by ΔG_0^\ddagger if the total free-energy in the PT process ΔG_0 is zero [Eq. (7)]:

$$\Delta G_0 = RT \ln 10 \Delta pK_a \quad (7)$$

The correlation of the determined rate constants k_{pt} of the compounds **1–3** and the pK_a^* values, estimated by the Förster

Table 1. Photoacidic properties of the excited state PAs of the Py-BIPS derivative **1**, the nitro-BIPS compound **2** and the dinitro-BIPS compound **3** in water.

	1 (HMCH)	2 (MCH)	3 (MCH)
pK_a	3.2	3.7	3.9
ΔpK_a	–8.7	–7.9	–8.3
$pK_a^{*[a]}$	–5.5	–4.2	–4.4
τ (ROH ⁺) [ps]	1.1	2.1	0.8
$k_{pt}^{[b]}$ [s ^{–1}]	$\sim 9.1 \times 10^{11}$	$\sim 6.3 \times 10^{11}$	$\sim 1.3 \times 10^{12}$

[a] Excited state pK_a^* values, determined by the Förster cycle approach, [b] ESPT rate coefficients obtained from GLA.

cycle, is depicted in Figure 7. The solid line represents the Marcus BEBO model fit including the reported PT rates of a variety of comparable photoacids with pK_a^* values around zero or below. Several phenol,^[10] 1N,^[75,76] 2N^[16] and hydroxy quinoline (HQ)^[73,77] derivatives are shown, as well as the beforementioned QCy^[20,78] compounds.

For PT reactions to bulk water the pK_a^* is corrected for the purely electrostatic contribution $pK_{a,el} = R_D/2.3a$.^[79] A charge of -1 for the conjugate base is assumed for the Debye radius R_D and the contact radius a was set to be 6.5 \AA .^[80] In the fitting procedure, k^* was treated as a free parameter and a value of roughly $5 \times 10^{12} \text{ s}^{-1}$ was obtained which represents the proton transfer rate for an activationless process. Similarly, an intrinsic free-energy barrier of $\Delta G_0^\ddagger = 3.5 \text{ kcal mol}^{-1}$ was found, which is close to reported values.^[81,82] Consequently, the determined rates k_{pt} of the herein investigated merocyanine PAs are in well agreement with the applied literature-based structure-reactivity correlation, including super-photoacids with pK_a^* values lower than -4 . The compounds 1–3 are significantly more acidic than most naphthol derivatives. They are situated in the highly exothermic regime of the correlation curve together with the structurally related QCy7, S-QCy7 and TS-QCy compounds. The photoacidity of the studied merocyanine PAs as well as the QCy dyes is additionally enhanced due to the high degree of charge delocalization through the molecular structure and the formation of the quinoid form. The strongest reported photoacid QCy9 even exceeds the boundaries of the correlation model with its remarkable proton transfer rate of $\sim 10^{13}$.^[22,78] This is close to the stretching mode frequency of an OH-bond which is on the order of almost $\sim 10^{14} \text{ s}^{-1}$.

The findings further corroborate the estimated pK_a^* values, that were derived from equilibrium conditions. These values can therefore hardly describe dynamic characteristics of ESPT processes. For instance, the compounds 1–3 exhibit several charged functional groups, such as the flexible ionic alkyl

residues at the indoline nitrogen, that may contribute to a pre-organization of the solvent shell which facilitates the ESPT processes. The establishment of an aligned solvent network stabilized by polar or hydrogen bonding moieties affects proton dissociation differently than bulk water arrangements and also extends the lifetime such water wires.^[83] Especially the anionic sulfonate group of 1 might exert a significant effect in this fashion. For S-QCy7 and TS-QCy, bearing similar functional groups, a sulfonate-assisted proton dissociation is suggested, too.^[20] Yet, because of the different PT rates found in the protic solvents MeOH and EtOH a direct proton transfer to the sulfonate group can be excluded here.

Regarding the measurements in alcoholic solvents, it has to be noted that minor amounts of water were present in the sample solutions, because of acidification with aqueous HCl. Again, the observed varying proton transfer rates compared to water indicate that it's not a pure water cluster that is arranged around the acidic proton and that it is transferred to, although the solvent distribution might not be homogeneous.^[79] Moreover, the measurements in MeOH and EtOH revealed an increased contribution of alternative decay channels of the excited PA that lower the efficiency of proton dissociation. For the Py-BIPS derivative 1, ESPT rates of $5.9 \times 10^{11} \text{ s}^{-1}$ and $5.3 \times 10^{11} \text{ s}^{-1}$ were estimated in MeOH and EtOH, respectively. For Nitro-BIPS 2, the contribution of competing pathways such as internal conversion is even more pronounced and similar ESPT rates of roughly $4.2 \times 10^{11} \text{ s}^{-1}$ were found in both protic solvents.

Conclusion

Our results show that the phenolic protonation sites of the Py- as well as the Nitro-BIPS merocyanine photoacids investigated herein represent outstanding excited state PAs. They are capable of transferring their phenolic proton to water within a few ps upon optical excitation. Except for the dinitro derivative 3, ESPT is highly efficient and the preferred deactivation pathway in aqueous solution. Compounds 1 and 2 are even capable of ESPT to protic organic solvents, although this is less efficient and slightly slowed down compared to water. Regarding compound 3, an ESPT to the *ortho*-located nitro group seems plausible that results in the formation of a transient *aci*-nitro form. Internal conversion and proton-induced quenching of the excited conjugate base are suggested by the major deactivation channels.

The proton-release mechanism itself has not yet been monitored directly on an ultrafast time scale but distinguishable pathways have been suggested, based on observations made in different steady-state experiments. Our findings imply that the release of the phenolic proton is the first step in the photo-dynamics upon excitation of merocyanine PAs. Hence, the involvement of the aforementioned protonated spirocyan species in the ring-closure reaction can be ruled out, as the proton is released prior to ring closing. This might furthermore not only be true for the presented photoacidic Py- and Nitro-BIPS derivatives but also for protonated merocyanine deriva-

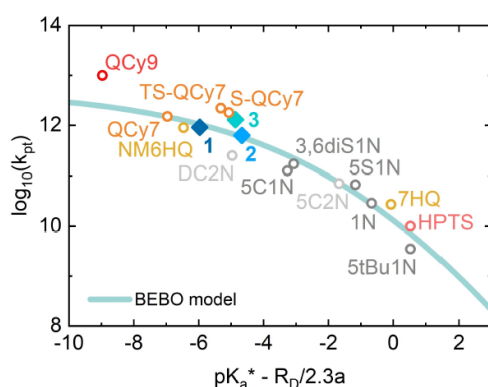


Figure 7. Free-energy correlation of determined rates k_{pt} of compounds 1, 2 and 3 (filled diamonds) compared with comparable reported photoacids (empty circles). The solid line represents the Marcus bond-energy-bond-order (BEBO) model according to Equations 5–7.

tives in general. The TA measurements of the ultrafast ESPT reactions of compound **1** and **2** enabled the assignment of the entire photoprolytic cycle, including the reprotonation in the ground state. As similar reprotonation lifetime components were determined for both compounds in water, the respective process is supposed to be solvent- and thus diffusion-controlled. The differently charged residues attached to the indoline nitrogen do not cause differences in the reprotonation dynamics. In contrast, this step seems to be influenced in the protic solvents. The negative charge of the sulfonate group of compound **1** is supposed to accelerate the reprotonation process partially with decreasing solvent polarity. On the contrary, the positive charge of the trimethylammonium group of compound **2** slows down the reprotonation in the protic solvents.

In addition, we could show that the N-protic site of compound **1** exhibits a fundamentally different reactivity. The proton is not released due to an enhanced excited state acidity, but subsequently upon isomerization to the spiropyran structure because of the ground state pK_a change. Hence, the respective protic site has to be considered a PAG rather than an excited state PA, although it also functions as a reversible photoacid. Yet, knowledge of the timescale and the dynamics of the proton-release is essential in view of potential applications of PAs. Especially when applied as a trigger for time-resolved studies of proton-mediated processes the proton transfer dynamics must be taken into account as well as limitations caused by diffusion.

The integration of the pyridine ring into the merocyanine structure of Py-BIPS derivatives has fascinating effects on the photochemistry and provides a valuable motif for future molecular design. Not only that this position allows for straightforward attachment of diverse substituents, but the photodynamics is understood quite well. Following a singlet pathway just as the original BIPS compound, the decay of the excited state is accelerated drastically starting from the unsubstituted pyridine nitrogen (MC) through the protonated (HMC) to the methylated Py-BIPS form.^[45] Besides the retained ultrafast singlet pathway, the photophysical steady-state properties are affected severely by the respective substituents and can thus be tuned. Essential differences are for example found when comparing the behaviour of compound **1** at pH 7.4 with the methylated Py-BIPS compound. The lack of the methyl group of compound **1** results in a pronounced stabilization of the ring-opened merocyanine, which allows for an operation of the photoswitch as a negatively photochromic one using visible light only.

Experimental Section

Sample preparation. The synthesis of compound **1** was performed following the published procedure via aldol condensation of the alkylated indoline and the corresponding pyridine salicylic aldehyde.^[48] The Nitro-BIPS compounds **2** and **3** were synthesized using the respective nitro-salicyl aldehydes.^[47] The spectroscopic investigation was carried out in phosphate buffered saline (PBS buffer) except for the measurements in organic solvents. The pH

values were adjusted with concentrated aqueous HCl. The absorption spectra of the particular photoisomers were recorded with a Specord S600 spectrophotometer (Analytik Jena AG, Jena, Germany) in 10 mm × 10 mm UV-grade quartz glass cuvettes (Starna GmbH, Pfungstadt, Germany). The emission spectra were measured with a JASCO FP 8500 spectrofluorometer (JASCO Germany GmbH, Groß-Umstadt, Germany) using 4 mm × 10 mm UV-grade quartz glass cuvettes (Starna GmbH). All spectra were offset corrected and the fluorescence spectra were additionally corrected for reabsorption effects as well as for the detector sensitivity of the spectrometer.

Femtosecond TA spectroscopy. The TA data were acquired with self-assembled UV/vis-pump/vis-probe setups, either supplied by a 1 kHz Ti:Sapphire amplifier (CPA, Clark-MXR, Michigan, USA) with a pulse duration of approximately 150 fs and a central wavelength of 775 nm or a Ti:Sapphire amplifier (Spitfire Ace, Newport Spectra-Physics GmbH, Darmstadt, Germany) with a pulse duration of 120 fs and a fundamental wavelength of 800 nm. The excitation pulses in the vis-range (520 nm) were generated with a non-collinear optical amplifier (NOPA) by guiding a supercontinuum pulse into a beta-barium borate crystal (β -BaB₂O₄, BBO) together with a second harmonic pulse at 388 nm. UV-pulses for excitation (420 nm) were generated by subsequent sum frequency generation (SFG) of the NOPA output and the fundamental in another BBO crystal. The white light continuum for probing (~350 nm–650 nm) was created by guiding the fundamental of the laser system through a 2 mm CaF₂ window. The samples for the time-resolved experiments were prepared in 1 mm UV-grade quartz glass cuvettes (Starna GmbH) and the concentrations were adjusted to an optical density of approximately 0.6. During the pump/probe experiments, the samples were illuminated with light emitting diodes (LED, Thorlabs Inc., Newton, New Jersey, USA) to accumulate the photoisomer of interest. In order to prevent a reexcitation of already excited molecules, the sample cuvettes were moved in an y-z-plane perpendicular to the excitation pulses. To eliminate anisotropy effects, the relative polarizations of the pump and probe pulses were adjusted to the magic angle (54.7°).

The obtained transient maps were processed and corrected for the group-velocity dispersion and the coherent artefact. The latter is fitted by a Gaussian function or its first and second derivative and subtracted from the data set. The TA spectra were then subjected to multiexponential fitting via global lifetime analysis (GLA) by using the kinetic fitting software OPTIMUS.^[52] From this, lifetime components and their corresponding decay associated spectra (DAS) could be extracted. Additionally, a lifetime distribution analysis (LDA) was performed as a complementary and model-free approach (see Supporting Information).

Acknowledgements

We thank the Deutsche Forschungsgemeinschaft (DFG) for funding through, SFB 902 „Molecular Principles of RNA-based Regulation“, GRK 1986 “CLiC – Complex Light Control” and grant number WA 1850/4-2. Open access funding enabled and organized by Projekt DEAL.

Conflict of Interest

The authors declare no conflict of interest.

Keywords: cyanines · photoacid · proton transfer · spiro compounds · ultrafast spectroscopy

- [1] S. Kohse, A. Neubauer, A. Pazidis, S. Lochbrunner, U. Kragl, *J. Am. Chem. Soc.* 2013, **135**, 9407–9411.
- [2] E. Lörcinci, M. Verhoefen, J. Wachtveitl, A. C. Woerner, C. Glaubitz, M. Engelhard, E. Bamberg, T. Friedrich, *J. Mol. Biol.* 2009, **393**, 320–341.
- [3] X. Xie, G. A. Crespo, G. Mistlberger, E. Bakker, *Nat. Chem.* 2014, **6**, 202–207.
- [4] S. Haghhighat, S. Ostresh, J. M. Dawlaty, *J. Phys. Chem. B* 2016, **120**, 1002–1007.
- [5] W. White, D. Christopher, D. M. Fabian, W. White, C. D. Sanborn, D. M. Fabian, S. Ardo, *Joule* 2018, **2**, 1–16.
- [6] X. Su, S. Voskian, R. P. Hughes, I. Arahamian, *Angew. Chem. Int. Ed.* 2013, **52**, 10734–10739; *Angew. Chem.* 2013, **125**, 10934–10939.
- [7] X. Pan, H. Li, K. T. Nguyen, G. Gru, Y. Zhao, *J. Phys. Chem. B* 2012, **116**, 4175–4181.
- [8] T. Förster, *Naturwissenschaften* 1949, **36**, 186–187.
- [9] J. F. Ireland, P. A. H. Wyatt, *Adv. Phys. Org. Chem.* 1976, **12**, 131–221.
- [10] S. Kaneko, S. Yotoriyama, H. Koda, S. Tobita, *J. Phys. Chem. A* 2009, **113**, 3021–3028.
- [11] I. Carmeli, D. Huppert, L. M. Tolbert, J. E. Haubrich, *Chem. Phys. Lett.* 1996, **4**, 109–114.
- [12] O. F. Mohammed, J. Dreyer, B.-Z. Magnes, E. Pines, E. T. J. Nibbering, *ChemPhysChem* 2005, **84125**, 625–636.
- [13] R. Simkovich, D. Huppert, *J. Phys. Chem. A* 2015, **119**, 1973–1982.
- [14] D. Huppert, L. M. Tolbert, S. Linares-Samaniego, *J. Phys. Chem. A* 1997, **5639**, 4602–4605.
- [15] L. M. Tolbert, K. M. Solntsev, *Acc. Chem. Res.* 2002, **35**, 19–27.
- [16] L. M. Tolbert, J. E. Haubrich, *J. Am. Chem. Soc.* 1990, **112**, 8163–8165.
- [17] T. G. Kim, M. R. Topp, *J. Phys. Chem. A* 2004, **108**, 10060–10065.
- [18] J. L. Pérez-Lustres, F. Rodríguez-Prieto, M. Mosquera, T. A. Senyushkina, N. P. Ernsting, S. A. Kovalenko, *J. Am. Chem. Soc.* 2007, **129**, 5408f5418.
- [19] E. A. Gould, A. V. Popov, L. M. Tolbert, I. Presiado, Y. Erez, D. Huppert, K. M. Solntsev, *Phys. Chem. Chem. Phys.* 2012, **14**, 8964–8973.
- [20] I. Presiado, N. Karton-Lifshin, Y. Erez, R. Gepshtein, D. Shabat, D. Huppert, *J. Phys. Chem.* 2012, **116**, 7353–7363.
- [21] N. Karton-Lifshin, I. Presiado, Y. Erez, R. Gepshtein, D. Shabat, D. Huppert, *J. Phys. Chem. A* 2012, **116**, 85–92.
- [22] R. Simkovich, S. Shomer, R. Gepshtein, M. E. Roth, D. Shabat, D. Huppert, *J. Photochem. Photobiol. A* 2014, **277**, 90–101.
- [23] J. V. Crivello, *J. Photopolym. Sci. Technol.* 2009, **22**, 575–582.
- [24] B. K. Keitz, R. H. Grubbs, *J. Am. Chem. Soc.* 2009, **131**, 2038–2039.
- [25] M. Shirai, I. Tsunooka, *Prog. Polym. Sci.* 1996, **21**, 1–45.
- [26] Z. Shi, P. Peng, D. Strohecker, Y. Liao, *J. Am. Chem. Soc.* 2011, **133**, 14699–14703.
- [27] N. Abeyrathna, Y. Liao, *J. Photochem. Photobiol. A* 2017, **332**, 196–199.
- [28] M. G. Ivan, J. C. Scaiano, in *Photochem. Photophysics Polym. Mater.* (Ed.: N. S. Allen), John Wiley & Sons, Inc., 2010, pp. 479–507.
- [29] Y. Liao, *Acc. Chem. Res.* 2017, **50**, 1956–1964.
- [30] J. Gurke, S. Budzák, B. M. Schmidt, D. Jacquemin, S. Hecht, *Angew. Chem. Int. Ed.* 2018, **57**, 4797–4801; *Angew. Chem.* 2018, **130**, 4888–4893.
- [31] L. Kortekaas, J. Chen, D. Jacquemin, W. R. Browne, *J. Phys. Chem. B* 2018, **122**, 6423–6430.
- [32] N. P. Ernsting, T. Arthen-Engeland, *J. Phys. Chem.* 1991, **95**, 5502–5509.
- [33] M. Rini, A. K. Holm, E. T. J. Nibbering, H. Fidler, *J. Am. Chem. Soc.* 2003, **125**, 3028–3034.
- [34] S. Silvi, A. Arduini, A. Pochini, A. Secchi, M. Tomasulo, F. M. Raymo, M. Baroncini, A. Credi, *J. Am. Chem. Soc.* 2007, **129**, 13378–13379.
- [35] M. Hammarson, J. R. Nilsson, S. Li, T. Beke-Somfai, J. Andréasson, *J. Phys. Chem. B* 2013, **117**, 13561–13571.
- [36] P. K. Kundu, D. Samanta, R. Leizrowice, B. Margulis, H. Zhao, M. Börner, T. Udayabhaskararao, D. Manna, R. Klajn, *Nat. Chem.* 2015, **7**, 646–652.
- [37] P. Remón, S. M. Li, M. Grotli, U. Pischel, J. Andréasson, *Chem. Commun.* 2016, **52**, 4659–4662.
- [38] S. Giordani, M. A. Cejas, F. M. Raymo, *Tetrahedron* 2004, **60**, 10973–10981.
- [39] Z. Shi, P. Peng, D. Strohecker, Y. Liao, *J. Am. Chem. Soc.* 2011, **133**, 14699–14703.
- [40] L. A. Tatum, J. T. Foy, I. Arahamian, *J. Am. Chem. Soc.* 2014, **136**, 17438–17441.
- [41] N. Abeyrathna, Y. Liao, *J. Am. Chem. Soc.* 2015, **137**, 11282–11284.
- [42] S. Kusumoto, T. Nakagawa, Y. Yokoyama, *Adv. Opt. Mater.* 2016, **4**, 1350–1353.
- [43] H. Chen, Y. Liao, *J. Photochem. Photobiol. A* 2015, **300**, 22–26.
- [44] V. K. Johns, Z. Wang, X. Li, Y. Liao, *J. Phys. Chem. A* 2013, **117**, 13101–13104.
- [45] J. Kohl-Landgraf, M. Braun, C. Özçoban, D. P. N. Gonçalves, A. Heckel, J. Wachtveitl, *J. Am. Chem. Soc.* 2012, **134**, 14070–14077.
- [46] C. Özçoban, T. Halbritter, S. Steinwand, L.-M. Herzig, J. Kohl-Landgraf, N. Askari, F. Groher, B. Fürtig, C. Richter, H. Schwalbe, B. Suess, J. Wachtveitl, A. Heckel, *Org. Lett.* 2015, **17**, 1517–1520.
- [47] C. Kaiser, T. Halbritter, A. Heckel, J. Wachtveitl, *ChemistrySelect* 2017, **2**, 4111–4123.
- [48] T. Halbritter, C. Kaiser, J. Wachtveitl, A. Heckel, *J. Org. Chem.* 2017, **82**, 8040–8047.
- [49] J. Zhou, Y. Li, Y. Tang, F. Zhao, X. Song, E. Li, *J. Photochem. Photobiol. A* 1995, **90**, 117–123.
- [50] S. Ruetzel, M. Diekmann, P. Nuernberger, C. Walter, B. Engels, T. Brixner, *J. Chem. Phys.* 2014, **140**, 1–10.
- [51] J. Buback, P. Nuernberger, M. Kullmann, F. Langhojer, R. Schmidt, F. Würthner, T. Brixner, *J. Phys. Chem. A* 2011, **115**, 3924–3935.
- [52] C. Slavov, H. Hartmann, J. Wachtveitl, *Anal. Chem.* 2015, **87**, 2328–2336.
- [53] E. W. Driscoll, J. R. Hunt, J. M. Dawlaty, *J. Phys. Chem. A* 2017, **121**, 7099–7107.
- [54] E. T. Ryan, T. Xiang, K. P. Johnston, M. A. Fox, *J. Phys. Chem. A* 1997, **101**, 1827–1835.
- [55] Y. Sheng, J. Leszczynski, A. A. Garcia, R. Rosario, D. Gust, J. Springer, *J. Phys. Chem. B* 2004, **108**, 16233–16243.
- [56] B. Marciniak, H. Kozubek, S. Paszyc, *J. Chem. Educ.* 1992, **69**, 247–249.
- [57] Z. R. Grabowski, W. Rubaszewska, *J. Lumin.* 1981, **24**, 559–562.
- [58] A. Weller, *Z. Elektrochem.* 1952, **56**, 662.
- [59] M. Eigen, *Angew. Chem. Int. Ed.* 1964, **3**, 1–19; *Angew. Chem.* 1963, **75**, 489–508.
- [60] N. Agmon, *J. Phys. Chem. A* 2005, **109**, 13–35.
- [61] B. Cohen, D. Huppert, N. Agmon, *J. Phys. Chem. A* 2001, **105**, 7165–7173.
- [62] N. Agmon, *Chem. Phys. Lett.* 1995, **50**, 456–462.
- [63] P. Debye, *J. Appl. Phys.* 1975, **46**, 265–272.
- [64] A. K. Chibisov, H. Görner, *J. Phys. Chem. A* 1997, **101**, 4305–4312.
- [65] H. Fidler, M. Rini, E. T. J. Nibbering, *J. Am. Chem. Soc.* 2004, **126**, 3789–3794.
- [66] H. Takahashi, Y. Watanabe, M. Sakai, M. Tachikawa, *Laser Chem.* 1999, **19**, 357–362.
- [67] J. Kohl-Landgraf, F. Bühr, D. Lefrançois, J. M. Mewes, H. Schwalbe, A. Dreuw, J. Wachtveitl, *J. Am. Chem. Soc.* 2014, **136**, 3430–3438.
- [68] P. Naumov, *J. Mol. Struct.* 2006, **783**, 1–8.
- [69] A. P. Pelliccioli, J. Wirz, *Photochem. Photobiol. Sci.* 2002, **1**, 441–458.
- [70] C. G. Bochet, *J. Chem. Soc. Perkin Trans. 1* 2002, **2**, 125–142.
- [71] M. Kullmann, S. Ruetzel, J. Buback, P. Nuernberger, T. Brixner, *J. Am. Chem. Soc.* 2011, **133**, 13074–13080.
- [72] A. O. Cohen, R. A. Marcus, *J. Phys. Chem.* 1968, **72**, 4249–4256.
- [73] M. Ekimova, F. Hoffmann, G. Bekçioğlu-Neff, A. Rafferty, O. Kornilov, E. T. J. Nibbering, D. Sebastiani, *J. Am. Chem. Soc.* 2019, **141**, 14581–14592.
- [74] O. F. Mohammed, D. Pines, E. Pines, E. T. J. Nibbering, *Chem. Phys.* 2007, **341**, 240–257.
- [75] M. Prémont-Schwarz, T. Barak, D. Pines, E. T. J. Nibbering, E. Pines, *J. Phys. Chem. B* 2013, **117**, 4594–4603.
- [76] E. Pines, D. Pines, T. Barak, B.-Z. Magnes, L. M. Tolbert, J. E. Haubrich, *Ber. Bunsenges. Phys. Chem.* 1998, **102**, 511–517.
- [77] E. Bardez, *Isr. J. Chem.* 1999, **39**, 319–332.
- [78] R. Simkovich, K. Akulov, S. Shomer, M. E. Roth, D. Shabat, T. Schwartz, D. Huppert, *J. Phys. Chem. A* 2014, **118**, 4425–4443.
- [79] E. Pines, G. R. Fleming, *J. Phys. Chem.* 1991, **95**, 10448–10457.
- [80] E. Pines, D. Huppert, N. Agmon, *J. Chem. Phys.* 1988, **88**, 5620–5630.
- [81] K. Adamczyk, M. Prémont-Schwarz, D. Pines, E. Pines, E. T. J. Nibbering, *Science* 2009, **326**, 1690–16994.
- [82] N. Agmon, *Int. J. Chem. Kinet.* 1981, **13**, 333–365.
- [83] G. Bekçioğlu, C. Alloio, D. Sebastiani, *J. Phys. Chem. B* 2015, **119**, 4053–4060.

Manuscript received: January 15, 2021
Accepted manuscript online: April 30, 2021
Version of record online: June 1, 2021

7.5 Kaiser et al., *Nucleic Acids Res.* 2021, 49

Reference [IV]

What Defines a Synthetic Riboswitch? - Conformational Dynamics of Ciprofloxacin Aptamers with Similar Binding Affinities but Varying Regulatory Potentials

C. Kaiser, J. Schneider, F. Groher, B. Suess, J. Wachtveitl,
Nucleic Acids Res. **2021**, *49*, 3661-3671.
(DOI: 10.1093/nar/gkab166)

What defines a synthetic riboswitch? – Conformational dynamics of ciprofloxacin aptamers with similar binding affinities but varying regulatory potentials

Christoph Kaiser¹, Jeannine Schneider², Florian Groher², Beatrix Suess^{2,3,*} and Josef Wachtveitl^{1,*}

¹Institute for Physical and Theoretical Chemistry, Goethe-Universität Frankfurt, Max-von-Laue-Straße 8, D-60438 Frankfurt am Main, Germany, ²Department of Biology, Technische Universität Darmstadt, Schnittspahnstraße 10, D-64287 Darmstadt, Germany and ³Centre for Synthetic Biology, Technische Universität Darmstadt, Darmstadt, Germany

Received July 09, 2020; Revised February 25, 2021; Editorial Decision February 27, 2021; Accepted March 23, 2021

ABSTRACT

Among the many *in vitro*-selected aptamers derived from SELEX protocols, only a small fraction has the potential to be applied for synthetic riboswitch engineering. Here, we present a comparative study of the binding properties of three different aptamers that bind to ciprofloxacin with similar K_D values, yet only two of them can be applied as riboswitches. We used the inherent ligand fluorescence that is quenched upon binding as the reporter signal in fluorescence titration and in time-resolved stopped-flow experiments. Thus, we were able to demonstrate differences in the binding kinetics of regulating and non-regulating aptamers. All aptamers studied underwent a two-step binding mechanism that suggests an initial association step followed by a reorganization of the aptamer to accommodate the ligand. We show that increasing regulatory potential is correlated with a decreasing back-reaction rate of the second binding step, thus resulting in a virtually irreversible last binding step of regulating aptamers. We suggest that a highly favoured structural adaption of the RNA to the ligand during the final binding step is essential for turning an aptamer into a riboswitch. In addition, our results provide an explanation for the fact that so few aptamers with regulating capacity have been found to date. Based on our data, we propose an adjustment of the selection protocol for efficient riboswitch detection.

INTRODUCTION

Synthetic biology provides innovative solutions for challenges in a wide range of fields including synthetic genetic circuit design, bio-based materials, bioremediation or diagnostics as well as various therapeutic applications in medicine. Engineered riboswitches are promising tools to explore many of the key questions in these disciplines. They are small and defined *cis*-regulatory elements, can operate protein-independently and allow for fast regulatory responses at different levels of gene regulation (e.g. transcription, translation, splicing (1)). Riboswitches usually consist of an aptamer domain and an expression platform. The aptamer domain couples the specific sensing of a small molecule to the expression of a downstream gene, thus enabling spatial, temporal and dosage-dependent control thereof. The expression platform implements the regulatory mechanism, in most cases transcription termination or sequestration of the ribosomal binding site. However, aptamers can also act without an expression platform as riboswitch by a road blocking mechanism. Such aptamers can be identified *de novo* by an *in vitro* evolution process called SELEX (Systematic Evolution of Ligands by EXponential enrichment), essentially binding any target of choice with high affinity and specificity (2,3). Depending on the nature of the target molecule and the selection protocol, it is possible to obtain aptamers with very different structures, yet similar K_D values. However, only a few of these have the potential to be further engineered into riboswitches. Interestingly, those sequences are mostly underrepresented in an enriched SELEX pool. Evidently, an *in vivo* screening subsequent to the SELEX process is required for effective identification of candidates with regulating capacity. The short list of examples for successfully engineered

*To whom correspondence should be addressed. Tel: +49 069 798 29351; Fax: +49 069 798 29709; Email: wveitl@theochem.uni-frankfurt.de
Correspondence may also be addressed to Beatrix Suess. Tel: +49 06151 16 22000; Fax: +49 06151 16 22003; Email: bsuess@bio.tu-darmstadt.de

© The Author(s) 2021. Published by Oxford University Press on behalf of Nucleic Acids Research.
This is an Open Access article distributed under the terms of the Creative Commons Attribution License (<http://creativecommons.org/licenses/by/4.0/>), which permits unrestricted reuse, distribution, and reproduction in any medium, provided the original work is properly cited.

riboswitches includes aptamers that bind theophylline (4), neomycin (5) and tetracycline (6) as well as the recent additions of ciprofloxacin- (7) and paromomycin-binding aptamers (8). Several types of engineered riboswitches have already been designed with the theophylline aptamer, such as self-cleaving ribozymes or riboswitches that regulate translation initiation by sequestration of the ribosomal binding site (9). Moreover, it has been applied as transcriptional riboswitch whose function relies on the ligand-induced formation of a terminator stem (10). The neomycin as well as the tetracycline aptamers were also implemented in ribozymes (11,12). Both aptamers have been also applied to exert translational control through ligand-dependent roadblock formation for the scanning ribosome (5,13). In this mechanism, the regulation relies on the aptamer roadblock stability, rather than the allosteric impact of ligand binding on the aptamer domain-expression platform interface. The ciprofloxacin and paromomycin aptamers have been found to be applicable for translation initiation control via roadblock formation, too (7,8). However, although some new ones have been added recently the specific selection and design of such efficient engineered riboswitches remains a challenge (14).

While the activity of natural riboswitches has specifically evolved in and is therefore adapted to specific cellular conditions and ligand concentrations, the features of *in vitro*-selected aptamers can only be shaped via restrictions in the selection protocol. In general, an exceptionally high affinity seems a pre-requisite for the development of a functional riboswitch. However, high affinity alone is insufficient to predict the activity of those aptamers (15,16). Affinity and several other factors such as the timescale of ligand binding are certainly key elements of riboswitch engineering. However, it is now common consensus that a conformational change due to ligand binding is equally essential to create a functional riboswitch in a cellular environment (8,12–14).

Furthermore, an increased complexity of both sequence and structure (17) is also beneficial and may even enhance the binding affinity (18,19). For neomycin, several aptamers with similar affinities and comparable sizes and structures that mediate different levels of regulation were systematically compared. The results revealed that preformed hairpin structures failed to perform *in vivo*, while other more complex structures with substantial conformational rearrangements were active (5,19). In general, conventional selection protocols often favour the simplest structural solution, i.e. aptamers that do not fold into very complex structures (17). Consequently, there might be a correlation between the increased enrichment of candidates with excellent binding properties, yet poor functionality for the control of gene expression.

In essence, a key question of synthetic riboswitch design has yet to be answered in full: what makes an aptamer a good riboswitch? Which factors and characteristics render an aptamer suitable as a high-performance riboswitch for reliable gene expression control? In this study, we explored a parameter potentially affecting the functionality of aptamers as riboswitches that has received little attention to date, the kinetics of the ligand binding process. For this purpose, we compared the ligand binding kinetics of three different aptamers known to bind ciprofloxacin (CFX) (7,20).

The three CFX-binding aptamers (Figure 1A) originated from the same SELEX experiment (7). Despite the obvious dissimilarities in their respective sequences and their rather diverse secondary structures, they share a common feature, i.e. their very similar K_D values. However, this similarity in affinity does not translate into equal performance, as only two of the candidates were found to be suitable riboswitches. The three aptamers represent the output of three stages in the design process: one was found after ten rounds of selection (candidate A), whereas the second was identified via *in vivo* screening of the enriched SELEX pool (candidate preRS). Interestingly, deep sequencing analysis (Figure 1C, (7)) revealed that candidate A was about 80-fold more abundant in the enriched SELEX pool than preRS. The deep sequencing data furthermore showed that the enrichment trajectory for R10K6 (precursor of A) was significantly steeper than for preRS, thus demonstrating that the selection protocol clearly favours R10K6. Finally, the third construct RS was obtained by distinct mutations of single nucleobases close to the binding pocket region of preRS to optimize activity (Figure 1B). In each of the investigated aptamers, the inherent fluorescence of the ligand is equally quenched upon binding which provides a convenient spectroscopic read-out for ligand binding studies. Our results for the binding kinetics and the Mg^{2+} dependence of the aptamers described above revealed key differences that we assume to be critical for riboswitch engineering of *in vitro* selected aptamers.

MATERIALS AND METHODS

Preparation of RNA aptamers

For *in vitro* analysis, RNA was transcribed from PCR-generated templates, all containing at least one 5'-terminal guanosyl residue to facilitate *in vitro* transcription using T7 RNA polymerase. For this, two oligonucleotides were designed with an overlap of 30 bp (CCAAGTAATACGAC TCACTATAGGGAGACGCAACAGACTAGGTTGT GACTGCTTAGGCAGTTGTGGACGG and GTGACG CGACTAGTTACGGACCTCTGGTGGGCTTAGCC GTCCACAACCTGCCTAAGCAGTCCACAACCTAGTC for A, CCAAGTAATACGACTCACTATAGGGAGA CGCAACTGAATGAACATAAGTGAACGCGACTC TATCTCCCTAACTAGG and GTGACGCGACTA GTTACGGATCGTGTAACCTCCGTGCCGCTATAT GACTCCTAGTTTAGGGAGATAGAGTCGGGTTTC for preRS and CCAAGTAATACGACTCACTATAGG GAGACGCACCTGAATCAACATACGTGAACG CGACTCTATCTCCCAAATTAGGCGTCAG and GTGACGCGACTAGTTACGGATCGTGTAACCTCC GTGCCGCTATCTGACGCCTAATTTGGGGAGA TAGAGTCGCGTTCACG for RS) and amplified using Q5® High-Fidelity DNA polymerase (NEB) according to the supplier's instructions. After ethanol precipitation, the DNA template was used for *in vitro* transcription by T7 RNA polymerase (NEB) as reported previously (7). The RNA was gel purified (21) and molarity was determined by spectrophotometric measurement using NanoDrop 1000 Spectrophotometer (Thermo Scientific).

The RNA samples were stored in highly purified water at -20°C . Prior to each experimental use, the RNA was pre-

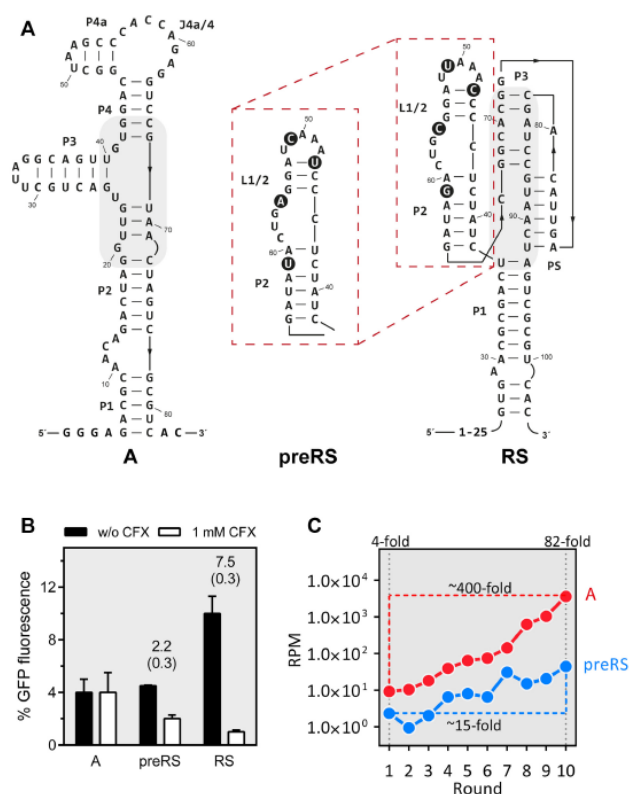


Figure 1. (A) Secondary structures of the aptamer A and the two riboswitches preRS and RS, confirmed by *inline* probing (7, 20). Nucleotides that differ between preRS and RS are highlighted with black circles. Regions involved in ligand binding are shaded in grey. (B) Regulation of GFP expression. The aptamer sequences A, preRS and RS are located in the 5' untranslated region of a GFP reporter gene in *Saccharomyces cerevisiae*. GFP expression is displayed in the absence (black bar) and presence of 1 mM CFX (white bar). The dynamic range of regulation is reported above the bars together with the corresponding errors in parenthesis. (C) Deep sequencing data from the SELEX experiment with CFX as target. Reads per million (RPM) are displayed for candidate A (red) and preRS (blue) that was further developed into RS (7).

pared using the following folding procedure: the aqueous RNA solutions were heated to 95°C for 5 min and snap-cooled on ice for 5 min. Next, buffer was added to a final concentration of 40 mM HEPES, 125 mM KCl, 5 mM MgCl₂, pH 7.4 and equilibrated for 20 min. The composition of this buffer is equivalent to the SELEX buffer.

Fluorescence titration experiments

Dissociation constants (K_D) for CFX@RNA complexes were determined by measuring the fluorescence quenching as a function of RNA concentration in the presence of a fixed CFX concentration of 50 nM. Fluorescence intensities were measured on a Fluorolog FL3-22 (Horiba Jobin Yvon) with an excitation wavelength set to 335 nm (slit 5 nm) and an emission wavelength of 420 nm (slit 5 nm). The integration time was set to 0.5 sec and temperature was adjusted to 25°C. In between the addition of RNA, the solution was stirred for 1 min and equilibrated for an extra

minute. For the titration experiments, 50 nM CFX in 40 mM Hepes, 125 mM KCl, 5 mM MgCl₂, pH 7.4 (F_0) was mixed with increasing amounts of gel-purified and folded RNA (see above: Preparation of RNA aptamers) and fluorescence intensity was measured (F). Curve fitting was done using Prism (GraphPad Software) and non-linear regression analysis with the modified Hill equation (1) by least squares fitting:

$$\frac{F}{F_0} = B_{\max} \frac{X^h}{(K_D^h + X^h)} \quad (1)$$

with B_{\max} = maximum binding, h = hill slope, X = concentration of RNA.

Time-correlated single photon counting

Spectroscopic measurements of fluorescence decay of the ligand CFX and the ligand-aptamer complexes were carried

out in the same buffer as used in the SELEX procedure and the fluorescence titrations. The experiments were performed with a self-assembled time-correlated single photon counting (TCSPC) setup incorporating a single-photon detection photomultiplier tube (PMT, PMA-C 182 M, PicoQuant, Berlin, Germany) and a TimeHarp 260 PICO Single PCIe card (PicoQuant) for data processing (22). Pulsed orthogonal excitation of the samples was achieved with a pulsed LED PLS310 (PicoQuant). Multi-exponential fitting was performed with FluoFit Pro 4.6 [PicoQuant, (23)]. The samples were measured in 4×10 mm quartz glass cuvettes at concentrations of $1 \mu\text{M}$ and $2 \mu\text{M}$ for CFX and RNA aptamers, respectively.

Stopped-flow spectroscopy

Stopped-flow measurements were carried out with a SFM-20 device (Bio-Logic Science Instruments, Seyssinet-Pariset, France) with Berger Ball mixer and a cuvette (FC08) with a volume of $20 \mu\text{l}$ and a light path of 0.8 mm attached. The stopped-flow device was coupled to a FP-8500 spectrofluorometer (Jasco, Groß-Umstadt, Germany) with a glass-fibre module (OBF-832, Jasco). The detected PMT signal was transferred to a transient recorder board (PCI-6052E, National Instruments, Austin, USA) using an A/D-adaptor (BNC-2110, National Instruments). Data acquisition was controlled with the Bio-Kine 32 software (Version 4.42, Bio-Logic Science Instruments). For every single mixing experiment, 33 ml of the two sample solutions were injected into the mixing compartment via syringes (Hamilton 1010C, Hamilton Company, Reno, USA) with a flow rate of 6.95 ml/s. The injection was stopped by a hard-stop valve which determined the start of the observed binding dynamics. The excitation wavelength for the measurements was 330 nm and fluorescence emission was detected at 420 nm and a 90° angle. The applied RNA concentration was $2 \mu\text{M}$ and the CFX concentrations were 4 , 8 , 12 , 16 and $20 \mu\text{M}$, both in 40 mM HEPES, 125 mM KCl, 5 mM MgCl_2 , pH 7.4 . The RNA was folded before use as described above (see Preparation of RNA aptamers). 20 – 30 traces were averaged for each concentration. All of the traces were baseline-corrected and normalized prior to the kinetic model analysis, which was carried out with the DynaFit4 software (24) (Biokin Ltd, Watertown, USA). A detailed description of the raw data processing routine (Supplementary Figure S2) and subsequent analysis (Supplementary Tables S2–S7 and Supplementary Figures S3–S5) may be found in the Supporting Information (SI).

RESULTS

Mg^{2+} dependence of ligand binding

Despite the relatively low chemical diversity compared to proteins, the conformational space of RNA is enormous. The distribution of defined structures can be greatly altered by interactions with substrate molecules or ions. There may even be novel structures that would not be stable without those interactions (25). Cations, especially divalent Mg^{2+} ions, are essential in stabilizing tertiary RNA structures and are thus required for most aptamers to fold into their native and binding-competent state. However, it is suggested

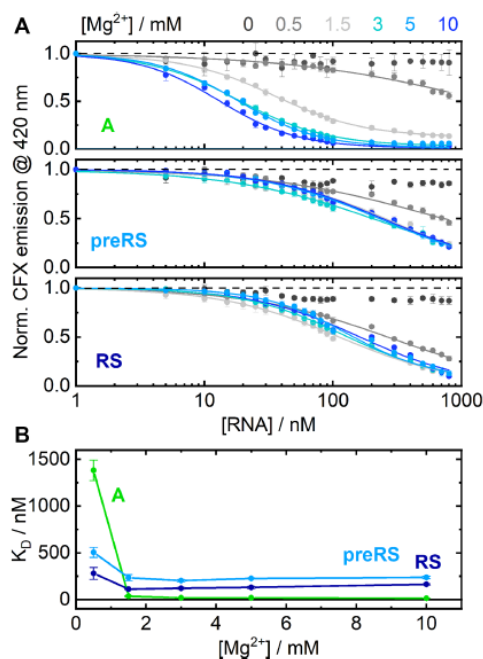


Figure 2. (A) RNA-titration series, showing the detected CFX emission at constant Mg^{2+} concentrations for candidate A (upper panel), preRS (middle panel) and RS (lower panel). (B) Calculated K_D values plotted as a function of the applied Mg^{2+} concentrations. Candidate A is shown in green, preRS in light blue and RS in dark blue.

that excess availability of divalent cations favours the accumulation of aptamers with poor structural complexity. Generally, more complex aptamer structures are assumed to undergo more profound conformational changes upon ligand binding (17). Although SELEX is often carried out at high ionic concentration conditions (5 – 10 mM Mg^{2+}) to obtain well-binding aptamers, synthetic riboswitches have to be able to cope with lower Mg^{2+} concentrations (around 1.5 mM) to remain functional in physiological conditions. Therefore, our first approach was to investigate whether the Mg^{2+} concentration had an influence on the ligand binding of our aptamer candidates in the relevant concentration range of Mg^{2+} .

We conducted fluorescence titration experiments at defined Mg^{2+} concentrations (Figure 2A). Comparison of the corresponding apparent K_D values (Figure 2B) revealed differences in RNA behaviour. Aptamer A showed a clear cation dependence at low Mg^{2+} concentrations. In the absence of divalent cations, no ligand binding to aptamer A was observed at all. At 0.5 mM Mg^{2+} , a drop in fluorescence of almost 50% was detected. Evidently, small amounts of Mg^{2+} are sufficient to enrich preformed structures and induce ligand binding to a considerable extent. From a concentration of 1.5 mM Mg^{2+} , the detected emission already decreased to a residual level. The conformational

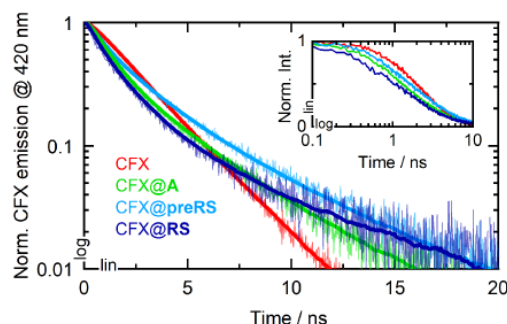


Figure 3. Fluorescence decays of CFX (red) and the ligand-bound complexes CFX@A (green), CFX@preRS (light blue) and CFX@RS (dark blue). The solid bold lines represent the fitted curves, yet they are omitted in the inset for better data visibility.

distribution was therefore mostly shifted towards binding-competent structures. The corresponding apparent K_D values were all in the low nanomolar range with no significant improvements upon further increase of the Mg^{2+} concentration. They reach a minimal K_D value of ~ 13 nM at 10 mM Mg^{2+} .

For the candidates preRS and RS, no evident Mg^{2+} dependence could be observed. At 0.5 mM Mg^{2+} , the conformation shift of candidate preRS towards a binding-competent state seemed to be already mostly complete, as implied by a total fluorescence drop of $>50\%$. Finally, very similar binding curves from a Mg^{2+} concentration of 1.5 mM upwards were detected for both active candidates. These experiments show that there are differences in ligand binding depending on the concentration of Mg^{2+} , but only at very low concentrations. No changes were observed at physiological concentration (1.5 mM) or higher (concentration used for the SELEX). Consequently, we decided to retain a concentration of 5 mM for all subsequent experiments to mimic SELEX conditions.

Fluorescence quenching

In a next step, we measured the fluorescence quenching effects upon binding. Fluorescence decays of CFX and the CFX@RNA complexes were recorded with time-correlated single photon counting (TCSPC) experiments (Figure 3). The datasets were subsequently analyzed by multi-exponential data fitting to determine the corresponding fluorescence lifetime contributions. The ligand CFX was measured in different buffer compositions because fluoroquinolones are known to form various types of metal complexes, which might influence the photophysical properties (26). The respective data and a description of the fitting routine may be found in the SI (see Supplementary Figure S1 and Supplementary Table S1). Most prominently, CFX bears a 1,3-dicarbonyl functional group that enables the formation of dimers like $[Mg(CFX)_2]$. The carbon acid or the piperazine moiety might also be able to form metal chelates. Without cations present, a mono-exponential decay with a lifetime of 1.3 ns was observed. Upon addition of potas-

sium or Mg^{2+} , biexponential decays were recorded with minor lifetime components around 6 ns. The faster components slightly differ from the 1.3 ns lifetime, supposedly due to the multiple coordination sites for metal ions and for water molecules. Moreover, CFX exhibits several protonation sites with pK_a values in the neutral regime, which can also have a significant impact on the fluorescence features (27,28).

Under buffer conditions applied during the SELEX, i.e. containing potassium as well as Mg^{2+} , the fluorescence decay of CFX was modelled biexponentially with a main time constant $\tau_1 = 1.3$ ns, accounting for the pure ligand (Table 1). A minor and slower component $\tau_2 = 2.9$ ns was assigned to the decay of chelate complexes mainly formed with Mg^{2+} . The average lifetime of CFX under these buffer conditions was determined to be 1.9 ns. For the CFX@RNA measurements, an additional sub-ns component was required for adequate fitting of the decay curves. This time constant has the largest amplitude of the corresponding decay curves and thus reflects the accelerated fluorescence emission due to quenching (τ_q) within the CFX@RNA complexes for all three candidates. For aptamer A, the contribution of $\tau_q = 0.64$ ns was the largest with 77%. The quenching lifetimes of the candidates preRS and RS were 0.43 ns and 0.49 ns, respectively, and showed significantly lower amplitudes.

These lower amplitudes are in line with the higher binding affinity of A in the given experimental conditions. The time constants τ_1 are in the range of 1.9–2.5 ns for the CFX@RNA measurements. They correspond to the residual unbound ligand that still fluoresces strongly and its resulting metal and hydrate complexes formed in aqueous solution. The lifetimes τ_1 found in the preRS and RS measurements are well in agreement with the average lifetime of the ligand CFX in buffered solution and their amplitudes are higher by a factor of 2.6 than that of the corresponding lifetime of CFX@A. The minor lifetime components τ_2 are clearly slowed down in each case and show amplitudes smaller than 10%. As lifetimes of roughly 6 ns were also found for the ligand in different buffer conditions, those lifetimes could again be assigned to particular chelate complexes or protonated states of CFX. Furthermore, the respective lifetimes might also account for discriminative aptamer-ligand complexes where the ligand encounters a different aptamer conformation, which may in turn affect emission properties. Although it is not clear whether the binding of CFX is stabilized via e.g. H-bonds or stacking interactions, the similar fluorescence quenching lifetimes suggest similar microenvironments for the ligand embedded in the binding pocket of preRS and RS compared to A. Possible quenching mechanisms are typically divided into static and dynamic quenching. Static quenching refers to the formation of an aptamer-ligand complex with altered ground state properties, so that the population of the original fluorescent state of the pure ligand is inhibited (29). Since the absorption spectrum of the ligand does not change upon addition of RNA and residual fluorescence at the same wavelength is detected for the free ligand as well as for the bound states, static quenching is unlikely to be the main mechanism. However, dynamic quenching refers to any interaction of the aptamer with the excited state of the fluorophore.

Table 1. Fluorescence lifetimes τ and their standard error values determined by multi-exponential curve-fitting with corresponding amplitudes A in percent provided in parentheses together with their relative errors.

	$\tau_q^{[a]} / \text{ns} (A_q / \%)$	$\tau_1^{[b]} / \text{ns} (A_1 / \%)$	$\tau_2^{[b]} / \text{ns} (A_2 / \%)$	χ^2
CFX	–	1.28±0.02 (65±2)	2.92±0.04 (35±2)	1.003
CFX@A	0.64±0.03 (77±3)	2.48±0.05 (14±5)	6.5±0.3 (9±5)	0.991
CFX@preRS	0.43±0.03 (53±5)	2.22±0.04 (37±2)	6.3±0.2 (10±3)	1.034
CFX@RS	0.49±0.03 (58±5)	1.90±0.06 (36±3)	8.3±0.5 (6±5)	1.051

^[a] τ_q represents the fluorescence quenching lifetimes of the CFX@RNA complexes, ^[b] τ_i represent the remaining consecutively numbered lifetime components.

As an accelerated fluorescence lifetime of the CFX@RNA complexes was detected, we assume that the emission of CFX is quenched dynamically in the excited state of the complexes.

Fluorescence-monitored binding kinetics

In the stopped-flow experiments, the decrease of CFX emission caused by aptamer binding was monitored in a time-resolved manner on the milliseconds timescale. The ligand CFX was supplied in excess relative to the specific RNAs (2, 4, 6, 8 and 10 equivalents = eq), which resulted in pseudo-first order complex formation. Due to the saturation of the particular RNAs with supplied ligand, a similar signal amplitude was obtained for each measurement series. The data were recorded under similar conditions as in the SELEX procedure. Hence, both the ligand CFX and the candidate RNAs were supplied in the same buffer conditions in the separate syringes of the stopped-flow apparatus, so that the buffer conditions were maintained upon mixing of components. RNA was properly folded prior to usage as described. At the applied Mg^{2+} concentration (5 mM), the ensemble of present RNA structures was expected to be mostly shifted towards the preformed state for each of the candidates, as shown by the Mg^{2+} -dependent titrations. The observed kinetics should therefore merely reflect the ligand binding event of binding-competent RNA conformations and no superimposed conformational dynamics should impede data analysis. The processed and averaged time-dependent traces of the CFX emission during ligand binding are illustrated in Figure 4.

In each case, binding is clearly accelerated with increasing amounts of ligand added. In essence, the observed dynamics were significantly faster for the aptamer A than for both potential riboswitches. For the 2 eq curves, the equilibrium level of the aptamer A was already reached after roughly 150 ms, whereas it took ~300 ms for RS and 400 ms for preRS. Moreover, the acceleration of the dynamics of A is almost at its limit with 6 eq of CFX, whereas the dynamics become continuously faster for higher amounts of supplied ligand for the potential riboswitches. Under pseudo-first order conditions, fitting the obtained stopped-flow transients monoexponentially allows for an estimation of the observed association rate for each ligand concentration. Plotted against the corresponding CFX concentration, this reveals the apparent k_{on} through linear regression (Figure 5).

Although a simple irreversible one-step binding model is clearly just an approximation of the actual kinetics, a monotonous increase of the association rate is evident. This

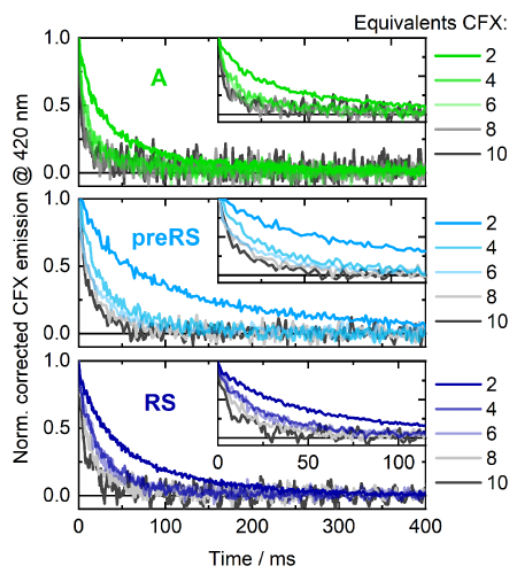
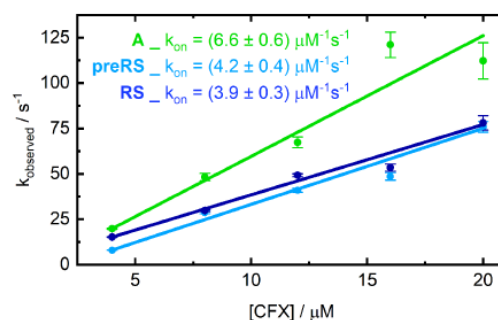
**Figure 4.** Fluorescence-detected stopped-flow measurements of the CFX-binding dynamics of the aptamer A (upper panel) and the riboswitches preRS (middle panel) and RS (lower panel) upon mixing the RNAs with different concentrations of ligand (relative equivalents indicated).**Figure 5.** Observed first order association rates obtained from monoexponential fitting of the stopped-flow traces plotted against the ligand concentration. The slope of the linear fits corresponds to the overall rate k_{on} .

Table 2. Reaction schemes of tested binding models.

Model	Reaction scheme
1	$\text{RNA} + \text{CFX} \xrightleftharpoons[k_{-1}]{k_1} \text{CFX@RNA}$
2	$\text{RNA}_{\text{inactive}}^{[a]} \xrightleftharpoons[k_{-1}]{k_1} \text{RNA}_{\text{active}}^{[b]} + \text{CFX} \xrightleftharpoons[k_{-2}]{k_2} \text{CFX@RNA}_{\text{active}}$
3	$\text{RNA} + \text{CFX} \xrightarrow{k_1} \text{CFX@RNA}^* \xrightleftharpoons[k_{-2}]{k_2} \text{CFX@RNA}$
4	$\text{RNA} + \text{CFX} \xrightleftharpoons[k_{-1}]{k_1} \text{CFX@RNA}^* \xrightleftharpoons[k_{-2}]{k_2} \text{CFX@RNA}$
5	$\text{RNA} + \text{CFX} \xrightleftharpoons[k_{-1}]{k_1} \text{CFX@RNA}^* \xrightarrow{k_2} \text{CFX@RNA}$

^[a] RNA_{inactive} – non-binding state of the aptamer, ^[b] RNA_{active} – binding-competent state of the aptamer, ^[c] CFX@RNA* – intermediate bound state.

indicates an induced fit mechanism of already pre-existing binding-competent aptamer structures (30) and confirms the preformation of the RNA candidates in the given conditions. However, there are no firm criteria to exclude the contribution of conformational selection (31). The existence of multiple active or inactive conformations cannot be ruled out, especially if the equilibration between those structures is even faster than the ligand binding event and thus not rate-limiting. For our data, the association rate k_{on} reached a plateau at ligand CFX concentrations higher than 10 equivalents relative to the applied RNA, which could indicate such a limitation by conformational selection in this ligand concentration range. A comparable behaviour was already observed for other *in vitro* selected aptamers like the theophylline-binding aptamer (32), whose apparent k_{on} is one order of magnitude smaller than the rates determined here. For natural riboswitches, e.g. the purine riboswitch (33), a rate-limiting conformational selection was also reported.

For more detailed analyses, the obtained and processed datasets were fitted globally (i.e. each time trace of the particular concentration series simultaneously) to multiple simple and meaningful kinetic models including different combinations of reversible and irreversible binding steps. The tested models are listed in Table 2 and the datasets were fitted with the corresponding sets of differential equations resulting from the reaction mechanisms. A detailed explanation of the fitting routine of the processed data and the particular differential equations may be found in the SI, complete with the obtained fit results (Supplementary Tables S2–S7) and the fitted curves (Supplementary Figures S3–S5).

Comparison of the respective fit qualities by means of the Akaike information criterion (AIC) and the Bayesian information criterion (BIC) allowed an evaluation of the applied models (24). Both criteria estimate relative fit qualities considering both the number of free parameters included in a particular statistical model and its accuracy (root mean square deviation, RMSD) to avoid over-parametrization. Compared to the AIC, the BIC penalizes the number of parameters more severely. For model assessment, the differences ΔAIC and ΔBIC of the compared models were calculated.

Table 3. Rate constants determined from kinetic analysis for the reversible one-step model 1. The ΔAIC and ΔBIC criteria show the fit accuracies compared to the other models.

	$k_1 / \mu\text{M}^{-1}\text{s}^{-1}$	k_{-1} / s^{-1}	RMSD ^[a]	$\Delta\text{AIC}^{[b]}$	$\Delta\text{BIC}^{[c]}$
A	7.78±0.09	0.33±0.03	0.044783	801	788
preRS	3.61±0.03	0.09±0.01	0.030391	742	733
RS	5.21±0.04	<10 ⁻⁶	0.03298	701	694

^[a] Obtained root mean square deviation values, ^[b] Akaike information criteria differences to the most accurate model, ^[c] Bayesian information criterion differences to the most accurate model.

In the simplest model 1, a reversible one-step binding was assumed. In contrast to the mono-exponential fitting shown before, this model takes the back reaction into account and therefore allows for an estimation of the apparent dissociation rate k_{-1} . The determined k_1 values, based on a reversible one-step binding, are in agreement to the k_{on} values obtained from mono-exponential fitting (Table 3). The obtained fit qualities were the poorest of all, which is reflected by the highest values for ΔAIC and ΔBIC . However, the estimated back rates k_{-1} considerably decrease from **A** to **preRS** to **RS**. For the active candidate **RS**, a meaningful value for k_{-1} could not be determined because the respective rate constant approached zero. The dissociation rate of **RS** is therefore almost negligible and the reduced k_{-1} values of **preRS** and **RS** seem to correlate with their increased *in vivo* activities.

Conformational selection (model 2) should play only a minor role under the given experimental conditions. The reaction scheme assumes a preformation of the aptamer from an inactive to an active binding-competent conformation, which then undergoes ligand binding in one reversible step. Indeed, application of model 2 did not result in a sufficient goodness of fit for any of the RNA candidates. The obtained rates of the ligand binding step were slightly higher than the association rates from model 1 and the preformation occurs on a similar timescale for **A** and **preRS**. Interestingly, the prefolding rate of the candidate **RS** is determined to be 8 times higher than those of the other two candidates. The two irreversible steps assumed in model 3 would be relevant if two highly favoured structural rearrangements occur sequentially. Such a behaviour was e.g. shown for the aptamer domain of the guanine-sensing riboswitch (34). However, model 3 also failed as the model of choice for aptamers explored here, according to the obtained fit criteria.

The most suitable two-step models for the three candidates and the determined rates and fit quality criteria are summarized in Table 4. For the binding kinetics of the aptamer **A**, the reversible two-step model 4 is the most adequate description, as it scores the lowest RMSD and both likelihood criteria ΔAIC and ΔBIC are zero. The analysis revealed the highest bimolecular association rate ($k_1 = 10 \mu\text{M}^{-1}\text{s}^{-1}$) and the lowest back-rate ($k_{-1} = 1.6 \text{s}^{-1}$) of the first binding step of all candidates. This step is considered as an initial association of the ligand to the binding site of the RNAs, presumably driven by unspecific electrostatic interactions or even hydrogen bonding. Starting from the intermediate complex CFX@RNA*, the formation of the final ligand-bound of **A** state is favoured because the rate

($k_2 = 4 \text{ s}^{-1}$) is 2.5 times higher than the dissociation rate k_{-1} . The second step accounts for a tightening of the binding pocket, accompanied by the establishment of specific interactions with CFX. The reverse rate of the second step ($k_{-2} = 2.3 \text{ s}^{-1}$) is significantly lower than the forward rate but in the same order of magnitude. Similar to aptamer A, application of model 4 also yielded the lowest RMSD and ΔAIC for preRS, although the determined rates are quite different. The initial association step is clearly less favoured ($k_1 = 4.33 \mu\text{M}^{-1}\text{s}^{-1}$) and the dissociation rate is increased ($k_{-1} = 5.7 \text{ s}^{-1}$). Furthermore, the back-rate of the second step ($k_{-2} = 0.06 \text{ s}^{-1}$) is almost negligible as it is substantially smaller than the forward rate ($k_2 = 13.2 \text{ s}^{-1}$). The k_2/k_{-2} ratio for aptamer A is only 1.8, but for preRS it is as high as 220. Although model 4 scores a slightly lower RMSD than model 5 for preRS, the latter is preferred because of the greater simplicity of the model, which is indicated by its lower ΔBIC value. The determined rates are all slightly lower than those obtained from model 4. Consequently, the second binding step of preRS is not only much faster than in the case of aptamer A, but it is virtually irreversible. For the final construct RS, model 4 achieves very good fit values, but model 5 is clearly the best approximation according to its lowest RMSD value and likelihood criteria. The determined association rate of RS ($k_1 = 7.6 \mu\text{M}^{-1}\text{s}^{-1}$) is almost two times higher than that of preRS. Additionally, the dissociation rate is lower ($k_{-1} = 3.1 \text{ s}^{-1}$), so the initial binding of RS proceeds much faster. The second binding step of RS exhibits the highest rate ($k_2 = 23 \text{ s}^{-1}$) among all investigated RNAs. Compared to preRS, it is accelerated by almost a factor of two and compared to A, it is even faster. Hence, there is a clear trend towards an accelerated conformational adaptation that seems to correlate with the increasing regulatory potential of the three RNA candidates.

Interestingly, the obtained reaction rates of the initial step substantially differ between the potential riboswitches and the inactive aptamer. The association of CFX with Aptamer A is significantly favoured over CFX association with the riboswitches, which indicates profound differences in the degree of preformation and the interactions established upon first encounter. In all likelihood, aptamer A exists in a rather compact conformation, due to the increased number of incorporated Mg^{2+} ions and is thus highly preformed. The initial binding to the potential riboswitches is supposedly less specific and the binding pocket less structured. However, the essential difference of the binding kinetics is the intense acceleration of the second step. The negligible rate k_{-2} renders the respective step virtually irreversible for preRS and RS during the recorded association phase.

We assume that for the riboswitch candidates, the second binding step corresponds to a highly favoured structural adaptation of the RNA that results in a tightening of the binding pocket. Put another way, a 'nearly' irreversible final binding step could indicate a structural rearrangement so substantial that it can mediate riboswitch activity. In addition, a distinct correlation between the reduction of the respective back-reaction rate and an increasing riboswitch activity in the order from candidate A to preRS to RS is observed.

DISCUSSION

Previous studies suggest that the overall association rate and the aptamer-ligand complex lifetime are essential characteristics to describe riboswitches, rather than the K_D value (16). Moreover, significant differences between kinetically derived K_D values and equilibrium values of *in vitro* selected aptamers are observed quite often (35). Such differences are of particular importance since *in vivo* riboswitch activity can generally rely on kinetic or thermodynamic control, which is apparently unknown for *de novo* engineered riboswitches. For kinetically driven riboswitches, the amount of ligand necessary for significant regulation is typically higher than the K_D derived estimate (36). The regulation mechanism for such riboswitches relies on the competition of ligand binding and riboswitch folding. However, the selection protocol prefers enrichment of thermodynamically controlled aptamers where the ligand-bound state is energetically favoured.

Binding kinetics similar to those observed here, i.e. an almost irreversible final binding step that accounts for a structural adaptation of the RNA as for candidate RS, were reported for the tetracycline-binding aptamer. The forward rate of the first step is only slightly faster as determined for candidate RS, but the back rate of the tetracycline-binding aptamer is drastically higher by a factor of almost 12. Moreover, the rate of the second irreversible step is as high as 155 s^{-1} (37). This step is supposed to rely on a ligand-induced structural adjustment of the aptamer (38,39). A reversible two-step binding mechanism has also been found to govern the neomycin-binding aptamer (N1), where the back rate of the second step is significantly reduced, relative to the forward rate (40). Additionally, a significant conformational adaptation was demonstrated for the ligand binding of the N1 aptamer that seems to be vital for its *in vivo* activity. Among the multiple neomycin-binding aptamers that were obtained via *in vitro* selection, other candidates with similar nanomolar K_D values but different riboswitching capabilities were identified by parallel *in vivo* screening (41). By comparing the NMR structures of the free and the ligand-bound states of three of those aptamers, a clear correlation between their structural complexity and the degree of preformation and conformational switching upon binding was shown (5). Consistently, the greatest regulatory potential is reported for the N1 aptamer as it exhibits the most profound structural change. For the theophylline aptamer, a similar linear increase of the apparent k_{on} was observed at low ligand concentrations in the micromolar range. However, a conformational preformation was identified as the rate-limiting step at millimolar theophylline concentrations and a structural adaptation was shown to occur upon ligand binding, which renders the aptamer functional *in vivo* (32). By comparing two selected streptomycin-binding aptamers with varying ligand specificities, the conformational change upon ligand binding was even assigned as the driving force for ligand discrimination (42). Furthermore, a significant stabilization of the streptomycin aptamer structure due to ligand binding is reported, indicating an energetically favoured complex formation (43).

Analogous binding kinetics have been reported for the aptamer domain of the purine riboswitch, thus indicating

Table 4. Rate constants determined from kinetic analysis for the most suitable two-step binding models 4 and 5 and RMSD values of the corresponding fits. The ΔAIC and ΔBIC criteria show the fit accuracies compared to the other models.

	Model	$k_1 / (\mu\text{M s})^{-1}$	k_{-1} / s^{-1}	k_2 / s^{-1}	k_{-2} / s^{-1}	RMSD ^[a]	$\Delta\text{AIC}^{[b]}$	$\Delta\text{BIC}^{[c]}$
A	4	10 ± 0.2	1.6 ± 0.2	4 ± 0.2	2.3 ± 0.2	0.041255	0	0
	5	10 ± 0.2	0.8 ± 0.2	6 ± 0.3	—	0.041582	75	69
preRS	4	4.33 ± 0.06	5.7 ± 0.5	13.2 ± 0.8	0.06 ± 0.03	0.028187	0	5
	5	4.31 ± 0.06	5.4 ± 0.4	12.1 ± 0.7	—	0.028198	2	0
RS	4	7.6 ± 0.1	3.1 ± 0.6	23 ± 1	0.27 ± 0.05	0.030741	4	10
	5	7.62 ± 0.11	2.9 ± 0.7	23 ± 1	—	0.030736	0	0

^[a] Obtained root mean square deviation values, ^[b] Akaike information criteria differences to the most accurate model, ^[c] Bayesian information criterion differences to the most accurate model.

that this binding behaviour is not limited to synthetic riboswitches, but can also be observed in their natural counterparts (33). A slow interconversion of an ensemble of disordered RNA structures towards one ligand binding state is preceding a highly favoured conformational change of the binding pocket to enclose the ligand. The same is true for the guanine-binding riboswitch, where the accommodation of the ligand can even be described by two consecutive irreversible steps to form the final complex (34). For the thiamine pyrophosphate (TPP) riboswitch, a pronounced ligand-induced structural adaption was confirmed by means of fluorescence stopped-flow experiments with 2-aminopurine labelled RNA variants (44). Moreover, kinetic analyses of ITC data revealed the dynamics of the two-step binding sequence, with a rapid initial association of TPP to the aptamer domain followed by the adjustment of the aptamer conformation. The back rate of the second step was determined to be several orders of magnitude smaller than the forward rate, indicating a virtually irreversible ligand induced folding (45). Other examples with similar trends are the adenine-sensing riboswitch (16) or the flavin mononucleotide (FMN) riboswitch (46). Therefore, it is plausible that the underlying ligand binding kinetics beyond the binding constant also dictate the regulatory potential of RNA aptamers. An irreversible second binding step apparently accounts for a highly favoured structural adjustment and extends the lifetime of the ligand-aptamer-complex, which seems to be a prerequisite for its functionality as a riboswitch. Furthermore, examples of similar binding kinetics are found for many possible regulatory mechanisms in both natural and engineered riboswitches. For some mechanisms of riboswitches, it is essential that ligand binding induces a structural change of the binding pocket that also affects the conformation of the expression platform. The formation of a terminator stem adjacent to the aptamer domain is required for transcriptional control, and the relative stabilities of the antiterminator and terminator conformations are thought to be an important parameter (47). Translation initiation is mechanistically based on the sequestration of the ribosomal binding site located at the junction of aptamer domain and expression platform. The roadblock mechanism that many engineered riboswitches can exert may be an outstanding example in this regard, as the aptamer alone performs the function as such. However, the reported successful applications of the tetracycline or the neomycin aptamer clearly reveal that also sophisticated regulatory mechanisms can be realized by engineered riboswitches in addition to roadblock formation. Further-

more, conformational studies on several riboswitches show that ligand induced adaption of the binding pocket region also results in subtle conformational changes in remote aptamer regions and that the adjustment even propagates to the expression platform (48). These subtle changes are often sufficient to mediate riboswitch activity and include both tertiary structure adjustments and changes of base pairings in secondary structure.

Beyond binding kinetics, the observed levels of Mg^{2+} dependence provide further insights. Especially at the lowest analyzed Mg^{2+} concentration, the binding affinity of A is substantially affected by the presence of cations. Starting from 0.5 mM Mg^{2+} to 1.5 mM, the K_D value is reduced by a factor of >50. Consequently, a steep transition from non-binding to binding conformations takes place, just below the physiological range. Fitting the aptamer data to the Hill equation yields a Hill coefficient of 4.6, suggesting that several distinct metal binding sites may be involved in folding into a compact binding-competent structure. The observed effect of Mg^{2+} on the conformation of aptamer A is in line with the model that has been proposed for the tetracycline-binding aptamer, which is also incapable of ligand binding in the absence of Mg^{2+} (38). However, the tetracycline-binding aptamer can be applied as a functional riboswitch *in vivo*, in contrast to aptamer A. A pronounced Mg^{2+} -dependent binding affinity has also been reported for the active theophylline-binding aptamer (49), so this behaviour does not conclusively explain the inactivity of aptamer A. In contrast, the K_D values of the *in vivo* active candidates preRS and RS are almost independent of Mg^{2+} at concentrations higher than 0.5 mM. This binding behaviour is similar to the neomycin riboswitch, whose binding is also independent of divalent cations. Aptamers in general clearly depend on the availability of divalent ions for binding and the extent of this dependence may vary between the individual aptamers. However, this cannot fully explain the observed differences in the *in vivo* activity of the aptamers explored here.

In sum, the data for the different angles explored here provide a consistent explanation why only a few *in vitro* selected aptamers are suitable for the design of synthetic riboswitches. Only if the two-step binding mechanism with nearly irreversible binding leads to the formation of a ligand-aptamer-complex that has an extended lifetime, is the aptamer thought to function as a gene regulatory element. This finding also explains why only very few such aptamers have been found to date. In the classic SELEX procedure, the ligand is coupled to a solid support. Aptamer can-

didates that bind to the ligand are usually specifically eluted by adding the free ligand. Candidates that have a longer lifetime of the ligand-bound state thus fail to elute. This is convincingly demonstrated by the deep sequencing data in Figure 1C. Despite a K_D in the similar range, candidate A is 400 times more enriched than the riboswitch precursor **preRS**.

Based on these results, it is now possible to adjust the selection strategy for better enrichment of aptamers with the desired properties. Extended elution times or unspecific elution, or a short pre-elution step with the specific ligand to remove species that show good binding properties but also a fast back-reaction rate, are possibilities to select specifically for the desired properties. However, we see the most promising route in an alternative SELEX strategy, the Capture-SELEX (8). Here the RNA pool is immobilized instead of the ligand. Elution is performed with the free ligand and only aptamers that detach from the immobilization via a capture oligonucleotide and bind the free ligand are recovered. We have recently shown that the chance of finding regulatory aptamers with Capture-SELEX is increased compared to a classical SELEX protocol (8). This may be due to the fact that Capture-SELEX also selects for conformational switching, but the kinetic properties described here certainly contribute to this effect. A slow back reaction of the aptamers bound to the immobilized ligand will prevent efficient elution and consequently enrichment during a classical SELEX procedure; however, it is not an issue for Capture-SELEX.

To conclude, this work enabled us to shed light on an enduring conundrum of synthetic riboswitch design, i.e. why only a very small proportion of the many small molecule-binding aptamers can be used to create synthetic riboswitches. The use of such RNA-based regulators is becoming more and more important, not only as versatile control elements of gene regulation, but also as biosensors to optimize the metabolite formation of synthetic pathways or as low-cost diagnostics for the detection of contaminations. The findings reported here should therefore fundamentally advance the field of RNA-based switches.

SUPPLEMENTARY DATA

Supplementary Data are available at NAR Online.

ACKNOWLEDGEMENTS

The authors thank Drs Julia Weigand, Markus Braun and Henrik Gustmann for constructive and helpful discussions.

FUNDING

Deutsche Forschungsgemeinschaft [SFB902] ‘Molecular principles of RNA based regulation’ (projects A2 and A5). Funding for open access charge: Deutsche Forschungsgemeinschaft.

Conflict of interest statement. None declared.

REFERENCES

- Spöring, M., Fink, M. and Hartig, J.S. (2020) Aptamers in RNA-based switches of gene expression. *Curr. Opin. Biotechnol.*, **63**, 34–40.
- Ellington, A.D. and Szostak, J.W. (1990) In vitro selection of RNA molecules that bind specific ligands. *Nature*, **346**, 818–822.
- Tuerk, C. and Gold, L. (1990) Systematic evolution of ligands by exponential enrichment: RNA ligands to bacteriophage T4 DNA polymerase. *Science*, **249**, 505–510.
- Jenison, R.D., Gill, S.C., Pardi, A. and Polisky, B. (1994) High-resolution molecular discrimination by RNA. *Science*, **263**, 1425–1430.
- Weigand, J.E., Schmidtke, S.R., Will, T.J., Duchardt-Ferner, E., Hammann, C., Wöhnert, J. and Suess, B. (2011) Mechanistic insights into an engineered riboswitch: a switching element which confers riboswitch activity. *Nucleic Acids Res.*, **39**, 3363–3372.
- Berens, C., Thain, A. and Schroeder, R. (2001) A tetracycline-binding RNA aptamer. *Bioorg. Med. Chem.*, **9**, 2549–2556.
- Groher, F., Bofill-Bosch, C., Schneider, C., Braun, J., Jäger, S., Geißler, K., Hamacher, K. and Suess, B. (2018) Riboswitching with ciprofloxacin—development and characterization of a novel RNA regulator. *Nucleic Acids Res.*, **46**, 2121–2132.
- Boussebayle, A., Torka, D., Ollivaud, S., Braun, J., Bofill-Bosch, C., Dombrowski, M., Groher, F., Hamacher, K. and Suess, B. (2019) Next-level riboswitch development—implementation of Capture-SELEX facilitates identification of a new synthetic riboswitch. *Nucleic Acids Res.*, **47**, 4883–4895.
- Wrist, A., Sun, W. and Summers, R.M. (2020) The theophylline aptamer: 25 years as an important tool in cellular engineering research. *ACS Synth. Biol.*, **9**, 682–697.
- Wachsmuth, M., Domin, G., Lorenz, R., Serfling, R., Findeiß, S., Stadler, P.F. and Mörl, M. (2015) Design criteria for synthetic riboswitches acting on transcription. *RNA Biol.*, **12**, 221–231.
- Sack, M., Stüfel, J., Kreft, S.G., Deuerling, E. and Hartig, J.S. (2019) Neomycin-dependent hammerhead ribozymes for the direct control of gene expression in *Saccharomyces cerevisiae*. *Methods*, **161**, 35–40.
- Beilstein, K., Wittmann, A., Grez, M. and Suess, B. (2015) Conditional control of mammalian gene expression by tetracycline-dependent hammerhead ribozymes. *ACS Synth. Biol.*, **4**, 526–534.
- Suess, B., Hanson, S., Berens, C., Fink, B., Schroeder, R. and Hillen, W. (2003) Conditional gene expression by controlling translation with tetracycline-binding aptamers. *Nucleic Acids Res.*, **31**, 1853–1858.
- Berens, C. and Suess, B. (2015) Riboswitch engineering — making the all-important second and third steps. *Curr. Opin. Biotechnol.*, **31**, 10–15.
- Awad, A.M. and McKeague, M. (2018) Riboswitches and synthetic aptamers: a head-to-head comparison. *Aptamers*, **2**, 1–10.
- Wickiser, J.K., Cheah, M.T., Breaker, R.R. and Crothers, D.M. (2005) The kinetics of ligand binding by an adenine-sensing riboswitch. *Biochemistry*, **44**, 13404–13414.
- Carothers, J.M., Oestreich, S.C., Davis, J.H. and Szostak, J.W. (2004) Informational complexity and functional activity of RNA structures. *J. Am. Chem. Soc.*, **126**, 5130–5137.
- Carothers, J.M., Goler, J.A., Kapoor, Y., Lara, L. and Keasling, J.D. (2010) Selecting RNA aptamers for synthetic biology: investigating magnesium dependence and predicting binding affinity. *Nucleic Acids Res.*, **38**, 2736–2747.
- Duchardt-Ferner, E., Gottstein-Schmidtke, S.R., Weigand, J.E., Ohlenschläger, O., Wurm, J.-P., Hammann, C., Suess, B. and Wöhnert, J. (2016) What a difference an OH makes: conformational dynamics as the basis for the ligand specificity of the neomycin-sensing riboswitch. *Angew. Chem. Int. Ed.*, **55**, 1527–1530.
- Jaeger, J., Groher, F., Stamm, J., Spiehl, D., Braun, J., Dörsam, E. and Suess, B. (2019) Characterization and inkjet printing of an RNA aptamer for paper-based biosensing of ciprofloxacin. *Biosensors*, **9**, 7.
- Rio, D.C. (2011) In: *RNA: a Laboratory Manual*. CSH Press, NY.
- Reuss, A.J., Grünwald, C., Braun, M., Engels, J.W. and Wachtveitl, J. (2016) The three possible 2-(pyrenylethynyl) adenosines: rotameric energy barriers govern the photodynamics of these structural isomers. *ChemPhysChem*, **17**, 1369–1376.
- Enderlein, J. and Erdmann, R. (1997) Fast fitting of multi-exponential decay curves. *Opt. Commun.*, **134**, 371–378.
- Kuzmic, P. (1996) Program DYNAFIT for the analysis of enzyme kinetic data: application to HIV proteinase. *Anal. Biochem.*, **237**, 260–273.
- Umuhire Juru, A., Patwardhan, N.N. and Hargrove, A.E. (2019) Understanding the contributions of conformational changes,

- thermodynamics, and kinetics of RNA-small molecule interactions. *ACS Chem. Biol.*, **14**, 824–838.
26. Uivarosi, V. (2013) Metal complexes of quinolone antibiotics and their applications: an update. *Molecules*, **18**, 11153–11197.
 27. Yang, R., Fu, Y., Li, L.-D. and Liu, J.-M. (2003) Medium effects on fluorescence of ciprofloxacin hydrochloride. *Spectrochim. Acta Part A Mol. Biomol. Spectrosc.*, **59**, 2723–2732.
 28. Anand, U., Kurup, L. and Mukherjee, S. (2012) Deciphering the role of pH in the binding of ciprofloxacin hydrochloride to bovine serum albumin. *Phys. Chem. Chem. Phys.*, **14**, 4250–4258.
 29. van de Weert, M. and Stella, L. (2011) Fluorescence quenching and ligand binding: a critical discussion of a popular methodology. *J. Mol. Struct.*, **998**, 144–150.
 30. Paul, F. and Weikl, T.R. (2016) How to distinguish conformational selection and induced fit based on chemical relaxation rates. *PLoS Comput. Biol.*, **12**, e1005067.
 31. Vogt, A.D. and Di Cera, E. (2012) Conformational selection or induced fit? A critical appraisal of the kinetic mechanism. *Biochemistry*, **51**, 5894–5902.
 32. Jucker, F.M., Phillips, R.M., McCallum, S.A. and Pardi, A. (2003) Role of a heterogeneous free state in the formation of a specific RNA-theophylline complex. *Biochemistry*, **42**, 2560–2567.
 33. Gilbert, S.D., Stoddard, C.D., Wise, S.J. and Batey, R.T. (2006) Thermodynamic and kinetic characterization of ligand binding to the purine riboswitch aptamer domain. *J. Mol. Biol.*, **359**, 754–768.
 34. Buck, J., Fürtig, B., Noeske, J., Wöhnert, J. and Schwalbe, H. (2007) Time-resolved NMR methods resolving ligand-induced RNA folding at atomic resolution. *Proc. Natl. Acad. Sci. U.S.A.*, **104**, 15699–15704.
 35. Chang, A.L., McKeague, M., Liang, J.C. and Smolke, C.D. (2014) Kinetic and equilibrium binding characterization of aptamers to small molecules using a label-free, sensitive, and scalable platform. *Anal. Biochem.*, **463**, 3273–3278.
 36. Coppins, R.L., Hall, K.B. and Groisman, E.A. (2007) The intricate world of riboswitches. *Curr. Opin. Microbiol.*, **10**, 176–181.
 37. Förster, U., Weigand, J.E., Trojanowski, P., Suess, B. and Wachtveitl, J. (2012) Conformational dynamics of the tetracycline-binding aptamer. *Nucleic Acids Res.*, **40**, 1807–1817.
 38. Reuss, A.J., Vogel, M., Weigand, J.E., Suess, B. and Wachtveitl, J. (2014) Tetracycline determines the conformation of its aptamer at physiological magnesium concentrations. *Biophys. J.*, **107**, 2962–2971.
 39. Müller, M., Weigand, J.E., Weichenrieder, O. and Suess, B. (2006) Thermodynamic characterization of an engineered tetracycline-binding riboswitch. *Nucleic Acids Res.*, **34**, 2607–2617.
 40. Gustmann, H., Segler, A.J., Gophane, D.B., Reuss, A.J., Grünewald, C., Braun, M., Weigand, J.E., Sigurdsson, S.T. and Wachtveitl, J. (2019) Structure guided fluorescence labeling reveals a two-step binding mechanism of neomycin to its RNA aptamer. *Nucleic Acids Res.*, **47**, 15–28.
 41. Weigand, J.E., Sanchez, M., Gunnesch, E., Zeiher, S., Schroeder, R. and Suess, B. (2008) Screening for engineered neomycin riboswitches that control translation initiation. *RNA*, **14**, 89–97.
 42. Wallace, S.T. and Schroeder, R. (1998) In vitro selection and characterization of streptomycin-binding RNAs: recognition discrimination between antibiotics. *RNA*, **4**, 112–123.
 43. Nick, T.A., De Oliveira, T.E., Pilot, D.W., Spenkuch, F., Butt, H.J., Helm, M., Netz, P.A. and Berger, R. (2016) Stability of a split streptomycin binding aptamer. *J. Phys. Chem. B*, **120**, 6479–6489.
 44. Lang, K., Rieder, R. and Micura, R. (2007) Ligand-induced folding of the thiM TPP riboswitch investigated by a structure-based fluorescence spectroscopic approach. *Nucleic Acids Res.*, **35**, 5370–5378.
 45. Burnouf, D., Ennifar, E., Guedich, S., Puffer, B., Hoffmann, G., Bec, G., Disdier, F., Baltzinger, M. and Dumas, P. (2012) KinITC: a new method for obtaining joint thermodynamic and kinetic data by isothermal titration calorimetry. *J. Am. Chem. Soc.*, **134**, 559–565.
 46. Wickiser, J.K., Winkler, W.C., Breaker, R.R. and Crothers, D.M. (2005) The speed of RNA transcription and metabolite binding kinetics operate an FMN riboswitch. *Mol. Cell*, **18**, 49–60.
 47. Wachsmuth, M., Findeiß, S., Weissheimer, N., Stadler, P.F. and Mörl, M. (2013) De novo design of a synthetic riboswitch that regulates transcription termination. *Nucleic Acids Res.*, **41**, 2541–2551.
 48. Haller, A., Soulière, M.F. and Micura, R. (2011) The dynamic nature of RNA as key to understanding riboswitch mechanisms. *Acc. Chem. Res.*, **44**, 1339–1348.
 49. Zimmermann, G.R., Wick, C.L., Shields, T.P., Jenison, R.D. and Pardi, A. (2000) Molecular interactions and metal binding in the theophylline-binding core of an RNA aptamer. *RNA*, **6**, 659–667.

7.6 Lotz et al., *Nucleic Acids Res.* 2019, 47

Reference [V]

A Light-Responsive RNA Aptamer for an Azobenzene Derivative

T. S. Lotz, T. Halbritter, C. Kaiser, M. M. Rudolph, L. Kraus, F. Groher, S. Steinwand,

J. Wachtveitl, A. Heckel, B. Suess,

Nucleic Acids Res. **2019**, *47*, 2029-2040.

(DOI: 10.1093/nar/gky1225)

A light-responsive RNA aptamer for an azobenzene derivative

Thea S. Lotz^{1,†}, Thomas Halbritter^{2,†}, Christoph Kaiser³, Martin M. Rudolph¹, Leon Kraus¹, Florian Groher¹, Sabrina Steinwand³, Josef Wachtveitl^{3,*}, Alexander Heckel^{2,*} and Beatrix Suess^{1,*}

¹Technische Universität Darmstadt, Department of Biology, Schnittspahnstrasse 10, 64287 Darmstadt, Germany, ²Goethe-University Frankfurt, Institute for Organic Chemistry and Chemical Biology, Max-von-Laue-Strasse 9, 60438 Frankfurt (M), Germany and ³Goethe-University Frankfurt, Institute for Physical and Theoretical Chemistry, Max-von-Laue-Strasse 7, 60438 Frankfurt (M), Germany

Received September 26, 2018; Revised November 22, 2018; Editorial Decision November 23, 2018; Accepted November 26, 2018

ABSTRACT

Regulation of complex biological networks has proven to be a key bottleneck in synthetic biology. Interactions between the structurally flexible RNA and various other molecules in the form of riboswitches have shown a high-regulation specificity and efficiency and synthetic riboswitches have filled the toolbox of devices in many synthetic biology applications. Here we report the development of a novel, small molecule binding RNA aptamer, whose binding is dependent on light-induced change of conformation of its small molecule ligand. As ligand we chose an azobenzene because of its reliable photoswitchability and modified it with chloramphenicol for a better interaction with RNA. The synthesis of the ligand 'azoCm' was followed by extensive biophysical analysis regarding its stability and photoswitchability. RNA aptamers were identified after several cycles of *in vitro* selection and then studied regarding their binding specificity and affinity toward the ligand. We show the successful development of an RNA aptamer that selectively binds to only the *trans* photoisomer of azoCm with a K_D of 545 nM. As the aptamer cannot bind to the irradiated ligand ($\lambda = 365$ nm), a light-selective RNA binding system is provided. Further studies may now result in the engineering of a reliable, light-responsive riboswitch.

INTRODUCTION

In recent years, light-controlled nucleotide tools have come into the focus of the biological and biochemical research (1–3). The development of new light sources has strengthened this progress. Light is an ideal tool that can be controlled spatially, temporally and in terms of its intensity without major technical effort. In biological systems, light can be used as an external, orthogonal trigger because (i) most of the cells do not respond to light (excepting photoreceptors), (ii) it does not provoke cell damage using an adequate wavelength and (iii) many cells and some organisms are at least partially translucent (1–3). The irradiation of biological samples can mostly be performed with a simple experimental setup and spatial and temporal control allows an exact location and timing of the desired effect. Biological regulation by light has often been carried out in transparent organisms such as *Caenorhabditis elegans* or zebra fish (4,5). For non-transparent organisms light can be used to address surface areas, like the skin. Furthermore, glass fibers can be used to facilitate deeper penetration and enable a possibility to treat internal organs. Lately, we could demonstrate that even ultraviolet (UV-) light can sufficiently penetrate the skin of mice (6).

Three technologies exist to couple a light signal to a biological effect: (i) Optogenetics makes use of endogenously expressible light-responsive proteins. (ii) Optochemical biology uses either photolabile groups installed in strategic places of molecules to temporarily block their activity ('caging'). Alternatively, (iii) photoswitchable compounds can be used that exist in at least two photoisomeric forms, which can be interconverted for example with light of two

*To whom correspondence should be addressed. Tel: +49 6151 16 22000; Fax: +49 6151 16 22003; Email: bsuess@bio.tu-darmstadt.de
Correspondence may also be addressed to Alexander Heckel. Tel: +49 69 798 42505; Fax: +49 69 762 42505; Email: heckel@em.uni-frankfurt.de
Correspondence may also be addressed to Josef Wachtveitl. Tel: +49 69 798 718; Fax: +49 69 798 29712; Email: wvteitl@theochem.uni-frankfurt.de
†The authors wish it to be known that, in their opinion, the first two authors should be regarded as Joint First Authors.
Present address: Thomas Halbritter, Department of Chemistry, University of Iceland, Science Institute, Dunhaga 3, 107 Reykjavik, Iceland.

© The Author(s) 2018. Published by Oxford University Press on behalf of Nucleic Acids Research.
This is an Open Access article distributed under the terms of the Creative Commons Attribution Non-Commercial License (<http://creativecommons.org/licenses/by-nc/4.0/>), which permits non-commercial re-use, distribution, and reproduction in any medium, provided the original work is properly cited. For commercial re-use, please contact journals.permissions@oup.com

different wavelengths. During the past decade, different photoswitchable molecules have been developed and investigated. Azobenzenes, spiropyran and diarylethenes are some of the most prominent photoswitchable compounds that have been used for biological applications. Particularly, azobenzenes are reliable and well-investigated photoswitches to control biomolecules and have been used in various biological applications also referred to as 'azalogization' (7–11). However, while numerous light-directed manipulations of proteins (e.g. enzymes, ion channels etc.) have already been investigated, reports about light-responsive oligonucleotides are rare though they are interesting targets for several reasons. They are small, can be easily produced within cells or synthesized by solid-phase synthesis.

RNA is a versatile biomolecule capable of performing many different roles in the cell. The discovery of RNA elements mediating gene control, chemical reaction catalysis and signal transduction go far beyond their well-established role as the carrier of the genetic information and impressively demonstrate their functional versatility. Its ability to form complex three-dimensional structures that precisely present chemical moieties is imperative in enabling RNA to function as a biological catalyst, regulator or structural scaffold. Riboswitches are an excellent example of such RNA-based regulation. They are highly structured RNA elements mostly located in the 5' UTR of many bacterial mRNAs as well as in the 3' UTR in some plant mRNAs (12,13). The RNA forms a binding pocket that can recognize metabolites with high affinity and specificity. The ligand binding to this binding pocket, also called aptamer domain, is then read out by a second domain, the expression platform that can affect gene expression (12). In recent years, a number of synthetic riboswitches have been developed that are modeled on natural riboswitches (14,15). As binding domains, they often use aptamers that are not necessarily derived from natural riboswitches, but can also be produced *de novo* through a process of *in vitro* selection, also called SELEX (Systematic Evolution of Ligands by Exponential Enrichment) (16,17). With the help of this method, aptamers can be selected against almost any ligand of choice.

The overall intention of this work was to create a light-dependent synthetic riboswitch with structural changes only occurring upon binding to one photoisomer of a ligand. Whereas the riboswitch is expressed in the cell, the light-responsive ligand is introduced into the cell system and undergoes a structural change only upon irradiation. As a first step to engineer such a system, an aptamer has to be selected that responds in a light-dependent manner to a photoswitchable small molecule. Therefore the ligand needs to fulfill various requirements, such as high solubility under physiological conditions, favorable interactions with RNA (hydrogen bonds, stacking interactions, Coulomb attractions), sufficient cellular uptake and no toxicity to mention only a few. Furthermore, the photophysical requirements such as the ability to undergo structural change under physiological conditions, high switching amplitude for an optimal 'ON'-'OFF' behavior, thermal stability (of the photoisomeric states) and no photobleaching should be guaranteed. Additionally, the photoswitches should not possess long tethers to allow an optimal hinge mechanism of the

photoswitch. To achieve the ambitious goal of reversible light-controlled riboswitch regulation systems, as many as possible of the above prerequisites need to be fulfilled.

To our knowledge, up to now only three studies on SELEX methods against photochromic molecules have been published (18–20). In all cases, the aim was to direct the aptamer-binding to only one of the possible two photoisomeric states of the small molecule. Hayashi *et al.* performed a SELEX against the *trans* isomer of the photoswitchable peptide KRAZR (20,21). In surface plasmon resonance (SPR) studies, they demonstrated that individual aptamers bound KRAZR_{trans} with a dissociation constant in the high nanomolar to low micromolar range. This binding was tenfold worse for the UV-exposed KRAZR_{cis} form, but could be completely restored by irradiation with visible light of 430 nm (conversion back to KRAZR_{trans}). Young and Deiters were also able to generate photoisomer-specific RNA aptamers, selecting for a spiropyran derivative (19). This allowed them to identify an aptamer, which exhibited a 14-fold discrimination between the closed spiropyran and open merocyanine form upon irradiation with UV light. However, the affinity was only at a K_D value of $\sim 10 \mu\text{M}$. Lee *et al.* obtained specific aptamers against the closed form of the dihydropyrene BDHP-COOH in their studies (18). The best candidate showed a 35-fold difference in its binding behavior between the respective photoisomers and a K_D value of $\sim 2 \mu\text{M}$.

Here, we present our approach toward generating RNA aptamers, which selectively bind to one isomer of a newly developed photoswitchable molecule in the nanomolar range, with 10^4 times better discrimination than the other photoisomer. These aptamers will extend the toolbox of synthetic biology compounds and provide now excellently suitable sensory domain for the engineering of light-responsive synthetic riboswitches.

MATERIALS AND METHODS

Biophysical characterization of the spectroscopic behavior of azoCm

The photophysical properties of the compound azoCm were determined in $1 \times \text{PBS}$ buffer (phosphate-buffered saline), except for the stability measurements that were carried out in HeLa cell extracts and experiments in presence of RNA which were performed in the corresponding SELEX buffer. For the UV/vis-absorption measurements, the concentrations were kept below $100 \mu\text{M}$ and the samples were prepared in UV-permeable quartz glass cuvettes with 1 cm path length. Absorption spectra were recorded using a Specord S600 or S100 spectrometer (Analytik Jena). For irradiation experiments, ThorLabs light emitting diodes (LEDs) controlled by a ThorLabs DC4100-Driver were applied. UV-light for *trans-cis* isomerization was provided by a $\lambda = 365 \text{ nm}$ LED while *cis-trans* isomerization was induced using a $\lambda = 420 \text{ nm}$ LED (type M365L2 and M420L2, 300 mW).

The CD measurements were executed with a Jasco J-710 spectrometer under constant nitrogen flow of 1.5 l/min. Here, cuvettes with 1 mm path length were used and irradiation was also carried out with the same set of ThorLabs LEDs. In these experiments, the RNA concentration was 10

μM and the ligand azoCm was provided in 10-fold excess with a concentration of 100 μM .

SELEX—Pool design

We used three different pool designs. For the first SELEX, a previously described pool design was used (22). For the second SELEX a completely randomized RNA library was used. This library consisted of 74 nucleotides (nt) flanked by constant regions (5' constant: 5'-GGA GCU CAG CCU UCA CUG C-3'/3' constant: 5'-GGC ACC ACG GUC GGA UCC AC-3') for amplification using the oligonucleotides PoolLwd (5'-TCT AAT ACG ACT CAC TAT AGG AGC TCA GCC TTC ACT GC-3', T7 promoter is underlined) and PoolRev (5'-GTG GAT CCG ACC GTG GTG CC-3'). The third SELEX was carried out with a partially structured library containing a 15-nt long motif sequence (5'-GGC CUA CGG GAA AGG-3') flanked by 30 random nt on the motifs 5' end, and 5 random nt on its 3' end (N30-motif-N5). The motif was partially randomized as well, with a 50% chance of a nucleotide exchange for the first two nt (GG), and a 2% chance for the remaining 13 nt. This partially structured library was flanked by constant regions (5' constant: 5'-CCA AGC UAG AUC UAC CGG U-3'/3' constant: 5'-AAA AUG GCU AGC AAA GGA GAA GAA CUU UUC ACU-3') for amplification using the oligonucleotides PoolLwd (5'-CCA AGT AAT ACG ACT CAC TAT AGG GCC AAG CTA GAT CTA CCG GT-3') and PoolRev (5'-AGT GAA AAG TTC TTC TCC TTT GCT AGC CAT TTT-3').

Pool preparation

All pools were amplified using the following polymerase chain reaction (PCR) conditions: 10 mM Tris-Cl pH 9.0, 50 mM KCl, 1.5 mM MgCl₂, 0.1% Triton X-100, 0.2 mM dNTPs (each), 30 nM pool template, 2 μM PoolLwd, 2 μM PoolRev, 50 U/ml Taq DNA Polymerase (NEB). 10¹⁵ pool template molecules were amplified in a 60 ml PCR reaction for only seven cycles to reduce PCR-induced bias. PCR efficiency was calculated according to Hall *et al.* (23).

After large-scale amplification, the DNA pool template was ethanol-precipitated and dissolved in MQ-H₂O [deionized water purified with ion exchange resin and filtered through a Biofilter (ELGA) to remove possible RNase contamination]. The purified DNA template was transcribed using T7 RNA polymerase as described previously (24). Afterward, the transcribed RNA was ethanol-precipitated, dissolved in formamide containing 25 mM ethylenediaminetetraacetic acid (EDTA) and loaded on a 6% denaturing polyacrylamide gel (8 M urea). The RNA was visualized by UV shadowing, sliced out and eluted overnight in 300 mM Na-acetate (pH 6.5). Hereafter, eluted RNA was ethanol-precipitated, the pellet was re-dissolved in a suitable amount of water and molarity was calculated.

Immobilization of the ligand azoCm

azoCm-amino was immobilized on Affi-Gel 10 (Bio-Rad). For this, the resin was pre-treated according to the manufacturer's instructions of anhydrous coupling. Afterward,

the resin was mixed 3:1 with a 3 mM solution of azoCm in dimethyl sulfoxid (DMSO). The reaction was incubated for 4 h at room temperature (RT) on an H5600 rotator (Labnet). After two washes of the derivatized resin with DMSO, the remaining active groups were blocked by incubation with 0.1 M ethanalamine (MEA) for 1 h. After washing the resin twice with DMSO, it was resuspended 1:1 in 0.002% (w/v) NaN₃ and 1 ml of the mix was distributed per SELEX column (bedvolume 1.2 ml). The columns were stored at 4°C in the dark.

Regular SELEX

1.2 $\times 10^{15}$ RNA molecules from the initial pool (1:1 mixture of completely randomized and pre-structured pool, see above (22)) were spiked with ~ 250 kCPM of the 5' 32P-labeled RNA pool in MQ-H₂O to use in the first round. RNA folding was performed by heating the mixture to 95°C for 5 min and subsequently placed on ice water for additional 5 min. After this folding step, yeast tRNA was added to a final concentration of 1 mg/ml and the volume was adjusted to 1 column volume of resin (CV, 500 μl) with 1 \times binding buffer (40 mM Hepes pH 7.4, 125 mM KCl, 5 mM MgCl₂, 5% DMSO). For depletion of RNAs able to bind the affinity matrix, the RNA library was first incubated for 30 min with 1 CV of a non-derivatized column (mock) during the first three rounds of SELEX. The mock column consisted of Affi-Gel 10 resin that had been treated with MEA only instead of azoCm. After negative selection, unbound RNAs were added to 1 CV azoCm-coupled resin and incubated for 30 min at RT. Next, the column was washed with 10 CV binding buffer and bound RNAs were eluted with either 4 CV 20 mM EDTA (round 1–5) or 4 CV 5 mM azoCm (round 6–9) in 1 \times binding buffer. To increase stringency, the number of washes was increased to 25 CV and an increased timeframe for the elution of the RNA from the column was used (round 8). Pre-elution steps were performed in round 8 and 9, adding an additional pre-elution step in round 9 (2 or 3 CV each). Details are described in Supplementary Table S1.

Light SELEX

During the second SELEX, 4.8 $\times 10^{14}$ RNA molecules from the initial pool (74 nt randomized region, see above) were spiked with ~ 250 kCPM of 5' 32P-labeled RNA pool in MQ-H₂O to use in the first round. The folding, addition of yeast tRNA and adjustment of volume were carried out like in the first SELEX. Mock columns were used (round 1–4), RNA was eluted by either 20 mM EDTA (round 1) or 5 mM azoCm (round 2–9). Stringency was increased raising the number of washes from 10 CV to 20 CV or a decreasing binding time of the RNA pool to the column to 15 min, respectively (round 7 and 9). Two pre-elution steps (1 CV each) were performed starting from round 7. Starting with round 7, light-elution was carried out in parallel to the affinity SELEX. RNA was eluted by irradiating the column with light ($\lambda = 365$ nm, UVLED-365-1000-SMD, 2W (0.15 A, 13.5 V), 16 \times 1 s) under exclusion of other light sources (distance from column to light source = 10 cm), while washing the column with 6 CV of 1 \times SELEX buffer (10 mM Tris-

HCl pH 7.6, 250 mM NaCl, 5 mM MgCl₂). Details are described in Supplementary Table S1.

Doped SELEX

For the third SELEX, 1.2×10^{15} RNA molecules from the initial pool (motif doped pool, see pool design) were spiked with ~250 kCPM of 5' 32P-labeled RNA pool in MQ-H₂O to use in the first round. The folding, addition of yeast tRNA and adjustment of volume were carried out like in the first SELEX. The columns with immobilized RNA were washed with 10 CV of 1× SELEX buffer, before RNA was eluted with 1 mM azoCm in 1× SELEX buffer (round 1–5). Details are described in Supplementary Table S1.

SELEX cycle

In all SELEX experiments and after each round, eluted RNA was ethanol-precipitated with Na-acetate pH 6.5 in the presence of 15 µg GlycoBlue™ Coprecipitant (Ambion) and washed twice with 70% (v/v) ethanol. The air-dried pellets were dissolved in a total volume of 50 µl MQ-H₂O and reverse-transcribed and amplified (RT-PCR). For RT-PCR, 50 µl eluted RNA was mixed with 1× PCR buffer (10 mM Tris–Cl pH 9.0, 50 mM KCl, 0.1% Triton X-100), 1× first strand buffer (Invitrogen), 2 mM dithiothreitol (DTT, Roche), 1 µM Pool_Lwd, 1 µM Pool_Lrev, 1.5 mM MgCl₂ and 0.3 mM dNTPs (each). The reaction was heated to 65°C for 5 min and then quickly placed on ice. After that, 5 U Taq DNA Polymerase (NEB) and 200 U SuperScript™ II (Thermo Fisher Scientific) were added to the reaction and RNA was reverse-transcribed and amplified (54°C for 10 min followed by 6 to 10 cycles of 95°C for 1 min, 58°C for 1 min and 72°C for 1 min). Product formation was monitored on a 3% agarose gel. For the following rounds (all except round 1), RNA was transcribed as follows: 10 µl of RT-PCR product was mixed with 40 mM Tris–Cl (pH 8.0), 5 mM DTT, 2.5 mM NTPs (each), 15 mM MgCl₂, 100 U T7 RNA Polymerase (NEB), 40 U ribonuclease inhibitor (moloX) and 33 nM 32P-α-UTP (Hartmann analytics) in a total volume of 100 µl. Transcription was carried out at 37°C for 1 h. Afterward, RNA was precipitated with NH₄-acetate/ethanol, washed twice with 70% EtOH and the pellet was dissolved in a suitable amount of water. A total of 500 kCPM RNA was folded, diluted in 1× binding buffer and subsequently loaded onto the column for the next round of SELEX.

NGS library preparation and data analysis

4-mer barcodes to assign each sequence to the specific round after sequencing were introduced by PCR (sequences available upon request). Forward and reverse oligonucleotides hybridized at the 5' and 3' constant regions, respectively, thus the sequence of the T7 polymerase promoter was removed. After amplification, the samples were Gel-purified (ZymoClean Gel DNA Recovery Kit, Zymo Research) and mixed in equimolar amounts for Illumina sequencing reaction (GenXPro GmbH, Frankfurt, Germany).

In vitro transcription of RNA

For *in vitro* analysis (binding studies and ITC measurements), RNA was transcribed from hybridized oligonucleotide containing a T7 promoter sequence in front of the aptamer (sequences are available upon request). After ethanol precipitation, the DNA template was used for *in vitro* transcription with T7 RNA polymerase (NEB) as done during the SELEX cycle. The RNA was gel purified and molarity was determined by spectrophotometric measurement using NanoDrop 1000 Spectrophotometer (Thermo Scientific).

Binding studies

The elution capacity of RNA aptamers by different solutions was tested using column binding assays. The aptamers were radioactively body labeled and after folding (in a total volume of 500 µl, in 1× SELEX buffer with a final concentration of 1 mg/ml yeast tRNA) applied on the azobenzene-derivatized columns. After incubation for 30 min at RT, the columns were washed 4× with 1 ml 1× SELEX buffer each, followed by two washing steps of 500 µl each. The binding RNA molecules were tried to be eluted with different solutions (*cis*- or *trans*-azoCm, UV-light and buffer or just buffer). Each aptamer measurement set was normalized to the RNA eluted by azoCm *trans* (100%).

ITC measurements

The 10 µM RNA were folded using the SELEX folding program (heating to 95°C for 5 min and subsequent cooling on ice water for 5 min) and diluted in 350 µl 1× SELEX buffer. Ligand was adjusted to a 100 or 200 µM solution in 1× SELEX buffer. ITC experiments were carried out with either an MicroCal iTC200 or a MicroCal PEAQ iTC200, with the ligand solution being titrated to the RNA. After thermal equilibration at 25°C, an initial 150 s delay and one initial 0.4 µl injection, 18 serial injections of 2.0 µl at intervals of 150 s and at a stirring speed of 750 rpm were performed. Raw data were recorded as power (µcal/s) over time (min). The temperature associated with each titration peak was integrated and plotted against the corresponding molar ratio of ligand and RNA. The dissociation constant (K_D) was extracted from a curve fit of the corrected data calculated using the Origin 7.0 ITC Software or the MicroCal PEAQ-ITC Analysis Software 1.1.0.1262. Measurements were repeated twice.

Toxicity tests

To test toxicity against *Escherichia coli* DH5a, *Bacillus subtilis* (strain 168) and *Saccharomyces cerevisiae* (strain RS453α), cells were plated densely on LB- or SD-URA-Agar plates. Sterile filter discs (diameter of 6 mm) were placed on the agar, allowing space between each other. Ligand solutions with different concentrations (0, 0.1, 0.5, 1, 2 and 5 mM, 25 µl each) were pipetted on the disks to allow radial diffusion into the agar. The cultures were grown over night at 37°C or 30°C until they formed a cell layer. Analysis of potential inhibition zone sizes around the filter

discs allowed judgement whether the ligand was toxic and at which concentration toxic effects occurred.

To test toxic effects on human cells, 2×10^3 HeLa cells per well were seeded in a 96-well plate in 100 μ l media (D-MEM). After incubation (37°C) for 24 h, 2 μ l of 500 μ M, 5 mM or 50 mM ligand solution in DMSO were added to the cells to reach concentrations of 10 μ M, 100 μ M or 1 mM ligand in the media, respectively. Controls consisted of adding DMSO to a final concentration of 2% (negative control) and 10 μ M Taxol (positive control) to wells with cells. After another 24 h of incubation, cells were washed twice with warm $1 \times$ PBS. After adding 110 μ l of a 1:10 WST-1:media mix (white D-MEM) per well, the cells were incubated again and samples were taken at intervals for analysis. Using a TECAN 200 pro reader, viable cells were quantified. Samples were measured in triplicates, shown are the averages and standard deviations of two independent measurements.

NMR measurements of compounds

Nuclear magnetic resonance (NMR) spectra for the characterization of the compounds were recorded on a Bruker AVIII-HD 500 MHz instrument equipped with a N_2 cooled cryogenic probe head using d_6 -DMSO as solvent. High resolution mass spectrometry (HRMS) spectra were recorded using a Thermo Scientific MALDI LTQ Orbitrap. For flash chromatography silica gel 60 by Macherey-Nagel was used. Thin layer chromatography (TLC) analyses were performed on aluminum plates coated with silica gel 60 F 254 (Merck).

RESULTS AND DISCUSSION

Synthesis of a light-switchable azobenzene compound

We chose azobenzene as the core of our light-switchable ligand because it is a very reliable photoswitch. However, azobenzene itself offers only poor interactions with RNA. Therefore, it has to be modified. The modification should have functional groups that can be easily recognized by RNA and do not have too many internal degrees of freedom in order to maximize the effect of photoswitching whereby this modification and hence also the RNA anchor points are moved through space. Due to previous good experience with the generation of aptamers against chloramphenicol (22) and its low toxicity, we chose the latter as binding motif. The synthesis of such a designed photoswitchable compound named azoCm (compound (3)) started from chloramphenicol (1) and followed Trauner's 'azalogization' strategy conceptually by converting the nitrophenyl group into an azobenzene derivative (9–11). To this end, chloramphenicol (1) was reduced with ammonium chloride and zinc to form the hydroxylamine which was oxidized with iron (III)-hexahydrate to form the nitroso derivative that was further reacted with 4-amino benzoic acid to form azoCm (3) (Figure 1). To arrive at the aminopropyl-modified azoCm-amino (7) we first protected the hydroxyls of chloramphenicol (1) with TBDMS groups (\rightarrow 2) and performed the same azo coupling (\rightarrow 4). After ester formation with *N*-Boc-protected aminopropanol using EDC as

coupling agent (\rightarrow 5) and deprotection, aminopropylated azoCm-amino (7) was obtained. Details about the synthesis of azoCm and its intermediates can be found in Supplementary Figures S1–6.

Characterization of spectroscopic behavior of azoCm

Prior to the application of azoCm as a photochromic ligand for selected RNA aptamers, the structurally modified azobenzene compound was characterized regarding its photophysical properties in aqueous media. The UV/vis spectrum of the thermally stable and favored *trans*-isomer of azoCm (Figure 2A) exhibits a pronounced $\pi\pi^*$ -band around 330 nm and a minor $n\pi^*$ -band around 420 nm, as typical for this class of photoswitches. Upon irradiation with 365 nm a photostationary state (PSS_{365nm}) containing about 80% of the *cis*-isomer can be accumulated. The reverse isomerization can be induced through 420 nm irradiation, resulting in a nearly quantitative conversion to the *trans*-isomer (containing less than 5% *cis*).

Thermal relaxation studies of pre-illuminated samples at different temperatures allowed for determination of the thermal recovery rate $k_{25^\circ C} = 3.8 \times 10^{-7} \text{ s}^{-1}$ for the *cis* to *trans* isomerization. This reveals an enormously high stability of the *cis*-isomer e.g. compared to the unsubstituted azobenzene (25) and corresponds to a lifetime of \sim 27 days for the respective conformation. Relying on the Arrhenius-equation, the energy barrier for this isomerization is calculated to be $E_A = (109 \pm 0.7) \text{ kJ/mol}$ (Figure 2B). Additionally, the compound showed virtually no decomposition due to photo- or hydrolysis throughout a photofatigue experiment over multiple alternating switching cycles (Figure 2C) and no additional absorption bands could be detected afterward. Moreover, the highly beneficial switching amplitude of roughly 75% is maintained throughout these multiple cycles. In view of a biological application of the compound, the outstanding stability of azoCm was also confirmed in HeLa-cell extracts, where the sample showed virtually no significant changes in its absorption spectrum after 120 h (Figure 2D). Thus, the compound can be used for days without considerable decomposition. Beside its outstanding photochemical and biological stability, we investigated the toxicity of the compound. We performed toxicity tests for bacteria (*E. coli*, *B. subtilis*), yeast (*S. cerevisiae*) and human cell lines (HeLa cells) and showed that azoCm has no significant influence on cell growth (Supplementary Figure S7).

Selection of azoCm-binding aptamers

The characterization showed that azoCm exhibits stable switching behavior even under cellular conditions and is therefore a very good candidate to start an aptamer selection. For the selection process, the aminopropyl derivative of azoCm containing an additional amino group (7) was immobilized on activated resin. For better access of the RNA library to the azoCm moiety a C10 linker was used. Two selections were started in parallel with two established library compositions, one with a randomized region of N74 and a smaller library (N64) being a 1:1 mixture of both a

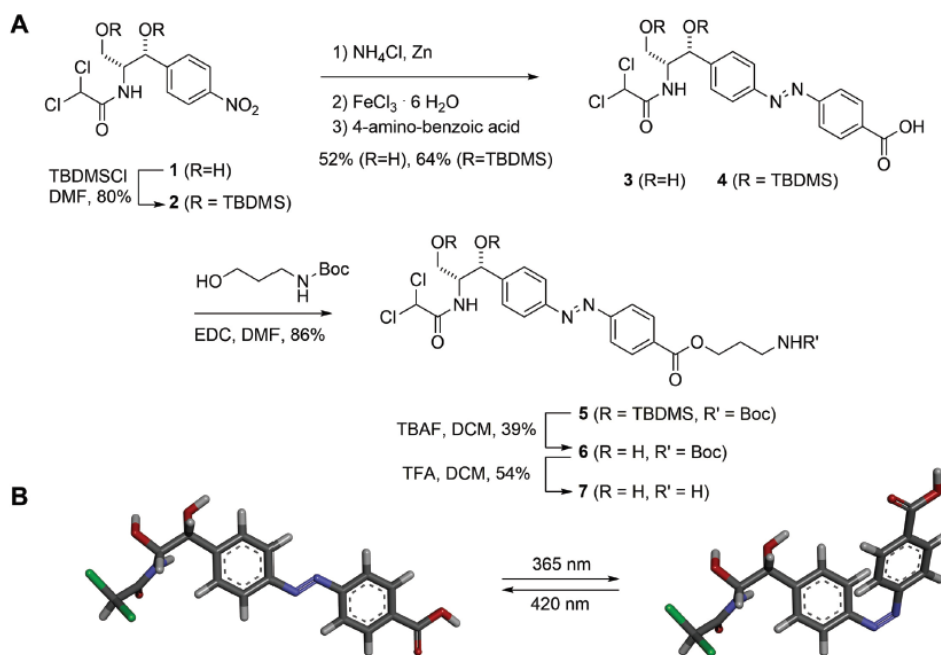


Figure 1. Synthesis of the light-switchable azobenzene compound azoCm. (A) Synthesis of azoCm (3) and the aminopropyl-derivative (7). (B) 3D model of the *cis-trans* conversion of azoCm. Details about the synthesis of azoCm and its intermediates can be found in Supplementary Figures S1–6.

completely randomized region and two shorter randomized regions (N26) separated by a preformed stem loop (Supplementary Figure S8). It was discussed that preformed stem-loops provide favorable conditions for aptamer selection by acting as nucleation sites for RNA structure formation (26–29). We had no *a priori* knowledge of the nature of the aptamer we were exploring, including both completely randomized regions of different size and a preformed stem loop gave us the full scope to unrestrainedly select for the best fit. Importantly, both library designs were already successfully applied for the selection of small molecule-binding aptamers (22,30).

A first selection was carried out using the N64 1:1 RNA library with a starting diversity of 1.2×10^{15} RNA molecules. In the first five rounds of selection, we eluted unspecifically with EDTA to ensure elution of every RNA molecule neglecting their binding properties. This approach was chosen to guarantee that the first enrichment of the pool introduces no bias toward low affinity aptamers because of the mild selection conditions. Negative selection steps during the first three rounds were carried out to remove RNA molecules that specifically recognize the resin or the linker region on which azoCm was immobilized. After an initial enrichment observed in round 5 (Figure 3A), a specific elution with 5 mM azoCm was performed in round 6. Stringency was increased in round 8 by raising the number of washing steps and longer elution times. Despite increased stringency, larger amounts of RNA were eluted

from the column. In consequence, we decided to implement a pre-elution step each in rounds 8 and 9 to eliminate RNA species with fast K_{off} rates (31). All selection rounds are summarized in Figure 3A and Supplementary Table S1.

In parallel, we performed a second selection approach with the N74 RNA library with a starting diversity of 4.8×10^{14} RNA molecules. Unspecific elution was reduced to only the first round, while negative selection was performed during the first four rounds. Starting from round two, specific elution was performed using a 5 mM azoCm solution. After a first enrichment in round 6, stringency was increased in rounds 7 and 9 by doubling the number of column washes or a decreased binding time of the RNA pool to the column, respectively. Additionally, two pre-elution steps were performed starting from round 7. All selection rounds are summarized in Figure 3B and Supplementary Table S1.

We also implemented a light elution step. From this we hoped for specific enrichment of light-dependent aptamers. Since the second selection (from the N74 library) led to a faster enrichment, we decided in favor of this. We split the RNA pool transcribed from round 6 to carry out a light elution parallel to the regular round 7. While the column was treated and washed using the same conditions as in the regular SELEX, the RNA-loaded column was then placed in a closed box, shutting out all external light sources (Figure 3C). Inside this box, the column was irradiated with UV-light of 365 nm inducing azoCm to change from its *trans*- to *cis*-conformation. After irradiation, the column was washed

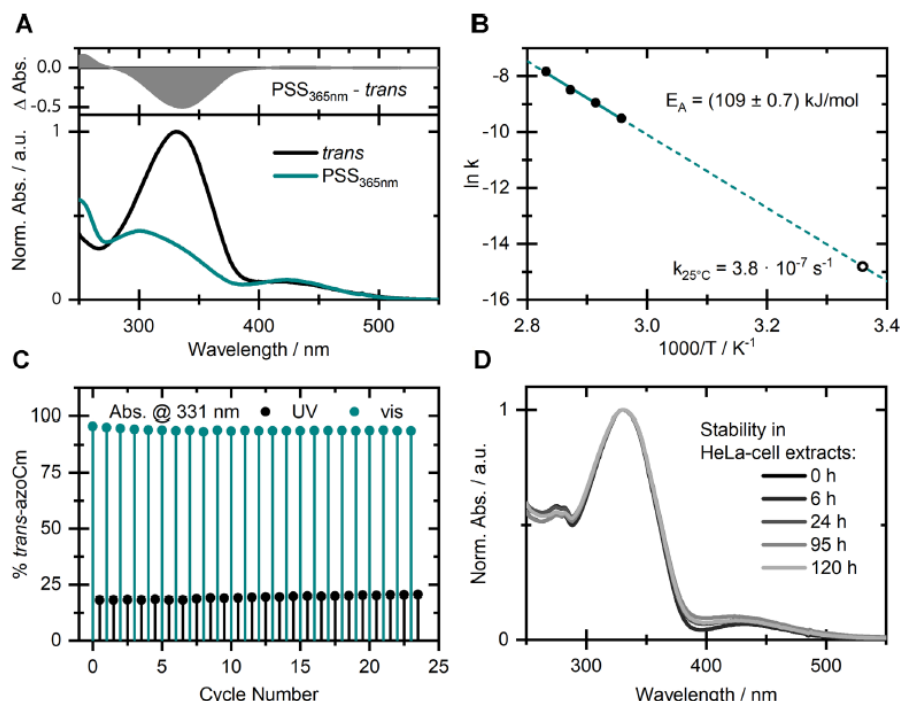


Figure 2. Spectroscopic behavior of azoCm. (A) UV/vis-spectra of *trans*-azoCm (black) and the PSS (cyan) obtained upon irradiation with $\lambda = 365$ nm of azoCm in 1xPBS buffer. (B) Arrhenius plot based on thermal *cis* to *trans* relaxation studies with determined activation energy (filled circles) and extrapolated rate (open circle) at 25°C. (C) Photofatigue resistance study monitoring the absorption at 331 nm throughout alternating irradiation with 420 and 365 nm. (D) Stability in HeLa cell extracts of a sample that was switched forth and back once prior to being stored in the dark for the given time.

with buffer to specifically elute those RNA aptamers that were detached from the ligand due to its conformational change. Amplification of these RNAs should result in an enrichment of light-responsive aptamers and were used for the next round of light SELEX. The data are included in Figure 3B as violet bars. A significant enrichment of aptamers that have been specifically eluted after irradiation with UV-light was clearly visible in round 10 of the light SELEX.

For a first glimpse into the selection progress, we sequenced 87 candidates (27 of round 9 of N64 1:1, 20 of round 9 of the regular SELEX (N74-R) and 40 of round 10 of the light SELEX (N74-L)). We obtained 27 unique sequences (11, 4 and 12, respectively, for the three different selections, shown in Supplementary Table S2) and analyzed their binding capacities by their interaction with azoCm derivatized columns. Only 6 out of 27 tested candidates could be specifically eluted from the column by 5 mM azoCm (Supplementary Figure S9). The remaining 21 candidates showed less than 15% RNA eluted and were not considered as binders. Interestingly, when comparing the sequences of the six candidates using the program MEME (<http://meme-suite.org/tools/meme> V5.0.2 (32)) we identified a 13-nt long motif in three of them (one from the N64

1:1 SELEX and two in the light branch of the N74 SELEX, displayed in Figure 4C).

Deep sequencing uncovers the enrichment of a 'light motif'

We performed deep sequencing to analyse whether and to what extent our identified sequence motif was enriched in the course of the different selections rounds. Therefore, we compared the regular with the light branch of the N74 SELEX (for financial reasons we limited ourselves to the N74 SELEX). By Illumina sequencing, we obtained a total number of 820 000 reads for all investigated rounds, of which 90.1% could be sorted according to their corresponding barcoding. Identical sequences were summed up and the total read count was normalized for each round to reads per million (RPM). To show the enrichment process we computed the sum of RPM of the 100 most enriched sequences (Figure 4A). For the most abundant sequences we see a clear exponential enrichment in the first six rounds and then a transition into saturation when the overall sum of the Top 100 did not change any more, in neither of both branches. We also tracked the enrichment of the 13 nt motif we identified. It was enriched until round six. Then, in the light branch of the SELEX, the motif was further enriched, whereas in the regular branch, the motif gradually

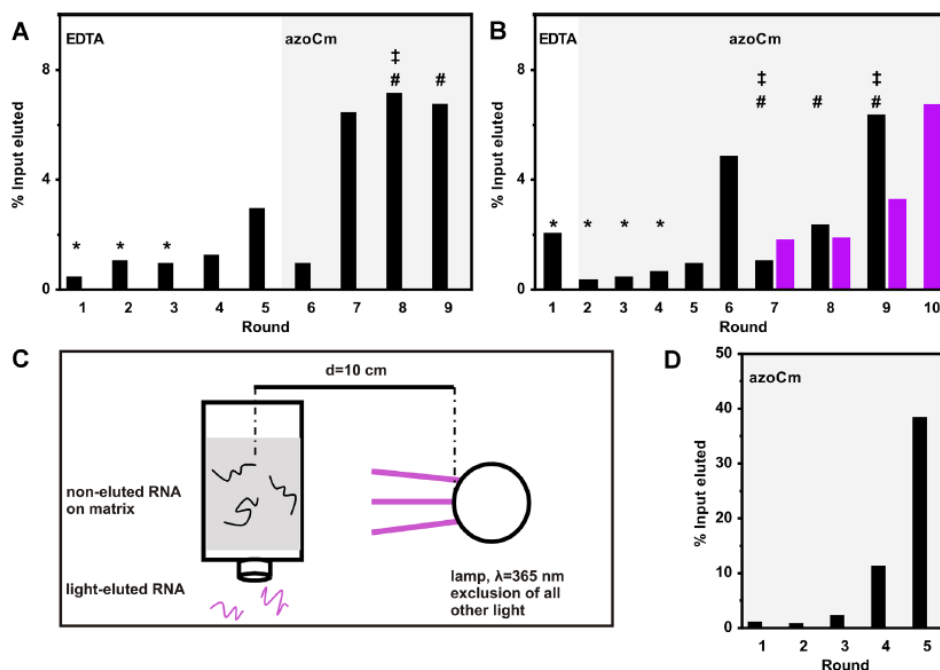


Figure 3. *In vitro* selections for azoCm binding aptamers. (A) Shown is the fraction of loaded RNA that could be eluted from azoCm-derivatized columns after each selection round. RNA was eluted by either 20 mM EDTA (round 1–5) or 5 mM azoCm (round 6–9). In the first three rounds, a negative selection was performed (*). In round 8, stringency was increased by raising the number of column washes from 10 to 25 and an increased timeframe for the elution of the RNA from the column, respectively (‡). Pre-elution steps were performed in round 8 and 9, adding an additional pre-elution step per round (#). Details are given in Supplementary Table S1. (B) Shown is the fraction of loaded RNA that could be eluted from azoCm-derivatized columns after each selection round. RNA was eluted by either 20 mM EDTA (round 1) or 5 mM azoCm (round 2–9) for regular SELEX (black bars). In the first four rounds, a negative selection was performed (*). In round 7 and 9, stringency was increased by doubling the number of column washes or a decreased binding time of the RNA pool to the column, respectively (‡). Two pre-elution steps were performed starting from round 7 (#). Starting with round 7, light elution was carried out in parallel to the regular SELEX (violet bars). For RNA elution, the column was irradiated with light ($\lambda = 365$ nm) under exclusion of other light sources, while washing the column with SELEX buffer. Details are given in Supplementary Table S1. (C) Set-up of light elution of RNA. The column was irradiated with UV-light ($\lambda = 365$ nm) under exclusion of other light sources, while washing the column with SELEX buffer to achieve elution of aptamers which lose binding affinity when the ligand is switched from *trans* to *cis*. The UV lamp was placed 10 cm from the column middle. (D) Doped SELEX. Shown is the fraction of loaded RNA that could be eluted from azoCm-derivatized columns after each selection round. RNA was eluted with 1 mM azoCm (round 1–5).

decreased over the rounds (Figure 4B). Due to its clear enrichment in the light branch, we have now called it ‘light motif’. It seems as if the increase of stringency we took in the regular SELEX to select for aptamers with a slow K_{off} rate lead to the disfavoring of aptamers containing the motif.

We then clustered the sequences for each round into families by comparing their sequence identities by Levenshtein distance (Lv dist) (33). We have previously evaluated that an Lv dist of five is ideal to split the sequence distribution into useful families (22). The distribution of families enriched in the regular and the light-branch, respectively, are displayed in the scatter plot in Figure 4C. It shows a clear separation of the two populations of families (comparing the blue with the violet dots). The detailed analysis of the families enriched by light SELEX revealed 131 unique sequence families, the most prominent ones marked with numbers in Figure 4C. Interestingly, only two of them carry the identified

‘light motif’ (marked with an arrow), but these are highly enriched and make up 14.4% of all sequences.

Motif doped SELEX

The deep sequencing analysis revealed the importance of the light motif. In order to generate highly specific aptamers of a smaller size able to selectively and reversibly bind to only the *trans*-isomer of azoCm we generated a new pool with the light motif included but flanked by random sequences. This should enable us to identify flanking sequences that present the light motif in the best possible way. As the motif occurred always in the 3' end of the randomized sequence, we designed a pool consisting of 30 randomized nts followed by two G's (often found by deep sequencing) and the 13 nt motif. Afterward, five more randomized nucleotides completed a total of 50 nt that represent the new, doped aptamer pool. In order to find potentially bet-

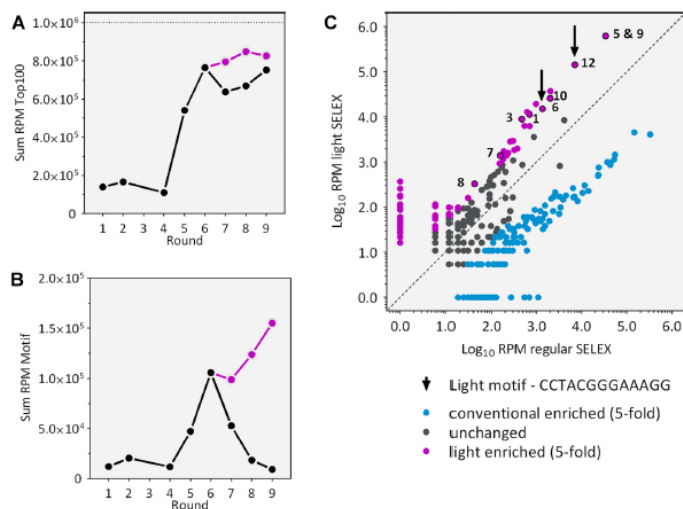


Figure 4. Deep sequencing analysis of all rounds of selection. (A) Enrichment of the 100 most enriched sequences in each round. Shown is the sum of the RPM in black for traditional SELEX and in violet for light SELEX. (B) Occurrence of the identified light motif within each selection round clearly shows an enrichment in the light SELEX compared to the regular SELEX. (C) Scatter plot of the families found in the regular and the light SELEX. Application of light clearly sets some families apart (at least 5-fold enriched). Analysed families are marked with numbers.

ter variants of the motif, a 6% mutation rate was allowed for the 13 nt of the motif. As it was unclear whether the two G's in front of the motif were a necessary or a helpful addition to the motif, they were added but were allowed to mutate with 50% probability (Supplementary Figure S8D). A fast enrichment took place when using this doped pool, reaching 38% RNA elution within five rounds of selection even with reduced ligand concentration (1 mM instead of 5 mM).

We sequenced 96 individual aptamers of rounds 2–5. Interestingly, within these sequences, we found barely any sequences more than twice. There were no dominant aptamer sequences, not even in round 5 with its exceptionally strong enrichment. This suggests that the motif indeed is the core binding region on which the ligand binding solely depends. While over the course of the doped SELEX no single aptamer could be found to dominate the pool, a re-enrichment of the original motif occurred. For 7 out of 13 positions, no single mutation was allowed, for the remaining positions, a mutation rate of only 1–2% occurred (with 6% mutation rate allowed for the complete motif, Supplementary Figure S8D). The analysis of the motif revealed as well that the first G's upstream of the motif are not essential for the binding. With the allowed nucleotide exchange rate of 50%, no preference for the first nucleotide have been identified. The position of the second G however showed a migration from a dominance of a G on this position in round 2 (80% probability) toward a preference of purine bases in general (A, 40% and G, 56%). But it seems like the sequences of the motif-adjacent nucleotides are not important for binding.

The analysis shows that the 13 nt long motif is essential for the binding of our light-dependent ligand. However it was unexpected that no specific sequence en-

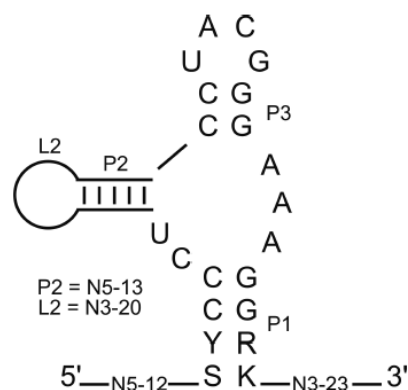


Figure 5. Structure motif. LocARNA analysis was performed to identify a common structural motif using 96 sequences from round 5 of the motif doped SELEX (34,35). Conserved nucleotides are shown in capital letters, variable sizes of the stem P2 and the corresponding loop L are displayed.

richment of the surrounding sequences could be found with the doped SELEX. We therefore considered whether the light motif is embedded in a structural motif. To test this, we used LocARNA (www.rna.informatik.uni-freiburg.de/LocARNA/V.1.9.1) (34,35) to search for a secondary structural motif within the 96 aptamers sequences. The analysis resulted in a small structural motif consisting of a three-way-junction with a 4-nt long closing stem P1 (see Figure 5). The two Gs of the upper two base pairs of P1 are formed by the last two nts of the light sequence motif.

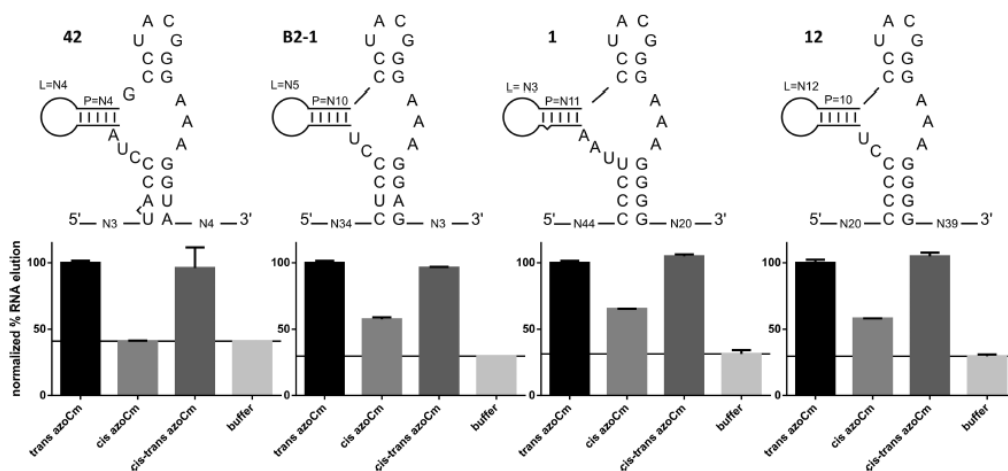


Figure 6. Aptamer binding studies. Above: Secondary structures of aptamer candidates 42, B2-1, 1 and 12 derived from common LocARNA analysis. Below: Radioactively labeled aptamer RNA was folded and immobilized on azoCm derivatized columns using the same conditions as during SELEX. Four individual elution steps with 50 μ M azoCm (in the *trans*, *cis* and *cis-trans* switched conformation) or buffer were performed. The percentage of eluted RNA versus total RNA was calculated. Each aptamers azoCm *trans* value was normalized to 100%. Buffer elution values are marked with a line in each graph.

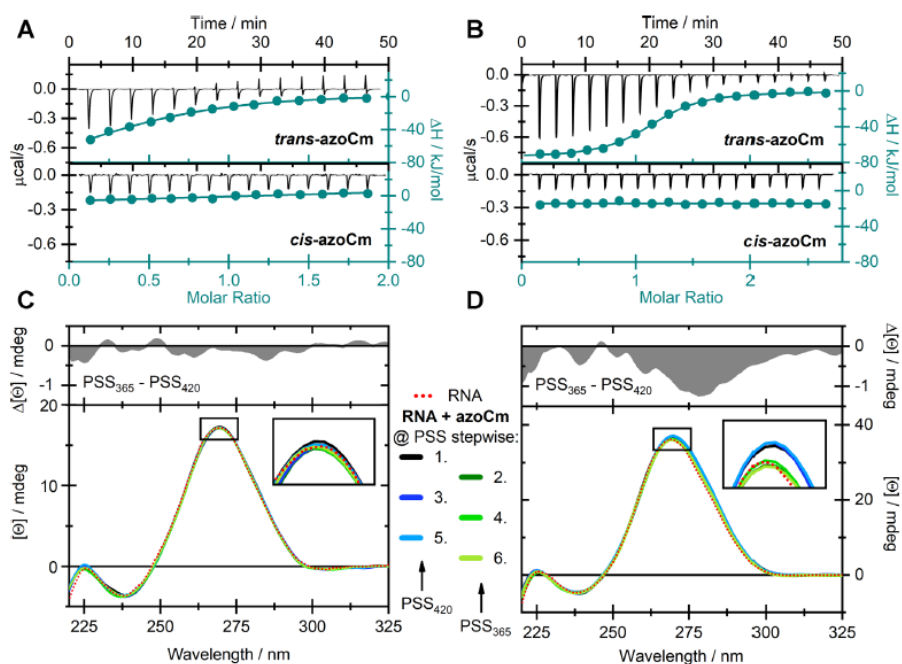


Figure 7. Biochemical characterization of light-responsive aptamers. ITC measurements of (A) 42 and (B) B2-1 with both the *trans*- (upper panels) and *cis*-isomer (lower panels) of azoCm. Measurements were performed using MicroCal iTC200 (aptamer 42) or MicroCal PEAQ iTC200 (aptamer B2-1). CD-monitored alternating photoswitching experiments of azoCm in presence of (C) 42 and (D) B2-1 at 40°C. The red dotted line represents the spectra of the pure RNA-aptamers and the solid colored lines indicate the spectra in the PSS while illuminated with either 420 or 365 nm. The upper panels display difference spectra of the aptamers at both PSS. All CD spectra were corrected for the contribution of the corresponding azoCm photoisomers.

Sequence and length of P2 are fully variable whereas P3 is defined by the motif. It consists of only two GC base pairs closed by an apical UNCG tetraloop that are connected to P1 by three As facing a CU. To prove the predicted secondary structure we performed in-line probing of the aptamer 42 (Supplementary Figure S10). The probing pattern supports the existence of P1 and P2 whereas it proposes that the short 2 nt long P2 is not formed for this candidate. However it clearly shows an involvement of the light motif in ligand binding. We observe a strong reduction of the cleavage for the nucleotide GGGAAAG (nt 6–12 of the motif), whereas the first 5 nucleotides are clearly accessible (showing that the small P2 helix is unlikely to be formed as such) and cleavage tends to increase. In sum, it can be stated that the light motif represents the binding pocket for the ligand that is held in place by the two helices P1 and P2.

Biochemical characterization of light-responsive aptamers

Four individual aptamers that all fold in the secondary structural motif predicted with LocARNA (Figure 5) were tested in column binding assays for their specific binding to the photoisomers of azoCm (candidate 42 from first affinity SELEX, candidates 1 and 12 from the light SELEX and candidate B2–1 from the motif doped SELEX). Aptamer RNA was radioactively labeled, folded and immobilized on azoCm-derivatized columns using the same conditions as during the SELEX. Immobilized RNA was eluted from the columns using azoCm in *trans*, *cis* and *cis-trans* switched conformation, or using 1× SELEX buffer. The fraction of RNA eluted was normalized (elution with *trans* azoCm was set to 100%). As shown in Figure 6, aptamer 42 shows the most prominent reduction when comparing elution of the *trans*-ligand to the *cis*-ligand (-60%), reaching buffer elution level (-59%). B2–1 shows a 43% reduction, aptamer 1 shows 35% reduction and aptamer 12 shows 42% reduction. To determine the binding affinities of the two best aptamers 42 and B2–1 to both the *trans*- and *cis*-azoCm photoisomer, ITC measurements were performed with preilluminated azoCm to accumulate the corresponding photoisomer. As depicted in Figure 7A and B, the K_D values of 42 and B2–1 binding to *trans*-azoCm were determined to be 1.9 μ M and 545 nM, respectively (Supplementary Table S3). On the contrary, the ITC experiments with *cis*-azoCm showed no binding curve at all. Thus, an exact K_D could not be determined, but considering the total amount of ligand that was titrated to the aptamers, it is reasonable to give an estimate for the lower boundary of the binding strength to the *cis*-isomer of at least mM. This discrimination is extremely high and with three and four orders of magnitude, respectively, much better than previously selected aptamers against light-switchable compounds.

In order to provide evidence, that the aptamers not only binds to *trans*-azoCm specifically but also releases the ligand upon irradiation, we conducted CD experiments to monitor conformational changes of the RNA upon photoisomerization of azoCm (Figure 7C and D). Generally, the spectral shape of both aptamers can be ascribed to hairpin structures (36–38), exhibiting a pronounced positive CD signal around 270 nm and a minor negative signal at 240 nm. Concerning the ligand azoCm, only the *cis*-

isomer shows a significant CD signal (Supplementary Figure S11). Throughout the depicted experiments, solutions of each RNA construct in presence of 10-fold excess of ligand, were alternately illuminated with 420 and 365 nm. As in the case of aptamer 42 no serious spectral variation was detected, we assume that a reversible release of *cis*-azoCm is not feasible once the *trans*-isomer is bound (Figure 7C). Yet, in the case of B2–1 a small decrease of the signal at 270 nm of ~3% was observed upon switching azoCm from *trans* to *cis* reversibly, which indicates a dissociation of the ligand accompanied by slight changes in the tertiary structure of the aptamer.

CONCLUSION

In summary, we have developed an RNA aptamer against an azobenzene-derived ligand, which can only bind to the *trans*-isomer of azoCm but not to its *cis*-photoisomer. The ligand itself is non-toxic, stable in biological medium and can be photoswitched multiple times without significant degradation and with high photoswitching amplitude. High-quantum yields, low-thermal rates of conversion and spectrally addressable photoisomers make the ligand ideal for an application in a biological context. In addition azoCm retains its switching properties in presence of RNA. A light SELEX protocol based on liberation of RNA after *trans*- to *cis*-conversion of azoCm was able to enrich a sequence motif which we had also found in a regular SELEX approach before. However, the RNA found with the latter approach did not perform any liberation of the ligand upon photoisomerization. By next-generation sequencing, we were able to show the enrichment of the photoisomerization-responsive RNA motif only in the light SELEX but not in the regular one performed in parallel. The 13-nt sequence motif identified in the light SELEX is embedded in a conserved a three-way-junction. With a K_D of 545 nM, the affinity of aptamer B2–1 to the *trans*-photoisomer of azoCm is relatively high while the K_D toward the *cis*-photoisomer is at least 1 mM. By CD spectroscopy, we could show that in multiple switching cycles the bound *trans*-azoCm was liberated and sequestered, repeatedly. All of these properties make this system of RNA aptamer and photoswitchable ligand ideal for many interesting applications, including the further development of a light-sensitive riboswitch.

SUPPLEMENTARY DATA

Supplementary Data are available at NAR Online.

ACKNOWLEDGEMENTS

We thank Britta Schreiber for technical assistance.

FUNDING

Deutsche Forschungsgemeinschaft [SFB902 A2/A6/A7 to J.W., A.H., B.S.]. Funding for open access charge: Deutsche Forschungsgemeinschaft [SFB902 A2/A6/A7].

Conflict of interest statement. None declared.

REFERENCES

- Ankenbruck, N., Courtney, T., Naro, Y. and Deiters, A. (2018) Optochemical control of biological processes in cells and animals. *Angew. Chem. Int. Ed. Engl.*, **57**, 2768–2798.
- Brieke, C., Rohrbach, F., Gottschalk, A., Mayer, G. and Heckel, A. (2012) Light-controlled tools. *Angew. Chem. Int. Ed. Engl.*, **51**, 8446–8476.
- Klan, P., Solomek, T., Bochet, C.G., Blanc, A., Givens, R., Rubina, M., Popik, V., Kostikov, A. and Wirz, J. (2013) Photoremovable protecting groups in chemistry and biology: reaction mechanisms and efficacy. *Chem. Rev.*, **113**, 119–191.
- Gripenburg, J.C., Rapp, T.L., Carroll, P.J., Eberwine, J. and Dmochowski, I.J. (2015) Ruthenium-Caged antisense morpholinos for regulating gene expression in zebrafish embryos. *Chem. Sci.*, **6**, 2342–2346.
- Husson, S.J., Gottschalk, A. and Leifer, A.M. (2013) Optogenetic manipulation of neural activity in *C. elegans*: from synapse to circuits and behaviour. *Biol. Cell*, **105**, 235–250.
- Lucas, T., Schafer, F., Muller, P., Eming, S.A., Heckel, A. and Dimmle, S. (2017) Light-inducible anti-miR-92a as a therapeutic strategy to promote skin repair in healing-impaired diabetic mice. *Nat. Commun.*, **8**, 15162.
- Kusebauch, U., Cadamuro, S.A., Musiol, H.-J., Lenz, M.O., Wachtveitl, J., Moroder, L. and Renner, C. (2006) Photo-controlled folding and unfolding of a collagen triple helix. *Angew. Chem. Int. Ed. Engl.*, **45**, 7015–7018.
- Spörlein, S., Carstens, H., Satzger, H., Renner, C., Behrendt, R., Moroder, L., Tavan, P., Zinth, W. and Wachtveitl, J. (2002) Ultrafast spectroscopy reveals sub-nanosecond peptide conformational dynamics and validates molecular dynamics simulation. *Proc. Natl. Acad. Sci. U.S.A.*, **99**, 7998–8002.
- Stein, M., Middendorp, S.J., Carta, V., Pejo, E., Raines, D.E., Forman, S.A., Sigel, E. and Trauner, D. (2012) Azo-propofols: photochromic potentiators of GABA(A) receptors. *Angew. Chem. Int. Ed. Engl.*, **51**, 10500–10504.
- Schonberger, M. and Trauner, D. (2014) A photochromic agonist for mu-opioid receptors. *Angew. Chem. Int. Ed. Engl.*, **53**, 3264–3267.
- Broichhagen, J., Frank, J.A. and Trauner, D. (2015) A roadmap to success in photopharmacology. *Acc. Chem. Res.*, **48**, 1947–1960.
- McCown, P.J., Corbino, K.A., Stav, S., Sherlock, M.E. and Breaker, R.R. (2017) Riboswitch diversity and distribution. *RNA*, **23**, 995–1011.
- Wachter, A., Tunc-Ozdemir, M., Grove, B.C., Green, P.J., Shintani, D.K. and Breaker, R.R. (2007) Riboswitch control of gene expression in plants by splicing and alternative 3' end processing of mRNAs. *Plant Cell*, **19**, 3437–3450.
- Berens, C., Groher, F. and Suess, B. (2015) RNA aptamers as genetic control devices: the potential of riboswitches as synthetic elements for regulating gene expression. *Biotechnol. J.*, **10**, 246–257.
- Berens, C. and Suess, B. (2015) Riboswitch engineering—making the all-important second and third steps. *Curr. Opin. Biotechnol.*, **31**, 10–15.
- Ellington, A.D. and Szostak, J.W. (1990) In vitro selection of RNA molecules that bind specific ligands. *Nature*, **346**, 818–822.
- Tuerk, C. and Gold, L. (1990) Systematic evolution of ligands by exponential enrichment: RNA ligands to bacteriophage T4 DNA polymerase. *Science*, **249**, 505–510.
- Lee, H.W., Robinson, S.G., Bandyopadhyay, S., Mitchell, R.H. and Sen, D. (2007) Reversible photo-regulation of a hammerhead ribozyme using a diffusible effector. *J. Mol. Biol.*, **371**, 1163–1173.
- Young, D.D. and Deiters, A. (2008) Light-regulated RNA-small molecule interactions. *ChemBiochem*, **9**, 1225–1228.
- Hayashi, G., Hagihara, M. and Nakatani, K. (2009) RNA aptamers that reversibly bind photoresponsive azobenzene-containing peptides. *Chemistry*, **15**, 424–432.
- Hayashi, G., Hagihara, M., Dohno, C. and Nakatani, K. (2007) Reversible regulation of binding between a photoresponsive peptide and its RNA aptamer. *Nucleic Acids Symp. Ser. (Oxf)*, **93**, 93–94.
- Groher, F., Bofill-Bosch, C., Schneider, C., Braun, J., Jäger, S., Geißler, K., Hamacher, K. and Suess, B. (2018) Riboswitching with ciprofloxacin—development and characterization of a novel RNA regulator. *Nucleic Acids Res.*, **46**, 2121–2132.
- Hall, B., Micheletti, J.M., Satya, P., Ogle, K., Pollard, J. and Ellington, A.D. (2009) Design, synthesis, and amplification of DNA pools for in vitro selection. *Curr. Protoc. Mol. Biol.*, doi:10.1002/0471142727.mb2402s88.
- Groher, F. and Suess, B. (2016) In vitro selection of antibiotic-binding aptamers. *Methods*, **106**, 42–50.
- Zimmerman, G., Chow, L.-Y. and Paik, U.-J. (1958) The photochemical isomerization of azobenzene. *J. Am. Chem. Soc.*, **80**, 3528–3531.
- Davis, J.H. and Szostak, J.W. (2002) Isolation of high-affinity GTP aptamers from partially structured RNA libraries. *Proc. Natl. Acad. Sci. U.S.A.*, **99**, 11616–11621.
- Nutiu, R. and Li, Y. (2005) In vitro selection of structure-switching signaling aptamers. *Angew. Chem. Int. Ed. Engl.*, **44**, 1061–1065.
- Uhlenbeck, O.C. (1990) Tetraloops and RNA folding. *Nature*, **346**, 613–614.
- Paige, J.S., Wu, K.Y. and Jaffrey, S.R. (2011) RNA mimics of green fluorescent protein. *Science*, **333**, 642–646.
- Berens, C., Thain, A. and Schroeder, R. (2001) A tetracycline-binding RNA aptamer. *Bioorg. Med. Chem.*, **9**, 2549–2556.
- McKeague, M., McConnell, E.M., Cruz-Toledo, J., Bernard, E.D., Pach, A., Mastrorardi, E., Zhang, X., Beking, M., Francis, T., Giamberardino, A. et al. (2015) Analysis of in vitro aptamer selection parameters. *J. Mol. Evol.*, **81**, 150–161.
- Bailey, T.L. and Elkan, C. (1994) Fitting a mixture model by expectation maximization to discover motifs in biopolymers. *Proc. Int. Conf. Intell. Syst. Mol. Biol.*, **2**, 28–36.
- Levenshtein, V. (1966) Binary codes capable of correcting deletions, insertions and reversals. *Soviet Phys. Doklady*, **10**, 707–710.
- Smith, C., Heyne, S., Richter, A.S., Will, S. and Backofen, R. (2010) Freiburg RNA Tools: a web server integrating INTARNA, EXPARNA and LOCARNA. *Nucleic Acids Res.*, **38**, W373–W377.
- Will, S., Joshi, T., Hofacker, I.L., Stadler, P.F. and Backofen, R. (2012) LocARNA-P: accurate boundary prediction and improved detection of structural RNAs. *RNA*, **18**, 900–914.
- Uhlenbeck, O.C., Borer, P.N., Dengler, B. and Tinoco, I. Jr. (1973) Stability of RNA hairpin loops: A 6-C m -U 6. *J. Mol. Biol.*, **73**, 483–496.
- Williams, D.J. and Hall, K.B. (1996) Thermodynamic comparison of the salt dependence of natural RNA hairpins and RNA hairpins with non-nucleotide spacers. *Biochemistry*, **35**, 14665–14670.
- Burke, D.H., Hoffman, D.C., Brown, A., Hansen, M., Pardi, A. and Gold, L. (1997) RNA aptamers to the peptidyl transferase inhibitor chloramphenicol. *Chem. Biol.*, **4**, 833–843.

7.7 Brilmayer et al., *ChemNanoMat*. 2020, 6

The Interplay of Nanoconfinement and pH from the Perspective of a Dye-Reporter Molecule

R. Brilmayer*, M. Bodrecht*, C. Kaiser, H. Breitzke, B. Kumari, J. Wachtveitl,
G. Buntkowsky, A. Andrieu-Brunsen,

ChemNanoMat **2020**, 6, 1843-1853.

(DOI: 10.1002/cnma.202000423)

The Interplay of Nanoconfinement and pH from the Perspective of a Dye-Reporter Molecule

Robert Brilmayer^{+, [a]} Martin Brodrecht^{+, [b]} Christoph Kaiser,^[c] Hergen Breitzke,^[b] Bharti Kumari,^[b] Josef Wachtveitl,^[c] Gerd Buntkowsky,^{*, [b]} and Annette Andrieu-Brunsen^{*, [a]}

Abstract: A novel thiazol-based ratiometric dye for the detection of local pH values is synthesized, and its properties are characterized by a combination of optical spectroscopy, solid-state NMR and DNP (dynamic nuclear polarization)-enhanced solid-state NMR. This novel dye covers a completely different sensitivity range with its acidic pKa value of 3.5 compared to other established dyes for ratiometric pH detection, such as SNARF. The dye is grafted to the surfaces

of mesoporous silica materials, which enables, for the first time, direct in situ measurements of the local pH values in silica mesopores by a simple UV-vis spectroscopy method. The obtained results, which are in good agreement with previous indirect techniques, indicate a background electrolyte-dependent pKa shift of at least one pH unit under nanoconfined conditions compared to the pKa of the dye in bulk solution.

Introduction

Since their discovery in 1992, template-based mesoporous silica materials (MSMs) have attracted increasing interest in various research fields.^[1] Currently, MSMs are commonly used in applications such as sensing,^[2] separation processes^[3] and energy conversion.^[4] MSMs have interesting properties, such as a high specific surface area, high chemical stability and high physical stability.^[5] In addition to these attributes, the surface silanol groups can be used to introduce organic functional groups in the inorganic framework.^[5–6] This has been particularly relevant for mesoporous silica thin films as well as for mesoporous silica nanoparticles.^[7] Functionalization with responsive organic moieties has led to the formation of smart materials in this research field, which has been of significant relevance in the past 15 years.^[6,8] In these smart or responsive materials as well as in the application areas of smart materials such as drug delivery or environmental sensing, pH plays a crucial role; thus, and its influence has been studied extensively.

For example, enzyme stabilization is pH-dependent.^[9] For drug delivery often minimal pH-changes in the exterior of mesoporous particles should induce a release.^[10]

In this context, differences between the pH value in solution and under nanoconfined conditions, for example, within silica mesopores, have been reported based on theoretical studies and indirect experimental observations.^[11] To date, experimental studies have been limited to indirect measurements such as ion flow through nanochannels or mesopore permselectivity to determine the charge of molecules inside nanoscale environments.^[7,9a,12] Although pH detection in MSMs has gained more importance in recent years, the direct measurement of the apparent pH value inside nanopores has not yet been fully explored.^[11b,13] The most prominent recent advances can be ascribed to theoretical studies by *Szleifer* and co-workers, who demonstrated the pKa shift of polyelectrolytes in nanochannels.^[11a] Until now, the experimental determination and prediction of pH values in nanopores or nanochannels has remained a challenge but represents a crucial confinement parameter to understand in detail the transport, release, and molecular stabilization processes of mesoporous materials.^[8b] One promising approach to investigate the pH value at the nanoscale has been the use of dyes.

In the context of dyes as pH reporter molecules, the main focus over the last few years has been to detect pH changes in cells. In this research field, various studies have explored pH changes in cancer cells compared to healthy cells, offering a new cancer detection method.^[14] Due to the nature of living cells, those studies focused on a very narrow pH detection range (pH 6.5–7.6). However, to cover the entire relevant range of functionalized nanopores and their applications, dyes with sensitivity ranges between pH 1 and 5 are also needed. Potential dye sensors that have been explored together with mesoporous silica materials are FRET (*Förster resonance energy transfer*) dye pairs consisting of a pH-sensitive reporter and a pH-insensitive dye for concentration calibration. Due to the distinct nature of FRET, a constant distance between the donor

[a] Dr. R. Brilmayer,⁺ Prof. Dr. A. Andrieu-Brunsen
Ernst-Berl-Institut für Technische und Makromolekulare Chemie
Technische Universität Darmstadt
Alarich-Weiss-Str. 12, 64287 Darmstadt (Germany)
E-mail: andrieu-brunsen@smartmem.tu-darmstadt.de

[b] Dr. M. Brodrecht,⁺ Dr. H. Breitzke, Dr. B. Kumari, Prof. Dr. G. Buntkowsky
Eduard-Zintl-Institut für Anorganische und Physikalische Chemie
Technische Universität Darmstadt
Alarich-Weiss-Str. 8, 64287 Darmstadt (Germany)
E-mail: gerd.buntkowsky@chemie.tu-darmstadt.de

[c] C. Kaiser, Prof. Dr. J. Wachtveitl
Institute for Physical and Theoretical Chemistry, Goethe University
Max-von-Laue-Str. 7, 60438 Frankfurt (Germany)

[*] Both authors contributed equally.

Supporting information for this article is available on the WWW under <https://doi.org/10.1002/cnma.202000423>

© 2020 The Authors. Published by Wiley-VCH GmbH. This is an open access article under the terms of the Creative Commons Attribution Non-Commercial NoDerivs License, which permits use and distribution in any medium, provided the original work is properly cited, the use is non-commercial and no modifications or adaptations are made.

and the acceptor molecule has to be retained to allow reproducible FRET with this pH detection method. Since this is a parameter that cannot be easily controlled in bulk solution and cannot be precisely characterized on surfaces or in mesopores, the use of FRET-dye pairs is not suitable for comparisons between measurements in nanoconfined conditions and in bulk solution.^[11b] Ratiometric dyes, which have a distinct absorption and/or emission maximum in their protonated and deprotonated states, can overcome the issues of FRET pH reporters for use in nanopores. Additionally, the spectral maxima of ratiometric dyes are concentration independent, which further facilitates comparisons between different measurements.^[13] Of the ratiometric dyes, many commonly applied in-cell dyes, such as the SNARF (Seminaphtharhodofluor) dye family, have a sensitivity region that does not overlap with the pKa value of silanol groups in mesoporous silica. One dye family that meets all the requirements mentioned above is the thiazol-based family of dyes such as the 5-methoxy-pyridylthiazole (MPT) dye reported by Zheng *et al.*^[13b] These dyes are of special interest in combination with silica materials since their pKa value is in the responsive range of silanol groups.^[12c,d,13b,15] Several similar dyes have been reported even recently as pH-reporters^[16] for sensing vapor chromism in halogenated solvents^[17] or ion sensors^[18] usually applied while being dissolved but not covalently grafted to a surface.

To address the pH region between 1.5 and 5.0 in nanoscale pores in this study, we synthesized and investigated the potential of a new MPT-based ratiometric pH reporter dye in conjunction with MSMs. In addition to the characterization and determination of the optical properties, the successful attachment of the dye to the silica framework was confirmed by solid-state NMR, TGA (thermogravimetric analysis), EA (elemental analysis) and BET (Brunauer-Emmett-Teller)-based nitrogen adsorption-desorption measurements. Last, MPT-Ph was successfully used to determine pH shifts between bulk solutions and silica mesopores with diameters smaller than 20 nm. Therefore, pH shifts of more than one pH unit were observed.

Results and Discussion

Synthesis and optical properties of MPT-Ph

MPT-Ph (4-(5-methoxy-2-(pyridin-4-yl)thiazol-4-yl)benzoic acid) **2** and MPT-amide (4-(5-methoxy-2-(pyridin-4-yl)thiazol-4-yl)-N-propylbenzamide) **3** were synthesized as outlined in Scheme 1a.

MPT-Br (4-bromo-5-methoxy-2-(pyridin-4-yl)thiazole) **1** was synthesized in three steps according to a method established for MPT-based dyes by Zheng *et al.*^[13b,15a] C–C bond formation was achieved by a Suzuki coupling reaction to form MPT-Ph **2**, followed by amination to yield MPT-Ph-amide **3**. Compounds **2** and **3** were characterized by 1D- and 2D-NMR as well as SI-MS (Figures S1–S8).

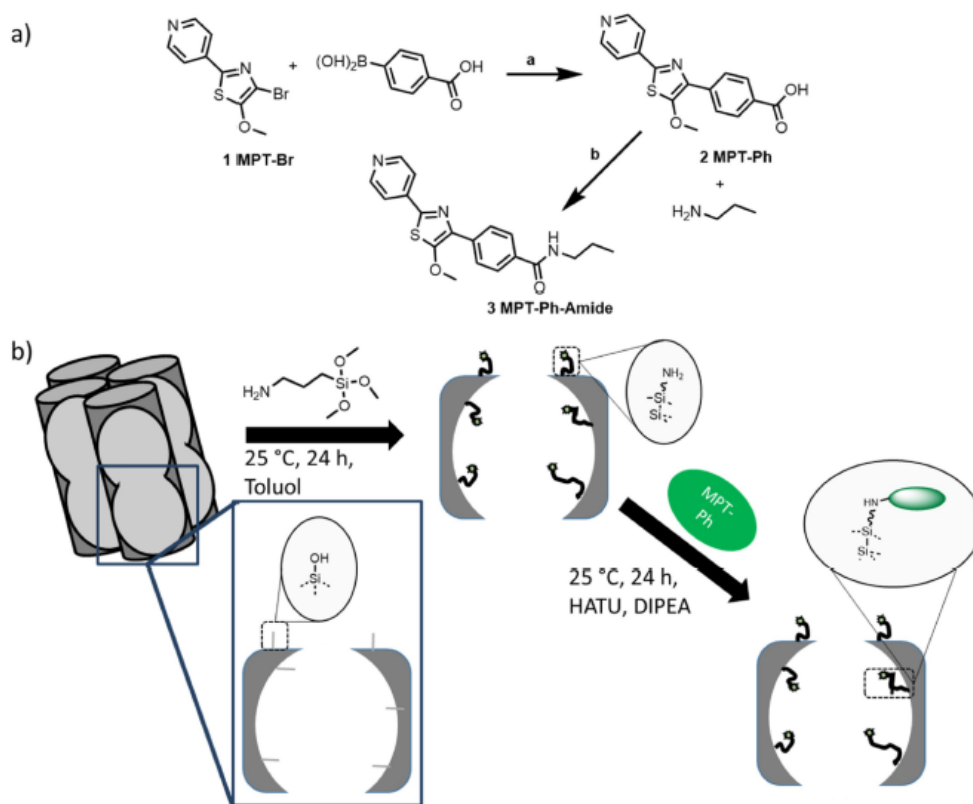
MPT compound **1** is an acidochromic chromophore since its absorbance and emission show a bathochromic shift upon acidification which probably results in protonation on the pyridine moiety.^[13b] The effects of the introduction of the

phenyl group (MPT-Ph **2**) on the photophysical properties of MPT-Br **1** are depicted in Figure 1b. For the protonated (Figure 1b, green) and deprotonated MPT-Ph species (Figure 1b, blue), the absorption and fluorescence peaks show a bathochromic shift by approximately 50 nm compared to those of MPT-Br **1**. This is ascribed to the significant enlargement of the electronic π -system of MPT-Ph **2**. Regarding MPT-Ph, protonation of the N-basic site results in a redshift of the emission band from approximately 450 nm to 510 nm. The introduction of the positive charge results in a more pronounced charge displacement and a reduced transition energy for MPT-Ph (Figure 1c).

The molar extinction coefficients of both MPT-Ph and MPT-Ph-H⁺ forms were determined by measurement of the concentration-dependent absorbance values at the maxima of their S1 bands. Following Lambert-Beer's law, the protonated and deprotonated forms exhibit extinction coefficients of 8070 ± 60 and $7440 \pm 30 \text{ M}^{-1} \text{ cm}^{-1}$, respectively (Figure S9). With the use of an integrating sphere, fluorescence quantum yields of 7% for the deprotonated form and 23% for the protonated form were calculated. The maximum emission signal can be obtained through excitation at the maxima of the S1 absorption bands for both species (Figure S10, 3D contour plots). The excitation spectrum, which is a vertical cut through the contour plots at the maximum emission wavelength, resembles the absorption spectrum. In the excitation wavelength-dependent contour plots, only the emission signals of the particular species are observed. Upon excitation of the deprotonated species at pH 7.4, no emission of the protonated form is detected, which indicates that the pyridine group does not act as a strong photobase and acquires a proton from the solvent, similar to related nitrogen-containing compounds reported in the literature.^[19] Interestingly, the fluorescence decays of MPT-Ph, recorded by means of the time-correlated single photon counting (TCSPC) method, are significantly accelerated compared to other MPT derivatives.^[13b] The decay curve of the protonated form MPT-Ph-H⁺ could be fitted monoexponentially, which revealed a lifetime of 1.4 ns (Figure 1d). For the deprotonated MPT-Ph, a sum of two exponential functions was required, where a 1.7% contribution of the 1.4 ns lifetime could be assigned to residual amounts of the protonated species at pH 7.4. The major contribution of 98.3% of a 0.3 ns lifetime accounts for the deprotonated form.

MPT-Ph as a pH reporter in silica mesopores

Two different mesoporous silica materials with comparable porous structures were used as frameworks to incorporate the MPT-Ph dye. Mesoporous silica thin films with pore diameters of 8 and 16 nm and film thicknesses of 200–1000 nm were prepared using sol-gel chemistry and evaporation-induced self-assembly as previously reported.^[9a,20] Additionally, amino-functionalized mesoporous silica SBA-15 (Santa Barbara amorphous 15) particles were prepared by a previously reported strategy.^[21] The amino groups were introduced by a cocondensation approach using tetraethyl orthosilicate (TEOS) and (3-amino-



Scheme 1. (a) Synthesis of MPT-Ph (4-(5-methoxy-2-(pyridin-4-yl)thiazol-4-yl)benzoic acid) 2 and MPT-amide (4-(5-methoxy-2-(pyridin-4-yl)thiazol-4-yl)-N-propylbenzamide) 3: a) X-Phos Pd G2 (chloro(2-dicyclohexylphosphino-2',4',6'-triisopropyl-1,1'-biphenyl)(2-(2'-amino-1,1'-biphenyl)palladium(II)), dioxan/H₂O, K₂CO₃, reflux for 24 h under an inert atmosphere, 70%; b) HATU (O-N, N, N', N'-tetramethyluronium-hexafluorophosphate), DIPEA (diisopropylethylamine), and DMF (N, N-dimethylformamide) reacted for 48 h under an inert atmosphere, 71%; (b) schematic illustration of silica modification. In the first step, aminopropyl trimethoxy silane (APTMS) is attached to the unfunctionalized silica pores. In a second step, MPT-Ph is coupled to the amino functional group through amide bond formation.

propyl)triethoxysilane (APTES). BET characterization of the SBA-15 materials is presented in detail in the supporting information (Figure S11–S14 and Table S1–S4).

To explore the influence of spatial confinement on the pH value inside of silica mesopores, the MPT-Ph pH reporter must be introduced into the silica framework while being accessible for the measurement solution, as illustrated for a postgrafting approach in Scheme 1b. For this purpose, covalent attachment of the dye is necessary to avoid leaching, which would result in a possible mixture of the dye in the mesopores and in the bulk solution.

The MPT-Ph dye carries a free carboxyl group that is not involved in pH detection and can thus be used as an anchor group. Amino groups are suitable reaction moieties resulting in amide bond formation under very mild reaction conditions. For this reason, the prepared mesoporous silica thin films were first functionalized with APTMS (aminopropyl trimethoxy silane) via

a postgrafting approach, while the amino functional groups in the SBA-15 material were introduced through cocondensation. In both cases, dye attachment through amide formation was performed using HATU (1-[Bis(dimethylamino)methylene]-1H-1,2,3-triazolo[4,5-b]pyridinium 3-oxide hexafluorophosphate) as the coupling reagent under identical reaction conditions.

Comparing TGA (thermogravimetric analysis) of the SBA-15 material before and after dye coupling (Figure S11), the weight fraction of the dye can be obtained (Table S1), leading to a dye loading of 0.33 ± 0.02 mmol/g. By applying elemental analysis (EA), the weight and molar fractions of the elements nitrogen, carbon and hydrogen are obtained (Table S2 and Table S3). Based on the result for nitrogen, a dye loading of 0.54 ± 0.05 mmol/g is calculated. The same process applies for carbon, leading to a dye loading of 0.55 ± 0.02 mmol/g.

The pore volume and specific surface area (Table S4) of the functionalized SBA-15 materials can be obtained by the

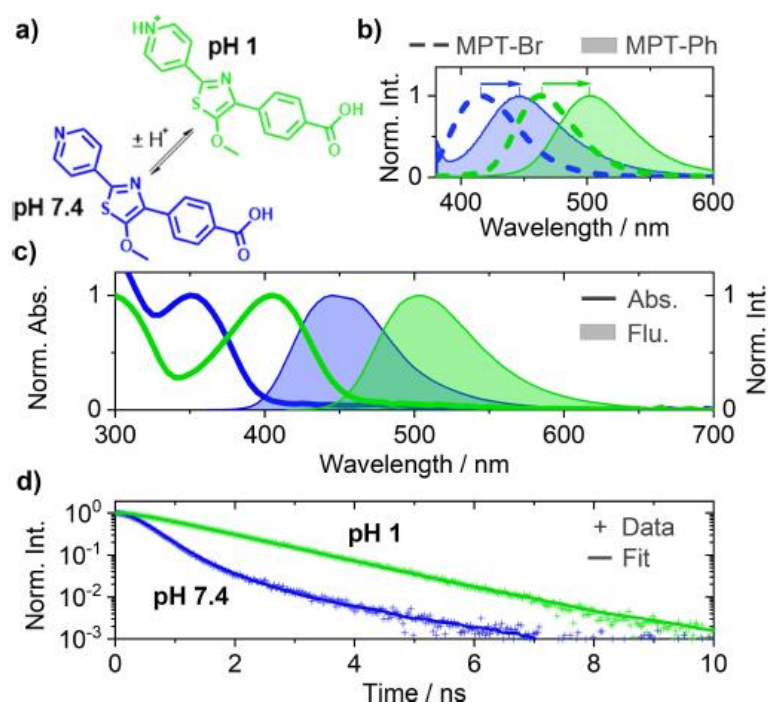


Figure 1. The protonated form of the MPT-Ph 2 dye and its spectrum at pH 1 is shown in green, and that of the deprotonated form at pH 7.4 is shown in blue. (a) Protonation reaction of MPT-Ph. (b) Emission spectra of the deprotonated and protonated forms of MPT-Br (dashed lines) and redshifted spectra of MPT-Ph (solid lines/green area). (c) Absorbance (solid lines) and emission spectra (filled areas) of MPT-Ph. (d) Fluorescence decays (+ symbols) and exponential fits (solid lines) of both forms of the MPT-Ph dye.

Brunauer-Emmett-Teller (BET) analysis of the nitrogen adsorption-desorption isotherms (Figure S12). To investigate changes in the pore diameter due to dye functionalization, Barrett-Joyner-Halenda (BJH) (Figure S13) and density functional theory (NLDFT) (Figure S14) methods are applied. While BJH analysis suggests a decrease in pore diameter from 5.6 ± 0.2 nm to 4.9 ± 0.3 nm, NLDFT analysis shows a decrease from 7.9 ± 0.2 nm to 6.6 ± 0.3 nm.

Combining the specific surface area of the dye-functionalized SBA-15 material (271 ± 7 m²/g) and the results of the molar dye grafting densities by TGA and EA analysis, surface grafting densities of the dye can be calculated, and the results are shown in Table 1.

Both methods suggest a high degree of surface functionalization of the functionalized SBA-15 material. To investigate the

coupling efficiency and to prove the covalent binding of the MPT-Ph dye, NMR techniques were used. Since solid-state NMR requires a large amount of sample and a high degree of functionalization, these investigations were carried out with functionalized SBA-15 nanoparticles.

To monitor the success of the MPT-Ph dye modification, ¹³C CP MAS solid-state NMR spectra were recorded before (Figure 2a) and after dye coupling (Figure 2c). A spectrum of the MPT-Ph dye was also included to facilitate the peak assignment (Figure 2b).

In the ¹³C CP MAS spectrum of the APTES functionalized SBA-15 (Figure 2a), the signals at 9 ppm, 21 ppm and 43 ppm are assigned to the α , β and γ carbon atoms of the APTES ((3-aminopropyl)triethoxysilane)-linker, respectively. The small additional features at 18 ppm and 59 ppm are assigned to the not fully hydrolyzed ethoxy groups of either APTES or TEOS (tetraethoxysilane).

The spectrum of the pure MPT-Ph dye (Figure 2b) shows a signal at 66 ppm, which is characteristic of the carbon atom for the methoxy group (Me). The resonances between 127 ppm and 144 ppm can be assigned to the aromatic carbon atoms of the phenyl (Ph) and pyridine (Py) rings. Additionally, the peaks at 117 ppm, 161 ppm and 168 ppm can be assigned to the

Table 1. Calculated surface grafting densities of the MPT-Ph dye-functionalized SBA-15 material obtained by the combination of the specific surface area obtained by nitrogen adsorption-desorption and molar dye grafting densities obtained by TGA and EA.

	TGA	EA (nitrogen)	EA (carbon)
Surface grafting density	0.73 ± 0.06	1.20 ± 0.14	1.22 ± 0.08

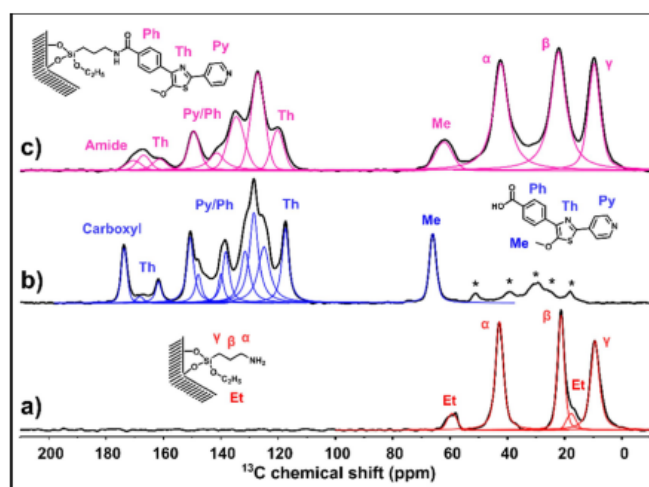


Figure 2. Comparison of the ^{13}C CP MAS spectra of the functionalized SBA-15 at a spinning rate of 6 kHz (10 kHz for (b) and (c)). From the bottom to the top spectra of the APTES functionalized SBA-15 (a), pure MPT-Ph dye (b) and MPT-Ph dye-functionalized SBA-15 species (c).

carbon atoms of the thiazole (Th) heterocycle. Finally, a peak at 173 ppm is assigned to the carbonyl carbon atom of the carboxyl group.

After coupling MPT-Ph to the silica mesopores (Figure 2c), the resonances of the α , β and γ carbon atoms of the APTES linker at 10 ppm, 22 ppm and 42 ppm are still observed, which suggests that the linker is still attached to the surface. The signal at 62 ppm can be assigned to the methoxy carbon atom of the MPT-Ph dye. The resonances between 120 ppm and 149 ppm of the aromatic carbon atoms of the phenyl (Ph) ring are preserved. The signals at 117 ppm and between 161 ppm and 170 ppm previously assigned to the carbon atoms of the thiazole heterocycle are also still obtained. Most importantly, the resonance at 170 ppm can be assigned to the carbon atom of the newly formed amide bond between the APTES-linker and the dye. The chemical shift change in the carbonyl carbon from 173 ppm to 170 ppm indicates the conversion of the carboxylic carbon to an amide carbon.

To investigate the binding situation between the surface-bound NH_2 group and the COOH group of the dye, DNP-enhanced ^{15}N solid-state NMR was applied, which can detect the ^{15}N nuclei of an amide bond in natural abundance and avoids costly ^{15}N isotope labeling.^[22]

The DNP-enhanced ^{15}N CP MAS NMR spectrum of the MPT-Ph dye-functionalized SBA-15 species (Figure 3a) shows a signal at -6 ppm. This signal is assigned either to the protonated (NH_3^+) or nonprotonated (NH_2) form of the nitrogen atom of the APTES-linker. The presence of this signal indicates unreacted amine groups on the surface. In addition, a second signal at 81 ppm is observed, which is assigned to the nitrogen atom of the amide group between the APTES-linker and the surface coupled dye. This clearly demonstrates the covalent binding of MPT-Ph to the mesoporous silica surface. Further-

more, the small signal at 165 ppm is characteristic of the pyridinium cation (Py^+-H). From the ^{15}N -chemical shift/pKa correlation data of heteroaromatic ring nitrogens in solid state complexes reported in a publication by Lorente *et al.*^[23] and the pyridine ^{15}N chemical shift of pyridine in the solid state,^[24] the high-field shift of 105 ± 10 ppm corresponds to a pKa of $0 \pm 1/2$. The residual signals at 251 ppm and 268 ppm can be assigned to the nonprotonated nitrogen atom of pyridine (Py) and the nitrogen atom of the thiazole heterocycle (Th).^[15b]

To investigate the pH responsiveness, the dye was grafted to the surface of the mesoporous silica, and the pH value of the DNP matrix was adjusted to 1 by the addition of DCl. The pH change results in a color change from blue (pH 7) to green (pH 1) under UV light irradiation (352 nm). This color is maintained even after removing the excess liquid (Figure 3c), which proves the pH response of the surface-bound dye.

Additionally, a DNP-enhanced ^{15}N CP MAS NMR spectrum of the acidic sample was recorded to investigate the chemical changes in the dye induced by the pH change (Figure 3b). Comparing the spectrum recorded before (Figure 3a) and after pH adjustment, the signal at -11 ppm is preserved. At this pH, this signal is assigned to the protonated (NH_3^+) form of the nitrogen atom of the APTES-linker. The resonance of the amide nitrogen is still observed at 76 ppm, which clearly reveals the stability of the covalent MPT-Ph binding to the silica surface even at pH 1. Additionally, the signal of the protonated pyridine nitrogen (Py^+-H) is preserved at pH 1 and seems to be increased in intensity compared to that at pH 7.

In the region of higher chemical shift, only the signal at 238 ppm remains, which is assigned to the nitrogen atom of the thiazole heterocycle (Th). The signal of the nonprotonated nitrogen atom of pyridine (Py) is no longer observed. The pH switching mechanism of the dye suggests protonation of the

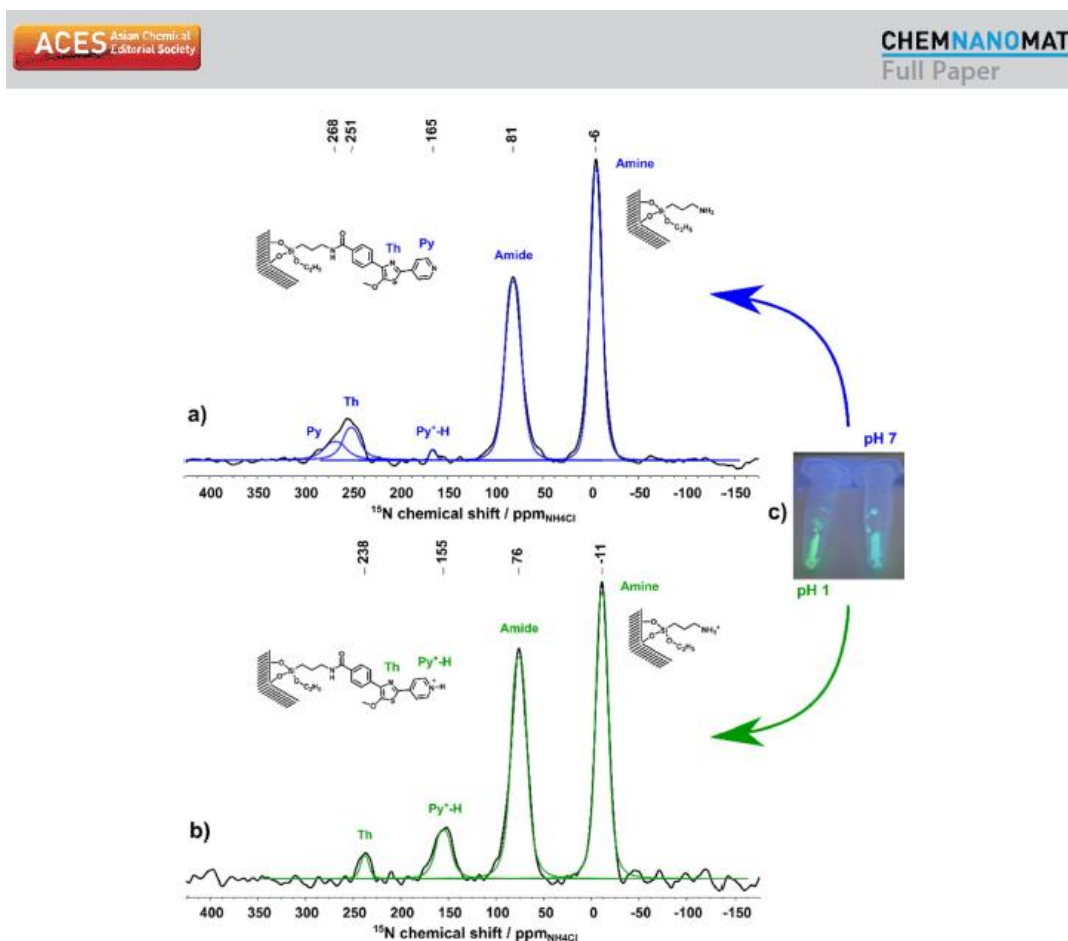


Figure 3. Comparison of DNP-enhanced ^{15}N CP MAS spectra of functionalized SBA-15 at a spinning rate of 8 kHz and at a nominal temperature of 110 K. Spectra of MPT-Ph dye-functionalized SBA-15 silica at pH 7 (a) and pH 1 (b). Comparison (c) of dried MPT-Ph dye-functionalized SBA-15 silica under UV light irradiation (352 nm) used for the NMR measurements.

pyridine nitrogen, which is in good agreement with this observation, since the signal intensity of the protonated pyridine nitrogen ($\text{Py}^+\text{-H}$) also increased.

Optical characterization of MPT-Ph functionalized silica thin films

From UV-vis measurements and determined by the *Lambert-Beer law* (Equation 1) where A is the measured Absorbance, d is twice the film thickness and the previously determined ϵ of $8070 \text{ mol}^{-1} \text{ cm}^{-1}$, it is clear that the large pores (16 nm) can incorporate higher dye concentrations (c) (0.24 mol^{-1}) than the 8 nm pores (0.12 mol^{-1}) (Figure 4 a red line and purple line).

$$A = \epsilon \cdot c \cdot d$$

(1)

In accordance with Lambert-Beer's law, the amount of dye per substrate surface (c) and thus the maximum absorbance (A) can be adjusted by changing the mesoporous silica film thickness (d). Thus, the film thickness and pore size are critical parameters to adjust the total detectable dye amount, which is crucial for a visible coloration of the mesoporous silica film (Figure 4b). The UV-vis measurements confirm the homogeneous dye functionalization along the mesoporous silica film thickness, as the absorbance approximately doubles when the mesoporous thin films are twice as thick as the original (Figure 4a blue line vs purple line).

To investigate the infiltration of the measurement solution and diffusion into the mesoporous thin films at a relevant time scale for the experiments performed in this study, UV-vis measurements were performed directly after immersing the MPT-Ph functionalized and dry film into a test solution. The film was kept in the measurement solution for 60 minutes while measuring one UV-vis spectrum per minute. This test showed

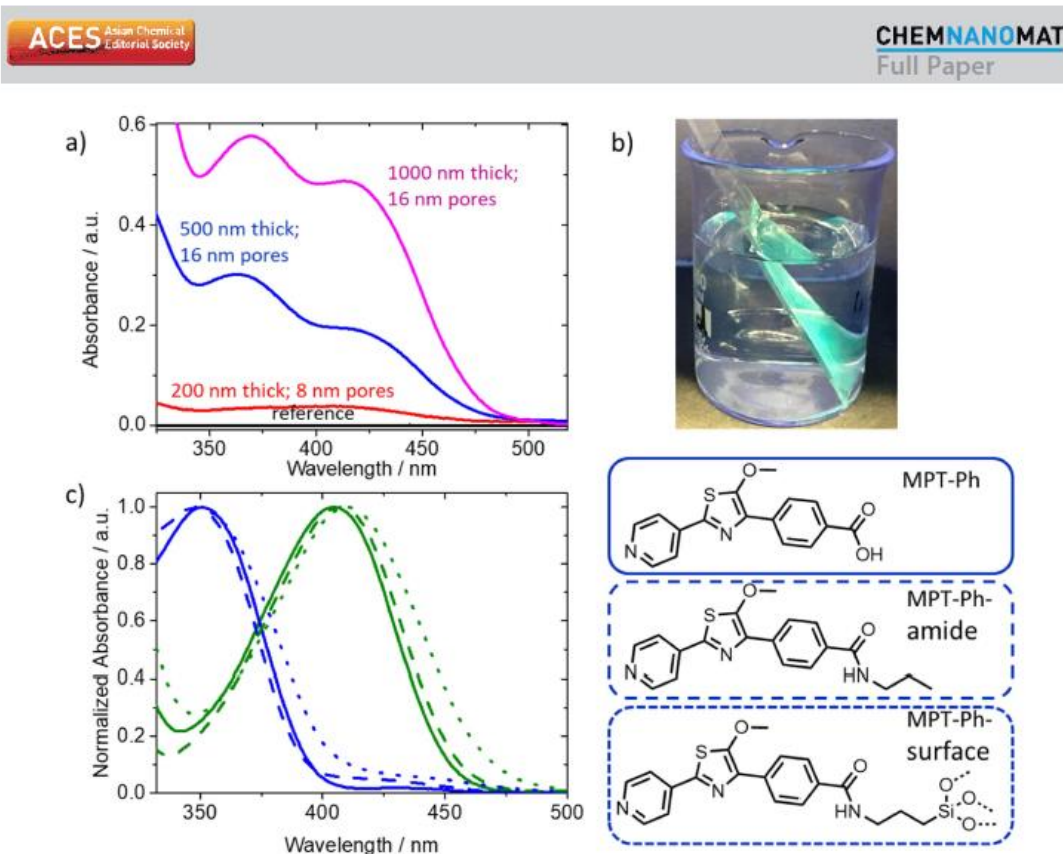


Figure 4. (a) UV-vis spectra of MPT-Ph functionalized mesoporous silica films with film thicknesses of 200 nm (red line), 500 nm (blue line) and 1000 nm (pink line). The black line is an unfunctionalized mesoporous silica film. Measurements were recorded at a solution pH of ~3; (b) Picture of an MPT-Ph functionalized mesoporous silica thin film under UV-light irradiation (365 nm); (c) UV-vis spectra and the corresponding chemical structures of MPT-Ph (solid lines), MPT-Ph-amide (dashed lines) and MPT-Ph-surface (dotted lines) of the protonated form at pH 1.5 (green) and the deprotonated form at pH 7.5 (blue).

no difference between the measurement at $t=0$ minutes and $t=60$ minutes (Figure S15), indicating that acid-base equilibrium of the incorporated MPT-Ph dye is obtained during sample preparation and that no dye leaching is observed. This also shows that the diffusion of solution through the film is not hindered and that the system can react quickly with a change in the solution pH. In addition, the UV-vis measurements show that the mesoporous silica film and the dye functionalization are stable towards the measurement solution for at least 60 minutes, while measurements are conducted in less than a minute.

To prove that the combination of MPT-Ph and mesoporous silica is suitable for pH investigation in thin mesoporous films, the pH responsiveness of the dye was confirmed after surface anchoring. As shown in Figure 4c, MPT-Ph-amide and the MPT-Ph-surface show the same pH responsive behavior as MPT-Ph. While MPT-Ph-amide (Figure 4c dashed lines) was used as a chemical analog to the surface-anchored MPT-Ph (Figure 4c solid lines), a slight influence of the surface is noticeable. The absorption maxima of the surface-anchored dye (Figure 4c dotted lines) are slightly redshifted compared to

both dyes measured in bulk solution. It is not differentiated if this slight redshift originates from influences due to confinement or surface chemistry as the apparent pH in such nanoscale pores is always depending on both. The influence of confinement on photophysical dye characteristics is increasingly discussed especially for pores with diameters below 2 nm.^[25] As the observed red-shift is minimal and the pH-response is still present we applied this grafted dye for apparent pH-detection.

Bulk vs confined pH measurements

For pH detection using MPT-Ph as a pH reporter, measurement solutions with a predetermined pH value between 8.4 and 1.7 were prepared. Their pH values were stabilized using PBS buffer solution (150 mM). Subsequently, UV-vis spectra were recorded. With decreasing pH, the absorption maximum at ~350 nm decreases, while the absorption maximum at 411 nm increases (Figure 5a). To determine the pKa value of MPT-Ph, the quotient of $\frac{[MPT-Ph-H^+]}{[MPT-Ph]}$ can be plotted against the measured

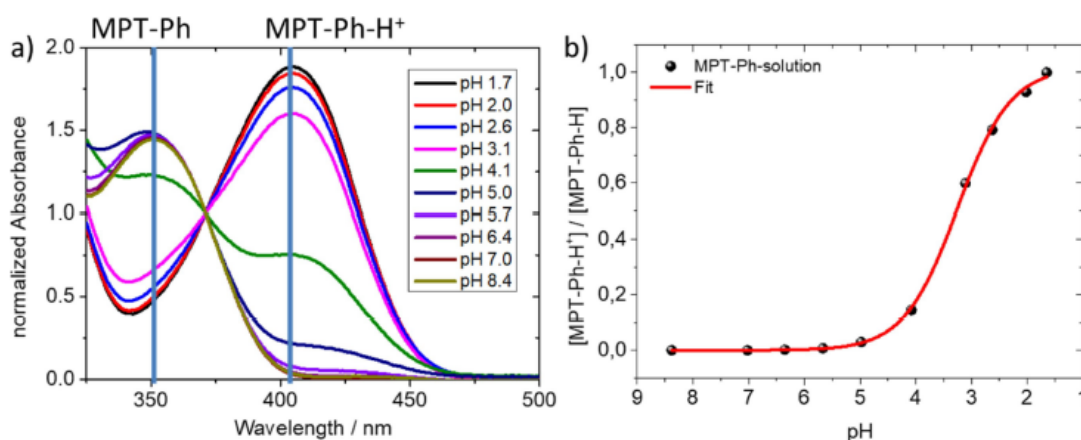


Figure 5. (a) UV-vis spectra of MPT-Ph at pH values between 8.4 and 1.7; (b) corresponding plot to measurements from (a), showing the quotient of MPT-Ph-H⁺/MPT-Ph plotted against the solution pH value (black spheres). The red line shows a mathematical sigmoidal fit to determine the pK_a value of MPT-Ph (pK_a = 3.3).

solution pH value. A mathematical sigmoidal fit was used to determine the pK_a value of 3.3 (Figure 4b).

The same procedure was further used to determine the pK_a value of MPT-Ph-amide and that of the surface-bound MPT-Ph-surface derivative (Figure 6a). The results show that the difference between the residual carboxyl group of the MPT-Ph dye

(pK_a 3.3) and the residual amide functional group in the MPT-Ph-amide dye (pK_a 3.5) towards the resulting pK_a value is very small. On the other hand, when entrapped in the nano-confined silica mesopores, MPT-Ph-surface shows a pK_a value of 2.1. This pK_a shift of more than one pH unit compared to its pK_a value in solution (Figure 6a) indicates a ten-fold more acidic

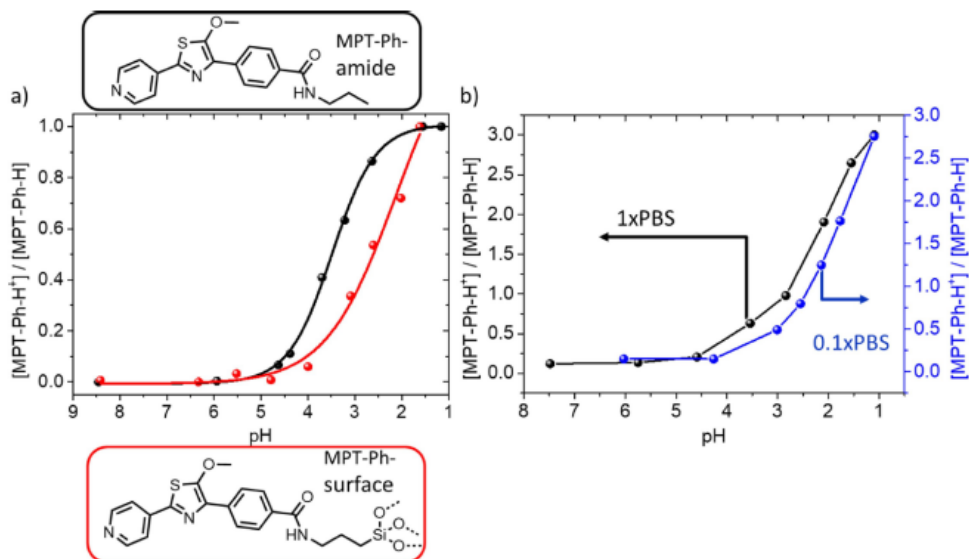


Figure 6. a) Quotient of MPT-Ph-amide-H⁺/MPT-Ph-amide (black spheres) and MPT-Ph-surface-H⁺/MPT-Ph-surface (red spheres) plotted against the solution pH value. Black and red lines show the corresponding mathematical sigmoidal fit to determine the pK_a value of MPT-Ph-amide (pK_a = 3.5) and MPT-Ph-surface (pK_a = 2.1). b) Quotient of MPT-Ph-surface-H⁺/MPT-Ph-surface plotted against the solution pH value at different ionic strengths of 150 mM (black line) and 15 mM (blue line)

environment in mesopores than the measurements in bulk solution. The observed confinement effects detected as equilibrium shift which result in the apparent pH of course relate to changes in surface chemistry as well as the influence of spatial confinement. Both aspects are not separated in this study.

These findings using MPT-Ph as a new pH-reporter dye molecule sensitive to the required pH region (pH 1–5) in which mesoporous silica responds are in accordance with previous findings from our group investigating the pKa value of short oligomer chains in silica mesopores as well as with theoretical simulations for short polymer chains in ion channels.^[9a,11a]

Additionally, titration experiments with the surface-attached MPT-Ph derivative were carried out at ionic strengths of 150 and 15 mM PBS buffer. The obtained results clearly show that at a lower salt concentration of 0.1xPBS (15 mM) compared to 1xPBS (150 mM) and thus an increased Debye-screening length from approximately 0.7 nm to 2.5 nm, the protonation process is even further shifted towards more extreme (here acidic) conditions (Figure 6b and Figure S16).

Conclusion

A new thiazol-based ratiometric pH reporting dye, compatible with the pKa value of mesoporous silica, has been synthesized and fully characterized regarding its optical properties. This MPT-Ph dye covers a completely different sensitivity range with an acidic pKa value of 3.5 compared to other established dyes for ratiometric pH detection, such as SNARF. As demonstrated in this study, this more acidic pH range is especially interesting to follow confinement effects in nanoscale pores on pH, such as in mesoporous silica, in which the pH value plays a crucial role for various applications from separation processes to drug delivery. MPT-Ph can be easily grafted to the silica surface and mesopore wall. This study proves the covalent bond between the dye and surface by solid-state NMR studies. Advanced solid-state NMR DNP methods further prove the protonation of the nitrogen atom of the MPT-Ph molecule at acidic pH within silica mesopores.

The developed ratiometric MPT-Ph dye has been successfully employed to measure pH variations between bulk solutions and nanoscale silica pores and enabled in situ readout of the “pH value” in silica mesopores by simple UV-vis measurements. The obtained results indicate a background electrolyte-dependent pKa shift of at least one pH unit under nanoconfined conditions compared to the pKa in bulk solution. To the best of our knowledge, this study is the first to employ a direct measurement approach using a covalently coupled reporter molecule to determine the pH value inside of silica mesopores and to compare it with data from the bulk solution to determine the confinement effect on the pH value in silica mesopores. The obtained results are in good agreement with previous experimental findings using indirect measurements and theoretical simulations.

Experimental Section

Preparation of 1x PBS buffer solution: In 1000 ml distilled water, 8.00 g (136.9 mmol) NaCl, 0.20 g (2.7 mmol) KCl, 1.42 g Na₂HPO₄ (10.0 mmol) and 0.27 g (2.0 mmol) KH₂PO₄ were dissolved, and the solution was stirred for 24 hours before being used for UV-vis measurements.

Preparation of Mesoporous Silica Thin Films: Mesoporous silica films were prepared via sol-gel chemistry using tetraethoxysilane (TEOS) as an inorganic precursor. The sol contained an amphiphilic triblock copolymer, Pluronic® F127 (BioReagent, Sigma-Aldrich, 13,800 g mol⁻¹), in different ratios, which undergoes micellization upon solvent evaporation, resulting in the formation of a porous inorganic network. A typical synthesis of films with 8 nm (or 16 nm) pores used 1.37 g (2.61 g) of Pluronic® F127, which was dissolved in 33.8 ml (24.0 ml) of absolute ethanol and 5.22 ml of H₂O, and 0.33 ml of 37% HCl (6.4 ml of 0.05 M HCl). Then, 6.55 mL (4.88 ml) of TEOS was added to the mixture, and the solution was stirred overnight under ambient conditions before being used to prepare films through evaporation-induced self-assembly (EISA). Dip-coating was performed in a climate-controlled chamber at a temperature of 23 °C and a relative humidity of 50%, at a withdrawal speed of 2 mm s⁻¹. After aging the films for 1 h at 50% relative humidity and at 23 °C, they were subjected to the following thermal treatment: two 1-h steps at 60 and 130 °C followed by heating to 350 °C with a heating rate of 1 °C/min. Finally, the films were stabilized at 350 °C for 2 h before cooling to room temperature.

Preparation of amino-functionalized SBA-15: Based on our protocol reported earlier^[21] in a typical procedure, 7.10 g (0.017 eq) Pluronic P123 was dissolved in 191.2 ml (165.0 eq) of deionized water, and 36.0 ml (6.0 eq) of 37 wt% HCl was added, which resulted in a HCl concentration of 1.9 mol/L. The solution was heated to 40 °C, and 12.0 g (0.8 eq) of tetraethyl orthosilicate (TEOS) was added slowly while stirring. Stirring was continued for 1 h, and a white precipitate was formed. After this prehydrolysis step, 3.19 g (0.2 eq) of (3-aminopropyl)triethoxysilane (APTES) was added. The suspension was stirred for 24 h at 40 °C and then transferred into a polypropylene (PP) bottle. The bottle was stored under static conditions at 100 °C for 48 h. The white precipitate was filtered off and washed two times with deionized water, ethanol and acetone. The product was dried in an oven at 90 °C overnight. The remaining template was removed by Soxhlet extraction with ethanol for 48 h. The product was dried under high vacuum, yielding 3.19 g of functionalized SBA-15.

Synthesis of MPT-Ph: A total of 489 mg of MPT-Br, 401 mg of 4-carboxyphenylboronic acid and 518 mg of K₂CO₃ were dissolved in a mixture of 40 ml dioxan and 10 ml H₂O, and this mixture was deoxygenated for 15 minutes by nitrogen bubbling. Then, the X-Phos Pd-G2 precatalyst was added (90 mg), and the reaction mixture was heated to 80 °C for 16 h. MPT-Ph was isolated by column chromatography using methanol and ethyl acetate as the eluent. The yield was 400 mg (71%). ¹H NMR (700 MHz, DMSO-d₆) δ 8.67 (d, J = 5.7 Hz, 2H), 8.25 (d, J = 6.0 Hz, 2H), 7.96 (d, J = 8.2 Hz, 2H), 7.81 (d, J = 8.2 Hz, 2H), 4.06 (s, 3H); HRMS (ESI) m/z: [M + H]⁺ calcd for C₁₆H₁₂N₂O₂S, 313.06; found, 313.07.

Synthesis of MPT-Ph-amide: Fifty milligrams of MPT-Ph was dissolved in 15 ml dimethyl formamide (DMF). Subsequently, 45 μl diisopropylethylamine (DIPEA) and 61 mg HATU were added, and the solution was stirred for 15 minutes. Then, 5.7 mg propylamine was added, and the reaction mixture was stirred for 24 h at room temperature. MPT-Ph-amide was isolated by column chromatography using methanol and ethyl acetate as the eluent as well as HPLC. The yield was 40 mg (71%). ¹H NMR (700 MHz, methanol-d₄) δ 8.78–8.75 (m, 2H), 8.38–8.35 (m, 2H), 8.22–8.18 (m, 2H), 7.92–7.88

(m, 2H), 4.29 (s, 3H), 3.37 (t, $J=7.2$ Hz, 2H), 1.67 (h, $J=7.4$ Hz, 2H), 1.00 (t, $J=7.4$ Hz, 3H); ^{13}C NMR (176 MHz, MeOD) δ 169.48, 165.90, 148.77, 146.06, 144.55, 137.66, 136.80, 134.49, 128.24, 127.63, 122.16, 65.46, 49.26, 49.10, 48.97, 48.85, 48.73, 48.61, 48.49, 48.37, 42.56, 23.49, 11.51; HRMS (ESI) m/z : $[\text{M}+\text{H}]^+$ calcd for $\text{C}_{19}\text{H}_{19}\text{N}_3\text{O}_3\text{S}$, 354.13; found, 354.13.

Aminopropyltrimethoxysilane (APTMS) grafting on mesoporous silica thin films: A 0.05 wt% solution of APTMS in dry toluene (51.1 μl in 140 ml of dry toluene) was prepared and used to overlay the glass substrates in a Schlenk flask. Afterwards, the samples in the Schlenk flasks were kept at room temperature overnight. Then, the samples were rinsed and extracted with ethanol.

Coupling of MPT-Ph to amino-functionalized mesoporous silica films: Under Schlenk conditions, 10 mg of MPT-Ph was dissolved in dry dimethyl formamide (DMF). Subsequently, 10.9 μl diisopropylethylamine (DIPEA) and 24.3 mg HATU were added, and the solution was stirred for 15 minutes. Then, the amino-functionalized mesoporous silica film was immersed in the solution for 24 h. Afterwards, the film was rinsed with DMF and methanol before being dried.

Coupling of MPT-Ph to amino-functionalized mesoporous silica (SBA-15): MPT-Ph was coupled by activating its COOH group with 1-[bis(dimethylamino)methylene]-1H-1,2,3-triazolo[4,5-b]pyridinium 3-oxide hexafluorophosphate (HATU) and N-ethyl-N-(propan-2-yl)propan-2-amine (DIEA). A total of 121 mg (1.0 eq) of MPT-Ph and 145 mg (0.98 eq) of HATU were dissolved in 8 ml of dry DMF. The solution was activated by adding 100 mg (2.0 eq) of DIEA and shaking for 2 min. Then, 400 mg of dried amino-functionalized SBA-15 was added to the activated amino acid solution. The suspension was shaken at 1000 rpm at RT for 16 h. The solid was filtered off and washed two times with DMF, distilled water and acetone. The functionalized SBA-15 was dried under reduced pressure at room temperature, which resulted in 475 mg of colorless solid.

NMR measurements: ^1H -, ^{13}C -, and 2D-NMR experiments were conducted on a Bruker AV-III 600 or Bruker AV-III HD 700 NMR spectrometer. To shift the water signal and to protonate, MPT-Ph and MPT-Ph-amide DCI (37%) were added to some samples.

Solid-state NMR measurements: ^{13}C -MAS and ^{29}Si CP-MAS solid-state NMR measurements were carried out at room temperature on a Bruker AVANCE II+400 spectrometer corresponding to a frequency of 400.13 MHz for ^1H , 100.62 MHz for ^{13}C , and 79.48 MHz for ^{29}Si employing a Bruker 4 mm double resonance probe. Spectra were recorded with a contact time of 1.5 ms for ^{13}C and 6.5 ms for ^{29}Si with a recycle delay of 2 s. Protons were decoupled during data acquisition with the tppm15 decoupling sequence.^[26] Referencing was performed with respect to tetramethylsilane (TMS) (0 ppm) employing adamantane (−38.5 ppm) and kaolin (−92.5 ppm) as external standards for ^{13}C and ^{29}Si , respectively.

Dynamic nuclear polarization (DNP)-enhanced NMR measurements: Samples for DNP experiments were prepared by impregnating approximately 15 mg of the sample with 15 μl of a 15 mM AMUPol in glycerol- d_4 /D₂O/H₂O (60:30:10 v/v/v) solution. Samples were packed into 3.2 mm sapphire rotors and sealed with a Teflon plug and a ZrO₂ driving cap. For pH adjustment of the matrix, 38% DCI was used.

All DNP experiments were performed on a Bruker Avance III 400 DNP spectrometer equipped with an Ascend 400 DNP magnet system and a low-temperature $^1\text{H}/\text{X}/\text{Y}$ probe. DNP-enhanced spectra were measured with microwave irradiation (MW on). All DNP-enhanced spectra were recorded at a field of 9.4 T corresponding to frequencies of 400.25 MHz for ^1H , 100.58 MHz for ^{13}C and 40.53 MHz for ^{15}N at a nominal temperature of 110 K and at a spinning rate of 8 kHz. The recycle delay was taken as 1.3 T_1 (^1H)

according to the literature,^[27] where T_1 (^1H) is the build-up time for ^1H obtained from a saturation recovery experiment recorded with microwave irradiation. During data acquisition, tppm20^[27] heteronuclear decoupling was applied to the ^{15}N CP MAS spectra. The ^{15}N CP MAS spectra were recorded with contact times of 6 ms and referenced with NH_4Cl as an external standard (chemical shift of 0 ppm).

UV-vis measurements: UV-vis measurements were performed using an Agilent Cary 60 UV-vis spectrophotometer or an AnalytikJena Specord S600 spectrophotometer using PMMA cuvettes. The concentrations of sample solutions were kept below 50 mM, and the dye-functionalized mesoporous silica films were fixed straight in the cuvette diagonal to the light beam.

Fluorescence measurements: The steady-state (time-integrated) fluorescence spectra were recorded with a Jasco FP-8500 spectrofluorometer in 4×10 mm UV-grade quartz cuvettes. The spectra were corrected for the offset, device detection sensitivity, wavelength-dependent excitation light intensity and reabsorption contributions. For the determination of the fluorescence quantum yields, the FP-8500 spectrofluorometer was equipped with a 100 mm integrating sphere from Jasco (ILF-835), and the calculations were carried out with Origin 2019 data analysis software.

The time-correlated single photon counting (TCSPC) measurements were performed with a self-assembled setup with a PicoQuant photomultiplier tube (PMT) PMA-C 182-M for single photodetection. Data were acquired with a TimeHarp 260 PICO single PCIe card, and data analysis and multiexponential fitting were executed with FluoFit Pro 4.6 software from PicoQuant. The samples were also prepared in 4×10 mm quartz glass cuvettes, and the excitation of the samples was carried out with pulsed light-emitting diodes (LEDs), enabling a maximum time resolution of approximately 200 ps. The instrumental response function (IRF) was recorded with a TiO₂ suspension as a scattering sample. For the detection of the sample fluorescence decay curves, colored glass filters (Schott AG) were used to suppress stray light.

Supporting Information

Supporting information is available from the Wiley Online Library or from the author.

Acknowledgments

The authors acknowledge funding in the frame of the LOEWE project iNAPO by the Hessen State Ministry of Higher Education, Research and the Arts, as part of the Centre for Synthetic Biology, Technische Universität Darmstadt, Germany. A.A.-B. acknowledges funding from the European Research Council (ERC) under the European Union's Horizon 2020 Research and Innovation Program (grant agreement no. 803758). Additionally, the financial support from the Deutsche Forschungsgemeinschaft through grants Bu-911/18-1/2 as well as for SFB 902 "RNA-based Regulation" is gratefully acknowledged. The authors especially thank Dr. Sharon Jeziorowski and Dr. Jonas Kind in the research group of Prof. Dr. Christina Thiele for NMR measurements as well as Dr. Lena Müller in the group of Dr. Alesia Tietze for support with HPLC measurements. Additionally, the authors thank Prof. Markus Biesalski for access to the

interface characterization facilities. Marlen Saalbach is acknowledged for UV-vis measurements. Open access funding enabled and organized by Projekt DEAL.

Conflict of Interest

The authors declare no conflict of interest.

Keywords: fluorescence dye · ratiometric · silica · mesopore · solid-state NMR

- [1] C. T. Kresge, M. E. Leonowicz, W. J. Roth, J. C. Vartuli, J. S. Beck, *Nature* **1992**, *359*, 710–712.
- [2] a) T. Nasir, G. Herzog, M. Hebrant, C. Despas, L. Liu, A. Walcarius, *ACS Sens.* **2018**, *3*, 484–493; b) A. Walcarius, E. Sibottier, M. Etienne, J. Ghanbaja, *Nat. Mater.* **2007**, *6*, 602–608; c) K. Wang, J. He, *ACS Appl. Mater. Interfaces* **2018**, *10*, 11189–11196.
- [3] a) Z. Allothman, *Materials* **2012**, *5*, 2874–2902; b) M. Kruk, *Isr. J. Chem.* **2012**, *52*, 246–255.
- [4] F. H. van der Heyden, D. J. Bonthuis, D. Stein, C. Meyer, C. Dekker, *Nano Lett.* **2006**, *6*, 2232–2237.
- [5] F. Hoffmann, M. Cornelius, J. Morell, M. Froba, *Angew. Chem. Int. Ed. Engl.* **2006**, *45*, 3216–3251.
- [6] R. Narayan, U. Y. Nayak, A. M. Raichur, S. Garg, *Pharmaceutics* **2018**, *10*, 118–166.
- [7] M. Tagliacucchi, O. Azzaroni, I. Szleifer, *J. Am. Chem. Soc.* **2010**, *132*, 12404–12411.
- [8] a) A. Brunson, J. Cui, M. Ceolin, A. del Campo, G. J. Soler-Illia, O. Azzaroni, *Chem. Commun. (Camb.)* **2012**, *48*, 1422–1424; b) K. Huang, I. Szleifer, *J. Am. Chem. Soc.* **2017**, *139*, 6422–6430; c) X. Hou, W. Guo, L. Jiang, *Chem. Soc. Rev.* **2011**, *40*, 2385–2401; d) X. Huang, D. Appelans, P. Formanek, F. Simon, B. Voit, *ACS Nano* **2012**, *6*, 9718–9726; e) G. Perez-Mitta, A. G. Albesa, W. Knoll, C. Trautmann, M. E. Toimil-Molares, O. Azzaroni, *Nanoscale* **2015**, *7*, 15594–15598; f) G. V. R. R. Qiang Fu, L. K. Ista, Y. Wu, B. P. Andrzejewski, L. A. Sklar, T. L. Ward, G. P. Lopez, *Adv. Mater.* **2003**, *15*, 1262–1266; g) J. Wen, K. Yang, F. Liu, H. Li, Y. Xu, S. Sun, *Chem. Soc. Rev.* **2017**, *46*, 6024–6045; h) F. Yu, X. Tang, M. Pei, *Microporous Mesoporous Mater.* **2013**, *173*, 64–69.
- [9] a) R. Brilmayer, S. Kubelbeck, A. Khalil, M. Brodrecht, U. Kunz, H. J. Kleebe, G. Buntkowsky, G. Baier, A. Andrieu-Brunsen, *Adv. Mater. Interfaces* **2020**, *7*; b) M. H. Sun, S. Z. Huang, L. H. Chen, Y. Li, X. Y. Yang, Z. Y. Yuan, B. L. Su, *Chem. Soc. Rev.* **2016**, *45*, 3479–3563.
- [10] S. E. Kim, L. Zhang, K. Ma, M. Riegman, F. Chen, I. Ingold, M. Conrad, M. Z. Turker, M. Gao, X. Jiang, S. Monette, M. Pauliah, M. Gonen, P. Zanzonico, T. Quinn, U. Wiesner, M. S. Bradbury, M. Overholzer, *Nat. Nanotechnol.* **2016**, *11*, 977–985.
- [11] a) F. M. Gilles, M. Tagliacucchi, O. Azzaroni, I. Szleifer, *J. Phys. Chem. C* **2016**, *120*, 4789–4798; b) M. Stanzel, R. Brilmayer, M. Langhans, T. Meckel, A. Andrieu-Brunsen, *Microporous Mesoporous Mater.* **2019**, *282*, 29–37; c) A. Yamaguchi, M. Namekawa, T. Kamijo, T. Itoh, N. Teramae, *Anal. Chem.* **2011**, *83*, 2939–2946; d) P. Gong, T. Wu, J. Genzer, I. Szleifer, *Macromolecules* **2007**, *40*, 8765–8773; e) O. Schepelina, I. Zharov, *Langmuir* **2008**, *24*, 14188–14194.
- [12] a) C. Richter, C. Schneider, M. T. Quick, P. Volz, R. Mahrwald, J. Hughes, B. Dick, U. Alexiev, N. P. Ernsting, *Phys. Chem. Chem. Phys.* **2015**, *17*, 30590–30597; b) C. Thörn, N. Carlsson, H. Gustafsson, K. Holmberg, B. Åkerman, L. Olsson, *Microporous Mesoporous Mater.* **2013**, *165*, 240–246;
- c) M. Sulpizi, M. P. Gaigeot, M. Sprik, *J. Chem. Theory Comput.* **2012**, *8*, 1037–1047; d) J. M. Rosenholm, T. Czuryzkiewicz, F. Kleitz, J. B. Rosenholm, M. Lindén, *Langmuir* **2007**, *23*, 4315–4323.
- [13] a) J. Lei, L. Wang, J. Zhang, *Chem. Commun. (Camb.)* **2010**, *46*, 8445–8447; b) M.-H. Zheng, J.-Y. Jin, W. Sun, C.-H. Yan, *New J. Chem.* **2006**, *30*, 1192.
- [14] a) S. Brasselet, W. E. Moerner, *Single Mol.* **2000**, *1*, 17–23; b) S. Wan, Y. Zheng, J. Shen, W. Yang, M. Yin, *ACS Appl. Mater. Interfaces* **2014**, *6*, 19515–19519; c) R. Martínez-Máñez, F. Sancenón, M. Biyikal, M. Hecht, K. Rurack, *J. Mater. Chem.* **2011**, *21*; d) J. Han, A. Loudet, R. Barhoumi, R. C. Burghardt, K. Burgess, *J. Am. Chem. Soc.* **2009**, *131*, 1642–1643; e) H. L. Lee, S. J. Lord, S. Iwanaga, K. Zhan, H. Xie, J. C. Williams, H. Wang, G. R. Bowman, E. D. Goley, L. Shapiro, R. J. Twieg, J. Rao, W. E. Moerner, *J. Am. Chem. Soc.* **2010**, *132*, 15099–15101; f) J. Ji, N. Rosenzweig, C. Griffin, Z. Rosenzweig, *Anal. Chem.* **2000**, *72*, 3497–3503.
- [15] a) L.-L. Li, H. Sun, C.-J. Fang, J. Xu, J.-Y. Jin, C.-H. Yan, *J. Mater. Chem.* **2007**, *17*, 4492; b) I. G. Shenderovich, G. Buntkowsky, A. Schreiber, E. Gedat, S. Sharif, J. Albrecht, N. S. Golubev, G. H. Findenegg, H.-H. Limbach, *J. Phys. Chem. B* **2003**, *107*, 11924–11939.
- [16] a) S. Charier, O. Ruel, J. B. Baudin, D. Alcor, J. F. Allemand, A. Meglio, L. Jullien, *Angew. Chem. Int. Ed. Engl.* **2004**, *43*, 4785–4788; b) M. H. Zheng, M. M. Zhang, H. H. Li, J. Y. Jin, *J. Fluoresc.* **2012**, *22*, 1421–1424.
- [17] K. Yamaguchi, T. Murai, Y. Tsuchiya, Y. Miwa, S. Kutsumizu, T. Sasamori, N. Tokitoh, *RSC Adv.* **2017**, *7*, 18132–18135.
- [18] a) M. Y. Yang, X. L. Zhao, M. H. Zheng, Y. Wang, J. Y. Jin, *J. Fluoresc.* **2016**, *26*, 1653–1657; b) Y. Watanabe, W. Sungnoi, A. O. Sartorio, M. Zeller, A. Wei, *Mater. Chem. Front.* **2020**, *4*, 899–904.
- [19] a) E. W. Driscoll, J. R. Hunt, J. M. Dawlaty, *J. Phys. Chem. A* **2017**, *121*, 7099–7107; b) A. Brenlla, M. Veiga, J. L. Perez Lustres, M. C. Rios Rodriguez, F. Rodriguez-Prieto, M. Mosquera, *J. Phys. Chem. B* **2013**, *117*, 884–896.
- [20] N. Herzog, R. Brilmayer, M. Stanzel, A. Kalyta, D. Spiehl, E. Dorsam, C. Hess, A. Andrieu-Brunsen, *RSC Adv.* **2019**, *9*, 23570–23578.
- [21] M. Brodrecht, H. Breitzke, T. Gutmann, G. Buntkowsky, *Chemistry* **2018**, *24*, 17814–17822.
- [22] a) M. Brodrecht, B. Kumari, A. Thankamony, H. Breitzke, T. Gutmann, G. Buntkowsky, *Chemistry* **2019**, *25*, 5214–5221; b) M. Werner, A. Heil, N. Rothermel, H. Breitzke, P. B. Groszewicz, A. S. Thankamony, T. Gutmann, G. Buntkowsky, *Solid State Nucl. Magn. Reson.* **2015**, *72*, 73–78.
- [23] P. Lorente, I. G. Shenderovich, N. S. Golubev, G. S. Denisov, G. Buntkowsky, H.-H. Limbach, *Magn. Reson. Chem.* **2001**, *39*, 518–529.
- [24] E. Gedat, A. Schreiber, G. H. Findenegg, I. Shenderovich, H. H. Limbach, G. Buntkowsky, *Magn. Reson. Chem.* **2001**, *39*, 5149–5157.
- [25] a) E. A. Dolgoplova, A. A. Berseneva, M. S. Faillace, O. A. Ejegbavwo, G. A. Leith, S. W. Choi, H. N. Gregory, A. M. Rice, M. D. Smith, M. Chruszcz, S. Garashchuk, K. Mythreye, N. B. Shustova, *J. Am. Chem. Soc.* **2020**, *142*, 4769–4783; b) A. Baldrige, S. R. Samanta, N. Jayaraj, V. Ramamurthy, L. M. Tolbert, *J. Am. Chem. Soc.* **2011**, *133*, 712–715; c) A. Ghodbane, W. Brett Fellows, J. R. Bright, D. Ghosh, N. Saffon, L. M. Tolbert, S. Fery-Forgues, K. M. Solntsev, *J. Mater. Chem. C* **2016**, *4*, 2793–2801; d) I. H. Choi, S. Bin Yoon, S. Huh, S. J. Kim, Y. Kim, *Sci. Rep.* **2018**, *8*, 9838.
- [26] I. Scholz, P. Hodgkinson, B. H. Meier, M. Ernst, *J. Chem. Phys.* **2009**, *130*, 114510.
- [27] S. Lange, A. H. Linden, U. Akbey, W. T. Franks, N. M. Loening, B. J. van Rossum, H. Oshchkinat, *J. Magn. Reson.* **2012**, *216*, 209–212.

Manuscript received: July 24, 2020

Revised manuscript received: September 9, 2020

Accepted manuscript online: September 25, 2020

Version of record online: October 23, 2020

LIST OF FIGURES

- Figure 2.1.** Illustration of the electromagnetic spectrum provided with scales of wavelength and frequency. The molecular transitions, corresponding to the different ranges of the spectrum are shown above. 5
- Figure 2.2.** Jablonski diagram: photochemical relaxation pathways after absorption of a photon. Radiative transitions are indicated by solid coloured arrows and non-radiative transitions by black wavy or dashed arrows. S_i and T_i represent the involved electronic singlet and triplets states, respectively, and the states v_i indicate excited vibrational modes. 8
- Figure 2.3.** Schematic depiction of the applied UV/vis-pump/probe setup supplied by a pulsed Ti:Sapphire laser with a wavelength conversion and a pulse compression unit for the pump pulse and a variable delay stage as well as a chopping wheel. The probe pulse is converted into a supercontinuum, passes the sample, and is guided into the detection unit. MC - monochromator, M - mirror, BS - beam splitter..... 10
- Figure 2.4.** Principle of chirped pulse amplification (CPA). An ultrashort fs pulse of low intensity is stretched temporally, prior to amplification. The amplification medium is pumped simultaneously, which amplifies the stretched pulse. The pulse is then compressed again to a much higher intensity. 11
- Figure 2.5.** Second order non-linear frequency mixing processes of two incident pulses in a non-linear crystal. 13
- Figure 2.6.** Schematic depiction of the setup assembly and the beam geometry for the NOPA process. L - Lens, M - mirror, DS - delay stage, Sa - sapphire window..... 14
- Figure 2.7.** Applied chopping scheme: Every second pump pulse is blocked for referencing to the absorbance of the unexcited sample..... 15
- Figure 2.8.** Origin of difference absorption signals in TA experiments and resulting difference spectrum with positive excited state absorption (ESA) and negative ground state bleach (GSB) and stimulated emission (SE) contributions. 15
- Figure 2.9.** Schematic depiction of the applied time-correlated single photon counting (TCSPC) setup. Excitation of the sample is either conducted with a pulsed Ti:Sapphire laser or with pulsed LEDs. The laser output is coupled to a module for frequency doubling and adjustment of the repetition rate by an acousto-optic modulator (AOM). PD - photodiode, PMT - photomultiplier tube, SHG - second harmonic generation..... 18
- Figure 2.10.** Schematic depiction of a stopped-flow device with 2 syringes. The solutions are injected into a mixing chamber prior to the cuvette. The hard

stop blocks the flow of the mixed solution and transmits a trigger signal to the connected detection device. 19

Figure 2.11. Illustration of the ground and excited state energetics of a photoswitch with two isomers A and B. Interconversion might occur thermally in the ground state or photochemically in the excited state..... 21

Figure 2.12. Overview of several prominent organic photoswitch classes, divided by their isomerization mechanisms..... 22

Figure 2.13. General behaviour of the spiropyran (SP) - merocyanine (MC) photowitch system in aqueous solution. The MC isomer is sensitive to hydrolytic decomposition. Upon acidification, both photoisomers are protonated at the indicated positions, where the MCH form is capable of photoprolytic ring-closure. 24

Figure 2.14. Illustration of riboswitch function. Shown as an example is a translational switch that regulates gene expression by sequestration of the ribosomal binding site (RBS) upon ligand (cyan pentagon) binding. The conformational RNA change involves the joining region between aptamer domain (blue) and gene expression platform (grey). 27

Figure 2.15. Principle of the systematic evolution of ligands by exponential enrichment (SELEX) process. 28

Figure 2.16. Examples of engineered riboswitch regulation mechanisms. Translational control by **A)** sequestration of the Shine-Dalgarno (SD) sequence in prokaryotes or by **B)** roadblock formation in eukaryotes. **C)** Transcriptional control by formation of a stable terminator stem. **D)** Conditional mRNA splicing. 31

Figure 3.1. Illustration of the main projects of this work. The characteristics of photoswitches as well as artificial RNA aptamers are investigated with regard to a potential biochemical use and both systems are finally combined to a photoresponsive RNA aptamer. 33

Figure 4.1. Photochromic interconversion of SP and MC (top) and merocyanine isomer structures of the investigated Py- and Nitro-BIPS compounds **1-4** (bottom). 38

Figure 4.2. Absorption spectra of the pure photoisomers SP and MC of MePy-BIPS **1** (top) and Py-BIPS **2** (bottom). 39

Figure 4.3. Cyclic photofatigue studies of compounds **1** (upper panel) and **2** (lower panels) with shown photoswitch operation modes..... 39

Figure 4.4. A) TA spectrum of the MC isomer of MePy-BIPS **1** and **B)** DAS of the lifetime components determined by GLA. **C)** TA spectrum of the MC isomer of Py-BIPS **2** and **D)** DAS of the lifetime components determined by GLA. 40

Figure 4.5. Photoreaction mechanism scheme for the ring-closure reactions of the Py-BIPS-type merocyanines **1** and **2**. 41

Figure 4.6. Absorption spectra of the pure photoisomers SP and MC of Nitro-BIPS 3 (top) and Dinitro-BIPS 4 (bottom).....	42
Figure 4.7. Cyclic photofatigue studies of compounds 3 (top) and 4 (bottom) with shown photoswitch operation modes.	42
Figure 4.8. A) TA spectrum of the ring-opening reaction of Nitro-BIPS 3 and B) DAS of the lifetime components determined by GLA. C) TA spectrum of the ring-opening reaction of Dinitro-BIPS 4 and D) DAS of the lifetime components determined by GLA.....	43
Figure 4.9. A) TA spectrum of the ring-opening reaction of Nitro-BIPS 3 and B) DAS of the lifetime components determined by GLA. C) TA spectrum of the ring-opening reaction of Dinitro-BIPS 4 and D) DAS of the lifetime components determined by GLA.....	44
Figure 4.10. Acidochromism of the Py-BIPS derivative 2. A) pH titration UV/vis absorption study. The individual absorption bands correspond to the indicated (non-)protonated species of both photoisomers. B) Absorption and scaled fluorescence spectra of the pure photoisomer states, measured at pH 7.4 (top), pH 5.5 (middle) and pH 1 (bottom). C) Schematic reaction model of the behaviour of compound 2 in the acidic pH range extracted from systematic pH-dependent switching experiments.....	46
Figure 4.11. Light-regulated pH switching with different concentrations of Py-BIPS 2 in diluted PBS buffer. Prior to the cyclic experiment the buffer pH value can be adjusted manually. Photoswitching is then carried out by alternating irradiation with 530 nm (cyan areas) and thermal recovery in the dark (empty areas).....	47
Figure 4.12. Generalized photoreaction mechanism schemes of excited state photoacids (PA) and photoacid generators (PAG).....	49
Figure 4.13. A) TA spectrum of the HMC isomer of Py-BIPS 2 in aqueous solution at pH 5.5 and B) DAS of the lifetime components determined by GLA. C) Photoreaction and proton-release mechanism scheme of HMC as a PAG..	50
Figure 4.14. A) TA spectrum of the HMCH isomer of Py-BIPS 2 in aqueous solution at pH 1 and B) DAS of the lifetime components determined by GLA.	52
Figure 4.15. Photoprotolytic reaction scheme according to the Förster cycle of the protonated merocyanine photoacid HMCH of Py-BIPS 2	53
Figure 4.16. A) TA spectrum of the MCH isomer of Nitro-BIPS 3 in aqueous solution at pH 1 and B) DAS of the lifetime components determined by GLA. C) Photoprotolytic reaction scheme of the protonated merocyanine photoacid MCH.	54
Figure 4.17. A) TA spectrum of the MCH isomer of Dinitro-BIPS 4 in aqueous solution at pH 1 and B) DAS of the lifetime components determined by GLA.	55

Figure 4.18. Free-energy - reactivity correlation. The proton-transfer rates are plotted versus the estimated pK_a^* values corrected by the electrostatic contribution for ESPT to water.....	57
Figure 4.19. A) Molecular structure of TC with the chelation site for a divalent Mg^{2+} cation (green sphere). The $R_{6\beta}$ -OH group of TC is indicated by an arrow. B) Secondary structure of the TC aptamer. The squares and circles indicate the highlighted nucleobases in D and E, respectively. C) Tertiary structure of the ligand-bound state of the TC aptamer based on the reported crystal structure ^[187] (PDB: 3EGZ). The ligand TC is depicted as ball and stick model and the incorporated Mg^{2+} ions are shown as green spheres along with coordinated water molecules shown as small red spheres. D) Close-up of the binding pocket. The nucleobases in proximity to the ligand are highlighted. E) Close-up of the triple helix motif.	59
Figure 4.20. Nucleobase positions A6, A7, G43, A49 and A58 that were substituted individually with fluorescent Ap labels.....	62
Figure 4.21. Fluorescence-monitored Mg^{2+} titration data in presence (solid lines) and absence of TC (dashed lines) for the variants G43Ap (top), A49Ap (middle) and A58Ap (bottom). Ap emission (coloured lines) was collected at 365 nm and TC emission (grey lines) at 520 nm.	63
Figure 4.22. Fluorescence-monitored Mg^{2+} titration data in presence (solid lines) and absence of TC (dashed lines) for the variants A6Ap (top) and A7Ap (bottom). Ap emission (coloured lines) was collected at 365 nm and TC emission (grey lines) at 520 nm.....	64
Figure 4.23. Fluorescence-detected stopped-flow experiments with A58Ap (top), G43Ap (middle) and A7Ap (bottom). Shown is the Ap emission change during Mg^{2+} -induced formation of the ligand bound state from the unfolded state.....	65
Figure 4.24. Proposed mechanisms and rate constants for sequential folding and ligand binding steps, determined by kinetic analysis of the fluorescence stopped-flow data. The sequence comprises an initial Mg^{2+} -induced prefolding step of a binding-competent conformation, followed by ligand binding which in turn induces a structural adjustment of the aptamer.....	71
Figure 4.25. Secondary structures of A) the investigated inactive aptamer A and B) the <i>in vivo</i> active riboswitches preRS and RS . The depicted structures are based on in-line probing experiments. ^[114] The binding pocket regions are highlighted (grey boxes). C) Molecular structure of the ligand CFX with shown metal binding site (top). The graphs show the normalized absorption and emission spectra of CFX (middle) and an excitation wavelength-dependent CFX emission contour plot (bottom).....	75

Figure 4.26. Mg ²⁺ -dependent binding affinities of the candidates A (green), preRS (cyan) and RS (blue). Fluorescence titration at 5 mM Mg ²⁺ (top) and Mg ²⁺ -dependent K _D values (bottom).....	77
Figure 4.27. A) Stopped-flow traces that show the time-resolved decrease of CFX emission upon binding by the aptamer candidates A (top), preRS (middle) and RS (bottom). The solid lines represent the most suitable model fits as discussed in the text. B) Association rates k _{on} determined by monoexponential fitting of the stopped-flow traces.....	78
Figure 4.28. Determined kinetic ligand binding models of aptamer A and the riboswitches preRS and RS . A decreasing contribution of a back reaction rate of the second binding step correlates with an increasing regulation factor, observed in a in vivo GFP expression assay.....	80
Figure 4.29. A) Molecular design route for the chloramphenicol-azobenzene (azoCm) compound with an anchor group for immobilization. B) Structures of the <i>cis</i> - and <i>trans</i> -photoisomers of azoCm. C) Spectroscopic studies of the ligand azoCm: The top panel shows the absorption spectra of <i>trans</i> -azoCm and of the photostationary state (PSS) obtained upon continuous irradiation at 365 nm. The PSS contains about 80% of <i>cis</i> -azoCm. The lower panel shows a photofatigue experiment over multiple cycles of alternating irradiation.	83
Figure 4.30. Illustration of the SELEX results. A) Sum of reads per million (RPM) of the light-motif sequence in the regular and light branch of the N74 SELEX. B) Fraction of loaded RNAs that could be eluted with an azoCm solution. C) Conserved structural motif determined by LocARNA analysis of the motif-doped SELEX pools. ^[211,212] The mutated light-motif is embedded within the common structure motif. The lengths of stem P2 and loop L2 are variable, as indicated.....	84
Figure 4.31. Isothermal titration calorimetry (ITC) studies of <i>cis</i> - and <i>trans</i> -azoCm and the aptamer B2-1.....	85
Figure 4.32. Circular dichroism (CD) studies. A) CD spectra of <i>trans</i> - (cyan) and <i>cis</i> -azoCm (grey). B) CD spectra of the pure aptamer B2-1 (dashed blue line), its ligand bound state <i>trans</i> @B2-1 (cyan line) and the dissociated state (<i>cis</i> + B2-1, grey line) obtained upon switching from the <i>trans</i> - to <i>cis</i> -isomer with 365 nm. C) CD signal change at 269 nm during a cyclic switching experiment with alternating illumination steps using 365 nm and 420 nm.	86
Figure A1. Secondary structure of the TC aptamer variants studied herein. The loop L2 is missing and the two strands are hybridized prior to experimental use. The strands are labelled with Ap individually at the indicated positions.	189

LIST OF TABLES

Table 4.1. Selected mechanistic models applied in the kinetic analysis of the fluorescence stopped-flow data of the three TC aptamer variants A58Ap, G43Ap and A7Ap.	67
Table 4.2. Results of the kinetic modelling analysis of the fluorescence stopped-flow data of the TC aptamer variant A58Ap, corresponding rate constants and obtained non-linear fit quality criteria. The models 1-3 refer to the tested folding mechanisms shown in Table 4.1.	69
Table 4.3. Results of the kinetic modelling analysis of the fluorescence stopped-flow data of the TC aptamer variant G43Ap, corresponding rate constants and obtained non-linear fit quality criteria. The models 1-3 refer to the tested folding mechanisms shown in Table 4.1.	69
Table 4.4. Results of the kinetic modelling analysis of the fluorescence stopped-flow data of the TC aptamer variant A7Ap, corresponding rate constants and obtained non-linear fit quality criteria. The models 1-3 refer to the tested folding mechanisms shown in Table 4.1.	70
Table A1. Eight mechanistic models A-H applied in the kinetic analysis of the fluorescence stopped-flow data of the three TC aptamer variants A58Ap, G43Ap and A7Ap. The models D, E and H correspond to the models 1, 2 and 3, respectively, as discussed in section 4.2.1,	189
Table A2. Results of the kinetic modelling analysis of the fluorescence stopped-flow data of the TC aptamer variant A58Ap, corresponding rate constants and obtained non-linear fit quality criteria. The models A-H refer to the tested folding mechanisms shown in Table A1.	190
Table A3. Results of the kinetic modelling analysis of the fluorescence stopped-flow data of the TC aptamer variant G43Ap, corresponding rate constants and obtained non-linear fit quality criteria. The models A-H refer to the tested folding mechanisms shown in Table A1.	191
Table A4. Results of the kinetic modelling analysis of the fluorescence stopped-flow data of the TC aptamer variant A7Ap, corresponding rate constants and obtained non-linear fit quality criteria. The models A-H refer to the tested folding mechanisms shown in Table A1.	192

ABBREVIATIONS

1N	1-Naphthol	FMN	Flavin mononucleotide
2N	2-Naphthol	GFP	Green fluorescent protein
AGS	Silver gallium sulfide		
AIC	Akaike information criterion	GSA	Ground state absorption
AOM	Acusto-optic modulator	GLA	Global lifetime analysis
Ap	2-Aminopurine	GSB	Ground state bleach
ATP	Adenosine triphosphate	GVD	Group velocity dispersion
BBO	β -Barium borate		
BIC	Bayesian information criterion	HOMO	Highest occupied molecular orbital
BIPS	Benzo-indolino-pyrano-spiran	HP	Hydrolysis products
CD	Circular dichroism	HPLC	High-performance liquid chromatography
CFX	Ciprofloxacin	HPTS	8-Hydroxypyrene-1,3,6-trisulfonic acid
CI	Conical intersection		
CPA	Chirped pulse amplification	IC	Internal conversion
cw	Continuous wave	IR	Infrared
DAS	Decay-associated spectrum	IRF	Instrumental response function
DC2N	5,8-Dicyano-2-naphthol	ISC	Intersystem crossing
DFG	Difference frequency generation	KTP	Potassium titanyl phosphate
DNA	Deoxyribonulceic acid	LASER	Light amplification by stimulated emission of radiation
DOI	Digital object identifier		
ESA	Excited state absorption		
ESPT	Excited state proton transfer	LDA	Lifetime distribution analysis
ESIPT	Excited state intra-molecular proton-transfer	LDM	Lifetime density map

LED	Light emitting diode	RNA	Ribonulceic acid
LUMO	Lowest unoccupied molecular orbital	RNAP	RNA polymerase
MC	Merocyanine	RPM	Reads per million
Nd:YAG	Neodymium-doped yttrium aluminium garnet	SAM	S-adenosyl methionine
Neo	Neomycin	SC	Supercontinuum
NGS	Next generation sequencing	SD	Shine Dalgarno
NM6HQ	6-Hydroxyquinolinium	SE	Stimulated emission
NMR	Nuclear magnetic resonance	SELEX	Systematic evolution of ligands by exponential enrichment
NLO	Non-linear optics	SHG	Second harmonic generation
NOPA	Non-collinear optical parametric amplifier	SFG	Sum frequency generation
OD	Optical density	SP	Spiropyran
OPA	Optical parametric amplifier	TA	Transient absorption
OPO	Optical parametric oscillation	TC	Tetracycline
PA	Photoacid	Ti:Sa	Titanium-doped sapphire crystal
PAG	Photoacid generator	UV	Ultraviolet
PBS	Phosphate-buffered saline	VC	vibrational cooling
PCR	Polymerase chain reaction	vis	Visible
PD	Photodiode		
PES	Potential energy surface		
PMT	Photomultiplier tube		
PPG	Photolabile protecting group		
PSS	Photostationary state		
Py-	Pyridinium-		
QCy	Quinone cyanine		
RBS	Ribosomal binding site		
RMSD	Root mean square deviation		

APPENDIX

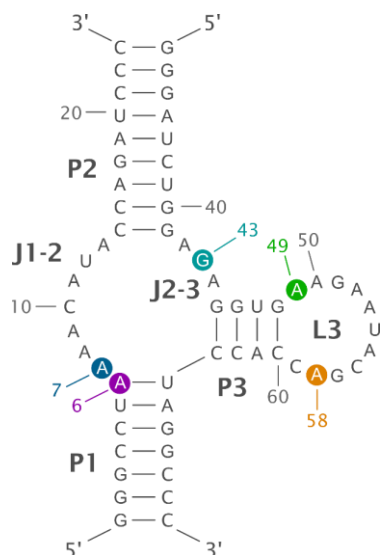


Figure A1. Secondary structure of the TC aptamer variants studied herein. The loop L2 is missing and the two strands are hybridized prior to experimental use. The strands are labelled with Ap individually at the indicated positions.

Table A1. Eight mechanistic models A-H applied in the kinetic analysis of the fluorescence stopped-flow data of the three TC aptamer variants A58Ap, G43Ap and A7Ap. The models D, E and H correspond to the models 1, 2 and 3, respectively, as discussed in section 4.2.1.

Model	Folding mechanism scheme
A	$\text{RNA} + \text{M} \xrightarrow{k_1} \text{RNA}_M^* + \text{TC} \xrightarrow{k_2} \text{TC@RNA}_M$
B	$\text{RNA} + \text{M} \xrightleftharpoons[k_{-1}]{k_1} \text{RNA}_M^* + \text{TC} \xrightarrow{k_2} \text{TC@RNA}_M$
C	$\text{RNA} + \text{M} \xrightarrow{k_1} \text{RNA}_M^* + \text{TC} \xrightarrow{k_2} \text{TC@RNA}_M^* \xrightarrow{k_3} \text{TC@RNA}_M$
D (1)	$\text{RNA} + \text{M} \xrightleftharpoons[k_{-1}]{k_1} \text{RNA}_M^* + \text{TC} \xrightarrow{k_2} \text{TC@RNA}_M^* \xrightarrow{k_3} \text{TC@RNA}_M$
E (2)	$\text{RNA} + \text{M} \xrightarrow{k_1} \text{RNA}_M^* + \text{TC} \xrightleftharpoons[k_{-2}]{k_2} \text{TC@RNA}_M^* \xrightarrow{k_3} \text{TC@RNA}_M$
F	$\text{RNA} + \text{M} \xrightleftharpoons[k_{-1}]{k_1} \text{RNA}_M^* + \text{TC} \xrightleftharpoons[k_{-2}]{k_2} \text{TC@RNA}_M^* \xrightarrow{k_3} \text{TC@RNA}_M$
G	$\text{RNA} + \text{M} \xrightarrow{k_1} \text{RNA}_M^* + \text{TC} \xrightarrow{k_2} \text{TC@RNA}_M^* + \text{M} \xrightarrow{k_3} \text{TC@RNA}_M$
H (3)	$\text{RNA} + \text{M} \xrightleftharpoons[k_{-1}]{k_1} \text{RNA}_M^* + \text{TC} \xrightarrow{k_2} \text{TC@RNA}_M^* + \text{M} \xrightarrow{k_3} \text{TC@RNA}_M$

Table A2. Results of the kinetic modelling analysis of the fluorescence stopped-flow data of the TC aptamer variant A58Ap, corresponding rate constants and obtained non-linear fit quality criteria. The models A-H refer to the tested folding mechanisms shown in Table A1.

Model	k_1 / $\mu\text{M}^{-1}\text{s}^{-1}$	k_{-1} / s^{-1}	k_2 / $\mu\text{M}^{-1}\text{s}^{-1}$	k_{-2} / s^{-1}	k_3 / s^{-1}	RMSD	ΔAIC	ΔBIC
A	0.017 ± 0.001	--	3.13 ± 0.05	--	--	0.05052	906	893
B	0.07 ± 0.01	70 ± 10	6.2 ± 0.1	--	--	0.04984	777	770
C	0.019 ± 0.001	--	14.9 ± 0.4	--	3.17 \pm 0.05	0.0467	142	135
D (1)	0.036 ± 0.003	35 ± 5	11.3 ± 0.3	--	2.5 \pm 0.1	0.04601	0	0
E (2)	0.019 ± 0.001	--	14.9 ± 0.4	$<10^{-9}$ $\pm \text{n.d.}^{[a]}$	3.2 ± 0.1	0.0467	144	144
F	0.035 ± 0.003	32 ± 6	11.3 ± 0.3	0.15 $\pm \text{n.d.}$	2.6 ± 0.2	0.04601	1	8
G	0.05 ± 0.01	--	7.2 ± 0.2	--	0.006 ^[b] ± 0.001	0.0521	1206	1200
H (3)	36 $\pm \text{n.d.}$	$>10^3$ $\pm \text{n.d.}$	0.96 ± 0.02	--	280 ^[b] $\pm \text{n.d.}$	0.191	13861	13861

^[a] n.d. (not determined), the rate constant approaches zero and its error is very large,

^[b] for models G and H, the third step is bimolecular and the rate k_3 is considered as a second order constants in units of $\mu\text{M}^{-1}\text{s}^{-1}$.

Table A3. Results of the kinetic modelling analysis of the fluorescence stopped-flow data of the TC aptamer variant G43Ap, corresponding rate constants and obtained non-linear fit quality criteria. The models A-H refer to the tested folding mechanisms shown in Table A1.

Model	k_1 / $\mu\text{M}^{-1}\text{s}^{-1}$	k_{-1} / s^{-1}	k_2 / $\mu\text{M}^{-1}\text{s}^{-1}$	k_{-2} / s^{-1}	k_3 / s^{-1}	RMSD	ΔAIC	ΔBIC
A	0.014 ± 0.001	--	2.77 ± 0.06	--	--	0.04940	993	980
B	0.014 ± 0.001	0.6 ± 0.3	2.9 ± 0.1	--	--	0.04935	985	979
C	0.015 ± 0.001	--	28 ± 1	--	2.84 ± 0.06	0.04527	143	137
D (1)	0.029 ± 0.002	57 ± 8	20 ± 1	--	2.1 ± 0.1	0.0446	0	0
E (2)	0.015 ± 0.001	--	23.3 ± 0.9	9.7 ± 0.6	4.1 ± 0.2	0.0453	142	142
F	0.029 ± 0.002	59 ± 9	20.1 ± 0.6	$<10^{-9}$ $\pm \text{n.d.}^{[a]}$	2.1 ± 0.1	0.0446	2	9
G	0.045 ± 0.002	--	15.8 ± 04	--	0.008 ^[b] ± 0.001	0.05089	1283	1277
H (3)	0.06 ± 0.01	129 ± 20	12.6 ± 0.3	--	0.0005 ^[b] ± 0.0002	0.05089	783	783

^[a] n.d. (not determined), the rate constant approaches zero and its error is very large,

^[b] for models G and H, the third step is bimolecular and the rate k_3 is considered as a second order constants in units of $\mu\text{M}^{-1}\text{s}^{-1}$.

Table A4. Results of the kinetic modelling analysis of the fluorescence stopped-flow data of the TC aptamer variant A7Ap, corresponding rate constants and obtained non-linear fit quality criteria. The models A-H refer to the tested folding mechanisms shown in Table A1.

Model	k_1 / $\mu\text{M}^{-1}\text{s}^{-1}$	k_{-1} / s^{-1}	k_2 / $\mu\text{M}^{-1}\text{s}^{-1}$	k_{-2} / s^{-1}	k_3 / s^{-1}	RMSD	ΔAIC	ΔBIC
A	0.015 ± 0.001	--	4.02 ± 0.04	--	--	0.05059	1686	1673
B	0.019 ± 0.01	30 ± 3	5.24 ± 0.05	--	--	0.04763	1095	1089
C	0.009 ± 0.001	--	2.5 ± 0.1	--	33 ± 1	0.04456	444	437
D (1)	0.011 ± 0.001	9 ± 2	14.5 ± 0.2	--	3.5 ± 0.1	0.04398	316	316
E (2)	0.009 ± 0.001	--	17.7 ± 0.2	$<10^{-9}$ $\pm \text{n.d.}^{[a]}$	3.98 ± 0.05	0.04403	327	327
F	0.024 ± 0.003	104 ± 11	$<10^3$ $\pm \text{n.d.}$	$<10^4$ $\pm \text{n.d.}$	68 ± 8	0.05392	2317	2323
G	0.042 ± 0.003	--	4.3 ± 0.1	--	0.009 ^[b] ± 0.001	0.04331	164	158
H (3)	0.034 ± 0.003	28 ± 3	4.7 ± 0.1	--	0.014 ^[b] ± 0.001	0.04258	0	0

^[a] n.d. (not determined) means that the rate constant approaches zero and its error is very large,

^[b] for models G and H, the third step is bimolecular and the rate k_3 is considered as a second order constants in units of $\mu\text{M}^{-1}\text{s}^{-1}$.

Christoph Kaiser



Persönliche Angaben

Geburtsdatum	15.06.1988
Geburtsort	Rotthalmünster
Staatsangehörigkeit	deutsch
Familienstand	ledig

Akademischer Werdegang

Seit 2016	Promotion in Physikalischer Chemie Institut für Physikalische und Theoretische Chemie Goethe Universität, Frankfurt/Main Betreuer: Prof. Dr. J. Wachtveitl
2013 - 2015	Master of Science (Chemie), 1.1 (ausgezeichnet) Goethe Universität, Frankfurt/Main Masterarbeit: <i>Second Generation of Water-Soluble Spiropyrans - Time-Resolved Spectroscopic Investigations</i> Institut für Physikalische und Theoretische Chemie Betreuer: Prof. Dr. J. Wachtveitl
2009 - 2013	Bachelor of Science (Chemie), 1.6 Goethe Universität, Frankfurt/Main Bachelorarbeit: <i>Synthese höherer Silane</i> Institut für Anorganische und Analytische Chemie Betreuer: Prof. Dr. A. Terfort
2008	Allgemeine Hochschulreife, 2.0 Wilhelm-Diess-Gymnasium, Pocking

Danksagung

An erster Stelle möchte ich mich bei meinem Doktorvater, Sepp Wachtveitl, für die Möglichkeit bedanken an diesem faszinierenden Thema zu arbeiten zu dürfen, sowie für die hervorragende Betreuung und die Unterstützung während meiner gesamten Promotion. Du hast auf deine niederbayrisch-sympathische Art immer eine selbstbestimmte Arbeitsweise gefördert und mir so erlaubt meine Forschungsprojekte eigenständig zu bearbeiten. Auf wissenschaftlicher sowie persönlicher Ebene waren es bereichernde Jahre, an die ich sehr gerne zurückdenken werde.

Alexander Heckel danke ich für die Begleitung auf diesem Weg, als Zweitgutachter und ebenso als langjähriger Kooperationspartner in erfolgreichen Projekten seit meiner Masterarbeit. Auch Beatrix Süß möchte ich hier für die herzliche Betreuung und die konstruktive Unterstützung bei der Bearbeitung der RNA Themen danken.

Für das Korrekturlesen dieser Arbeit danke ich Markus Braun, aber ebenso für die vielen wissenschaftlichen Diskussionen und erleuchtenden Erklärungen undurchsichtiger Daten. Unseren Postdocs Lars Dworak und Chavdar Slavov sei in diesem Zuge ebenfalls gedankt, sowohl für Hilfestellungen an aufsässigen Lasern als auch beim Auswerten von Messungen.

Besonderer Dank gilt außerdem Sabrina Wahl, für die geduldige Betreuung meiner Masterarbeit, die Hinführung zum Thema der Photoschalter und die Integration in den Arbeitskreis. Zusammen mit Andreas Reuss und Henrik Gustmann haben wir professionell einen bedeutenden Beitrag zum SFB 902 geleistet, auch wenn unsere Vorliebe für RNA manchmal etwas zu schwinden begann. Auch Thomas Halbritter möchte ich für die konstruktive und freundschaftliche Zusammenarbeit danken, sowie für die Lehrstunden in Spiropyransynthese und Säulenchromatographie.

Auch allen Kolleg*innen, deren Namen über die Jahre den Weg auf das Türschild von Raum 227 fanden, Elias Eckert, Dinh Du Tran, Chahinez Abdellaoui, Florian Hurter und Yagmur Aydogan sei hier gedankt. Ihr wart immer mit Rat, Tat oder einem aufheiternden Spruch zur Stelle, je nachdem was es bedurfte. Mit euch als Büronachbarn war der ultraschnelle Arbeitsalltag stets wunderbar entschleunigt und meist höchst amüsant.

Der gesamten Arbeitsgruppe Wachtveitl, mit ihrer wechselnden Besetzung, danke ich von Herzen für das positive Arbeitsklima und die zahlreichen schönen Stunden zusammen, beim Justieren der Anlagen, bei mehr oder weniger gutem Kaffee im Seminarraum oder bei kaltem Bier während des Grillens, auf den grandiosen Gruppenausflügen oder in den Bergen bei unserem Institutsseminar. Wir konnten sowohl in stressigen Zeiten uns immer gegenseitig motivieren, als auch in entspannten Zeiten zusammen feiern. Teil dieser Gruppe zu sein war für mich etwas Besonderes und zugleich die ideale Rahmenbedingung für meine Promotion.

Den zahlreichen hier nicht genannten Freund*innen, Kommiliton*innen, Mitarbeiter*innen, Koautor*innen und Wegbegleiter*innen, die außerdem zum Erfolg dieser Arbeit beigetragen haben, soll hier natürlich auch gedankt sein.

Zuletzt gilt mein größter Dank meiner gesamten Familie, meinen Geschwistern Kerstin und Stefan, meinen Großeltern Therese und Georg, meinem Vater Bernd und vor allem meiner Mutter Elisabeth. Ihr habt mich immer bedingungslos unterstützt und ohne zu zögern so einige Steine aus meinem Weg entfernt. Ohne euch wäre ich heute nicht an diesem Punkt. Danke dafür, dass ihr da seid.

